Università degli Studi di Padova
Communauté Université Grenoble Alpes

Università degli Studi di Padova

Doctoral Thesis

Extending the Unstructured PEEC Method to Magnetic, Transient, and Stochastic Electromagnetic Problems

Author: Riccardo Torchio

A thesis submitted in partial fulfillment of the requirements for the degree of Doctor of Philosophy

in the

Computational Electromagnetic Lab. & G2ELab
Department of Industrial Engineering & Grenoble Electrical Engineering
Electrical Energy Engineering Curricula, XXXII cycle

Supervisors and Coordinator:

Federico Moro	(supervisor at UniPD)
Olivier Chadebec	(supervisor at G2ELab)
Gérard Meunier	(Co-supervisor at G2ELab)
Roberto Turri	(Coordinator at UniPD)

Reviewers:

Alessandro Formisano, Full Professor, Università degli Studi della Campania
Lionel Pichon, Full Professor, Directeur de Recherche CNRS, GeePs

Jury Composition:

Piergiorgio Alotto, Full Professor, Università degli Studi di Padova	(examiner)
Fabio Freschi, Associate Professor, Politecnico di Torino	(examiner)
Zhuoxiang Ren, Full Professor, Sorbonne Université	(examiner)
Jean-Luc Schanen, Full Professor, G2Elab Grenoble	(examiner)
Olivier Chadebec, Directeur de recherche, G2Elab Grenoble	(invited)
Gérard Meunier, Directeur de recherche, G2Elab Grenoble	(invited)
Federico Moro, Researcher, Università degli Studi di Padova	(invited)

Defense date: December 12, 2019

Declaration of Authorship

I, Riccardo Torchio, declare that this thesis titled, "Extending the Unstructured PEEC Method to Magnetic, Transient, and Stochastic Electromagnetic Problems" and the work presented in it are my own. I confirm that:

- This work was done wholly or mainly while in candidature for a (joint) PhD degree at the *Università degli Studi di Padova* and *Communauté Univertsité Grenoble Alpes*.
- Where I have consulted the published work of others, this is always clearly attributed.
- Where I have quoted from the work of others, the source is always given. With the exception of such quotations, this thesis is entirely my own work.
- I have acknowledged all main sources of help.
- Where the thesis is based on work done by myself jointly with others, I have made clear exactly what was done by others and what I have contributed myself.

Signed:

Date: November 8, 2019

"*Perché scrivi solo cose tristi? - Perché quando sono felice, esco.*"

Luigi Tenco

UNIVERSITÀ DEGLI STUDI DI PADOVA
COMMUNAUTÉ UNIVERSITÉ GRENOBLE ALPES

Abstract

Electrical Energy Engineering Curricula, XXXII cycle
Department of Industrial Engineering & Grenoble Electrical Engineering

Doctor of Philosophy

Extending the Unstructured PEEC Method to Magnetic, Transient, and Stochastic Electromagnetic Problems

by Riccardo Torchio

The main focus of this thesis is to extend and improve the applicability and the accuracy of the Unstructured Partial Element Equivalent Circuit (PEEC) method. The interest on this subject is spurred by the growing need of fast and efficient numerical methods, which may help engineers during the design and other stages of the production of new generation electric components.

First, the PEEC method in its unstructured form is extended to magnetic media. In this regard, two formulations are developed and compared: the first one, based on the Amperian interpretation of the magnetization phenomena, is derived from the existing literature concerning the standard (structured) version of PEEC; the second one, based on the Coulombian interpretation of the magnetization phenomena, is proposed by the author with the aim of collocating PEEC in the context of Volume Integral Equation methods.

Then, the application of low–rank compression techniques to PEEC is investigated. Two different methods are applied: the first is based on hierarchical matrices ($\mathcal{H}$ and $\mathcal{H}^2$ matrices) whereas the second is based on hierarchical–semi–separable (HSS) matrices. The two methods are compared and the main numerical issues which emerge by applying low–rank techniques to PEEC are analyzed.

Finally, the developed unstructured PEEC method is combined with the Marching On–in–Time scheme for the study of fast transient phenomena with wide range of harmonics. Moreover, two different stochastic PEEC methods are developed for uncertainty quantification analysis. The first is based on the Polynomial Chaos expansion while the second is based on the Parametric Model Order Reduction technique coupled with spectral expansion.

Acknowledgements

I would like to thank my supervisors Prof. Federico Moro, Prof. Olivier Chadebec, and Prof. Gérard Meunier for the support and motivation during my PhD. Their advices and knowledge have been precious in both research and writing activities.

My sincere thanks also goes to Prof. Piergiorgio Alotto and Prof. Paolo Bettini for their continuous support and fruitful discussions.

I thank my lab mates for the nice time shared together in the last three years and for inspiring discussions.

Finally, I would like to thank my family and friends: my parents Berardo and Mariangela, my sister Marianna and my girlfriend Martina for the patience and unceasing economical and moral support.

Contents

List of Symbols

Symbol	Name	Unit
$\mathbf{A}$	vector potential	Wbm^{-1}
$\tilde{\mathbf{a}}^{e}$	corresponding DoFs in the electric domain	Wb
$\tilde{\mathbf{a}}^{m}$	corresponding DoFs in the magnetic domain	Wb
$\tilde{\mathbf{a}}^{m_b}$	corresponding DoFs in the magnetic domain boundary	Wb
$\mathbf{A}_e$	electric vector potential	Wbm^{-1}
$\tilde{\mathbf{a}}_e^{e}$	corresponding DoFs in the electric domain	Wb
$\tilde{\mathbf{a}}_e^{m}$	corresponding DoFs in the magnetic domain	Wb
$\mathbf{A}_m$	magnetic vector potential	Cm^{-1}
$\mathbf{a}_m^{e}$	corresponding DoFs in in the electric domain	C
$\mathbf{a}_m^{m}$	corresponding DoFs in the magnetic domain	C
$\mathbf{B}$	(total) magnetic flux density field	T
$\tilde{\mathbf{b}}$	corresponding DoFs	Wb
$\mathbf{B}_{sca}$	(scattered) magnetic flux density field	T
$\mathbf{B}_{ext}$	(external) magnetic flux density field	T
$\tilde{\mathbf{b}}_0$	corresponding DoFs	Wb
$\mathbf{C}_{\Omega_c}$, $\mathbf{C}_{\Omega_d}$, $\mathbf{C}_{\Omega_e}$, $\mathbf{C}_{\Omega_m}$	primal curl matrix of conductive (c), dielectric (d), electric (e), magnetic (m), domain	-
$\tilde{\mathbf{C}}_{\Omega_c}$, $\tilde{\mathbf{C}}_{\Omega_d}$, $\tilde{\mathbf{C}}_{\Omega_e}$, $\tilde{\mathbf{C}}_{\Omega_m}$	dual curl matrix of conductive (c), dielectric (d), electric (e), magnetic (m), domain	-
$\mathbf{C}_{\Gamma_m}$	primal curl selection matrix (boundary edges) of magnetic domain	-
$\mathbf{C}^{a}_{\Omega_m}$	primal augmented curl matrix of magnetic domain	-
$\tilde{\mathbf{C}}_{\Gamma_m}$	dual curl selection matrix (boundary edges) of magnetic domain	-
$\tilde{\mathbf{C}}^{a}_{\Omega_m}$	dual augmented curl matrix of magnetic domain	-
c_0	speed of light in vacuum	ms^{-1}
$\mathbf{D}_{\Omega_c}$, $\mathbf{D}_{\Omega_d}$, $\mathbf{D}_{\Omega_e}$, $\mathbf{D}_{\Omega_m}$	primal divergence matrix of conductive (c), dielectric (d), electric (e), magnetic (m), domain	-
$\tilde{\mathbf{D}}_{\Omega_c}$, $\tilde{\mathbf{D}}_{\Omega_d}$, $\tilde{\mathbf{D}}_{\Omega_e}$, $\tilde{\mathbf{D}}_{\Omega_m}$	dual divergence matrix of conductive (c), dielectric (d), electric (e), magnetic (m), domain	-
$\mathbf{D}_{\Gamma_e}$	primal divergence selection matrix (boundary faces) of conductive domain	-
$\tilde{\mathbf{D}}_{\Gamma_m}$	dual divergence selection matrix (boundary faces) of magnetic domain	-

$\mathbf{D}^a_{\Omega_e}$	primal augmented divergence matrix of electric domain	-
$\tilde{\mathbf{D}}^a_{\Omega_m}$	dual augmented divergence matrix of magnetic domain	-
$\mathbf{D}$	electric displacement field	Cm^{-2}
$\mathbf{E}$	(total) electric field	Vm^{-1}
$\tilde{\mathbf{e}}$	corresponding DoFs	V
$\mathbf{E}_{sca}$	scattered electric field	Vm^{-1}
$\mathbf{E}_{ext}$	external electric field	Vm^{-1}
$\tilde{\mathbf{e}}_0$	corresponding DoFs	V
e_c, e_d, e_e, e_m	primal conductive (c), dielectric (d), electric (e), magnetic (m), edges	-
$\tilde{e}_c$, $\tilde{e}_d$, $\tilde{e}_e$, $\tilde{e}_m$	dual conductive (c), dielectric (d), electric (e), magnetic (m), edges	-
e^b_m	set of primal boundary magnetic edges	-
$\tilde{e}^b_m$	dual boundary magnetic edges	-
$\mathbf{F}$	amperian constitutive magnetic PEEC matrix	H
f_c, f_d, f_e, f_m	primal conductive (c), dielectric (d), electric (e), magnetic (m), faces	-
$\tilde{f}_c$, $\tilde{f}_d$, $\tilde{f}_e$, $\tilde{f}_m$	dual conductive (c), dielectric (d), electric (e), magnetic (m), faces	-
f^b_c, f^b_d, f^b_e	set of primal boundary conductive (c), dielectric (d), electric (e), faces s	-
$\tilde{f}^b_m$	set of dual boundary magnetic faces	-
$\mathbf{G}_{\Omega_c}$, $\mathbf{G}_{\Omega_d}$, $\mathbf{G}_{\Omega_e}$, $\mathbf{G}_{\Omega_m}$	primal gradient matrix of conductive (c), dielectric (d), electric (e), magnetic (m), domain	-
$\tilde{\mathbf{G}}_{\Omega_c}$, $\tilde{\mathbf{G}}_{\Omega_d}$, $\tilde{\mathbf{G}}_{\Omega_e}$, $\tilde{\mathbf{G}}_{\Omega_m}$	dual gradient matrix of conductive (c), dielectric (d), electric (e), magnetic (m), domain	-
$\tilde{\mathbf{G}}_{\Gamma_c}$	dual gradient selection matrix of conductive domain	-
$\mathbf{G}_{\Gamma_m}$	primal gradient selection matrix of magnetic domain	-
$\tilde{\mathbf{G}}^a_{\Omega_c}$, $\tilde{\mathbf{G}}^a_{\Omega_d}$, $\tilde{\mathbf{G}}^a_{\Omega_e}$	dual augmented gradient matrix of conductive (c), dielectric (d), electric (e) domain	-
$\mathbf{G}^a_{\Omega_m}$	primal augmented gradient incidence matrix of the magnetic domain	-
$\mathcal{G}_{\Omega_c}$, $\mathcal{G}_{\Omega_d}$, $\mathcal{G}_{\Omega_e}$, $\mathcal{G}_{\Omega_m}$	primal conductive (c), dielectric (d), electric (e), magnetic (m), grid	-
$\tilde{\mathcal{G}}_{\Omega_c}$, $\tilde{\mathcal{G}}_{\Omega_d}$, $\tilde{\mathcal{G}}_{\Omega_e}$, $\tilde{\mathcal{G}}_{\Omega_m}$	dual conductive (c), dielectric (d), electric (e), magnetic (m), grid	-
$\tilde{\mathcal{G}}^a_{\Omega_c}$, $\tilde{\mathcal{G}}^a_{\Omega_d}$, $\tilde{\mathcal{G}}^a_{\Omega_e}$, $\tilde{\mathcal{G}}^a_{\Omega_m}$	dual augmented conductive (c), dielectric (d), electric (e), magnetic (m), grid	-
$\mathcal{G}^a_{\Omega_m}$	primal augmented magnetic grid	-
g_0	static green function	m^{-1}
g	dynamic green function	m^{-1}
$\mathbf{H}$	(total) magnetic field	Am^{-1}

$\mathbf{h}$	corresponding DoFs	A
$\mathbf{H}_{sca}$	(scattered) magnetic field	Am^{-1}
$\mathbf{H}_{ext}$	(external) magnetic field	Am^{-1}
$\mathbf{h}_0$	corresponding DoFs	A
i	imaginary unit	-
$\mathbf{J}_a$	volume amperian current density	Am^{-2}
$\mathbf{j}_a$	corresponding DoFs	A
$\mathbf{J}_c$	conduction current density	Am^{-2}
$\mathbf{j}_c$	corresponding DoFs	A
$\mathbf{J}_d$	polarization current density	Am^{-2}
$\mathbf{j}_d$	corresponding DoFs	A
$\mathbf{J}_e$	electric current density	Am^{-2}
$\mathbf{j}_e$	corresponding DoFs	A
$\mathbf{J}_e^{tot}$	total electric current density	Am^{-2}
$\mathbf{j}_e^{tot}$	corresponding DoFs	A
$\mathbf{J}_m$	magnetic current density	Vm^{-2}
$\mathbf{j}_m$	corresponding DoFs	V
$\mathbf{J}_m^{tot}$	total magnetic current density	Vm^{-2}
$\mathbf{j}_m^{tot}$	corresponding DoFs	V
$\mathbf{K}_a$	surface amperian current density	Am^{-1}
$\mathbf{k}_a$	corresponding DoFs	A
$\mathbf{K}_e^m$	electric–to–magnetic PEEC matrix	-
$\tilde{\mathbf{K}}_m^e$	magnetic–to–electric PEEC matrix	-
$\mathbf{L}_e^e$, $\mathbf{L}_m^m$, $\mathbf{L}_m^e$, $\mathbf{L}_e^m$	(volume) electric inductance PEEC matrices	H
$\mathbf{L}_{\Gamma_m}^e$, $\mathbf{L}_e^{\Gamma_m}$, $\mathbf{L}_{\Gamma_m}^m$, $\mathbf{L}_m^{\Gamma_m}$	(volume–surface) electric inductance PEEC matrices	
$\mathbf{L}_{\Gamma_m}^{\Gamma_m}$	(surface) electric inductance PEEC matrices	
$\tilde{\mathbf{L}}_m^m$	(volume) magnetic inductance PEEC matrices	F
$\mathbf{M}$	magnetization	Am^{-1}
$\mathbf{m}$	corresponding DoFs	A
$\mathbf{M}_{1/\varepsilon_0}$	projection matrix $\frac{1}{\varepsilon_0}$	F^{-1}
$\tilde{\mathbf{M}}_{1/\mu_0}$	projection matrix $\frac{1}{\mu_0}$	H^{-1}
$\mathbf{N}_e^m$	(discrete–hodge) electric–to–magnetic PEEC matrix	H
$\tilde{\mathbf{N}}_m^e$	(discrete–hodge) magnetic–to–electric PEEC matrix	F
n_c, n_d, n_e, n_m	primal conductive (c), dielectric (d), electric (e), magnetic (m), nodes	-
$\tilde{n}_c$, $\tilde{n}_d$, $\tilde{n}_e$, $\tilde{n}_m$	dual conductive (c), dielectric (d), electric (e), magnetic (m), nodes	-
$\tilde{n}_c^b$, $\tilde{n}_d^b$, $\tilde{n}_e^b$	dual boundary conductive (c), dielectric (d), electric (e), nodes	-
n_m^b	primal boundary magnetic nodes	-
$\mathbf{P}$	polarization current density	$\mathrm{Am}^{-2}\mathrm{s}$
$\mathbf{p}$	corresponding DoFs	A s

$\mathbf{P}_e^{vv}$	volume electric potential PEEC matrix	
$\mathbf{P}_e^{ss}$	surface electric potential PEEC matrix	F^{-1}
$\mathbf{P}_e^{vs}$, $\mathbf{P}_e^{sv}$	volume–surface electric potential PEEC matrix	
$\tilde{\mathbf{P}}_m^{vv}$	volume magnetic potential PEEC matrix	
$\tilde{\mathbf{P}}_m^{ss}$	surface magnetic potential PEEC matrix	H^{-1}
$\tilde{\mathbf{P}}_m^{vs}$, $\tilde{\mathbf{P}}_m^{sv}$	volume–surface magnetic potential PEEC matrix	
$\mathbf{R}_e$	resistance electric PEEC matrix	Ω
$\tilde{\mathbf{R}}_m$	resistance magnetic PEEC matrix	S
$\mathbf{r}$	field point	m
$\mathbf{r}'$	integration point	m
v_c, v_d, v_e, v_m	primal conductive (c), dielectric (d), electric (e), magnetic (m), volumes	-
$\tilde{v}_c$, $\tilde{v}_d$, $\tilde{v}_e$, $\tilde{v}_m$	dual conductive (c), dielectric (d), electric (e), magnetic (m), volumes	-
$\mathbf{w}^f$	Whitney face shape function	m^{-2}
$\mathbf{w}^e$	Whitney edge shape function	m^{-1}
α_m	magnetic material coefficient	Hm^{-1}
β	propagation constant	m^{-1}
Γ_c, Γ_d, Γ_e, Γ_m, Γ_a	boundary of conductive (c), dielectric (d), electric (e), magnetic (m), active (a) domain	-
$\bar{\Gamma}_c$, $\bar{\Gamma}_d$, $\bar{\Gamma}_e$, $\bar{\Gamma}_m$	set of surfaces of discontinuity for $\mathbf{J}_c$, $\mathbf{J}_d$, $\mathbf{J}_e$, $\mathbf{J}_m$,	-
ε_0	vacuum electric permittivity	Fm^{-1}
ε_r	relative electric permittivity	-
λ	electromagnetic wavelength	m
μ_0	vacuum magnetic permeability	Hm^{-1}
μ_r	relative magnetic permeability	-
ρ_c	electric resistivity	$\Omega\,\mathrm{m}$
ρ_d	equivalent electric resistivity for dielectric media	$\Omega\,\mathrm{m}$
ρ_e	equivalent electric resistivity	$\Omega\,\mathrm{m}$
ρ_m	magnetic resistivity	$\mathrm{S\,m}$
ϱ_c	free volume electric charge density	Cm^{-3}
$\mathbf{q}_c^v$	corresponding DoFs	C
ϱ_d	bound volume polarization charge density	Cm^{-3}
$\mathbf{q}_d^v$	corresponding DoFs	C
ϱ_e	volume electric charge density	Cm^{-3}
$\mathbf{q}_e^v$	corresponding DoFs	C
ϱ_m	bound volume magnetic charge density	Wbm^{-3}
$\tilde{\mathbf{q}}_m^v$	corresponding DoFs	Wb
σ_c	electric conductivity	Sm^{-1}
σ_d	equivalent electric conductivity for dielectric media	Sm^{-1}

σ_e	equivalent electric conductivity	Sm^{-1}
σ_m	magnetic conductivity	$\Omega\mathrm{m}^{-1}$
ς_c	free surface electric charge density	Cm^{-2}
$\mathbf{q}_c^s$	corresponding DoFs	C
ς_d	bound surface polarization charge density	Cm^{-2}
$\mathbf{q}_d^s$	corresponding DoFs	C
ς_e	surface electric charge density	Cm^{-2}
$\mathbf{q}_e^s$	corresponding DoFs	C
ς_m	bound surface magnetic charge density	Wbm^{-2}
$\tilde{\mathbf{q}}_m^s$	corresponding DoFs	Wb
φ_e	electric scalar potential	V
$\tilde{\boldsymbol{\phi}}_e$	corresponding DoFs	V
φ_m	magnetic scalar potential	A
$\boldsymbol{\phi}_m$	corresponding DoFs	A
Ω_c, Ω_d, Ω_e, Ω_m, Ω_a	conductive (c), dielectric (d), electric (e), magnetic (m), active (a) domain	-
Ω_0	inactive domain	-

Chapter 1

General introduction

1.1 Context

In recent years, many industrial sectors are facing a progressive electrification. For instance, in the automotive industry (which is probably one of the most affected industrial sectors), the interest in the development of full and hybrid electric vehicles is constantly growing, which is a crucial point in the discussion concerning global warming and environmental awareness.

Moreover, other industrial contexts are facing an increasing electrification with the aim of improving the efficiency and the accuracy of the devices and to contribute in the safety and security of people and environmental protection [1].

Thus, more and more sophisticated and dense electric and electronic systems will be embedded in several kind of complex devices (e.g. electric and traditional vehicles, see Fig. 1.1) leading to an increasing need for numerical simulations, required during the design of new components and other steps of the process, e.g. pre-certification.

In this framework, one of the main issue that engineers have to face concerns the study of Electromagnetic Interferences (EMI), which may compromise the functionality and the efficiency of the electric components, and then of the overall device.

Most of the new generation electric components is based on the Printed Circuit Board (PCB) technology. Thus, such components often include very thin conductive traces (e.g. thickness from 35 μm to 70 μm) printed on multi layers dielectric supports and ferrite magnetic cores (e.g.

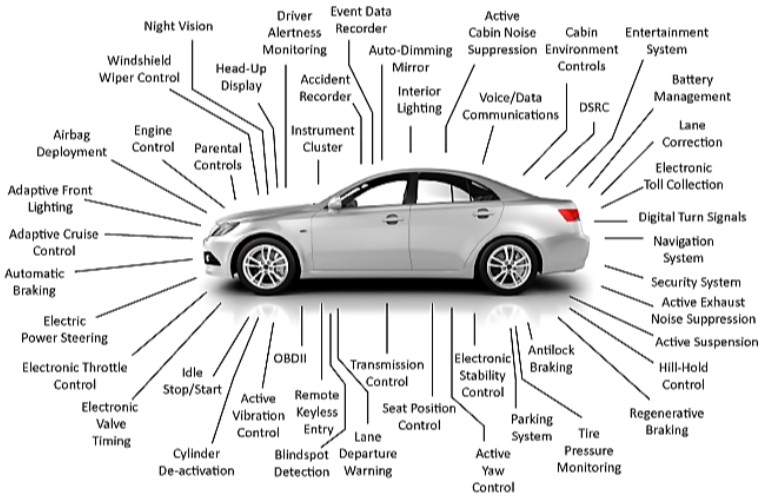

Figure 1.1: Electric and electronic devices in a standard vehicle.

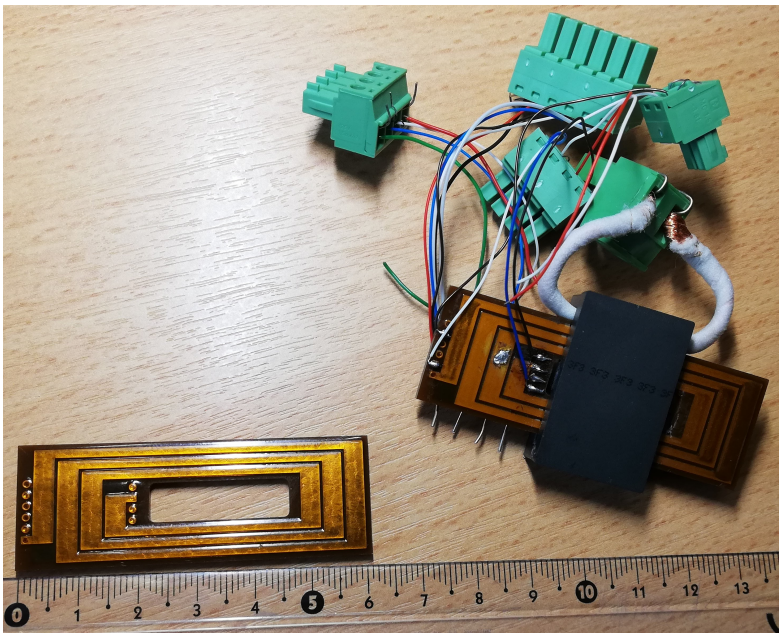

Figure 1.2: L–C–T transformer, thin conductive traces printed on multilayer dielectric substrates and ferrite magnetic core.

Fig. 1.2 shows an L–C–T transformer device [2]). The characteristic dimension of these devices is usually between 5 cm to 30 cm and the working frequency is in the range of 20 MHz to 200 MHz. From the electromagnetic analysis point of view, these geometrical and operational features require to include both inductive and capacitive effects in the numerical simulations. Moreover, in some cases (e.g. antennas for wireless communication), the electromagnetic devices cannot be considered electrically small and the time delays on the propagation of the electromagnetic fields must be considered.

Furthermore, nowadays electromagnetic devices are often connected with power conditioning units, which requires a comprehensive circuit interpretation (e.g. inverters). Thus, when devices are connected with those modeled by means of lumped circuit components, a coupled electromagnetic-circuit problem should be considered.

1.2 Finite Element Method vs Integral Equation Method. A quick survey

One of the most popular methods for the solution of (low–frequency) electromagnetic problems is the well–known Finite Element Method (FEM), which relies on the differential formulation of the Maxwell's equations [3]. Such a method has been widely studied and optimized for the solution of several kind of electromagnetic problems (e.g electrostatic, magneto-static, magneto quasi-static, full–wave) involving all kinds of electromagnetic material (i.e. inhomogeneous, anisotropic, non–linear media) and it has been efficiently coupled also with other physics, e.g. thermodynamics.

Beyond its wide generality and level of optimization, the FEM method shows some critical issues when applied to problems of the kind described in the previous section. Indeed, one of the main features of FEM is the need of discretizing both the active (i.e. conductive, dielectric different from vacuum, and magnetic media) and inactive domains (e.g. the air). Moreover,

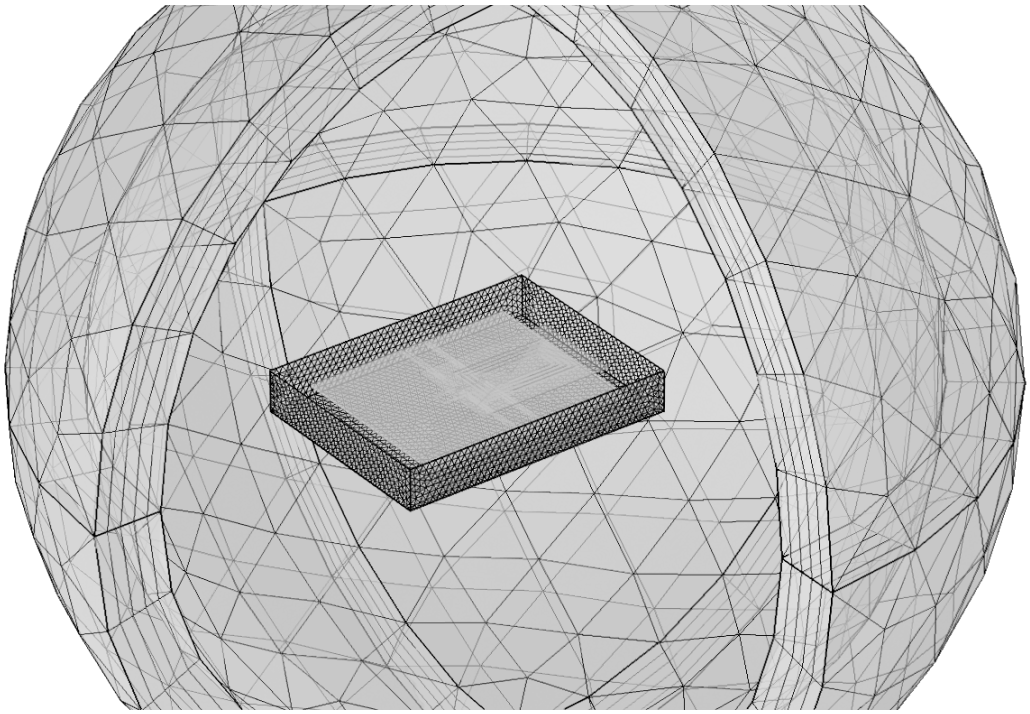

Figure 1.3: Near Field Communication Antenna, FEM model and mesh (only some domains are shown for clarity).

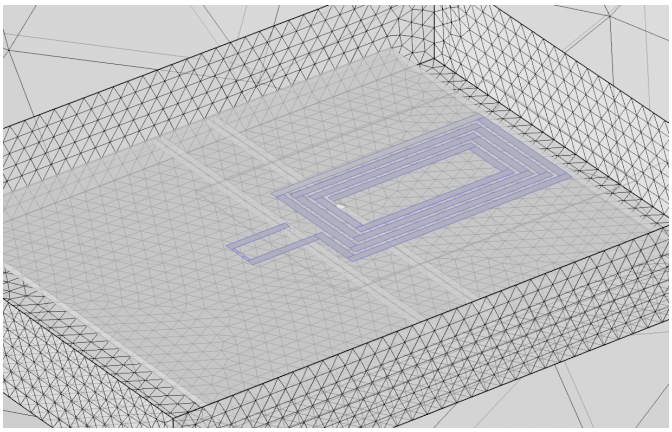

Figure 1.4: Near Field Communication Antenna, detail of the FEM model and mesh (only some domains are shown for clarity).

when an open boundary problem is solved by means of FEM, the computational domain must be restricted to a *big enough* space portion which surrounds the devices and an *artificial* boundary condition must be typically imposed; although special techniques exist.

Thus, when small geometrical details and thin conductive parts (such as the car body or conductive traces printed on multilayer dielectric substrates) must be discretized, FEM easily incurs in prohibitive computational costs. Moreover, also the time required for the construction of the model and its discretization is often considerable and requires a great expertise by the final software users (e.g. see Fig. 1.3 and Fig. 1.4 for the case of a Near Field Communication antenna). On the other hand, the final algebraic system of equations obtained from FEM is usually very sparse and, over the years, a lot of efficient numerical techniques have been developed to efficiently solve it (e.g. iterative solvers combined with ad-hoc preconditioning techniques).

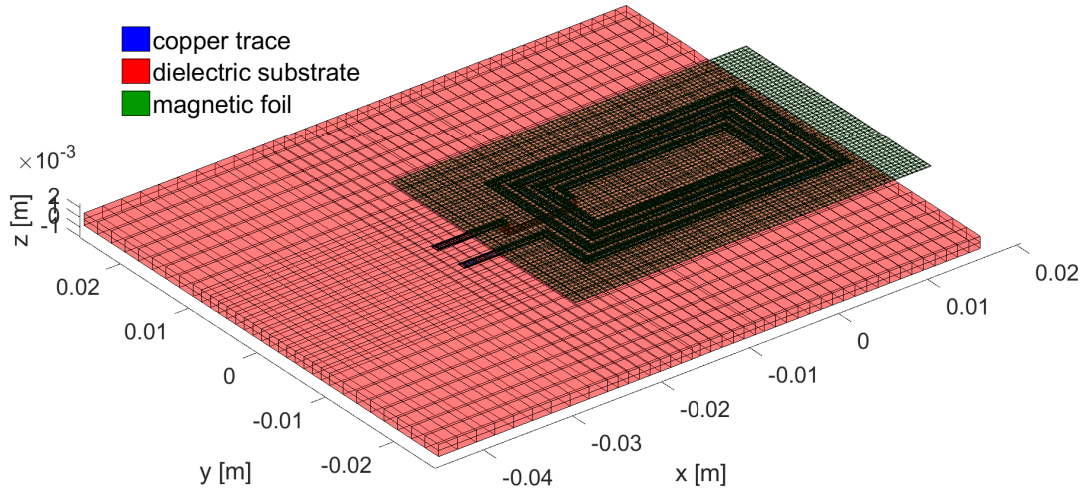

Figure 1.5: Near Field Communication Antenna (IEM model and mesh).

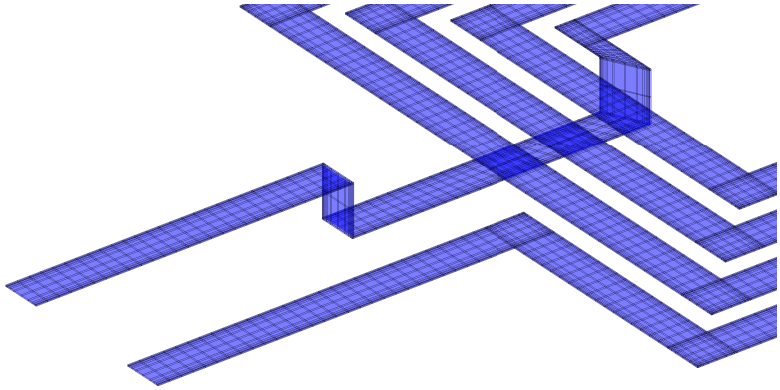

Figure 1.6: Near Field Communication Antenna (detail of IEM model and mesh for the conductive copper trace).

As an alternative to FEM, Integral Equation Methods (IEMs) can be adopted. Two big families of IEMs are: the Volume Integral Equation (VIE), which relies on the Volume Equivalence Principle (VEP), and the Surface Integral Equation (SIE), which relies on the Surface Equivalence Principle (SEP) [4]. Then, other integral approaches such as the Boundary Element Method (BEM) have also been introduced [5].

Contrary to FEM, VIE and SIE rely on the integral formulation of the Maxwell's equations. IEMs have been mostly developed in the context of high frequency electromagnetic problems. Indeed, with the increase of the frequency, the propagation of the electromagnetic fields becomes more significant and the FEM method would require a larger computational domain (or the adoption of sophisticated boundary conditions, e.g. perfectly matched layers) which would results in an increasing computational effort. One of the most characteristic features of IEMs is the need of discretizing the active domains only (or just their boundaries in the context of SIE). Thus, with respect to FEM, IEMs allow for a very fast discretization of the models, without the need of significant expertise by the final users (see Fig. 1.5 and Fig. 1.6).

However, the main drawback of IEMs is the generation of dense algebraic systems of equations which suffer from quadratic complexity in terms of storage and basic arithmetic operations.

Moreover, the use of iterative methods combined with preconditioning techniques is still a matter of research in the context of IEMs [6]. Thus, the only possible solution is often the adoption of direct solvers (e.g. LU decomposition) which however suffer from cubic complexity with respect to the amount of degrees of freedom.

With the aim of reducing the computational cost of IEMs, over the years, several low–rank compression techniques have been developed [7]. In the electromagnetic and acoustic framework, one of the most popular and oldest method adopted for matrix compression is probably the Fast Multiple Method (FMM) [8, 9]. Such method requires an explicit knowledge of the kernel function resulting in problem-dependent method. Nevertheless, FMM efficiently allows reducing the complexity of the storage and the assembly of IEMs systems of equations.

More recently, different algebraic compression techniques have been developed. Such new techniques are mostly based on Hierarchical matrix representation coupled with Adaptive Cross Approximation (a purely algebraic method) or Hybrid Cross Approximation (a semi-analytical method) [10, 11]. Such numerical methods are usually very general tools (contrary to FMM, they do not require the explicit knowledge of the kernel function) and allow for increasing the size of the largest solvable problem. Thus, in most of the cases, their use becomes mandatory. Such methods provide a great speed up in algebraic operations, such as matrix multiplication and solution of linear systems of equations.

In the last years, the development of these new compression techniques has boosted the interest on IEMs also for the study of low and medium frequency electromagnetic problems.

Finally, for the sake of completeness, it is worth noting that numerical methods which combine the features of FEM and IEMs have been actually developed, e.g. FEM coupled with Boundary Element Method (FEM–BEM). These methods allows merging the advantages of FEM and IEMs but they also introduce other numerical issues. Thus, it can be stated that a general and multi–purpose numerical method which allows efficiently solving all the kind of electromagnetic problems does not currently exist.

1.3 The Partial Element Equivalent Circuit method

The Partial Element Equivalent Circuit (PEEC) method was first introduced by A. Ruehli in the 70s for the solution of electromagnetic problems coupled with lumped circuit components [12].

PEEC is a particular form of VIE in which the discretization approach provides a useful circuit interpretation of the electromagnetic problem [13]. Indeed, the geometric entities of the mesh are interpreted as electric circuit nodes and branches (see Fig. 1.7), which can be easily connected with lumped circuit components. Thus, the final electromagnetic–circuit problem is interpreted as an equivalent and fully coupled circuit (i.e. the discretized domains) possibly connected with a lumped external circuit.

In the original form, only conductive media were considered in PEEC models. Later, the method was extended to include dielectric regions with electric properties different from those of vacuum [14] and numerous extensions have been proposed to consider, e.g., retardation effects and incident fields [15, 16]. More recently, the method was extended to magnetic media under the quasi–static assumption [17].

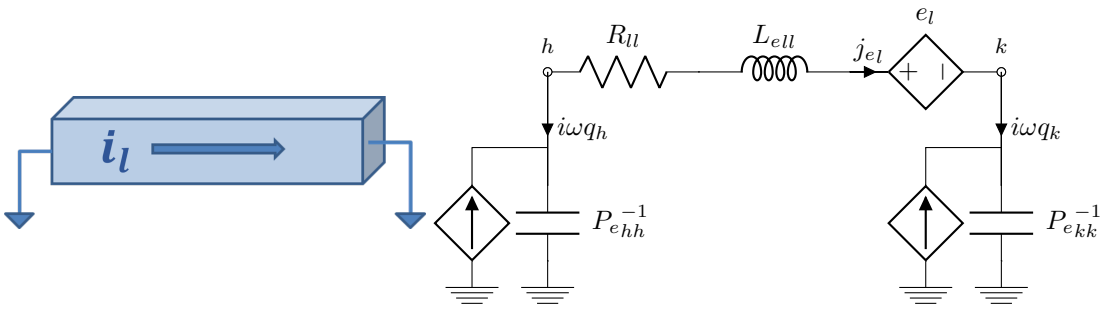

Figure 1.7: PEEC method: from physical discretization to equivalent circuit.

For historical reasons, the PEEC method was initially developed and extended outside the context of VIE. Indeed, in the 70s, due to the limited computing power, the studied systems were made by very coarse meshes and, at that time, the main interest on the PEEC method was the possibility to include electromagnetic interactions between poorly discretized devices in the (even large) circuit problem. Thus, the final electromagnetic–circuit problem mainly consisted of lumped circuit components, therefore it was natural to solve it by means of Spice–like solvers. For this reason, PEEC was mostly related to the use of Spice–like solvers in the context of coupled circuit problems [18].

However, with the massive increase of the computing power and available RAM for standard workstations, the interest in performing increasingly complex and computationally expensive electromagnetic simulations has grown.

This, together with the progressive electrification and the development of more and more sophisticated and dense electric and electronic systems, spurred renewed interest in the PEEC method which provides the advantages of standard IEMs together with a useful circuit interpretation. However, nowadays the coupled electromagnetic–circuit problem is usually more biased toward to the electromagnetic problem rather than the circuit one. Indeed, compared to the past, the current computing power allows for very fine discretizations of the devices.

Thus, for these reasons, although the basic theory of PEEC method has not changed, nowadays different solution strategies are more likely to be applied for the solution of the PEEC problem, which is also used in contexts other than those of the past [19]. Moreover, for the different nature of the problems of interest, the formulation and the theoretical background of PEEC have been changed in the recent years and by different communities, leading to some difficulties and misunderstandings in the definition of what PEEC is and what it is not [20].

Another important aspect which usually creates some misunderstanding is the discretization process adopted for the PEEC method.

Indeed, in the original PEEC method a peculiar discretization process was adopted. The discretization process of the PEEC method was ruled by the main goal of providing a direct circuit interpretation of the mesh of the modeled devices [13]. However, beyond its intuitiveness, such discretization method only allowed for structured meshes (Manhattan type) and zero order shape functions (Fig. 1.8). Moreover, the assumptions made in the derivation of such scheme sometimes lacked of a systematic background and may lead to a un–precise numerical method [21] since the property of the electromagnetic unknowns are not strongly enforced.

In recent years, the PEEC discretization scheme has been re–formulated introducing the concept of *duality* and *primal* and *dual* grids (Fig. 1.8). The unstructured PEEC discretization scheme was pioneeringly introduced in [21] for equivalent surface conductive models where the

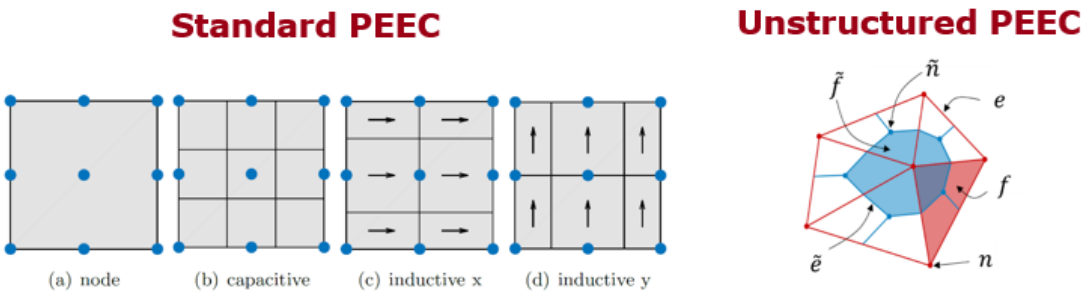

Figure 1.8: PEEC method, standard discretization vs unstructured discretization. 2–D model.

concepts of primal and dual grids (common to the Cell Method discretization approach [22]) have been introduced in the framework of the PEEC discretization. Then, the unstructured PEEC discretization was extended to the case of volume conductive and dielectric media [6, 23]. Moreover, this theoretically sound formalization of the PEEC tessellation allows for the study of structured and unstructured meshes without any particular additional effort and the electromagnetic properties of the unknowns are naturally and strongly imposed.

In recent years, both the original and the unstructured PEEC methods have been extended and adopted by different communities. The original PEEC method is usually named as *Standard*–PEEC method while the unstructured version introduced in [21] has been named as *Dual*–PEEC [24] or *Unstructured*–PEEC [6].

1.4 Aim of the thesis

The main goal of the work is to extend the applicability of the Unstructured–PEEC method and improve its efficiency and accuracy.

In this regard, the extension of the Unstructured–PEEC formulation for the inclusion of conductive, dielectric, and magnetic media is the first objective of the research. Moreover, the basic idea of the research is to properly collocate the PEEC method in the context of VIE, with the aim of developing a sound and rigorous formalization, taking advantage of the results and the wide research carried out in the context of VIE. Indeed, the intention is to maintain a high generality without limiting the method only to very specific cases.

Moreover, with the aim of providing at once natural and sound circuit interpretation of the electromagnetic problem, the Cell Method approach is adopted for the discretization process.

Although the thesis deals with the PEEC method in general, the extension and the improvement of the applicability of the method for the study of industrial problems (such as the ones discussed in the first section of this introduction and others which appear during the PhD thesis) is the long term goal in which this thesis is taking place.

Therefore, considerations concerning the accurate evaluation of the distribution of the electromagnetic quantities are consider as crucial aspects. Indeed, these matters strongly affect the accuracy of the evaluation of quantities of industrial interest, such as losses and EMI.

Thus, since VIE (and IEMs in general) have been mainly developed for problems of different nature (e.g. scattering), a particular attention is given to aspects that instead may be labeled as *minor* in standard VIE for high frequency problems.

Another ambitious goal of the thesis is the coupling of the PEEC method with efficient compression techniques. In this regard, this thesis aims to continue the work of a former PhD student of G2ELab, Grenoble, concerning PEEC and compression techniques [6]. A particular attention is given to the analysis of the issues which may appear when different electromagnetic problems are solved with PEEC coupled with compression techniques. Moreover, different kinds of compression techniques are investigated.

As a further goal, the thesis aims to provide a comprehensive description and analysis concerning the main numerical aspects of the Unstructured–PEEC method and it aims to provide an exhaustive reference and a starting point for future investigations and researches. For these reasons, physical and mathematical aspects which may be well–known for readers experienced in IEMs are however thoroughly discussed.

In this regard, particular attention is also given to the theoretical background concerning Maxwell's equations, the interpretation of the magnetization phenomena, and the integral representation of the electromagnetic problem. These aspects are very well–established. However, different assumptions and different interpretations are usually made by different communities (e.g. low frequency and high frequency communities). Thus, the author believes that misunderstandings may arise if such aspects are not adequately discussed.

Once obtained a proper expertise concerning the theoretical background of the Unstructured–PEEC method and after having contributed to its extension and development, the interest shifts on the combination of the PEEC method with different numerical techniques. In this regard, the study of transient phenomena with a rich harmonic content is investigated. Moreover, the application of the PEEC method in the context of stochastic analysis for uncertainty quantification is also investigated. Furthermore, the efficiency and accuracy of the developed methods are analyzed by studying challenging problems of industrial interest.

Finally, as a background goal, the thesis aims to promote international collaborations with several groups of research. In this regard, the main work has been carried out under the joint–PhD agreement between Università degli Studi di Padova, Padova, Italy, and University Grenoble Alpes, CNRS, Grenoble, (G2ELab). During the PhD activity the following collaborations have been undertaken:

- Institute for Fundamentals and Theory in Electrical Engineering, TU Graz, Austria,
- Department of Energy "G. Ferraris", Politecnico di Torino, Italy,
- Dipartimento di Elettronica, Informazione e Bioingegneria, Politecnico di Milano, Milan, Italy.

The rest of the work is organized as follows. In Chapter 2, the formulation of the PEEC method is derived and discussed. Two alternative formulations are presented: 1) The *Amperian* one, which was first proposed in [25] for the standard PEEC method and then has been developed by the author in its unstructured form [26], and 2) the *Coulombian* one, which has been mainly developed by the author during the thesis [27] and which makes it possible to collocate PEEC in the framework of VIE.

In Chapter 3, both the Amperian and the Coulombian PEEC formulations are discretized by means of the Cell Method with specific focus on inhomogeneous media and equivalent surface models.

Chapter 4 concerns the solution and the choice of the best structure of the PEEC system of equations when different electromagnetic problems are considered. Numerical issues which may arise during the solution of the PEEC problem and how to prevent them are matters of thorough discussions.

Chapter 5 instead collects the experiences and the numerical analysis concerning the coupling of the PEEC with low–rank compression techniques. Critical numerical aspects which may appear when low–rank techniques are applied to the PEEC are discussed and some possible solutions are presented.

The remaining chapters concern the extension of the PEEC method for the study of fast transient phenomena and stochastic analysis. In particular, chapter 6 concerns the coupling of the PEEC method with the Marching On–in–Time scheme for time domain analysis while in Chapter 6 the PEEC method is combined with Polynomial Chaos and Parametric Model Order Reduction techniques for uncertainty quantification analysis.

Finally, in Chapter 8 conclusions are drawn and in the appendices some secondary aspects are discussed (i.e. charge density distribution inside electromagnetic media and axisymmetric problems).

Chapter 2

PEEC formulations

This chapter deals with the development of the mathematical formulation of the PEEC method under the frequency domain assumption. The PEEC formulation is first presented in its original form, i.e. the Amperian–PEEC (A–PEEC) formulation. Then, the Coulombian–PEEC (C–PEEC) formulation, introduced by the author during the PhD research, is presented and discussed.

The aim of this chapter is to derive the integral equations which represent the electromagnetic problem. Then, these integral equations will be discretized and then numerically solved as presented in Chapter 3 and Chapter 4, respectively. Both the PEEC formulations are presented in their more general form and the most significant mathematical and physical aspects are thoroughly discussed in order to provide a complete and self–consistent presentation.

2.1 Domain definition

Since PEEC is a particular form of VIE method, only the *active domains* must be discretized and the electromagnetic interactions are considered by means of inductive and capacitive couplings. For isotropic media, the term *active domains* refers to conductive (materials with electric conductivity, σ_c, different from 0), dielectric (materials with relative electric permittivity, ε_r, different from 1), and magnetic (materials with relative permeability, μ_r, different from 1) media. These three domains are defined as Ω_c, Ω_d, and Ω_m, respectively, and $\Omega_c, \Omega_d, \Omega_m \in \mathbb{R}^3$.

When anisotropic media are considered σ_c, ε_r, and μ_r are tensor quantities, thus the definition of *active domains* must be properly changed by using tensors instead of scalars. However, the development of the mathematical formulation and its discretization is the same for both scalar and tensor material quantities. Thus, in the following (unless specifically noted otherwise), the material parameters σ_c, ε_r, and μ_r can be indistinctly considered as scalar or tensor quantities.

The three active domains can consist of non–connected sub–domains (i.e. $\Omega_c = \bigcup_k^{N_s} \Omega_{c_k}$, where N_s is the number of conductive sub–domains) and any intersection involving Ω_c, Ω_d, and Ω_m can be in general different from the empty set, as exemplified in Fig. 2.1. The active domains are surrounded by the unbounded domain $\Omega_0 \in \mathbb{R}^3 \setminus (\Omega_c \cup \Omega_d \cup \Omega_m)$, having characteristics of vacuum (inactive region). The boundaries of Ω_c, Ω_d, and Ω_m are defined as $\Gamma_c = \partial\Omega_c$, $\Gamma_d = \partial\Omega_d$, and $\Gamma_m = \partial\Omega_m$, respectively.

The union of the conductive and the dielectric domains, $\Omega_e = \Omega_c \cup \Omega_d$, is defined as the *electric domain*, having boundary $\Gamma_e = \partial\Omega_e$. Moreover, $\Omega_a = \Omega_c \cup \Omega_d \cup \Omega_m$ is defined as the *active domain* with boundary $\Gamma_a = \partial\Omega_a$.

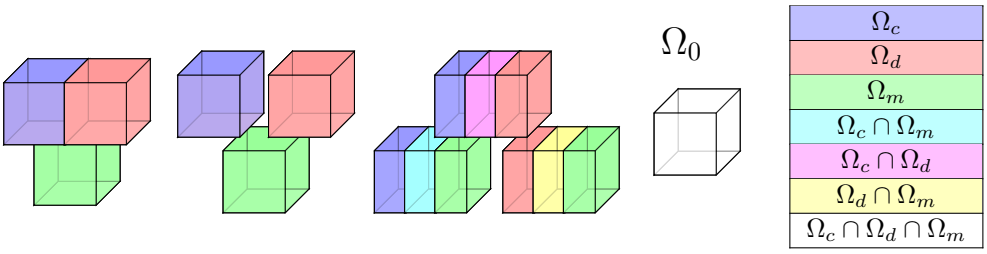

Figure 2.1: Domain subdivision and intersections.

For the sake of clarity, in this chapter homogeneous media only are considered, i.e. σ_c, ε_r, and μ_r are uniform quantities inside each kth sub–domain Ω_{c_k}, Ω_{d_k}, and Ω_{m_k}. The case of non–homogeneous materials will be treated in Chapter 3. The cases of lossless and lossy materials are both considered, while the case of nonlinear materials has not been investigated in the context of this PhD thesis.

In this and the following chapter, for the sake of generality, the full Maxwell's equations have been considered. Then, in Chapter 4, the systems of equations for the cases of quasi–static and static assumptions are derived such as particular cases of the most general one. However, by imposing *a priori* the proper assumption (static or quasi–static) ,such quasi–static and static cases could be also directly derived following the procedure of this and the next chapter.

2.2 Amperian PEEC formulation

In order to simplify the discussion and following the chronological evolution of the A–PEEC method (i.e. the PEEC method based on the amperian interpretation of the magnetization phenomena), the formulation is first developed for conductive media only. Then, the extension of the method to lossless and lossy dielectric media is given in Section 2.2.2. Finally, the more general method considering conductive, dielectric, and magnetic media is presented in Section 2.2.3.

2.2.1 Conductive media

For its great importance, the derivation of the integral equations which link the electromagnetic potentials to their sources are thoroughly discussed in this section. Therefore, the well–known *Electric Field Integral Equation* (EFIE) (i.e. the starting point of the PEEC formulation) is obtained and the final *PEEC electric equation* is then presented.

Maxwell's equations and potentials

Full Maxwell's equations in the frequency domain read [28]:

$$\begin{aligned} \nabla \cdot \mathbf{D} &= \varrho_c, \qquad & \nabla \times \mathbf{E} &= -i\omega\mathbf{B}, \\ \nabla \cdot \mathbf{B} &= 0, \qquad & \nabla \times \mathbf{H} &= \mathbf{J}_c + i\omega\mathbf{D}, \end{aligned} \tag{2.1}$$

where i is the imaginary unit, ω is the angular frequency, $\mathbf{D}$, $\mathbf{E}$, $\mathbf{B}$, and $\mathbf{H}$ are the electric displacement field, the electric field, the magnetic flux density field, and the magnetic field, respectively. ϱ_c is the free volume electric charge density and $\mathbf{J}_c$ is the conduction current density (bold letters indicate complex vectors). Since no dielectric and magnetic media are considered

in this section, the following linear constitutive (material) equations can be introduced:

$$\mathbf{D} = \varepsilon_0 \mathbf{E}, \tag{2.2}$$

$$\mathbf{B} = \mu_0 \mathbf{H}, \tag{2.3}$$

where ε_0 and μ_0 are the permittivity and permeability of vacuum, respectively.

Because $\mathbf{B}$ is divergence free, the vector potential $\mathbf{A}$ can be introduced:

$$\mathbf{B} = \nabla \times \mathbf{A}.$$

This expression for $\mathbf{B}$ can be inserted into the second equation of (2.1), yielding:

$$\nabla \times (\mathbf{E} + i\omega \mathbf{A}) = 0. \tag{2.4}$$

Then, by using the vector calculus identity

$$\nabla \times \nabla[\bullet] = 0, \tag{2.5}$$

(2.4) allows writing:

$$\mathbf{E} = -i\omega \mathbf{A} - \nabla \varphi_e, \tag{2.6}$$

where φ_e is the electric scalar potential.

It is worth noting that, in the low frequency community, $\mathbf{A}$ is usually called *magnetic vector potential*. However, in order to avoid misunderstandings with the names of the potentials defined in Section 2.3, in this work the author always refers to $\mathbf{A}$ as *vector potential*.

Integral equations for $\mathbf{A}$ and φ_e

In order to obtain an integral expression which links the electric field $\mathbf{E}$ to its sources, the integral expressions of the potentials $\mathbf{A}$ and φ_e must be obtained.

Considering the fourth equation in (2.1), since $\mathbf{H} = \frac{1}{\mu_0} \nabla \times \mathbf{A}$ and using (2.2), provides:

$$\frac{1}{\mu_0} \nabla \times (\nabla \times \mathbf{A}) = \mathbf{J}_c + i\omega \varepsilon_0 \mathbf{E}. \tag{2.7}$$

By letting (2.6) in (2.7) and applying

$$\nabla \times (\nabla \times [\bullet]) = \nabla(\nabla \cdot [\bullet]) - \nabla^2 [\bullet], \tag{2.8}$$

to the left side of the equation, one obtains

$$\frac{1}{\mu_0} (\nabla(\nabla \cdot \mathbf{A}) - \nabla^2 \mathbf{A}) = \mathbf{J}_c + i\omega \varepsilon_0 (-i\omega \mathbf{A} - \nabla \varphi_e). \tag{2.9}$$

The Lorenz gauge choice $\nabla \cdot \mathbf{A} = -i\omega \varepsilon_0 \mu_0 \varphi_e$ allows decoupling $\mathbf{A}$ from φ_e in (2.9). It should be noted that a different and interesting approach based on the Coulomb gauge could also be adopted [29] to develop an integral Equation method, however this would not lead to the traditional PEEC approach.

Therefore, (2.9) simplifies to:

$$\nabla^2 \mathbf{A} - (i\omega)^2 \mu_0 \varepsilon_0 \mathbf{A} = -\mu_0 \mathbf{J}_c, \tag{2.10}$$

or, equivalently, to

$$\Box \mathbf{A} = \mu_0 \mathbf{J}_c, \tag{2.11}$$

where $\Box = (i\omega)^2 c_0^{-2} - \nabla^2$ is the d'Alembert operator and c_0 is the speed of light in vacuum.

The solution of (2.11) can be derived from the following fundamental partial differential equation (PDE) [30, 31]:

$$\nabla^2 G(x-y) + \beta G(x-y) = -\delta(x-y), \tag{2.12}$$

where

$$G(x-y) = \frac{e^{-i\beta(x-y)}}{x-y}, \tag{2.13}$$

and $\delta(x-y)$ is the Dirac delta function and x,y,$\beta \in \mathbb{R}$.

When the frequency dependent term is negligible ($\omega^2 \mu_0 \varepsilon_0 \to 0$), i.e. low frequency assumption, (2.11) becomes the vector Poisson equation, which is solved by the following integral expression:

$$\mathbf{A}(\mathbf{r}) = \mu_0 \int_{\Omega_c} \mathbf{J}_c(\mathbf{r}') g_0(\mathbf{r}, \mathbf{r}') d\Omega', \tag{2.14}$$

where $\mathbf{r}$ is the field point and $\mathbf{r}'$ is the integration (or source) point moving in Ω_c and

$$g_0(\mathbf{r}, \mathbf{r}') = \frac{1}{4\pi r}, \tag{2.15}$$

is the *static Green's function* (derived from (2.13)) and $r = \parallel \mathbf{r} - \mathbf{r}' \parallel$ is the distance between the two points .

When the low frequency assumption does not hold, the effect of the time delay on the field's propagation must be taken into account, so that the solution of (2.11) becomes:

$$\mathbf{A}(\mathbf{r}) = \mu_0 \int_{\Omega_c} \mathbf{J}_c(\mathbf{r}') g(\mathbf{r}, \mathbf{r}') d\Omega', \tag{2.16}$$

where

$$g(\mathbf{r}, \mathbf{r}') = e^{-i\beta r} g_0(\mathbf{r}, \mathbf{r}'), \tag{2.17}$$

is the *dynamic Green's function* and $\beta = \frac{\omega}{c_0}$ is the propagation constant.

In (2.14), the single value of $\mathbf{J}_c(\mathbf{r}')$, in a specific point $\mathbf{r}'$, gives a contribution to the vector potential $\mathbf{A}(\mathbf{r})$ *in phase* with itself, while in (2.16), $\mathbf{J}_c(\mathbf{r}')$ and its contribution to $\mathbf{A}(\mathbf{r})$ are generally out of phase by a quantity equal to βr; this is the role of the exponential term in the expression of $g(\mathbf{r}, \mathbf{r}')$. The corresponding time domain integral expression links $\mathbf{A}(\mathbf{r}, t)$ to $\mathbf{J}_c(\mathbf{r}', t')$, where $t' = t - \frac{r}{c}$ and, with a slight abuse of notation, $\mathbf{A}(\mathbf{r}, t)$ and $\mathbf{J}_c(\mathbf{r}', t')$ are now considered as real vectors and not as phasor vectors.

For low frequency electromagnetic problems (i.e. when $l << \lambda$, where l is the characteristic dimension of the computational domain and λ is the electromagnetic wavelength) the time delay

effects can be neglected, i.e. (2.14) can be adopted instead of (2.16). In the following discussion, for the sake of generality, (2.16) is considered, but a low frequency PEEC formulation can be easily derived by substituting $g(\mathbf{r},\mathbf{r}')$ with $g_0(\mathbf{r},\mathbf{r}')$. Comments on the low frequency assumption are given when required.

From (2.16), and with the Lorenz gauge assumption, an integral expression for φ_e can be obtained:

$$-i\omega\varphi_e(\mathbf{r}) = \frac{\nabla\cdot\mathbf{A}(\mathbf{r})}{\varepsilon_0\mu_0} = \varepsilon_0^{-1}\int_{\Omega_c}\nabla\cdot(\mathbf{J}_c(\mathbf{r}')g(\mathbf{r},\mathbf{r}'))d\Omega', \tag{2.18}$$

where the symbol ∇ operates with respect to the field point $\mathbf{r}$.

Then, the vector calculus identity:

$$\nabla\cdot(\alpha\mathbf{\Lambda}) = \alpha\nabla\cdot\mathbf{\Lambda} + \nabla\alpha\cdot\mathbf{\Lambda}, \tag{2.19}$$

where $\mathbf{\Lambda}$ is a vector field and α is a scalar field, can be used to derive an integral expression for the electric scalar potential φ_e from (2.18).

By applying (2.19) to the integrand of (2.18), one obtains:

$$\nabla\cdot(\mathbf{J}_c(\mathbf{r}')g(\mathbf{r},\mathbf{r}')) = g(\mathbf{r},\mathbf{r}')\nabla\cdot\mathbf{J}_c(\mathbf{r}') + \nabla g(\mathbf{r},\mathbf{r}')\cdot\mathbf{J}_c(\mathbf{r}'). \tag{2.20}$$

Noting that $\nabla\cdot\mathbf{J}_c(\mathbf{r}') = 0$ [30], and applying $\nabla g(\mathbf{r},\mathbf{r}') = -\nabla' g(\mathbf{r},\mathbf{r}')$ [30], where ∇' means that the operator ∇ operates on $\mathbf{r}'$, (2.18) can be written as:

$$-i\omega\varphi_e(\mathbf{r}) = -\varepsilon_0^{-1}\int_{\Omega_c}\mathbf{J}_c(\mathbf{r}')\cdot\nabla' g(\mathbf{r},\mathbf{r}')d\Omega'. \tag{2.21}$$

As proposed in [23] and by the author in [27], this equation can be directly adopted for the development of a PEEC method. However, with the aim of presenting the formulation related to the canonical PEEC method, (2.21) must be further handled.

Applying the identity (2.19) to the integrand of (2.21), the following expression can be obtained:

$$i\omega\varphi_e(\mathbf{r}) = \varepsilon_0^{-1}\left[\int_{\Omega_c}\nabla'\cdot(\mathbf{J}_c(\mathbf{r}')g(\mathbf{r},\mathbf{r}'))d\Omega' - \int_{\Omega_c} g(\mathbf{r},\mathbf{r}')\nabla'\cdot\mathbf{J}_c(\mathbf{r}')d\Omega'\right]. \tag{2.22}$$

Now, we have to define the following continuity equations for $\mathbf{J}_c$:

$$\nabla'\cdot\mathbf{J}_c(\mathbf{r}') = -i\omega\varrho_c(\mathbf{r}'), \qquad \left(\mathbf{J}_c^+(\mathbf{r}') - \mathbf{J}_c^-(\mathbf{r}')\right)\cdot\mathbf{n} = -i\omega\varsigma_c(\mathbf{r}'), \tag{2.23}$$

where ς_c is the *free surface electric charge density* laying on a surface over which $\mathbf{J}_c$ is discontinuous; the superscripts $+$ and $-$ indicate the two sides of the surface, and $\mathbf{n}$ is the outgoing unit norm vector. The set of these surfaces of discontinuity is indicated by $\bar{\Gamma}_c$. When only homogeneous media are considered, as assumed in this chapter, the only surface of discontinuity is the boundary of Ω_c, thus $\bar{\Gamma}_c = \Gamma_c$ and the second equation in (2.23) reduces to:

$$\mathbf{J}_c^-(\mathbf{r}')\cdot\mathbf{n} = i\omega\varsigma_c(\mathbf{r}') \rightarrow \mathbf{J}_c(\mathbf{r}')\cdot\mathbf{n} = i\omega\varsigma_c(\mathbf{r}'). \tag{2.24}$$

Indeed the *positive side* of the surface belongs to Ω_0, thus $\mathbf{J}_c^+(\mathbf{r}') = 0$.

The divergence theorem can be applied to the first integral of (2.22):

$$\int_{\Omega_c} \nabla' \cdot (\mathbf{J}_c(\mathbf{r}')g(\mathbf{r},\mathbf{r}'))d\Omega' = \int_{\bar{\Gamma}_c} \left(\mathbf{J}_c^+(\mathbf{r}') - \mathbf{J}_c^-(\mathbf{r}')\right) \cdot \mathbf{n}\; g(\mathbf{r},\mathbf{r}')d\Gamma'. \tag{2.25}$$

By using these relationships, the final integral expression for φ_e is obtained:

$$\varphi_e(\mathbf{r}) = \varepsilon_0^{-1}\left[\int_{\bar{\Gamma}_c} \varsigma_c(\mathbf{r}')g(\mathbf{r},\mathbf{r}')d\Gamma' + \int_{\Omega_c} \varrho_c(\mathbf{r}')g(\mathbf{r},\mathbf{r}')d\Omega'\right]. \tag{2.26}$$

As stated above, since only homogeneous media are considered in this chapter, $\bar{\Gamma}_c$ can be substituted with Γ_c. It must be noticed that the free volume electric charge density ϱ_c is completely negligible in almost all engineering problems. This argument is further discussed in the Appendix A. However, for the sake of clarity and generality, ϱ_c is maintained during the development of the formulation.

EFIE, Electric Field Integral Equation

The derivation of the *Electric Field Integral Equation* [31] is now straightforward. In (2.6), $\mathbf{A}$ can be substituted with (2.16), whereas φ_e can be substituted with (2.26), yelling:

$$\mathbf{E}(\mathbf{r}) = -i\omega\mu_0 \int_{\Omega_c} \mathbf{J}_c(\mathbf{r}')g(\mathbf{r},\mathbf{r}')d\Omega' - \nabla\left[\varepsilon_0^{-1}\int_{\bar{\Gamma}_c} \varsigma_c(\mathbf{r}')g(\mathbf{r},\mathbf{r}')d\Gamma' + \varepsilon_0^{-1}\int_{\Omega_c} \varrho_c(\mathbf{r}')g(\mathbf{r},\mathbf{r}')d\Omega'\right], \tag{2.27}$$

where $\mathbf{E}$ is directly linked to its sources: the current density $\mathbf{J}_c$ and the charge densities ϱ_c and ς_c.

By using (2.23), the EFIE can also be rearranged in order to relate $\mathbf{E}$ to $\mathbf{J}_c$ only:

$$\begin{aligned}\mathbf{E}(\mathbf{r}) = &- i\omega\mu_0 \int_{\Omega_c} \mathbf{J}_c(\mathbf{r}')g(\mathbf{r},\mathbf{r}')d\Omega' \\ &- \frac{\nabla}{i\omega\varepsilon_0}\left[\int_{\bar{\Gamma}_c} \left(\mathbf{J}_c^+(\mathbf{r}') - \mathbf{J}_c^-(\mathbf{r}')\right) \cdot \mathbf{n} g(\mathbf{r},\mathbf{r}')d\Gamma' - \int_{\Omega_c} \nabla' \cdot \mathbf{J}_c(\mathbf{r}')g(\mathbf{r},\mathbf{r}')d\Omega'\right].\end{aligned} \tag{2.28}$$

Since ω appears in the denominator of the second part of the right side of the equation, this expression of the EFIE can only be used when the frequency is different from zero.

PEEC electric equation

Now the attention is focused on the derivation of the equation that will be discretized in Chapter 3. The total electric field, $\mathbf{E}$, is split into the scattered electric field, $\mathbf{E}_{sca}$, and the external electric field, $\mathbf{E}_{ext}$, as

$$\mathbf{E} = \mathbf{E}_{sca} + \mathbf{E}_{ext}. \tag{2.29}$$

Inside conductive media (Ω_c), Ohm's law, which locally links the total electric field, $\mathbf{E}$, to the conduction current density, $\mathbf{J}_c$, is given by:

$$\mathbf{E}(\mathbf{r}) = \rho_c(\mathbf{r})\mathbf{J}_c(\mathbf{r}) = \frac{\mathbf{J}_c(\mathbf{r})}{\sigma_c(\mathbf{r})}, \tag{2.30}$$

where $\rho_c = \sigma_c^{-1}$ is the electric resistivity. Instead, the scattered electric field, $\mathbf{E}_{sca}$, is given by the EFIE, (2.27) or (2.28).

The external electric field (incident electric field), $\mathbf{E}_{ext}$, is the field produced by external sources (current and/or charge densities) that are not considered inside the computational domain $\Omega = \Omega_a \cup \Omega_0$. Thus, the following *PEEC electric equation* can be obtained:

$$\mathbf{E}_{ext}(\mathbf{r}) = \mathbf{E}(\mathbf{r}) - \mathbf{E}_{sca}(\mathbf{r}), \tag{2.31}$$

that, by choosing (2.27), in explicit form becomes:

$$\begin{aligned}\mathbf{E}_{ext}(\mathbf{r}) =& \frac{\mathbf{J}_c(\mathbf{r})}{\sigma_c(\mathbf{r})} + i\omega\mu_0 \int_{\Omega_c} \mathbf{J}_c(\mathbf{r}')g(\mathbf{r},\mathbf{r}')d\Omega' \\ &+ \nabla\left[\varepsilon_0^{-1}\int_{\bar{\Gamma}_c} \varsigma_c(\mathbf{r}')g(\mathbf{r},\mathbf{r}')d\Gamma' + \varepsilon_0^{-1}\int_{\Omega_c} \varrho_c(\mathbf{r}')g(\mathbf{r},\mathbf{r}')d\Omega'\right].\end{aligned} \tag{2.32}$$

Whereas, by choosing (2.28), it becomes:

$$\begin{aligned}\mathbf{E}_{ext}(\mathbf{r}) =& \frac{\mathbf{J}_c(\mathbf{r})}{\sigma_c(\mathbf{r})} + i\omega\mu_0 \int_{\Omega_c} \mathbf{J}_c(\mathbf{r}')g(\mathbf{r},\mathbf{r}')d\Omega' \\ &- \frac{\nabla}{i\omega\varepsilon_0}\left[\int_{\bar{\Gamma}_c} \left(\mathbf{J}_c^+(\mathbf{r}') - \mathbf{J}_c^-(\mathbf{r}')\right)\cdot\mathbf{n}g(\mathbf{r},\mathbf{r}')d\Gamma' + \int_{\Omega_c} \nabla'\cdot\mathbf{J}_c(\mathbf{r}')g(\mathbf{r},\mathbf{r}')d\Omega'\right].\end{aligned} \tag{2.33}$$

It should be noted that the above approaches are integral equation methods which avoid the discretization of the unbounded air domain. This feature is extremely attractive for high frequency electromagnetic problems and when complex structures are embedded in a large air domain.

Equations (2.32) and (2.33) are derived from two different expression of EFIE given by (2.27) and (2.28), respectively. However, in the original PEEC method the final PEEC electric equation is given by:

$$\mathbf{E}_{ext}(\mathbf{r}) = \frac{\mathbf{J}_c(\mathbf{r})}{\sigma_c(\mathbf{r})} + i\omega\mu_0 \int_{\Omega_c} \mathbf{J}_c(\mathbf{r}')g(\mathbf{r},\mathbf{r}')d\Omega' + \nabla\varphi_e(\mathbf{r}), \tag{2.34}$$

where the electric scalar potential φ_e remains as unknown. Thus, this last equation is solved together with

$$\varphi_e(\mathbf{r}) = -\frac{1}{i\omega\varepsilon_0}\left[\int_{\bar{\Gamma}_c} \left(\mathbf{J}_c^+(\mathbf{r}') - \mathbf{J}_c^-(\mathbf{r}')\right)\cdot\mathbf{n}g(\mathbf{r},\mathbf{r}')d\Gamma' + \int_{\Omega_c} \nabla'\cdot\mathbf{J}_c(\mathbf{r}')g(\mathbf{r},\mathbf{r}')d\Omega'\right], \tag{2.35}$$

obtained as the combination of (2.23) and (2.26).

2.2.2 Conductive and dielectric media

In order to consider the presence of dielectric media, the formulation presented above must be revised. For the sake of clarity and simplicity, ideal (lossless) dielectric media are first considered and then the extension to lossy media is given.

Lossless dielectric media

The main idea is to introduce the electric polarization $\mathbf{P}$ as an equivalent source in vacuum. Therefore, when dielectric media are present, equation (2.2) must be changed in:

$$\mathbf{D} = \varepsilon_0\mathbf{E} + \mathbf{P} \quad or \quad \mathbf{D} = \varepsilon_0\varepsilon_r\mathbf{E}. \tag{2.36}$$

Following the discussion of Section 2.2.1, by using (2.36) instead of (2.2), we get the following differential equation:

$$\nabla^2\mathbf{A} - (i\omega)^2\mu_0\varepsilon_0\mathbf{A} = -\mu_0(\mathbf{J}_c + i\omega\mathbf{P}). \tag{2.37}$$

The term $i\omega\mathbf{P}$, in the right–hand side of the equation, is usually called the *polarization current density vector*, $\mathbf{J}_d = i\omega\mathbf{P}$. This quantity is non vanishing in the dielectric domain Ω_d.

Now, since (from a mathematical point of view) $\mathbf{J}_d$ acts exactly as the conduction current density $\mathbf{J}_c$, the electric current density vector, $\mathbf{J}_e = \mathbf{J}_c + \mathbf{J}_d$, can be introduced. This quantity is zero outside Ω_e. In this section, lossless dielectric media are considered, thus no conduction current flows in Ω_d, i.e. $\Omega_c \cap \Omega_d = \emptyset$, and $\mathbf{J}_e = \mathbf{J}_c$ in Ω_c and $\mathbf{J}_e = \mathbf{J}_d$ in Ω_d.

After the introduction of $\mathbf{J}_e$, the proceeding of the formulation is straightforward. The solution of (2.37) is proven to be:

$$\mathbf{A}(\mathbf{r}) = \mu_0 \int_{\Omega_e} \mathbf{J}_e(\mathbf{r}')g(\mathbf{r},\mathbf{r}')d\Omega'. \tag{2.38}$$

Likewise Section 2.2.1, the integral expression of φ_e is now obtained from (2.38) applying the Lorenz gauge:

$$i\omega\varphi_e(\mathbf{r}) = \varepsilon_0^{-1}\left[\int_{\Omega_e} \nabla'\cdot\Big(\mathbf{J}_e(\mathbf{r}')g(\mathbf{r},\mathbf{r}')\Big)d\Omega' - \int_{\Omega_e} g(\mathbf{r},\mathbf{r}')\nabla'\cdot\mathbf{J}_e(\mathbf{r}')d\Omega'\right]. \tag{2.39}$$

Now, complementary to (2.23), the following continuity equations are introduced:

$$\begin{aligned} \nabla'\cdot\mathbf{P}(\mathbf{r}') &= -\varrho_d(\mathbf{r}'), & \big(\mathbf{P}^+(\mathbf{r}') - \mathbf{P}^-(\mathbf{r}')\big)\cdot\mathbf{n} &= -\varsigma_d(\mathbf{r}'), \\ \nabla'\cdot\mathbf{J}_d(\mathbf{r}') &= -i\omega\varrho_d(\mathbf{r}'), & \big(\mathbf{J}_d^+(\mathbf{r}') - \mathbf{J}_d^-(\mathbf{r}')\big)\cdot\mathbf{n} &= -i\omega\varsigma_d(\mathbf{r}') \end{aligned} \tag{2.40}$$

where ϱ_d is the *volume polarization charge density* (volume bound electric charge density), and ς_d is the *surface polarization charge density* (surface bound electric charge density) laying on a surface over which $\mathbf{P}$ is discontinuous. Likewise for the conductive media, the set of these surfaces is indicated by $\bar{\Gamma}_d$. As discussed in Appendix A, when homogeneous dielectric media are considered ϱ_d vanishes and $\bar{\Gamma}_d = \Gamma_d$. Thus, since the *positive side* of the surface of discontinuity belongs to Ω_0, $\mathbf{P}^+$ and $\mathbf{J}_d^+$ are also equal to zero. However, for the sake of clarity and generality, ϱ_d, $\mathbf{P}^+$ and $\mathbf{J}_d^+$ are maintained during the development of the formulation.

With the introduction of $\mathbf{J}_e$, the continuity relationships (2.23) and (2.40) can be combined resulting in:

$$\nabla'\cdot\mathbf{J}_e(\mathbf{r}') = -i\omega\varrho_e(\mathbf{r}'), \qquad \big(\mathbf{J}_e^+(\mathbf{r}') - \mathbf{J}_e^-(\mathbf{r}')\big)\cdot\mathbf{n} = -i\omega\varsigma_e(\mathbf{r}'), \tag{2.41}$$

where $\varrho_e = \varrho_c + \varrho_d$ is the *volume electric charge density* and $\varsigma_e = \varsigma_c + \varsigma_d$ is the *surface electric charge density* laying on $\bar{\Gamma}_e = \bar{\Gamma}_c \cup \bar{\Gamma}_d$.

Inserting this continuity equations in (2.39), the following expression is obtained:

$$\varphi_e(\mathbf{r}) = \varepsilon_0^{-1}\left[\int_{\bar{\Gamma}_e} \varsigma_e(\mathbf{r}')g(\mathbf{r},\mathbf{r}')d\Gamma' + \int_{\Omega_e} \varrho_e(\mathbf{r}')g(\mathbf{r},\mathbf{r}')d\Omega'\right], \tag{2.42}$$

where, thank to the homogeneous media assumption, $\bar{\Gamma}_e = \Gamma_e$.

Now, the derivation of the EFIE for conductive and dielectric media is straightforward:

$$\mathbf{E}(\mathbf{r}) = -i\omega\mu_0 \int_{\Omega_e} \mathbf{J}_e(\mathbf{r}')g(\mathbf{r},\mathbf{r}')d\Omega' - \nabla\left[\varepsilon_0^{-1}\int_{\bar{\Gamma}_e} \varsigma_e(\mathbf{r}')g(\mathbf{r},\mathbf{r}')d\Gamma' + \varepsilon_0^{-1}\int_{\Omega_e} \varrho_e(\mathbf{r}')g(\mathbf{r},\mathbf{r}')d\Omega'\right], \tag{2.43}$$

or analogously, by using the continuity relationships:

$$\begin{aligned}\mathbf{E}(\mathbf{r}) = &- i\omega\mu_0 \int_{\Omega_e} \mathbf{J}_e(\mathbf{r}')g(\mathbf{r},\mathbf{r}')d\Omega' \\ &+ \frac{\nabla}{i\omega\varepsilon_0}\left[\int_{\bar{\Gamma}_e} \left(\mathbf{J}_e^+(\mathbf{r}') - \mathbf{J}_e^-(\mathbf{r}')\right)\cdot\mathbf{n}g(\mathbf{r},\mathbf{r}')d\Gamma' + \int_{\Omega_e}\Big(\nabla'\cdot\mathbf{J}_e(\mathbf{r}')\Big)g(\mathbf{r},\mathbf{r}')d\Omega'\right].\end{aligned} \tag{2.44}$$

In Section 2.2.1, the PEEC electric equation for conductive media is obtained by combining Ohm's law (which *locally* links $\mathbf{E}$ to $\mathbf{J}_c$) with the EFIE equation (which links $\mathbf{E}$ to its sources by means of an integral equations). Now, a corresponding constitutive relation which locally links $\mathbf{E}$ to $\mathbf{J}_d$ must be obtained. This equation can be easily derived combining the two equations in (2.36):

$$\mathbf{E}(\mathbf{r}) = \rho_d(\mathbf{r})\mathbf{J}_d(\mathbf{r}) = \frac{\mathbf{J}_d(\mathbf{r})}{\sigma_d(\mathbf{r})}, \quad \mathbf{r}\in\Omega_d, \tag{2.45}$$

where $\sigma_d = i\omega\varepsilon_0(\varepsilon_r - 1)$ and $\rho_d = \sigma_d^{-1}$ are and the *equivalent electric conductivity* and *resistivity* defined for dielectric media, respectively.

Therefore, the following constitutive equation can be introduced:

$$\mathbf{E}(\mathbf{r}) = \rho_e(\mathbf{r})\mathbf{J}_e(\mathbf{r}) = \frac{\mathbf{J}_e(\mathbf{r})}{\sigma_e(\mathbf{r})}, \quad \mathbf{r}\in\Omega_e, \tag{2.46}$$

where σ_e and ρ_e are the equivalent electric conductivity and resistivity, respectively, defined as

$$\sigma_e(\mathbf{r}) = \begin{cases}\sigma_c(\mathbf{r}),\ for\ \mathbf{r}\in\Omega_c \\ \sigma_d(\mathbf{r}),\ for\ \mathbf{r}\in\Omega_d\end{cases}, \quad \rho_e(\mathbf{r}) = \begin{cases}\rho_c(\mathbf{r}),\ for\ \mathbf{r}\in\Omega_c \\ \rho_d(\mathbf{r}),\ for\ \mathbf{r}\in\Omega_d\end{cases}. \tag{2.47}$$

Finally, likewise Section 2.2.1, the PEEC electric equation for conductive and dielectric media is obtained by combining the constitutive equation (2.46) with the new EFIE expression (2.43):

$$\mathbf{E}_{ext}(\mathbf{r}) = \frac{\mathbf{J}_e(\mathbf{r})}{\sigma_e(\mathbf{r})} + i\omega\mu_0\int_{\Omega_e}\mathbf{J}_e(\mathbf{r}')g(\mathbf{r},\mathbf{r}')d\Omega' + \frac{\nabla}{\varepsilon_0}\left[\int_{\Gamma_e}\varsigma_e(\mathbf{r}')g(\mathbf{r},\mathbf{r}')d\Gamma' + \int_{\Omega_e}\varrho_e(\mathbf{r}')g(\mathbf{r},\mathbf{r}')d\Omega'\right]. \tag{2.48}$$

Clearly, likewise Section 2.2.1, (2.42) and (2.48) can be written avoiding the use of the free and bound charge densities by simply using the continuity relationship (2.41).

Lossy dielectric media

Inside lossy dielectric media, several phenomena can cause the dissipation of electromagnetic energy. One of them occurs for materials having electric conductivity greater than zero (*non–ideal* dielectric media). In this kind of materials the presence of free charge is not negligible and therefore the effect of Joule losses, due to the emergence of conduction currents, must be taken into account. Therefore, $\Omega_c \cap \Omega_d \neq \emptyset$. This kind of regions can be modeled by extending the

definition of the equivalent electric conductivity and resistivity, that become:

$$\sigma_e(\mathbf{r}) = \sigma_c(\mathbf{r}) + j\omega\varepsilon_0(\varepsilon_r(\mathbf{r}) - 1), \quad \rho_e(\mathbf{r}) = \frac{1}{\sigma_c(\mathbf{r}) + j\omega\varepsilon_0(\varepsilon_r(\mathbf{r}) - 1)}, \quad \mathbf{r} \in \Omega_e.$$

Then, the PEEC electric equation in (2.48) still holds.

Another phenomenon which causes the dissipation of electromagnetic energy is due to the time delay on the polarization of the dielectric media [32]. This phenomenon can be easily modeled by defining a complex electric permittivity. For this kind of materials the whole discussion presented for lossless dielectrics still holds, keeping in mind that ε_r is this time a complex value (or a complex tensor).

2.2.3 Conductive, dielectric, and magnetic media

When magnetic media are involved, the formulation presented above for the case of conductive and dielectric media must be complemented. In this section, the extension of the formulation to magnetic media is addressed by following the Amperian PEEC (A–PEEC) formulation. As discussed in Chapter 1, this formulation was presented in [33, 34, 35] for the Standard PEEC formulation and then by the author in [26] for the Unstructured PEEC formulation. It is worth noting that other methods have been presented in the literature for the inclusion of magnetic media, e.g. [36] where PEEC and Method Of Moment (MOM) [37] are combined or [38] where PEEC and Boundary Integral Method (BIM) are combined. However, these alternative methods do not allow the same circuit interpretation of the classical PEEC method.

First, the case of ideal (lossless) magnetic media is considered and then the case of lossy media is discussed.

Lossless magnetic media

When conductive, dielectric, and magnetic media are considered, (2.3) modifies to

$$\mathbf{B} = \mu_0\mathbf{H} + \mu_0\mathbf{M} = \mu_0\mu_r\mathbf{H}, \tag{2.49}$$

where the magnetization $\mathbf{M}$ acts as an equivalent source in vacuum.

Thus, since $\mathbf{H} = \frac{1}{\mu_0}\nabla \times \mathbf{A} - \mathbf{M}$, equation (2.37) now becomes

$$\nabla^2\mathbf{A} - (i\omega)^2\mu_0\varepsilon_0\mathbf{A} = -\mu_0(\mathbf{J}_e + \nabla \times \mathbf{M}). \tag{2.50}$$

The solution of this differential equation is given by

$$\mathbf{A}(\mathbf{r}) = \mu_0\left[\int_{\Omega_e} \mathbf{J}_e(\mathbf{r}')g(\mathbf{r},\mathbf{r}')d\Omega' + \int_{\Omega_m} \mathbf{J}_a(\mathbf{r}')g(\mathbf{r},\mathbf{r}')d\Omega' + \int_{\bar{\Gamma}_m} \mathbf{K}_a(\mathbf{r}')g(\mathbf{r},\mathbf{r}')d\Gamma'\right], \tag{2.51}$$

where $\mathbf{J}_a(\mathbf{r}') = \nabla \times \mathbf{M}(\mathbf{r}')$ and $\mathbf{K}_a(\mathbf{r}') = \left(\mathbf{M}^-(\mathbf{r}') - \mathbf{M}^+(\mathbf{r}')\right) \times \mathbf{n}$ are the volume and surface *amperian* currents, respectively. $\bar{\Gamma}_m$ is the set of surfaces for which $\mathbf{M}$ is discontinuous. Likewise the previous Sections, when only homogeneous magnetic media are considered $\bar{\Gamma}_m = \Gamma_m$, therefore $\mathbf{M}^+ = 0$ and $\mathbf{K}_a(\mathbf{r}') = \mathbf{M}(\mathbf{r}') \times \mathbf{n}$. It is worth noting that $\nabla \times \mathbf{M}(\mathbf{r}')$ is not defined for $\mathbf{r}' \in \bar{\Gamma}_m$. Indeed (2.51) is obtained from (2.50) by using mathematical concepts belonging to the *distribution theory* (generalized functions). From a physical point of view, the EM effects due to the magnetized regions are taken into account by introducing the amperian currents which

depends on the curl of the magnetization. This interpretation is called the *amperian model*. For a further discussion about this topic the author refers to [39].

The integral expression of φ_e can be obtained again by combining (2.51) with the Lorenz gauge condition. This leads again to (2.39) and (2.42). Indeed $\mathbf{J}_a$ and $\mathbf{K}_a$ are obtained from the curl of $\mathbf{M}$ and thus they are divergence free. As a matter of fact, in ideal (non–conductive) magnetic media free and bound electric charge are not present, thus the presence of magnetic media does not *directly* affect the electric scalar potential.

From (2.6), the derivation of the EFIE for the case of conductive, dielectric, and magnetic media is now straightforward:

$$\begin{aligned}\mathbf{E}(\mathbf{r}) = &- i\omega\mu_0\left[\int_{\Omega_e}\mathbf{J}_e(\mathbf{r}')g(\mathbf{r},\mathbf{r}')d\Omega' + \int_{\Omega_m}\mathbf{J}_a(\mathbf{r}')g(\mathbf{r},\mathbf{r}')d\Omega' + \int_{\bar{\Gamma}_m}\mathbf{K}_a(\mathbf{r}')g(\mathbf{r},\mathbf{r}')d\Gamma'\right]\\ &- \nabla\left[\varepsilon_0^{-1}\int_{\bar{\Gamma}_e}\varsigma_e(\mathbf{r}')g(\mathbf{r},\mathbf{r}')d\Gamma' + \varepsilon_0^{-1}\int_{\Omega_e}\varrho_e(\mathbf{r}')g(\mathbf{r},\mathbf{r}')d\Omega'\right],\end{aligned} \tag{2.52}$$

or analogously, by using the continuity relationships (2.41):

$$\begin{aligned}\mathbf{E}(\mathbf{r}) = &- i\omega\mu_0\left[\int_{\Omega_e}\mathbf{J}_e(\mathbf{r}')g(\mathbf{r},\mathbf{r}')d\Omega' + \int_{\Omega_m}\mathbf{J}_a(\mathbf{r}')g(\mathbf{r},\mathbf{r}')d\Omega' + \int_{\bar{\Gamma}_m}\mathbf{K}_a(\mathbf{r}')g(\mathbf{r},\mathbf{r}')d\Gamma'\right]\\ &+ \frac{\nabla}{i\omega\varepsilon_0}\left[\int_{\bar{\Gamma}_e}\left(\mathbf{J}_e^+(\mathbf{r}') - \mathbf{J}_e^-(\mathbf{r}')\right)\cdot\mathbf{n}g(\mathbf{r},\mathbf{r}')d\Gamma' + \int_{\Omega_e}\Big(\nabla'\cdot\mathbf{J}_e(\mathbf{r}')\Big)g(\mathbf{r},\mathbf{r}')d\Omega'\right].\end{aligned} \tag{2.53}$$

By using (2.46) and (2.52), the PEEC electric equation for the case of conductive, dielectric, and magnetic media can be obtained:

$$\begin{aligned}\mathbf{E}_{ext}(\mathbf{r}) = &\frac{\mathbf{J}_e(\mathbf{r})}{\sigma_e(\mathbf{r})} + i\omega\mu_0\left[\int_{\Omega_e}\mathbf{J}_e(\mathbf{r}')g(\mathbf{r},\mathbf{r}')d\Omega' + \int_{\Omega_m}\mathbf{J}_a(\mathbf{r}')g(\mathbf{r},\mathbf{r}')d\Omega' + \int_{\bar{\Gamma}_m}\mathbf{K}_a(\mathbf{r}')g(\mathbf{r},\mathbf{r}')d\Gamma'\right]\\ &+ \frac{\nabla}{\varepsilon_0}\left[\int_{\Gamma}\varsigma_e(\mathbf{r}')g(\mathbf{r},\mathbf{r}')d\Gamma' + \int_{\Omega}\varrho_e(\mathbf{r}')g(\mathbf{r},\mathbf{r}')d\Omega'\right], \quad \mathbf{r}\in\Omega_e,\end{aligned} \tag{2.54}$$

or equivalently

$$\begin{aligned}\mathbf{E}_{ext}(\mathbf{r}) = &\frac{\mathbf{J}_e(\mathbf{r})}{\sigma_e(\mathbf{r})} + i\omega\mu_0\left[\int_{\Omega_e}\mathbf{J}_e(\mathbf{r}')g(\mathbf{r},\mathbf{r}')d\Omega' + \int_{\Omega_m}\mathbf{J}_a(\mathbf{r}')g(\mathbf{r},\mathbf{r}')d\Omega' + \int_{\bar{\Gamma}_m}\mathbf{K}_a(\mathbf{r}')g(\mathbf{r},\mathbf{r}')d\Gamma'\right]\\ &+ \nabla\varphi_e(\mathbf{r}), \quad \mathbf{r}\in\Omega_e,\end{aligned} \tag{2.55}$$

where $\varphi_e(\mathbf{r})$ is given by (2.39) or (2.42).

However, since no constitutive relationship exists between the amperian currents and the electric field, the electric equation must be complemented by the *PEEC magnetic equation*:

$$\mathbf{B}_{ext}(\mathbf{r}) = \mathbf{B}(\mathbf{r}) - \mathbf{B}_{sca}(\mathbf{r}), \tag{2.56}$$

where $\mathbf{B}$ is the (total) magnetic flux density field, $\mathbf{B}_{ext}$ is the field produced by external sources that are not considered inside the computational domain $\Omega = \Omega_a \cup \Omega_0$, and $\mathbf{B}_{sca}$ is the scattered magnetic flux density produced by the electric and amperian currents.

Likewise for the PEEC electric equation, the scattered field is obtained through an integral expression whereas the total field is obtained through a constitutive relationship.

Since $\mathbf{B}_{sca} = \nabla \times \mathbf{A}_{sca}$, the integral expression of the scattered field is directly obtained from (2.51). The constitutive expression instead is obtained by combining the two equations in (2.49), resulting in:

$$\mathbf{B}(\mathbf{r}) = \frac{\mu_0 \mu_r(\mathbf{r})}{\mu_r(\mathbf{r}) - 1} \mathbf{M}(\mathbf{r}), \quad \mathbf{r} \in \Omega_m. \tag{2.57}$$

Likewise the Ohm's law, this expression locally links $\mathbf{B}$ to $\mathbf{M}$.

Finally, from (2.56), the PEEC magnetic equation results in:

$$\begin{aligned} \mathbf{B}_{ext}(\mathbf{r}) =& \alpha_m(\mathbf{r})\mathbf{M}(\mathbf{r}) - \mu_0 \nabla \times \left[\int_{\Omega_e} \mathbf{J}_e(\mathbf{r}') g(\mathbf{r}, \mathbf{r}') d\Omega' \right. \\ &\left. + \int_{\Omega_m} \mathbf{J}_a(\mathbf{r}') g(\mathbf{r}, \mathbf{r}') d\Omega' + \int_{\bar{\Gamma}_m} \mathbf{K}_a(\mathbf{r}') g(\mathbf{r}, \mathbf{r}') d\Gamma' \right], \quad \mathbf{r} \in \Omega_m, \end{aligned} \tag{2.58}$$

where $\alpha_m = \frac{\mu_0 \mu_r}{\mu_r - 1}$.

Finally, (2.53) (or the combination of (2.52) and (2.41)) and (2.58) are the electric and magnetic integral equations which represent the EM problem for the general case of conductive, dielectric, and magnetic media.

Lossy magnetic media

Inside lossy magnetic media, several phenomena can cause the dissipation of electromagnetic energy. One of them occurs for materials having electric conductivity greater than zero. In this kind of materials the presence of free charge is not negligible and therefore the effect of Joule losses, due to the emergence of conduction currents, must be taken into account. Therefore, $\Omega_c \cap \Omega_m \neq \emptyset$. This kind of regions can be modeled by simply imposing both the PEEC electric and magnetic equations for the domain $\Omega_c \cap \Omega_m$. Thus, the formulation developed in the previous Section is still valid for the case of both conductive and magnetic media.

Another phenomenon which causes the dissipation of electromagnetic energy is due to the time delay on the magnetization of the magnetic media. This phenomenon can be easily modeled by defining a complex relative permeability. For this kind of materials the whole discussion presented for lossless magnetic media still holds, keeping in mind that μ_r is in this case a complex value (or a complex tensor) and not a real one.

2.3 Coulombian PEEC formulation

In the previous section, the A–PEEC formulation has been presented where electric (conductive and dielectric) and magnetic media are considered in two different manners. In this section, an alternative PEEC formulation, introduced by the author in [40, 27], is presented. This formulation is based on electric and magnetic (vector and scalar) potentials derived from the Hertz potentials. This alternative approach, similar to the VIE method presented in [41], leads to a formulation where electric and magnetic media are treated in a completely equivalent way and it is based on the coulombian interpretation of the magnetization phenomena. As discuss in Chapter 3, this formulation present some advantages with respect the A–PEEC formulation.

The development of the Coulombian PEEC (C–PEEC) formulation is carried out considering the more general case with conductive, dielectric, and magnetic media from the beginning. It is worth noting that when magnetic media are not actually involved, the A–PEEC and the C–PEEC formulations are equivalent, i.e. they only differs for the symbolic point of view.

2.3.1 Conductive, dielectric, and magnetic media

In this section, the formulation is derived by introducing electric and magnetic potentials which have different definitions with respect to Section 2.2. Moreover, following [39], the equivalent magnetic currents and charges are introduced and a symmetrized form of Maxwell's equations is adopted.

For its great importance, the derivation of the new integral equations which link the new EM potentials to their sources is thoroughly discussed in this section. Indeed, the literature concerning this subject is sometime misleading and not fully exhaustive. Therefore, the derivation of the EFIE and the Magnetic Field Integral Equation (MFIE) are throughly discussed and the new PEEC electric and magnetic equations are then derived.

Homogeneous media are assumed hereafter. In Section 2.3.1, an alternative formulation which allows the direct study of inhomogeneous media is derived. In this section, the discussions of Section 2.2 concerning lossless and lossy media still hold and thus no additional considerations are made.

Maxwell's equations and potentials

Following [39] (Chapter 5, 7), the magnetization phenomena can be interpreted by using a different mathematical interpretation, commonly adopted in classical Integral Equation Methods for high frequency problems, which is called the *magnetic–charge model*. Thus, the *magnetic current density vector*, $\mathbf{J}_m$, and the *volume magnetic charge density*, ϱ_m, are introduced as:

$$\mathbf{J}_m = i\omega\mu_0\mathbf{M}, \quad \varrho_m = -\nabla\cdot(\mu_0\mathbf{M}). \tag{2.59}$$

By using $\mathbf{J}_m$ and ϱ_m, Maxwell's equations in the frequency domain can be written in a more symmetric form, avoiding the use of $\mathbf{D}$ and $\mathbf{B}$ [39, 42]:

$$\begin{aligned} \nabla\cdot\mathbf{E} &= \frac{\varrho_e}{\varepsilon_0}, \qquad & -\nabla\times\mathbf{E} &= \mathbf{J}_m + i\omega\mu_0\mathbf{H}, \\ \nabla\cdot\mathbf{H} &= \frac{\varrho_m}{\mu_0}, \qquad & \nabla\times\mathbf{H} &= \mathbf{J}_e + i\omega\varepsilon_0\mathbf{E}. \end{aligned} \tag{2.60}$$

It is worth noting that this way to write the Maxwell's equations is completely equivalent to (2.1). Indeed, by using (2.36), (2.49), and (2.59), equations (2.60) can be derived from (2.1) and vice-versa.

As shown in [30] and [43], the electric and the magnetic fields can now be written as:

$$\mathbf{E} = -i\omega\mathbf{A}_e - \nabla\varphi_e - \frac{1}{\varepsilon_0}\nabla\times\mathbf{A}_m, \qquad \mathbf{H} = -i\omega\mathbf{A}_m - \nabla\varphi_m + \frac{1}{\mu_0}\nabla\times\mathbf{A}_e, \tag{2.61}$$

where $\mathbf{A}_e$ is the *electric vector potential*, $\mathbf{A}_m$ is the *magnetic vector potential*, and φ_m is the *magnetic scalar potential*. The definition of φ_e is completely equivalent to that one already given in Section 2.2. The potentials $\mathbf{A}_e$ and $\mathbf{A}_m$ are equivalent to the electric and magnetic vector Hertz potentials scaled by $i\omega$ and they are related to the vector potential $\mathbf{A}$ by

$$\mathbf{A} = \mathbf{A}_e + \frac{1}{i\omega\varepsilon_0}\nabla\times\mathbf{A}_m. \tag{2.62}$$

Integral equations for $\mathbf{A}_e$, $\mathbf{A}_m$, φ_e, and φ_m

In order to obtain two integral expressions which link $\mathbf{E}$ and $\mathbf{H}$ to their sources, the integral expressions of the potentials $\mathbf{A}_e$, $\mathbf{A}_m$, φ_e and φ_m are obtained.

Combining the fourth equation in (2.60) with (2.61) yields:

$$-i\omega\nabla\times\mathbf{A}_m-\nabla\times\nabla\varphi_m+\nabla\times\Big(\frac{1}{\mu_0}\nabla\times\mathbf{A}_e\Big)=\mathbf{J}_e+i\omega\varepsilon_0\Big(-i\omega\mathbf{A}_e-\nabla\varphi_e-\frac{1}{\varepsilon_0}\nabla\times\mathbf{A}_m\Big). \quad (2.63)$$

After some basic calculations and applying the vector identity (2.5), this last equation becomes:

$$\nabla\times\nabla\times\mathbf{A}_e+(i\omega)^2\mu_0\varepsilon_0\mathbf{A}_e+i\omega\varepsilon_0\mu_0\nabla\varphi_e=\mu_0\mathbf{J}_e. \quad (2.64)$$

Then, applying the vector identity (2.8) to the term $\nabla\times\nabla\times\mathbf{A}_e$, (2.64) becomes:

$$\nabla\nabla\cdot\mathbf{A}_e-\nabla^2\mathbf{A}_e+(i\omega)^2\mu_0\varepsilon_0\mathbf{A}_e+i\omega\varepsilon_0\mu_0\nabla\varphi_e=\mu_0\mathbf{J}_e. \quad (2.65)$$

By introducing the Lorenz gauge condition:

$$\nabla\cdot\mathbf{A}_e=-i\omega\mu_0\varepsilon_0\varphi_e, \quad (2.66)$$

Equation (2.65) simplifies in:

$$\nabla^2\mathbf{A}_e-(i\omega)^2\mu_0\varepsilon_0\mathbf{A}_e=-\mu_0\mathbf{J}_e, \quad (2.67)$$

or equivalently:

$$\Box\mathbf{A}_e=\mu_0\mathbf{J}_e. \quad (2.68)$$

Combining the second equation in (2.60) with (2.61), introducing the Lorenz gauge condition:

$$\nabla\cdot\mathbf{A}_m=-i\omega\mu_0\varepsilon_0\varphi_m, \quad (2.69)$$

and following the same procedure as above, the following PDE is obtained:

$$\nabla^2\mathbf{A}_m-(i\omega)^2\mu_0\varepsilon_0\mathbf{A}_m=-\varepsilon_0\mathbf{J}_m, \quad (2.70)$$

or, equivalently,

$$\Box\mathbf{A}_m=\varepsilon_0\mathbf{J}_m. \quad (2.71)$$

The solution of (2.68) and (2.71) is obtained likewise in Section 2.2.1, resulting in the following:

$$\mathbf{A}_e(\mathbf{r})=\mu_0\int_{\Omega_e}\mathbf{J}_e(\mathbf{r}')g(\mathbf{r},\mathbf{r}')d\Omega', \quad (2.72)$$

$$\mathbf{A}_m(\mathbf{r})=\varepsilon_0\int_{\Omega_m}\mathbf{J}_m(\mathbf{r}')g(\mathbf{r},\mathbf{r}')d\Omega'. \quad (2.73)$$

It is clear now that the source of the vector electric potential $\mathbf{A}_e$ is the electric current density vector $\mathbf{J}_e$, whereas the source of the vector magnetic potential $\mathbf{A}_m$ is the magnetic current density vector $\mathbf{J}_m$. As shown by (2.51), the sources of the vector potential $\mathbf{A}$ are instead $\mathbf{J}_e$ and the amperian currents $\mathbf{J}_a$ and $\mathbf{K}_a$. Indeed, when the *amperian model* is adopted, the magnetized

media are considered as regions affected by the flowing of equivalent electric currents (i.e. the amperian currents). On the contrary, when the *magnetic–charge model* is adopted, no electric currents flows in the (non–conductive) magnetic regions and the electromagnetic effects of the magnetized domains are taken into account by introducing the magnetic current and charge densities $\mathbf{J}_m$ and ϱ_m (Vm^{-2}), which are proportional to the magnetization and its divergence, respectively. Both the *amperian model* and the *magnetic–charge model* (Coulombian) are two valid interpretations of the magnetization phenomena; although the *amperian model* is criticized in [39] (Chapter 7) for reasons concerning the electromagnetic energy inside permanent magnets, and the *magnetic–charge model* (Coulombian model) is criticized in [44] for reasons concerning the microscopic interpretation of the magnetization phenomena.

The integral expressions of φ_e is obtained by combining (2.66) with (2.72). This leads again to (2.39) and (2.42). The integral expression of φ_m can be obtained by combining (2.69) with (2.73) and following the same procedure adopted for the derivation of φ_e. This results in:

$$-i\omega\varphi_m(\mathbf{r}) = \frac{\nabla\cdot\mathbf{A}_m(\mathbf{r})}{\varepsilon_0\mu_0} = \mu_0^{-1}\int_{\Omega_m}\nabla\cdot(\mathbf{J}_m(\mathbf{r}')g(\mathbf{r},\mathbf{r}'))d\Omega'. \tag{2.74}$$

Then, applying (2.19) to the integrand of (2.74), after some algebraic manipulations, one obtains:

$$-i\omega\varphi_m(\mathbf{r}) = -\mu_0^{-1}\int_{\Omega_m}\mathbf{J}_m(\mathbf{r}')\cdot\nabla' g(\mathbf{r},\mathbf{r}')d\Omega', \tag{2.75}$$

that can be further rearranged resulting in

$$i\omega\varphi_m(\mathbf{r}) = \mu_0^{-1}\left[\int_{\Omega_m}\nabla'\cdot(\mathbf{J}_m(\mathbf{r}')g(\mathbf{r},\mathbf{r}'))d\Omega' - \int_{\Omega_m} g(\mathbf{r},\mathbf{r}')\nabla'\cdot\mathbf{J}_m(\mathbf{r}')d\Omega'\right]. \tag{2.76}$$

Now, we have to define the following continuity equations:

$$\nabla'\cdot\mathbf{J}_m(\mathbf{r}') = -i\omega\varrho_m(\mathbf{r}'), \qquad \left(\mathbf{J}_m^+(\mathbf{r}') - \mathbf{J}_m^-(\mathbf{r}')\right)\cdot\mathbf{n} = -i\omega\varsigma_m(\mathbf{r}'), \tag{2.77}$$

where ς_n is the *bound surface magnetic charge density* laying on a surface over which $\mathbf{J}_m$ is discontinuous; the superscripts $+$ and $-$ indicate the two sides of the surface. The set of these surfaces of discontinuity is again indicated by $\bar{\Gamma}_m$. When only homogeneous media are considered, as assumed in this chapter, the only surface of discontinuity is the boundary of Ω_m, thus $\bar{\Gamma}_m = \Gamma_m$ and the second equation in (2.77) reduces to:

$$\mathbf{J}_m^-(\mathbf{r}')\cdot\mathbf{n} = i\omega\varsigma_m(\mathbf{r}') \rightarrow \mathbf{J}_m(\mathbf{r}')\cdot\mathbf{n} = i\omega\varsigma_m(\mathbf{r}'). \tag{2.78}$$

Indeed the *positive side* of the surface belongs to Ω_0, thus $\mathbf{J}_m^+(\mathbf{r}') = 0$.

Applying the divergence theorem to the first integral of (2.22) and using (2.77) the final integral expression for φ_m is obtained:

$$\varphi_m(\mathbf{r}) = \mu_0^{-1}\left[\int_{\bar{\Gamma}_m}\varsigma_m(\mathbf{r}')g(\mathbf{r},\mathbf{r}')d\Gamma' + \int_{\Omega_m}\varrho_m(\mathbf{r}')g(\mathbf{r},\mathbf{r}')d\Omega'\right]. \tag{2.79}$$

As stated above, since only homogeneous media are considered in this chapter, $\bar{\Gamma}_m$ can be substituted with Γ_m. It must be noticed that the bound magnetic charge density ϱ_m is zero when homogeneous media are considered. Further details are given in the Appendix A. However, for the sake of clarity and generality, ϱ_m is maintained during the development of the formulation.

EFIE and MFIE, Electric and Magnetic Field Integral Equations

In the following, two integral equations which link the electric and the magnetic fields to their sources are derived.

In (2.61), the potentials $\mathbf{A}_e$, $\mathbf{A}_m$, φ_e, and φ_m can be substituted with their integral expression (2.72), (2.73), (2.26), and (2.79), respectively.

Thus, the electric and magnetic field integral equations are obtained, where $\mathbf{E}$ and $\mathbf{H}$ are directly linked to their sources, i.e. the current densities $\mathbf{J}_e$ and $\mathbf{J}_m$ and the charge densities ϱ_e, ς_e, ϱ_m, and ς_m, as

$$\begin{aligned}\mathbf{E}(\mathbf{r}) = &- i\omega\mu_0 \int_{\Omega_e} \mathbf{J}_e(\mathbf{r}')g(\mathbf{r},\mathbf{r}')d\Omega' - \nabla\left[\varepsilon_0^{-1}\int_{\bar{\Gamma}_e} \varsigma_e(\mathbf{r}')g(\mathbf{r},\mathbf{r}')d\Gamma' + \varepsilon_0^{-1}\int_{\Omega_e} \varrho_e(\mathbf{r}')g(\mathbf{r},\mathbf{r}')d\Omega'\right] \\ &- \frac{1}{\varepsilon_0}\nabla\times\int_{\Omega_m} \mathbf{J}_m(\mathbf{r}')g(\mathbf{r},\mathbf{r}')d\Omega', \qquad (2.80)\\ \mathbf{H}(\mathbf{r}) = &- i\omega\varepsilon_0 \int_{\Omega_m} \mathbf{J}_m(\mathbf{r}')g(\mathbf{r},\mathbf{r}')d\Omega' - \nabla\left[\mu_0^{-1}\int_{\bar{\Gamma}_m} \varsigma_m(\mathbf{r}')g(\mathbf{r},\mathbf{r}')d\Gamma' + \mu_0^{-1}\int_{\Omega_m} \varrho_m(\mathbf{r}')g(\mathbf{r},\mathbf{r}')d\Omega'\right] \\ &+ \frac{1}{\mu_0}\nabla\times\int_{\Omega_e} \mathbf{J}_e(\mathbf{r}')g(\mathbf{r},\mathbf{r}')d\Omega'. \qquad (2.81)\end{aligned}$$

By using the continuity equations (2.41) and (2.77), the electric and magnetic integral equations can also be rearranged in order to relate $\mathbf{E}$ and $\mathbf{H}$ to $\mathbf{J}_e$ and $\mathbf{J}_m$ only:

$$\begin{aligned}\mathbf{E}(\mathbf{r}) = &- i\omega\mu_0 \int_{\Omega_e} \mathbf{J}_e(\mathbf{r}')g(\mathbf{r},\mathbf{r}')d\Omega' \\ &- \frac{\nabla}{i\omega\varepsilon_0}\left[\int_{\bar{\Gamma}_e} \left(\mathbf{J}_e^+(\mathbf{r}') - \mathbf{J}_e^-(\mathbf{r}')\right)\cdot\mathbf{n}g(\mathbf{r},\mathbf{r}')d\Gamma' - \int_{\Omega_e} \nabla'\cdot\mathbf{J}_e(\mathbf{r}')g(\mathbf{r},\mathbf{r}')d\Omega'\right] \qquad (2.82)\\ &- \frac{1}{\varepsilon_0}\nabla\times\int_{\Omega_m} \mathbf{J}_m(\mathbf{r}')g(\mathbf{r},\mathbf{r}')d\Omega', \\ \mathbf{H}(\mathbf{r}) = &- i\omega\varepsilon_0 \int_{\Omega_m} \mathbf{J}_m(\mathbf{r}')g(\mathbf{r},\mathbf{r}')d\Omega' \\ &- \frac{\nabla}{i\omega\mu_0}\left[\int_{\bar{\Gamma}_m} \left(\mathbf{J}_m^+(\mathbf{r}') - \mathbf{J}_m^-(\mathbf{r}')\right)\cdot\mathbf{n}g(\mathbf{r},\mathbf{r}')d\Gamma' - \int_{\Omega_m} \nabla'\cdot\mathbf{J}_m(\mathbf{r}')g(\mathbf{r},\mathbf{r}')d\Omega'\right] \qquad (2.83)\\ &+ \frac{1}{\mu_0}\nabla\times\int_{\Omega_e} \mathbf{J}_e(\mathbf{r}')g(\mathbf{r},\mathbf{r}')d\Omega'.\end{aligned}$$

Since ω appears in the denominator of the second part of the right hand side of the equations, these two expressions can only be used when the frequency is different from zero.

C–PEEC integral equations

Now the attention is focused on the derivation of the two equations that will be discretized in Chapter 3. Likewise in Section 2.2, the total electric field, $\mathbf{E}$, and the total magnetic field, $\mathbf{H}$, are written as the sum of the scattered fields, $\mathbf{E}_{sca}$ and $\mathbf{H}_{sca}$, and the external fields, $\mathbf{E}_{ext}$ and $\mathbf{H}_{ext}$:

$$\mathbf{E} = \mathbf{E}_{sca} + \mathbf{E}_{ext}, \quad \mathbf{H} = \mathbf{H}_{sca} + \mathbf{H}_{ext}. \qquad (2.84)$$

The total electric field, $\mathbf{E}$, is locally related to $\mathbf{J}_e$ by (2.46). Similarly, the total magnetic field, $\mathbf{H}$, can be locally related to $\mathbf{J}_m$ by the following:

$$\mathbf{H}(\mathbf{r}) = \rho_m(\mathbf{r})\mathbf{J}_m(\mathbf{r}) = \frac{\mathbf{J}_m(\mathbf{r})}{\sigma_m(\mathbf{r})}, \quad \mathbf{r}\in\Omega_m, \qquad (2.85)$$

where

$$\rho_m(\mathbf{r}) = \frac{1}{i\omega\mu_0(\mu_r(\mathbf{r})-1)}, \quad \mathbf{r}\in\Omega_m, \tag{2.86}$$

is the *magnetic resistivity* and $\sigma_m = \rho_m^{-1}$ is the *magnetic conductivity*. Equation (2.85) can be easily obtained combining the first equation in (2.59) with (2.49).

Instead, the scattered fields, $\mathbf{E}_{sca}$ and $\mathbf{H}_{sca}$, are given by (2.80) and (2.81) or, equivalently, by (2.82) and (2.83).

The external fields (incident fields), $\mathbf{E}_{ext}$ and $\mathbf{H}_{ext}$, can be interpreted as the fields produced by external sources (current or charge densities) that are not considered inside the computational domain $\Omega = \Omega_a \cup \Omega_0$.

Thus, the following electric and magnetic equations can be obtained:

$$\mathbf{E}_{ext}(\mathbf{r}) = \mathbf{E}(\mathbf{r}) - \mathbf{E}_{sca}(\mathbf{r}), \quad \mathbf{H}_{ext}(\mathbf{r}) = \mathbf{H}(\mathbf{r}) - \mathbf{H}_{sca}(\mathbf{r}), \tag{2.87}$$

that, by choosing (2.80) and (2.81), in explicit form become:

$$\begin{aligned}\mathbf{E}_{ext}(\mathbf{r}) =& \frac{\mathbf{J}_e(\mathbf{r})}{\sigma_e(\mathbf{r})} + i\omega\mu_0\int_{\Omega_e}\mathbf{J}_e(\mathbf{r}')g(\mathbf{r},\mathbf{r}')d\Omega' \\ &+ \nabla\left[\varepsilon_0^{-1}\int_{\bar\Gamma_e}\varsigma_e(\mathbf{r}')g(\mathbf{r},\mathbf{r}')d\Gamma' + \varepsilon_0^{-1}\int_{\Omega_e}\varrho_e(\mathbf{r}')g(\mathbf{r},\mathbf{r}')d\Omega'\right] \\ &+ \frac{1}{\mu_0}\nabla\times\int_{\Omega_m}\mathbf{J}_m(\mathbf{r}')g(\mathbf{r},\mathbf{r}')d\Omega',\end{aligned} \tag{2.88}$$

$$\begin{aligned}\mathbf{H}_{ext}(\mathbf{r}) =& \frac{\mathbf{J}_m(\mathbf{r})}{\sigma_m(\mathbf{r})} + i\omega\varepsilon_0\int_{\Omega_m}\mathbf{J}_m(\mathbf{r}')g(\mathbf{r},\mathbf{r}')d\Omega' \\ &+ \nabla\left[\mu_0^{-1}\int_{\bar\Gamma_m}\varsigma_m(\mathbf{r}')g(\mathbf{r},\mathbf{r}')d\Gamma' + \mu_0^{-1}\int_{\Omega_m}\varrho_m(\mathbf{r}')g(\mathbf{r},\mathbf{r}')d\Omega'\right] \\ &- \frac{1}{\varepsilon_0}\nabla\times\int_{\Omega_e}\mathbf{J}_e(\mathbf{r}')g(\mathbf{r},\mathbf{r}')d\Omega'.\end{aligned} \tag{2.89}$$

Whereas, by choosing (2.82) and (2.83), they become:

$$\begin{aligned}\mathbf{E}_{ext}(\mathbf{r}) =& \frac{\mathbf{J}_e(\mathbf{r})}{\sigma_e(\mathbf{r})} + i\omega\mu_0\int_{\Omega_e}\mathbf{J}_e(\mathbf{r}')g(\mathbf{r},\mathbf{r}')d\Omega' \\ &+ \frac{\nabla}{i\omega\varepsilon_0}\left[\int_{\bar\Gamma_e}\left(\mathbf{J}_e^+(\mathbf{r}') - \mathbf{J}_e^-(\mathbf{r}')\right)\cdot\mathbf{n}g(\mathbf{r},\mathbf{r}')d\Gamma' - \int_{\Omega_e}\nabla'\cdot\mathbf{J}_e(\mathbf{r}')g(\mathbf{r},\mathbf{r}')d\Omega'\right] \\ &+ \frac{1}{\mu_0}\nabla\times\int_{\Omega_m}\mathbf{J}_m(\mathbf{r}')g(\mathbf{r},\mathbf{r}')d\Omega',\end{aligned} \tag{2.90}$$

$$\begin{aligned}\mathbf{H}_{ext}(\mathbf{r}) =& \frac{\mathbf{J}_m(\mathbf{r})}{\sigma_m(\mathbf{r})} + i\omega\varepsilon_0\int_{\Omega_m}\mathbf{J}_m(\mathbf{r}')g(\mathbf{r},\mathbf{r}')d\Omega' \\ &+ \frac{\nabla}{i\omega\mu_0}\left[\int_{\bar\Gamma_m}\left(\mathbf{J}_m^+(\mathbf{r}') - \mathbf{J}_m^-(\mathbf{r}')\right)\cdot\mathbf{n}g(\mathbf{r},\mathbf{r}')d\Gamma' - \int_{\Omega_m}\nabla'\cdot\mathbf{J}_m(\mathbf{r}')g(\mathbf{r},\mathbf{r}')d\Omega'\right] \\ &- \frac{1}{\varepsilon_0}\nabla\times\int_{\Omega_e}\mathbf{J}_e(\mathbf{r}')g(\mathbf{r},\mathbf{r}')d\Omega'.\end{aligned} \tag{2.91}$$

In the original PEEC method φ_e is taken to unknown. Thus, similarly to the original PEEC method, φ_e and φ_m can be considered as unknowns and then the following four equations are

solved together:

$$\mathbf{E}_{ext}(\mathbf{r}) = \frac{\mathbf{J}_e(\mathbf{r})}{\sigma_e(\mathbf{r})} + i\omega\mu_0 \int_{\Omega_e} \mathbf{J}_e(\mathbf{r}')g(\mathbf{r},\mathbf{r}')d\Omega' + \nabla\varphi_e + \frac{1}{\mu_0}\nabla \times \int_{\Omega_m} \mathbf{J}_m(\mathbf{r}')g(\mathbf{r},\mathbf{r}')d\Omega', \tag{2.92}$$

$$\mathbf{H}_{ext}(\mathbf{r}) = \frac{\mathbf{J}_m(\mathbf{r})}{\sigma_m(\mathbf{r})} + i\omega\varepsilon_0 \int_{\Omega_m} \mathbf{J}_m(\mathbf{r}')g(\mathbf{r},\mathbf{r}')d\Omega' + \nabla\varphi_m - \frac{1}{\varepsilon_0}\nabla \times \int_{\Omega_e} \mathbf{J}_e(\mathbf{r}')g(\mathbf{r},\mathbf{r}')d\Omega', \tag{2.93}$$

$$\varphi_e(\mathbf{r}) = -\frac{1}{i\omega\varepsilon_0}\left[\int_{\bar{\Gamma}_e} \left(\mathbf{J}_e^+(\mathbf{r}') - \mathbf{J}_e^-(\mathbf{r}')\right)\cdot\mathbf{n}g(\mathbf{r},\mathbf{r}')d\Gamma' + \int_{\Omega_e} \nabla'\cdot\mathbf{J}_e(\mathbf{r}')g(\mathbf{r},\mathbf{r}')d\Omega'\right], \tag{2.94}$$

$$\varphi_m(\mathbf{r}) = -\frac{1}{i\omega\mu_0}\left[\int_{\bar{\Gamma}_m} \left(\mathbf{J}_m^+(\mathbf{r}') - \mathbf{J}_m^-(\mathbf{r}')\right)\cdot\mathbf{n}g(\mathbf{r},\mathbf{r}')d\Gamma' + \int_{\Omega_m} \nabla'\cdot\mathbf{J}_m(\mathbf{r}')g(\mathbf{r},\mathbf{r}')d\Omega'\right]. \tag{2.95}$$

Total div–free currents formulation

In the previous Section, the electric and magnetic currents have been chosen as unknowns. However, when inhomogeneous media are considered, these currents are in general not–divergence free. Thus, during the discretization of the formulations they must be properly handled in order to correctly impose their electromagnetic behavior. This issue will be further discussed in the next chapter.

In [27], the author proposes an alternative PEEC formulation where the total divergence free electric and magnetic current densities are introduced as problem unknowns:

$$\mathbf{J}_e^{tot} = \mathbf{J}_e + i\omega\varepsilon_0\mathbf{E}, \qquad \mathbf{J}_m^{tot} = \mathbf{J}_m + i\omega\mu_0\mathbf{H}. \tag{2.96}$$

By combining (2.46) and (2.85) with (2.96) the following relationships hold:

$$\mathbf{J}_e(\mathbf{r}) = \frac{\sigma_e(\mathbf{r})}{\sigma_e^*(\mathbf{r})}\mathbf{J}_e^{tot}(\mathbf{r}),\ \mathbf{r}\in\Omega_e, \qquad \mathbf{J}_m(\mathbf{r}) = \frac{\sigma_m(\mathbf{r})}{\sigma_m^*(\mathbf{r})}\mathbf{J}_m^{tot}(\mathbf{r}),\ \mathbf{r}\in\Omega_m, \tag{2.97}$$

where

$$\sigma_e^* = \sigma_c + i\omega\varepsilon_0\varepsilon_r \tag{2.98}$$

is the total electric conductivity and

$$\sigma_m^* = i\omega\mu_0\mu_r \tag{2.99}$$

is the total magnetic conductivity.

Then, (2.97) are inserted in (2.92), (2.93), (2.21) and (2.75), as shown in [27]. Thus, final electric and magnetic integral equations are obtained where the unknowns are $\mathbf{J}_e^{tot}$ and $\mathbf{J}_m^{tot}$ only, which are divergence free quantities.

Therefore, the final integral continuum equations considered in this formulation are given by:

$$\begin{aligned}\mathbf{E}_{ext}(\mathbf{r}) =& \frac{\mathbf{J}_e(\mathbf{r})}{\sigma_e^*(\mathbf{r})} + i\omega\mu_0 \int_{\Omega_e} \frac{\sigma_e(\mathbf{r}')}{\sigma_e^*(\mathbf{r}')}\mathbf{J}_e^{tot}(\mathbf{r}')g(\mathbf{r},\mathbf{r}')d\Omega' + \nabla\varphi_e \\ &+ \frac{1}{\mu_0}\nabla \times \int_{\Omega_m} \frac{\sigma_m(\mathbf{r}')}{\sigma_m^*(\mathbf{r}')}\mathbf{J}_m^{tot}(\mathbf{r}')g(\mathbf{r},\mathbf{r}')d\Omega',\end{aligned} \tag{2.100}$$

$$\begin{aligned}\mathbf{H}_{ext}(\mathbf{r}) =& \frac{\mathbf{J}_m(\mathbf{r})}{\sigma_m^*(\mathbf{r})} + i\omega\varepsilon_0 \int_{\Omega_m} \frac{\sigma_m(\mathbf{r}')}{\sigma_m^*(\mathbf{r}')}\mathbf{J}_m^{tot}(\mathbf{r}')g(\mathbf{r},\mathbf{r}')d\Omega' + \nabla\varphi_m \\ &- \frac{1}{\varepsilon_0}\nabla \times \int_{\Omega_e} \frac{\sigma_e(\mathbf{r}')}{\sigma_e^*(\mathbf{r}')}\mathbf{J}_e^{tot}(\mathbf{r}')g(\mathbf{r},\mathbf{r}')d\Omega',\end{aligned} \tag{2.101}$$

$$\varphi_e(\mathbf{r}) = \frac{1}{i\omega\varepsilon_0}\int_{\Omega_e}\frac{\sigma_e(\mathbf{r}')}{\sigma_e^*(\mathbf{r}')}\mathbf{J}_e^{tot}(\mathbf{r}')\cdot\nabla' g(\mathbf{r},\mathbf{r}')d\Omega', \tag{2.102}$$

$$\varphi_m(\mathbf{r}) = \frac{1}{i\omega\mu_0}\int_{\Omega_m}\frac{\sigma_m(\mathbf{r}')}{\sigma_m^*(\mathbf{r}')}\mathbf{J}_m^{tot}(\mathbf{r}')\cdot\nabla' g(\mathbf{r},\mathbf{r}')d\Omega'. \tag{2.103}$$

The total div–free currents formulation, mostly developed in the framework of a collaboration with G2ELab group, has the advantage of naturally considering inhomogeneous media. However, as more deeply discussed in the next chapter, the introduction of material parameters inside the integral equations (2.100)–(2.103) leads to lose the energy interpretation of the PEEC matrices (i.e. the ones derived from the discretization of the PEEC formulation). Moreover, when parametric simulations or frequency sweep analysis are performed such formulation is generally less efficient.

Thus, such formulation presents pros and cons with respect the previous one where non–divergence free currents are adopted instead. Therefore, depending on the kind of the problem to be solved, one of the two formulation would be more convenient respect to the other one.

Chapter 3

PEEC discretization

With the aim of obtaining an approximate numerical solution of the electromagnetic problem (i.e. the solution of the Maxwell's equations), PEEC integral equations derived in the previous chapter are to be discretized.

In the original PEEC approach (*standard* PEEC method [13]), the active domains are discretized by means of a Manhattan–type discretization (structured, orthogonal grids). More recently, the *standard* PEEC method has been extended to the more general case of non–orthogonal grids [13, 45] through ad–hoc adjustments.

In recent years, the so–called *unstructured* PEEC method, which naturally allows modeling general structures without restrictions on the geometry, has been developed. This approach has been first proposed in [21] for surface conductive models. Later on, thanks to the contribution of research groups from the University of Padova and Grenoble (including the author), the Unstructured PEEC method has been extended to volume models, dielectric media, and magnetic media, for both A–PEEC and C–PEEC formulations [6, 27, 26, 23].

In this chapter, the discretization of the A–PEEC formulation is first discussed and then the C–PEEC case is presented. For the sake of simplicity, both the discretizations of the A–PEEC and C–PEEC formulations, are first presented for the case of homogeneous media and, then, the more general case of the inhomogeneous media is considered. The discretization of the C–PEEC formulation based on the use of total divergence free currents (which formulation is presented at the end of the previous chapter, Section 2.3.1) is also considered. The equivalent 1–D and 2–D PEEC models are finally discussed.

3.1 Discretization of the A–PEEC formulation

This section deals with the discretization of the A–PEEC formulation presented in Section 2.2. First, the well established standard discretization scheme is shortly presented. Then, the unstructured discretization procedure based on the Cell Method and developed by the author during the PhD thesis is presented.

3.1.1 Standard discretization approach

The standard discretization procedure is here presented in its basic and original form. More exhaustive references can be found in [13, 45, 46]. The discretization is carried out considering conductive media only. Then, the extension to dielectric and magnetic media is shortly discussed and appropriate references are given.

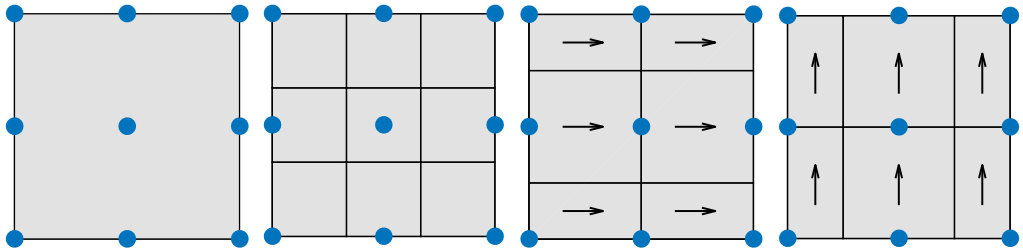

Figure 3.1: Mesh Standard PEEC.

In the original PEEC formulation introduced by Ruheli in 1972 [47], the conductive domains (that are the only active media considered in the original PEEC formulation) are subdivided into rectangular volume and surface cells, thus restricting the analysis to Manhattan–type model geometries. Thus, once obtained a regular discretization of the conductive domains, an *inductive* mesh (consisting of three meshes oriented along the orthogonal axes x, y, and z) and a *capacitive* mesh are defined [13]. Then, the unknown current and charge density distributions are approximated by using locally uniform functions whose supports are the elements of the inductive and capacitive mesh, respectively.

For instance, Fig. 3.1 shows a 2-D mesh used to approximate the current and charge distribution of a thin conductive structure, with negligible thickness (e.g. a metallic chassis or a planar antenna).

The current density $\mathbf{J}_c$ is approximated by the following expansion

$$\mathbf{J}_c(\mathbf{r}) = \sum_{k=1}^{N_j} j_{c,k}\mathbf{p}_k(\mathbf{r}), \tag{3.1}$$

where N_j is the number of inductive cells, $\mathbf{p}_k$ is the vector pulse basis function, and $j_{c,k}$ is the unknown degree of freedom (DoF) related to the kth element of the inductive mesh. Thus, the current density vector $\mathbf{J}_c$ is discretized into N_j *volume (inductive) cells* by vector pulse functions $\mathbf{p}_k(\mathbf{r})$ defined as

$$\mathbf{p}_k(\mathbf{r}) = \begin{cases} A_k^{-1}\mathbf{u}_\gamma, & \mathbf{r} \in \Lambda_k \\ \mathbf{0}, & elsewhere \end{cases}, \tag{3.2}$$

where $\gamma = x, y, z$ depending on the *orientation* of the inductive mesh, $\mathbf{u}_\gamma$ is the unit vector along the orthogonal direction γ, A_k is the cross section of the kth element of the inductive mesh and Λ_k is the support of the kth basis function (i.e. the kth element of the inductive mesh).

The volume and surface charge densities, ϱ_c and ς_c are approximated by

$$\varrho_c(\mathbf{r}) = \sum_{k=1}^{N_q^v} q_{c,k}^v p_k^v(\mathbf{r}), \quad \varsigma_c(\mathbf{r}) = \sum_{k=1}^{N_q^s} q_{c,k}^s p_k^s(\mathbf{r}), \tag{3.3}$$

where p_k^v and p_k^s are the pulse functions defined for the volume and surface capacitive cells, respectively, and $q_{c,k}^v$ and $q_{c,k}^s$ are the unknown DoFs related to the kth volume and surface element of the capacitive mesh, respectively. N_q^v and N_q^s are the number of volume and surface capacitive cells, respectively. Thus, ϱ_c and ς_c are discretized into N_q^v *volume* and N_q^s *surface*

capacitive cells, respectively, by pulse functions $p_k^v(\mathbf{r})$ and $p_k^s(\mathbf{r})$, defined as

$$p_k^v(\mathbf{r}) = \begin{cases} V_k^{-1}, \ \mathbf{r} \in \Lambda_k^v \\ 0, \ elsewhere \end{cases}, \quad p_k^s(\mathbf{r}) = \begin{cases} A_k^{-1}, \ \mathbf{r} \in \Lambda_k^s \\ 0, \ elsewhere \end{cases}, \tag{3.4}$$

where V_k is the volume of the kth volume–capacitive cell, A_k is the area of the kth surface–capacitive cell, Λ_k^v is the support of p_k^v (i.e. the volume–capacitive cell), and Λ_k^s is the support of p_k^s (i.e. the surface–capacitive cell).

Expansions (3.1) and (3.3) are then inserted in (2.34) and (2.26), resulting in

$$\mathbf{E}_{ext}(\mathbf{r}) = \sigma_c^{-1}(\mathbf{r}) \sum_{k=1}^{N_k} \big(j_{c,k}\mathbf{p}_k(\mathbf{r})\big) + i\omega\mu_0 \int_{\Omega_c} \sum_{k=1}^{N_k} \big(j_{c,k}\mathbf{p}_k(\mathbf{r\prime})\big) g(\mathbf{r},\mathbf{r}')d\Omega' + \nabla\varphi_e(\mathbf{r}), \tag{3.5}$$

and

$$\varphi_e(\mathbf{r}) = \frac{1}{\varepsilon_0}\Bigg[\int_{\bar{\Gamma}_c} \sum_{k=1}^{N_q^s} \big(q_{c,k}p_k(\mathbf{r})\big) g(\mathbf{r},\mathbf{r}')d\Gamma' + \int_{\Omega_c} \sum_{k=1}^{N_q^v} \big(q_{c,k}p_k(\mathbf{r})\big) g(\mathbf{r},\mathbf{r}')d\Omega'\Bigg]. \tag{3.6}$$

According to the Galerkin's scheme, the pulse functions $\mathbf{p}_k$, p_k^v and p_k^s are also used for testing (3.5) and (3.6). This procedure leads to the following matrix equations

$$\mathbf{e}_{ext} = \mathbf{R}\mathbf{j}_c + i\omega\mathbf{L}\mathbf{j}_c + \mathbf{A}_c^T\boldsymbol{\phi}_e, \tag{3.7}$$

$$\boldsymbol{\phi}_e = \mathbf{P}_e\mathbf{q}, \tag{3.8}$$

where

- $\mathbf{e}_{ext}$ is the vector array with coefficients $e_{ext,h} = \int_\Omega \mathbf{p}_h(\mathbf{r}) \cdot \mathbf{E}_{ext}(\mathbf{r})d\Omega$, for $h = 1, \cdots, N_j$.
- $\mathbf{R}$ is the $N_j \times N_j$ *resistance matrix* defined as

$$R_{h,k} = \int_\Omega \mathbf{p}_h(\mathbf{r}) \cdot \mathbf{p}_k(\mathbf{r})\sigma_c^{-1}(\mathbf{r})d\Omega. \tag{3.9}$$

- $\mathbf{j}_c$ is the vector array with coefficients $j_{c,k}$, for $k = 1, \cdots, N_j$.
- $\mathbf{L}$ is the $N_j \times N_j$ *inductance matrix* defined as

$$L_{h,k} = \mu_0 \int_\Omega \int_\Omega \mathbf{p}_h(\mathbf{r}) \cdot \mathbf{p}_k(\mathbf{r}')g(\mathbf{r},\mathbf{r}')d\Omega' d\Omega. \tag{3.10}$$

- $\mathbf{A}_c$ is the $(N_q^v + N_q^s) \times N_j$ incidence matrix of the equivalent circuit obtained from the discretization of the conductive domains: each inductive cell is interpreted as a circuit branch connected to two circuit nodes (i.e. the nodes of the mesh).
- $\boldsymbol{\phi}_e$ is the vector array which stores the DoFs related to φ_e. $\boldsymbol{\phi}_e$ is subdivided into $\boldsymbol{\phi}_e = [\boldsymbol{\phi}_e^v; \boldsymbol{\phi}_e^s]$ where $\phi_{e,k}^v = \int_\Omega p_k^v(\mathbf{r})\varphi_e(\mathbf{r})d\Omega$ for $k = 1, \cdots, N_q^v$, and $\phi_{e,k}^s = \int_\Gamma p_k^s(\mathbf{r})\varphi_e(\mathbf{r})d\Gamma$ for $k = 1, \cdots, N_q^s$; the scalar electric potential is instead related to the nodes of the mesh in a one–to–one relationship with the volume and surface cells of the capacitive mesh.

- $\mathbf{P}_e$ is the $(N_q^v + N_q^s) \times (N_q^v + N_q^s)$ *potential matrix* subdivided into $\mathbf{P}_e = \begin{bmatrix} \mathbf{P}_e^{vv} & \mathbf{P}_e^{vs} \\ \mathbf{P}_e^{sv} & \mathbf{P}_e^{ss} \end{bmatrix}$, where

$$P_{e_{h,k}}^{vv} = \varepsilon_0^{-1} \int_{\Omega_h} \int_{\Omega_k} p_h^v(\mathbf{r}) p_k^v(\mathbf{r}') g(\mathbf{r}, \mathbf{r}') d\Omega' d\Omega, \tag{3.11}$$

$$P_{e_{h,k}}^{ss} = \varepsilon_0^{-1} \int_{\Gamma_h} \int_{\Gamma_k} p_h^s(\mathbf{r}) p_k^s(\mathbf{r}') g(\mathbf{r}, \mathbf{r}') d\Gamma' d\Gamma, \tag{3.12}$$

$$P_{e_{h,k}}^{vs} = \varepsilon_0^{-1} \int_{\Omega_h} \int_{\Gamma_k} p_h^v(\mathbf{r}) p_k^s(\mathbf{r}') g(\mathbf{r}, \mathbf{r}') d\Gamma' d\Omega, \tag{3.13}$$

$$P_{e_{h,k}}^{sv} = \varepsilon_0^{-1} \int_{\Gamma_h} \int_{\Omega_k} p_h^s(\mathbf{r}) p_k^v(\mathbf{r}') g(\mathbf{r}, \mathbf{r}') d\Omega' d\Gamma. \tag{3.14}$$

- $\mathbf{q}$ is the vector array whose coefficients are related to ϱ_c and ς_c. $\mathbf{q}$ is subdivided into $\mathbf{q} = [\mathbf{q}^v; \mathbf{q}^s]$ where $\mathbf{q}^v$ stores the DoFs q_k^v, for $k = 1, \cdots, N_q^v$, and $\mathbf{q}^s$ with DoFs q_k^s, for $k = 1, \cdots, N_q^s$.

$\mathbf{A}_c^T$ represents the algebraic equivalent of the gradient operator in (3.5). Moreover, since $\mathbf{j}_c$ stores the fluxes of $\mathbf{J}_c$ through the cross sections of the inductive cells of the mesh and $\mathbf{q}$ stores the electric charges enclosed inside the capacitive cell of the mesh, the continuity equations (2.23) can be represented in an equivalent algebraic form as

$$\mathbf{A}_c \mathbf{j}_c = i\omega \mathbf{q}, \tag{3.15}$$

where $\mathbf{A}_c$ represents the algebraic equivalent of the divergence operator.

Since the vector pulse function $\mathbf{p}_k$ has local support which coincides with the kth inductive mesh element, $\mathbf{R}$ is a diagonal matrix and the term $\mathbf{R}\mathbf{j}_c$ in (3.7) can be interpreted as the ohmic voltage drop along the γ direction, with $\gamma = x, y, z$ depending on the orientation of the kth inductive mesh element.

Matrix $\mathbf{L}$ is a symmetric matrix characterized by three diagonal dense matrix blocks:

$$\mathbf{L} = \begin{bmatrix} \mathbf{L}^{xx} & \mathbf{0} & \mathbf{0} \\ \mathbf{0} & \mathbf{L}^{yy} & \mathbf{0} \\ \mathbf{0} & \mathbf{0} & \mathbf{L}^{zz} \end{bmatrix}, \tag{3.16}$$

indeed the inductance coefficient (3.10) vanishes when $\mathbf{p}_k$ and $\mathbf{p}_h$ have mutually orthogonal directions. The term $i\omega\mathbf{L}\mathbf{j}_c$ in (3.7) can be interpreted as an inductive voltage drop due to the self and mutual inductive couplings between the elements of the inductive mesh.

Finally, the last term in (3.7) can be interpreted as a capacitive voltage drop obtained as the algebraic difference between the potentials of the ends nodes of the inductive mesh elements (i.e. the circuit branches). In (3.8), the potentials are related to the electric charges by means of the dense symmetric potential matrix $\mathbf{P}_e$.

Following the circuit interpretation, equations in (3.7) can be interpreted as Kirchhoff Voltage Laws (KVLs) written for each branch of the electric circuit. The KVLs are complemented by the charge conservation law (3.15), i.e. the Kirchhoff Current Laws (KCLs).

Then, (3.8) and (3.15) can be combined together resulting in

$$\mathbf{A}_c \mathbf{j}_c - i\omega \mathbf{C} \boldsymbol{\phi}_e = \mathbf{0}, \tag{3.17}$$

where $\mathbf{C} = \mathbf{P}_e^{-1}$ is defined as the *capacitance matrix*.

Finally, (3.7) and (3.17) (i.e. KVL and KCL) can be assembled into a unique matrix system of algebraic linear equations:

$$\begin{bmatrix} \mathbf{R} + i\omega\mathbf{L} & \mathbf{A}_c^T \\ \mathbf{A}_c & -i\omega\mathbf{C} \end{bmatrix} \begin{bmatrix} \mathbf{j}_c \\ \boldsymbol{\phi}_e \end{bmatrix} = \begin{bmatrix} \mathbf{e}_{ext} \\ \mathbf{0} \end{bmatrix}. \tag{3.18}$$

Thanks to this circuit interpretation, the electromagnetic problem can be easily coupled with external circuit elements (not related to the EFIE). Thus, the currents and the potentials on the branch and the nodes of the lumped circuit elements can be added as unknown in (3.18). The, KVL and the KVC are written for this extra unknowns and solved together with (3.18). Moreover, the incidence matrix $\mathbf{A}_c$ must be properly modified in order to consider the possible connections of the lumped circuit components with the circuit nodes of the mesh. The zero vector in the right–hand–side (rhs) of (3.18) can be also substituted with $\mathbf{j}_{e0}$, which is the vector array of the external currents $j_{0,k}$ injected in the kth node of the mesh. Thus, (3.18) becomes

$$\begin{bmatrix} \mathbf{R} + i\omega\mathbf{L} & \mathbf{A}_c^T \\ \mathbf{A}_c & -i\omega\mathbf{C} \end{bmatrix} \begin{bmatrix} \mathbf{j}_c \\ \boldsymbol{\phi}_e \end{bmatrix} = \begin{bmatrix} \mathbf{e}_{ext} \\ \mathbf{j}_{e0} \end{bmatrix}. \tag{3.19}$$

Matrix system in (3.18) (and (3.19) as well) is a complex symmetric matrix and it generally owns good numerical properties (more detail are given in Chapter 4). Unfortunately, $\mathbf{C}$ is obtained from the inverse of $\mathbf{P}_e$ and this operation requires a considerable computational cost which grows as $\mathcal{O}((N_q^v + N_q^s)^3)$. However, by agreeing to losing the symmetry of the system, (3.19) can be also written avoiding the inversion of $\mathbf{P}_e$:

$$\begin{bmatrix} \mathbf{R} + i\omega\mathbf{L} & \mathbf{A}_c^T \\ \mathbf{P}_e\mathbf{A}_c & -i\omega\mathbf{1} \end{bmatrix} \begin{bmatrix} \mathbf{j}_c \\ \boldsymbol{\phi}_e \end{bmatrix} = \begin{bmatrix} \mathbf{e}_{ext} \\ \mathbf{P}_e\mathbf{j}_{e0} \end{bmatrix}, \tag{3.20}$$

where $\mathbf{1}$ is the identity matrix. Finally, (3.20) can also be reduced by eliminating $\boldsymbol{\phi}_e$ with the Schur complement approach, as:

$$\left(\mathbf{R} + i\omega\mathbf{L} + \frac{1}{i\omega}\,\mathbf{A}_c^{\mathrm{T}}\mathbf{P}_e\mathbf{A}_c\right)\mathbf{j}_c = \mathbf{e}_{ext} + \frac{1}{i\omega}\mathbf{A}_c^{\mathrm{T}}\mathbf{P}_e\mathbf{j}_{e0}. \tag{3.21}$$

System (3.21) is the discrete version of the continuum integral equation (2.33). This system is also complex symmetric and of a smaller size than (3.19). However, since ω is at the denominator, (3.21) can be adopted only when the frequency is sufficiently larger than zero. Indeed, although the system is theoretically solvable for $\omega \neq 0$, the inductive term $i\omega\mathbf{L}$ and the capacitive term $\frac{1}{i\omega}\,\mathbf{A}_c{}^{\mathrm{T}}\mathbf{P}_e\mathbf{A}_c$ scale differently with ω and for relative small values of the frequency this different behavior could lead to the well known *breakdown in frequency* problem, which is deeply discussed in Section 4.2.3.

The extension to dielectric media can be easily obtained by applying the expansions (3.1) and (3.3) to $\mathbf{J}_e$, ϱ_e and ς_e. Then, the same discretization process is applied to the integral equations presented in Section 2.2.2 for the case of conductive and dielectric media [32].

When magnetic media are also considered the magnetization is also expanded by using local pulse vector basis functions. Electric and magnetic PEEC integral equations (2.55) and (2.58)

in Section 2.2.3 are both discretized with a Galerkin approach. A comprehensive literature concerning the extension of the Standard PEEC method to magnetic media can be found in [13, 48, 49, 17, 25, 33, 38].

The standard PEEC discretization scheme is based on an intuitive circuit interpretation of the continuum electromagnetic equations. However, the assumptions made in the derivation of that scheme sometimes lack of a systematic background and leads to a inaccurate numerical method [21] since the conservation properties (e.g. divergence) of the electromagnetic unknowns are not explicitly enforced. For these reasons, in the recent years the PEEC discretization scheme has been re–formulated introducing the concept of *duality* and *primal* and *dual* grids. In the next Section, this more sound discretization approach (i.e. unstructured PEEC discretization) is applied to the A–PEEC formulation presented in Section 2.2.3 for the case of conductive, dielectric, and magnetic media.

3.1.2 Unstructured discretization approach

The unstructured PEEC discretization scheme has been pioneering introduced in [21] for equivalent surface conductive models where the concepts of primal and dual grids (common to the Cell Method discretization approach and with some similarities with the Finite Element Networks [50]) have been introduced in the framework of the PEEC discretization. Then, the unstructured PEEC discretization of the A–PEEC formulation has been extended to the case of volume conductive and dielectric media in [6, 23] and finally to the general case of volume conductive, dielectric, and magnetic media in [26].

This section deals with the discretization of the A–PEEC formulation by means of the Cell Method. The more general case consisting of conductive, dielectric, and magnetic media is here considered.

Conductive and dielectric media are subject to the same discretization procedure, thus, the electric domain Ω_e (i.e. $\Omega_e = \Omega_c \cup \Omega_d$) is here considered (instead, when the conductive and the dielectric media require to be considered as distinct domains, it will be specified). From now on, the subscript e indicates quantities related to the electric domain Ω_e, while c and d indicate quantities related to the conducting Ω_c and dielectric Ω_d domains, respectively; the subscript m indicates quantities related to the magnetic domain Ω_m. All the definitions introduced for Ω_e are still valid for Ω_c and Ω_d by simply changing the subscript e with c and d, respectively.

Ω_e is first discretized into a primal tetrahedral or hexahedral grid $\mathcal{G}_{\Omega_e} = \mathcal{G}_{\Omega_c} \cup \mathcal{G}_{\Omega_d}$ consisting of $n_e = n_c + n_d$ nodes, $e_e = e_c + e_d$ edges, $f_e = f_c + f_d$ faces, and $v_e = v_c + v_d$ volumes [22]. Then, a dual grid $\tilde{\mathcal{G}}_{\Omega_e} = \tilde{\mathcal{G}}_{\Omega_c} \cup \tilde{\mathcal{G}}_{\Omega_d}$ consisting of dual geometric entities ($\tilde{n}_e$, $\tilde{e}_e$, $\tilde{f}_e$, $\tilde{v}_e$) can be obtained by taking the barycentric subdivision of $\mathcal{G}_{\Omega_e}$ [51].

Since the dual grid has been obtained as the barycentric subdivision of the primal one, a one–to–one relationship exists between the entities of the primal and the dual grid: $n_e \leftrightarrow \tilde{v}_e$, $e_e \leftrightarrow \tilde{f}_e$, $f_e \leftrightarrow \tilde{e}_e$, $v_e \leftrightarrow \tilde{n}_e$. The primal and dual grid entities for the particular case of a hexahedral structured mesh are represented in Fig. 3.2. In this particular case, both the primal and the dual grids consist of hexahedral elements, whereas, for a general unstructured primal grid, the dual grid obtained by its barycentric subdivision consists of generic polyhedra (more exhaustive representation of the primal and dual grids can be found in [22]).

The same discretization approach can be applied to the magnetic domain Ω_m, then the primal grid $\mathcal{G}_{\Omega_m}$ (n_m, e_m, f_m, v_m) and the dual grid $\tilde{\mathcal{G}}_{\Omega_m}$ ($\tilde{n}_m$, $\tilde{e}_m$, $\tilde{f}_m$, $\tilde{v}_m$) are defined. Again, a

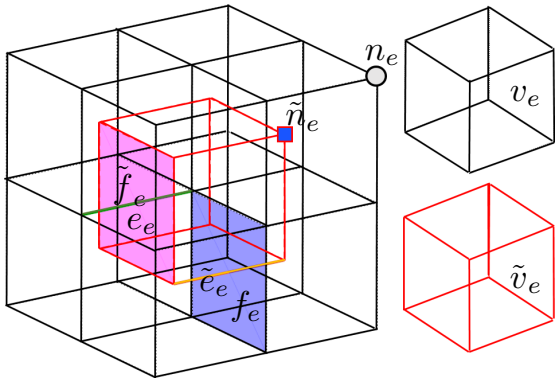

$\mathcal{G}_{\Omega_e} \leftrightarrow \tilde{\mathcal{G}}_{\Omega_e}$	
v_e	$\leftrightarrow \tilde{n}_e$
f_e	$\leftrightarrow \tilde{e}_e$
e_e	$\leftrightarrow \tilde{f}_e$
n_e	$\leftrightarrow \tilde{v}_e$

Figure 3.2: Primal and dual grids for the case of an hexahedral structured mesh.

one–to–one relationship exists between the elements of the two grids: $n_m \leftrightarrow \tilde{v}_m$, $e_m \leftrightarrow \tilde{f}_m$, $f_m \leftrightarrow \tilde{e}_m$, $v_m \leftrightarrow \tilde{n}_m$. Thus, $\mathcal{G}_{\Omega_m}$ is chosen to consist of tetrahedral/hexahedral elements, while $\tilde{\mathcal{G}}_{\Omega_m}$is obtained by its barycentric subdivision.

The electric current density is expanded by means of vector face shape functions related to the faces of the mesh [23, 52]:

$$\mathbf{J}_e(\mathbf{r}) = \sum_{k=1}^{f_e} \mathbf{w}_k^f(\mathbf{r}) j_{e_k}, \tag{3.22}$$

where $\mathbf{w}_k^f$ is the Whitney face shape function [53, 54] related to the kth primal face f_{e_k} of $\mathcal{G}_{\Omega_e}$. A different choice of shape functions can be however made [55, 56, 57], leading to the possibility of considering general polyhedral elements for the mesh discretization. Thus, once selected some proper shape functions, the use of general polyhedral elements would not affect the following discussion and considerations in this thesis. However, this topic has not been deeply investigated in the context of this PhD thesis.

In (3.22), j_{e_k} represent the flux of $\mathbf{J}_e$ through f_{e_k}, i.e. $j_{e_k} = \int_{f_{e_k}} \mathbf{J}_e \cdot d\mathbf{s}$. The fluxes j_{e_k}, for $k = 1, \cdots, f_e$, form the array of degrees of freedom (DoF) $\mathbf{j}_e = (j_{e_k})$ on faces $f_{e_k} \in \mathcal{G}_{\Omega_e}$. An equivalent definition holds for the conduction and polarization currents, leading the the array of DoFs $\mathbf{j}_c$ and $\mathbf{j}_p$.

According to Tonti's scheme [58] for classification of physical variables, the magnetization $\mathbf{M}$ is expanded by means of vector edge shape functions [26]:

$$\mathbf{M}(\mathbf{r}) = \sum_{s=1}^{e_m} \mathbf{w}_s^e(\mathbf{r}) m_s, \tag{3.23}$$

where $\mathbf{w}_s^e$ is the Whitney edge shape function [53] related to the sth primal edge e_{m_s} belonging to $\mathcal{G}_{\Omega_m}$. m_s is defined as $m_s = \int_{e_{m_s}} \mathbf{M} \cdot d\mathbf{l}$ along $e_{m_s} \in \mathcal{G}_{\Omega_m}$, leading to the array in the array $\mathbf{m} = (m_s)$.

The following incidence matrices [51] representing discrete gradient, curl, and divergence operators are then defined for the primal grids $\mathcal{G}_{\Omega_e}$ and $\mathcal{G}_{\Omega_m}$: $\mathbf{G}_{\Omega_\alpha}$ (*primal* edges–*primal* nodes), $\mathbf{C}_{\Omega_\alpha}$ (*primal* faces–*primal* edges), and $\mathbf{D}_{\Omega_\alpha}$ (*primal* volumes–*primal* faces), on $\mathcal{G}_{\Omega_\alpha}$, where $\alpha = e, m$ indicates the domain.

Dual gradient, curl, and divergence matrices can be obtained also for $\tilde{\mathcal{G}}_{\Omega_\alpha}$, i.e. $\tilde{\mathbf{G}}_{\Omega_\alpha}$ (*dual* edges–*dual* nodes), $\tilde{\mathbf{C}}_{\Omega_\alpha}$ (*dual* faces–*dual* edges), $\tilde{\mathbf{D}}_{\Omega_\alpha}$ (*dual* volumes–*dual* faces).

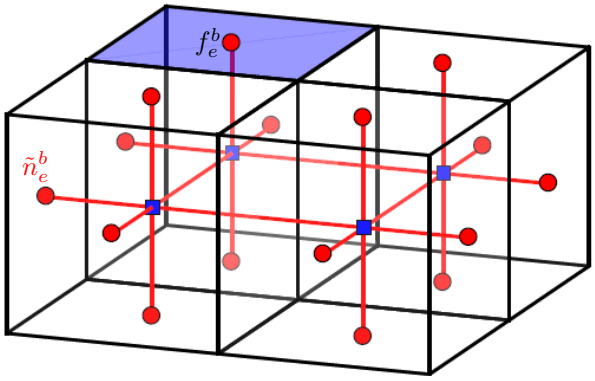

Figure 3.3: Primal ($\mathcal{G}_{\Omega_e}$) and augmented dual *electric* CM grids ($\tilde{\mathcal{G}}^a_{\Omega_e}$) for the A–PEEC method. Boundary primal faces f_e^b (blu face) and *dual boundary* nodes $\tilde{n}_e^b$ (red dots) are named in the figure.

These matrices consist of 0, 1, and -1 entries and (in analogy with the corresponding continuum operators) fulfill $\mathbf{D}_{\Omega_\alpha}\mathbf{C}_{\Omega_\alpha} = \mathbf{0}$ and $\mathbf{C}_{\Omega_\alpha}\mathbf{G}_{\Omega_\alpha} = \mathbf{0}$, the same for the dual matrices. Moreover, since $\tilde{\mathcal{G}}_{\Omega_\alpha}$ is obtained as the barycentric subdivision of $\mathcal{G}_{\Omega_\alpha}$, the following relations hold: $\mathbf{D}^T_{\Omega_\alpha} = -\tilde{\mathbf{G}}_{\Omega_\alpha}$, $\mathbf{C}^T_{\Omega_\alpha} = \tilde{\mathbf{C}}_{\Omega_\alpha}$, $\mathbf{G}^T_{\Omega_\alpha} = -\tilde{\mathbf{D}}_{\Omega_\alpha}$, with $\alpha = e, m$. As proposed in [51] and applied to the unstructured PEEC formulation by the author in [26], the $f_e^b \times f_e$ divergence selection matrix $\mathbf{D}_{\Gamma_e}$ which extracts the *boundary* faces f_e^b of $\mathcal{G}_{\Omega_e}$ is introduced. Moreover, the *dual boundary* nodes $\tilde{n}_e^b$ are added to $\tilde{\mathcal{G}}_{\Omega_e}$, leading to the augmented dual grid defined as $\mathcal{G}^a_{\Omega_e}$. These *dual boundary* nodes are in a one–to–one relation with the boundary faces of the mesh: $\tilde{n}_e^b \leftrightarrow f_e^b$, indeed they are located in the barycenter of the the boundary faces f_e^b, as exemplified in Fig. 3.3.

In order to consider the presence of the *dual boundary* nodes $\tilde{n}_e^b$ (i.e. the endpoints of the dual edges related to the primal boundary faces), the gradient selection matrix $\tilde{\mathbf{G}}_{\Gamma_e} = -\mathbf{D}^T_{\Gamma_e}$ is also introduced and the *augmented* divergence and *augmented* gradient matrices are defined as $\mathbf{D}^a_{\Omega_e} = [\mathbf{D}_{\Omega_e}; \mathbf{D}_{\Gamma_e}]$ and $\tilde{\mathbf{G}}^a_{\Omega_e} = -\mathbf{D}^{aT}_{\Omega_e} = [\tilde{\mathbf{G}}_{\Omega_e}, \tilde{\mathbf{G}}_{\Gamma_e}]$, respectively.

In the A–PEEC formulation, electric and magnetic media are differently handled, thus they also need different discretization procedures. Thus, the $e_m^b \times e_m$ curl selection matrix $\mathbf{C}_{\Gamma_m}$ which extracts the *primal boundary* edges e_m^b of $\mathcal{G}_{\Omega_m}$ is introduced and the *augmented* curl matrix is defined as $\mathbf{C}^a_{\Omega_m} = [\mathbf{C}_{\Omega_m}; \mathbf{C}_{\Gamma_m}]$.

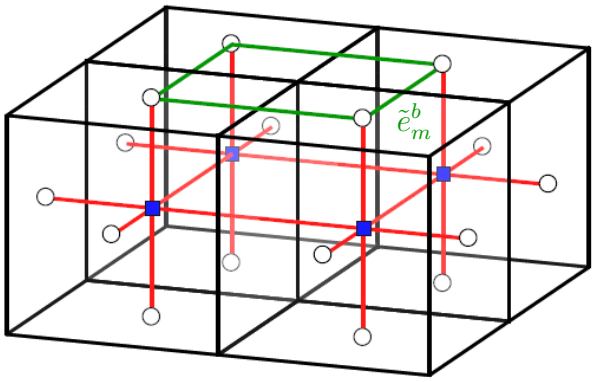

Figure 3.4: Primal ($\mathcal{G}_{\Omega_m}$) and augmented dual *magnetic* CM grids ($\tilde{\mathcal{G}}^a_{\Omega_m}$) for the A–PEEC method. *Dual boundary* edges $\tilde{e}_m^b$ (red dots) are in green in the figure.

Moreover, the dual magnetic grid, $\tilde{\mathcal{G}}_{\Omega_m}$, is augmented by introducing the *dual boundary* edges $\tilde{e}_m^b$ (in a one–to–one relation with e_m^b) leading to the *augmented* dual magnetic grid $\tilde{\mathcal{G}}_{\Omega_m}^a$, as exemplified in Fig. 3.4. Dual magnetic boundary nodes are not needed in the A–PEEC discretization of the magnetic media, thus they are not represented in Fig. 3.4 (empty circles).

In order to consider the presence of $\tilde{e}_m^b$ which close the contour of the dual faces that are in a one–to–one relationship with the primal boundary edges e_m^b, the dual augmented curl matrix is defined as $\tilde{\mathbf{C}}_{\Omega_m}^a = \mathbf{C}_{\Omega_m}^{aT} = [\tilde{\mathbf{C}}_{\Omega_m}, \tilde{\mathbf{C}}_{\Gamma_m}]$.

Thus, when the A–PEEC method is adopted, the discretization of electric media is given by Fig. 3.3, where dual boundary nodes $\tilde{n}_e^b$ have been added to $\tilde{\mathcal{G}}_{\Omega_e}$. Instead, the augmented grid for magnetic media is given by Fig. 3.4, where $\tilde{e}_m^b$ have been added to $\tilde{\mathcal{G}}_{\Omega_m}$.

In the CM discretization, in order to comply with the Tonti's scheme [22, 58], the electromagnetic fields, charges, and potentials are associated to algebraic quantities properly related to the geometric entities of the primal and the dual grids. The following arrays of DoFs which *live* on the primal and dual entities of the electric domains can be introduced for the A–PEEC formulation:

- $\tilde{\mathbf{e}} = (\tilde{e}_{e_k})$ on dual edges $\tilde{e}_e$, $\tilde{e}_{e_k} = \int_{\tilde{e}_{e_k}} \mathbf{E} \cdot d\mathbf{l}$,
- $\tilde{\mathbf{e}}_0 = (\tilde{e}_{0_k})$ on dual edges $\tilde{e}_e$, $\tilde{e}_{0_k} = \int_{\tilde{e}_{e_k}} \mathbf{E}_{ext} \cdot d\mathbf{l}$,
- $\tilde{\boldsymbol{\phi}}_e = (\tilde{\phi}_{e_k})$ on dual nodes $\tilde{n}_e$ and dual boundary nodes $\tilde{n}_e^b$, $\tilde{\phi}_{e_k} = \varphi_e(\mathbf{r}_{n_{e,k}})$,
- $\mathbf{q}_e^v = (q_{e_k}^v)$ on primal volumes v_e, $q_{e_k}^v = \int_{v_{e_k}} \varrho_e dv$,
- $\mathbf{q}_e^s = (q_{e_k}^s)$ on boundary primal faces f_e^b, $q_{e_k}^s = \int_{f_{e_k}^b} \varsigma_e ds$,
- $\tilde{\mathbf{a}}^e = (\tilde{a}_k^m)$ on dual edges $\tilde{e}_e$, $\tilde{a}_k^e = \int_{\tilde{e}_{e_k}} \mathbf{A} \cdot d\mathbf{l}$,

whereas, the following arrays of DoFs *living* on the primal and dual entities of the magnetic domains are defined:

- $\tilde{\mathbf{a}}^m = (\tilde{a}_k^m)$ on dual edges $\tilde{e}_m$, $\tilde{a}_k^m = \int_{\tilde{e}_{m_k}} \mathbf{A} \cdot d\mathbf{l}$,
- $\tilde{\mathbf{a}}^{m_b} = (\tilde{a}_k^{m_b})$ on dual boundary edges $\tilde{e}_m^b$, $\tilde{a}_k^m = \int_{\tilde{e}_{m_k}^b} \mathbf{A} \cdot d\mathbf{l}$,
- $\tilde{\mathbf{b}} = (\tilde{b}_k)$ on dual faces $\tilde{f}_m$, $\tilde{b}_k = \int_{\tilde{f}_{m_k}} \mathbf{B} \cdot d\mathbf{s}$,
- $\tilde{\mathbf{b}}_0 = (\tilde{b}_{0_k})$ on dual faces $\tilde{f}_m$, $\tilde{b}_{0_i} = \int_{\tilde{f}_{m,i}} \mathbf{B}_{ext} \cdot d\mathbf{s}$,
- $\mathbf{j}_a = (j_{a_i})$ on primal faces f_m, $j_{a_k} = \int_{f_{m_k}} \mathbf{J}_a \cdot d\mathbf{s}$,
- $\mathbf{k}_a = (k_{a_k})$ on primal boundary edges e_m^b, $k_{a_k} = \int_{e_{m_k}} \mathbf{M} \cdot d\mathbf{l}$.

The array of DoF $\tilde{\boldsymbol{\phi}}_e$ associated to the electric potential, φ_e, can be subdivided into $\tilde{\boldsymbol{\phi}}_e = [\tilde{\boldsymbol{\phi}}_e^v; \tilde{\boldsymbol{\phi}}_e^s]$, where $\tilde{\boldsymbol{\phi}}_e^v$ refers to the *interior* dual nodes of $\tilde{\mathcal{G}}_{\Omega_e}$ (in a one–to–one relation with v_e) and $\tilde{\boldsymbol{\phi}}_e^s$ to the *boundary* nodes $\tilde{n}_e^b$ (in a one–to–one relation with f_e^b). Thus, a one–to–one relationship exists between $\tilde{\boldsymbol{\phi}}_e = [\tilde{\boldsymbol{\phi}}_e^v; \tilde{\boldsymbol{\phi}}_e^s]$ and $\mathbf{q}_e = [\mathbf{q}_e^v; \mathbf{q}_e^s]$. The primal and dual electric grids with the related DoFs are exemplified in Fig. 3.5 for an equivalent 2–D case.

Thanks to the choice of the Whitney shape functions and to the definition of the primal and dual grids, the arrays of DoFs introduced above can be placed in the Tonti's scheme of Fig. 3.6

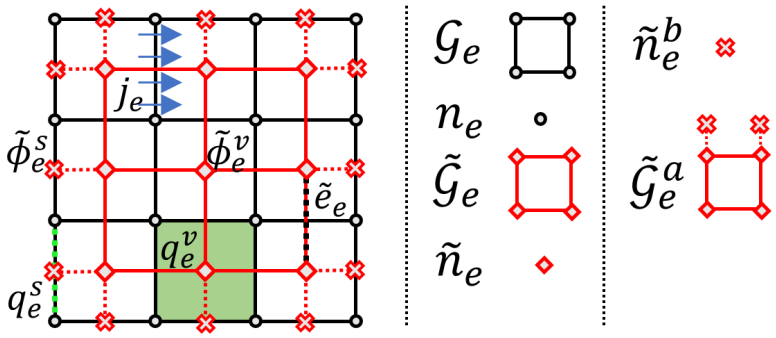

Figure 3.5: Primal ($\mathcal{G}_{\Omega_e}$) and augmented dual *electric* CM grids ($\tilde{\mathcal{G}}^a_{\Omega_e}$), 2–D case exemplification.

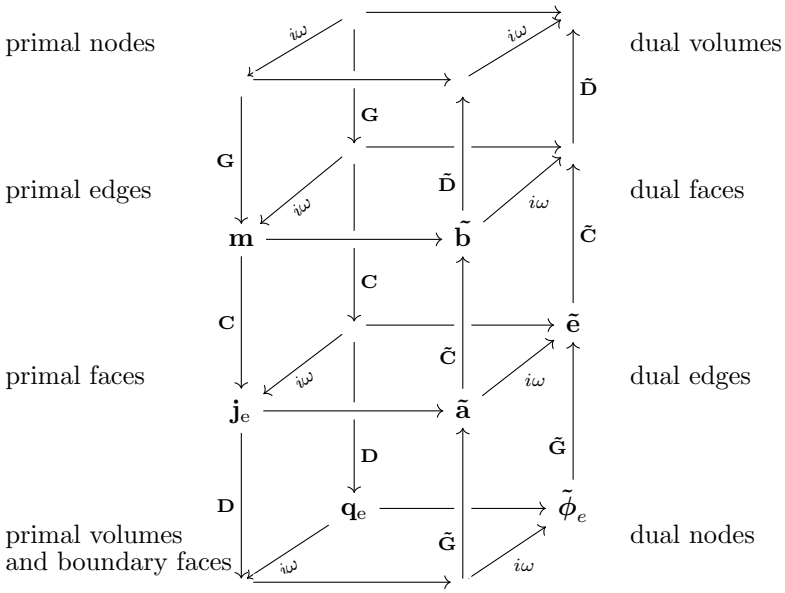

Figure 3.6: Tonti scheme for the A–PEEC method. Arrows without a label refer to resistance, inductance, and potential PEEC matrices.

and they satisfy algebraic relations equivalent to the differential equations introduced in Section 2.2.

For instance, the continuity equation (2.41) (in terms of DoFs) is given by the following

$$\mathbf{D}_{\Omega_e}\mathbf{j}_e = -i\omega\mathbf{q}_e^v, \qquad \mathbf{D}_{\Gamma_e}\mathbf{j}_e = -i\omega\mathbf{q}_e^s, \qquad \mathbf{D}^a_{\Omega_e}\mathbf{j}_e = -i\omega\mathbf{q}_e, \tag{3.24}$$

the relationships between the electromagnetic fields and the potentials are given by

$$\tilde{\mathbf{e}} = -i\omega\tilde{\mathbf{a}}^e - \tilde{\mathbf{G}}^a_{\Omega_e}\tilde{\boldsymbol{\phi}}_e + \tilde{\mathbf{e}}_0, \qquad \tilde{\mathbf{b}} = \tilde{\mathbf{C}}^a_{\Omega_m}\tilde{\mathbf{a}}^m + \tilde{\mathbf{b}}_0, \tag{3.25}$$

while the relationship between the magnetization and the amperian currents are represented by:

$$\mathbf{j}_a = \mathbf{C}_{\Omega_m}\mathbf{m}, \qquad \mathbf{k}_a = \mathbf{C}_{\Gamma_m}\mathbf{m}, \qquad [\mathbf{j}_a, \mathbf{k}_a] = \mathbf{C}^a_{\Omega_m}\mathbf{m}. \tag{3.26}$$

In the A–PEEC formulation derived in Section 2.2, the amperian volume and surface currents are adopted in the integral expressions of the electromagnetic potentials. Thus, it is convenient

to introduce expansions for both $\mathbf{J}_a$ and $\mathbf{K}_a$. Therefore, $\mathbf{J}_a$ is expanded by the following:

$$\mathbf{J}_a(\mathbf{r}) = \sum_{k=1}^{f_m} \mathbf{w}_k^f(\mathbf{r}) j_{a_k}, \tag{3.27}$$

the fluxes j_{a_k}, for $k = 1, \cdots, f_m$, are stored in the already defined array of DoF $\mathbf{j}_a = (j_{a_k})$. Moreover, $\mathbf{j}_a$ must satisfy also the first relation of (3.26).

$\mathbf{K}_a$ is instead expanded by the following:

$$\mathbf{K}_a(\mathbf{r}) = \sum_{k=1}^{e_m^b} \mathbf{w}_k^{f_\Gamma}(\mathbf{r}) k_{a_k}, \tag{3.28}$$

where $\mathbf{w}_k^{f_\Gamma} = \mathbf{n} \times \mathbf{w}_k^e$ is the surface face shape function related to the kth boundary edge e_k^b with triangular of quadrilateral support, $\mathbf{n}$ is the unit normal vector of the boundary support (i.e. the boundary face), and k_{a_k}, for $k = 1, \cdots, e_m^b$, are stored in the already defined array of DoF $\mathbf{k}_a = (k_{a_k})$. Moreover, $\mathbf{k}_a$ must satisfy also the second relation of (3.26). Expansion (3.28) can be also derived by combining (3.23) with the definition of $\mathbf{K}_a = \mathbf{M} \times \mathbf{n}$.

The expansions (3.22), and (3.23), (3.27), and (3.28) can now be inserted in the integral equation (2.55) derived in Section 2.2.3. Moreover, according to the Galerkin scheme, face elements are adopted as test functions for (2.55).

By doing this, and thanks to a property of Whitney elements (consistency property) [59], e.g.:

$$\tilde{a}_{e_i} = \int_{\tilde{e}_i} \mathbf{A}_e(\mathbf{r}) \cdot d\mathbf{l} = \int_\Omega \mathbf{w}_i^f(\mathbf{r}) \cdot \mathbf{A}_e(\mathbf{r}) d\Omega, \tag{3.29}$$

the continuum integral equation (and thus the whole electromagnetic problem) can now be written directly in terms of the previously defined arrays of DoFs. Thus, the discrete form of (2.55) is given by

$$\mathbf{R}_e \mathbf{j}_e + i\omega \tilde{\mathbf{a}}^e + \tilde{\mathbf{G}}_{\Omega_e}^a \tilde{\boldsymbol{\phi}}_e = \tilde{\mathbf{e}}_0, \tag{3.30}$$

where

$$\tilde{\mathbf{a}}^e = \mathbf{L}_e^e \mathbf{j}_e + \mathbf{L}_m^e \mathbf{j}_a + \mathbf{L}_{\Gamma_m}^e \mathbf{k}_a, \tag{3.31}$$

$$\tilde{\boldsymbol{\phi}}_e = \mathbf{P}_e \mathbf{q}_e. \tag{3.32}$$

$\mathbf{R}_e$ is the sparse $f_e \times f_e$ PEEC electric resistance matrix representing the discrete form of the constitutive equation (2.46). Its coefficients are

$$R_{e_{uk}} = \int_{\Omega_e} \rho_e(\mathbf{r}) \mathbf{w}_u^f(\mathbf{r}) \cdot \mathbf{w}_k^f(\mathbf{r}) d\Omega. \tag{3.33}$$

$\mathbf{L}_e^e$, $\mathbf{L}_m^e$, and $\mathbf{L}_{\Gamma_m}^e$ are instead the dense PEEC electric inductance matrices that represent the integral terms of equations (2.51). The dimension of the *volume* matrices $\mathbf{L}_e^e$, $\mathbf{L}_m^e$ is $f_e \times f_e$ and $f_e \times f_m$, respectively, while the dimension of *volume/surface* matrix $\mathbf{L}_{\Gamma_m}^e$ is $f_e \times e_m^b$. For the sake of conciseness, defining $\alpha = e, m$ and $\beta = e, m$, matrix inductance coefficients are

$$L_{\beta_{ku}}^{\alpha} = L_{\alpha_{uk}}^{\beta} = \mu_0 \int_{\Omega_\beta} \mathbf{w}_u^f(\mathbf{r}) \cdot \int_{\Omega_\alpha} \mathbf{w}_k^f(\mathbf{r}') g(\mathbf{r}, \mathbf{r}') d\Omega' d\Omega, \tag{3.34}$$

and

$$L_{\alpha_{ku}}^{\Gamma_m} = L_{\Gamma_{m_{uk}}}^{\alpha} = \mu_0 \int_{\Omega_\alpha} \mathbf{w}_u^f(\mathbf{r}) \cdot \int_{\Gamma_m} \mathbf{w}_k^{f_\Gamma}(\mathbf{r}') g(\mathbf{r}, \mathbf{r}') d\Gamma' d\Omega, \tag{3.35}$$

which are symmetric due to the symmetry of the shape function.

$\mathbf{P}_e$ is instead the dense $((v_e + f_e^b) \times (v_e + f_e^b))$ PEEC potential electric matrix representing the discrete form of (2.42). $\mathbf{P}_e$ is subdivided into

$$\mathbf{P}_e = \begin{bmatrix} \mathbf{P}_e^{vv} & \mathbf{P}_e^{vs} \\ \mathbf{P}_e^{sv} & \mathbf{P}_e^{ss} \end{bmatrix}, \tag{3.36}$$

where $\mathbf{P}_e^{vv}$, $\mathbf{P}_e^{ss}$, and $\mathbf{P}_e^{vs} = \mathbf{P}_e^{svT}$ are the *volume*, *surface*, and *volume/surface* potential matrices defined as:

$$\begin{aligned} P_{e_{uk}}^{vv} &= \frac{1}{\varepsilon_0 V_u V_k} \int_{v_{e_u}} \int_{v_{e_k}} g(\mathbf{r}, \mathbf{r}') d\Omega' d\Omega, \\ P_{e_{uk}}^{ss} &= \frac{1}{\varepsilon_0 S_u S_k} \int_{f_{e_u}} \int_{f_{e_k}} g(\mathbf{r}, \mathbf{r}') d\Gamma' d\Gamma, \\ P_{e_{uk}}^{vs} = P_{e_{ku}}^{sv} &= \frac{1}{\varepsilon_0 V_u S_k} \int_{v_{e_u}} \int_{f_{e_k}} g(\mathbf{r}, \mathbf{r}') d\Gamma' d\Omega, \end{aligned} \tag{3.37}$$

in which V_h and S_h indicate the volume and the area of a generic hth volume and surface cell, respectively.

Expressions (3.37) can be derived from the Galerkin testing of (2.55) (combined with the expansions (3.22), (3.27), and (3.28)) by applying the following property of the Whitney face elements:

$$\nabla \cdot \mathbf{w}_k^f = \frac{1}{V_u}, \qquad \mathbf{w}_h^f \cdot \mathbf{n} = \frac{1}{S_h^b} \tag{3.38}$$

where V_u is the volume of the support of $\mathbf{w}^f$ and S_h^b is the area of the boundary face f_h^b related to the kth Whitney face element. Indeed, the expansion of $\mathbf{J}_e$ in (3.22) induces the following expansion of the charge densities because of (3.38)

$$\varrho_e(\mathbf{r}) = \sum_k^{v_e} p_k^v(\mathbf{r}) q_{e_k}^v, \qquad \varsigma_e(\mathbf{r}) = \sum_k^{f_e^b} p_k^s(\mathbf{r}) q_{e_k}^s, \tag{3.39}$$

in which $p_k^v = \frac{1}{V_k}$ and $p_k^s = \frac{1}{S_k^b}$, where V_k is the volume of the kth tetrahedral/hexahedral element of the mesh and S_k^b if the area of the kth boundary triangular/quadrilateral face.

Matrices $\mathbf{R}_e$, $\mathbf{L}_e$, and $\mathbf{P}_e$ represent constitutive and integral interactions between the electromagnetic DoFs. In the CM discretization these kind of matrices define relationships between DoFs which live on the primal grid with DoFs which live on the dual grid, following the one–to–one relationships between the geometric entities of the two grids. Thus, $\mathbf{R}_e$, $\mathbf{L}_e$, and $\mathbf{P}_e$ matrices represent the unlabeled arrows of the Tonti's scheme in Fig. 3.6.

Expansions (3.22), (3.23), (3.27), and (3.28) can now be inserted in the integral continuum equation (2.58) and, following the Galerkin scheme, the resulting equation is then tested with the Whitney edge functions. Thus, the discrete form of (2.58) results in

$$\mathbf{F}\mathbf{m} - \tilde{\mathbf{C}}_{\Omega_m}^a[\tilde{\mathbf{a}}^m; \tilde{\mathbf{a}}^{m_b}] = \tilde{\mathbf{b}}_0, \tag{3.40}$$

where

$$\begin{aligned}\tilde{\mathbf{a}}^{m} =&\mathbf{L}_{e}^{m}\mathbf{j}_{e}+\mathbf{L}_{m}^{m}\mathbf{j}_{a}+\mathbf{L}_{\Gamma_m}^{m}\mathbf{k}_{a},\\ \tilde{\mathbf{a}}^{m_b} =&\mathbf{L}_{e}^{\Gamma_m}\mathbf{j}_{e}+\mathbf{L}_{m}^{\Gamma_m}\mathbf{j}_{a}+\mathbf{L}_{\Gamma_m}^{\Gamma_m}\mathbf{k}_{a}.\end{aligned} \tag{3.41}$$

$\mathbf{F}$ is the constitutive magnetic $e_m \times e_m$ matrix which represents the discrete form of the constitutive equation (2.57) and its coefficients are given by

$$F_{zs}=\int_{\Omega_m}\alpha_m(\mathbf{r})\mathbf{w}_z^e(\mathbf{r})\cdot\mathbf{w}_s^e(\mathbf{r})d\Omega. \tag{3.42}$$

The expression of the coefficients of the *volume* inductance matrices $\mathbf{L}_e^m$, $\mathbf{L}_m^m$ in (3.41) is still given by (3.34), whereas the ones of the *volume/surface* matrices $\mathbf{L}_{\Gamma_m}^m$, $\mathbf{L}_e^{\Gamma_m}$, $\mathbf{L}_m^{\Gamma_m}$ are given by (3.35). The coefficients of the *surface* inductance matrix $\mathbf{L}_{\Gamma_m}^{\Gamma_m}$ are instead given by

$$L_{\Gamma_{m_{uk}}}^{\Gamma_m}=\mu_0\int_{\Gamma_m}\mathbf{w}_u^{f_\Gamma}(\mathbf{r})\cdot\int_{\Gamma_m}\mathbf{w}_k^{f_\Gamma}(\mathbf{r}')g(\mathbf{r},\mathbf{r}')d\Gamma' d\Gamma. \tag{3.43}$$

The evaluation of the inductance and potential coefficients requires the computation of double volume or surface integrals. When the support of the basis and the test functions overlap the integrand shows a singularity due the Green's function. Thus, singularity extraction techniques should be adopted in order to properly evaluate matrix coefficients. In the literature, several singularity extraction techniques are proposed for the evaluation of the coefficients and the computation of the electromagnetic fields in the post–processing. Some useful references are [60, 61, 62, 63, 64, 65, 66, 67].

The third equation in (3.24) can be combined with (3.32) leading to:

$$\mathbf{D}_{\Omega_e}^{a}\mathbf{j}_e+i\omega\mathbf{P}_e^{-1}\tilde{\boldsymbol{\phi}}_e=\mathbf{0}. \tag{3.44}$$

Then, (3.30), (3.40), and (3.44) can be written together, resulting in the final system of equations

$$\begin{bmatrix}\mathbf{R}_e+i\omega\mathbf{L}_e^e & \tilde{\mathbf{G}}_{\Omega_e}^{a} & i\omega[\mathbf{L}_m^e,\mathbf{L}_{\Gamma_m}^e]\mathbf{C}_{\Omega_m}^{a}\\ \mathbf{P}_e\mathbf{D}_{\Omega_e}^{a} & i\omega\mathbf{1} & \mathbf{0}\\ -\tilde{\mathbf{C}}_{\Omega_m}^{a}\begin{bmatrix}\mathbf{L}_e^m\\ \mathbf{L}_e^{\Gamma_m}\end{bmatrix} & \mathbf{0} & \mathbf{F}-\tilde{\mathbf{C}}_{\Omega_m}^{a}\mathbf{L}_m^{a}\mathbf{C}_{\Omega_m}^{a}\end{bmatrix}\begin{bmatrix}\mathbf{j}_e\\ \tilde{\boldsymbol{\phi}}_e\\ \mathbf{m}\end{bmatrix}=\begin{bmatrix}\tilde{\mathbf{e}}_0\\ \mathbf{0}\\ \tilde{\mathbf{b}}_0\end{bmatrix}, \tag{3.45}$$

where

$$\mathbf{L}_m^{a}=\begin{bmatrix}\mathbf{L}_m^m & \mathbf{L}_{\Gamma_m}^m\\ \mathbf{L}_m^{\Gamma_m} & \mathbf{L}_{\Gamma_m}^{\Gamma_m}\end{bmatrix}, \tag{3.46}$$

is the *amperian* inductance matrix.

The solution of this final system of equations provides also an approximate solution of the continuum electromagnetic problem. Indeed, once obtained the values of $\mathbf{j}_e$ and $\mathbf{m}$, $\mathbf{q}_e$, $\mathbf{j}_a$, and $\mathbf{k}_a$ are obtained from (3.49) and (3.26). Then, the (approximate) distribution of $\mathbf{J}_e$, $\mathbf{J}_a$, $\mathbf{K}_a$, ρ_e, σ_e, and $\mathbf{M}$ can be obtained from the expansions (3.22), (3.27), (3.28), (3.23), and (3.39). Therefore, the electric and the magnetic fields can be evaluated for field sources in the whole space by using the integral expressions derived in Chapter 2.

The numerical features of (3.45) and the strategies to be adopted for its solution are thoroughly discussed in Chapter 4.

3.1.3 Circuit interpretation

When the A–PEEC formulation is discretized, and hence (3.45) is solved, the CM approach offers a natural circuit interpretation of the electromagnetic problem for the electric domain. Indeed, the nodes $\tilde{n}_e$ together with the boundary nodes $\tilde{n}_e^b$ can be interpreted as electric circuit nodes, while the edges $\tilde{e}_e$ can be interpreted as electric circuit branches carrying the electric currents $\mathbf{j}_e$. Thus, as in the standard PEEC discretization, the first row of (3.45) can be interpreted as KVLs written for each branch of the equivalent electric circuit (dual edges $\tilde{e}_e$) and $\tilde{\mathcal{G}}_{\Omega_e}$ represent the graph of the equivalent electric circuit. The second row of (3.45) can be instead interpreted as KCLs written for each node of the equivalent electric circuit (dual nodes $\tilde{n}_e$ and dual boundary nodes $\tilde{n}_e^b$). Thus, for the electric domain *only*, the structure of the original PEEC elementary circuit cell shown in Fig. 3.7 [21] can be adopted to represent the equivalent circuit derived from the discretization of the electric domains.

However, the third row of (3.45) derived from the discretization of the magnetic domains, does not offer the same circuit interpretation by means of the traditional PEEC elementary circuit cell. Thus, when magnetic media are actually involved and the A–PEEC formulation is discretized, the whole electromagnetic problem cannot be interpreted with the same circuit interpretation introduced for the original non–magnetic PEEC method.

Thus an MNA Spice–like solver can not be directly used to solve (3.45) since a circuit with the same structure as the electric one cannot be constructed for the magnetic domains.

Nevertheless, since the discretization of the electric domain allows an useful circuit interpretation, the electromagnetic problem can now be easily coupled with lumped circuit components with port currents j_{l_k}, with $k = 1, ..., N_l$ where N_l is the number of the lumped element ports [68]. As for the standard PEEC discretization, the coupling is handled by adding the lumped elements to the circuit graph (as exemplified in Fig. 3.8) and solving the electromagnetic problem together with the KVLs and KCLs written for the lumped elements, so the array of DoFs $\mathbf{j}_l = (j_{l^k})$ and $\tilde{\boldsymbol{\phi}}_{e_l} = (\tilde{\phi}_{e_{l,k}})$, with $k = 1, ..., N_n$ where N_n is the number of the lumped nodes, are added to the problem unknowns. Lumped ports can also be connected to internal $\tilde{n}_e$ or external $\tilde{n}_e^b$ nodes of $\tilde{\mathcal{G}}_{\Omega_e}$ (usually the external ones for cases of practical interest), in which case the incidence matrices $\mathbf{A}_{e,l}$ must be introduced in order to consider the connections between the lumped elements and the nodes $\tilde{n}_e$ and $\tilde{n}_e^b$. Moreover, as done in Section 3.1.1, the zero vector in

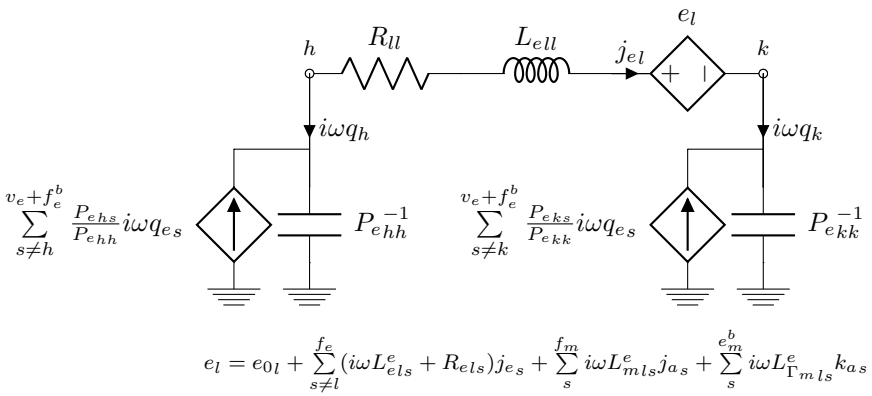

Figure 3.7: Elementary A–PEEC circuit cell for the lth electric face.

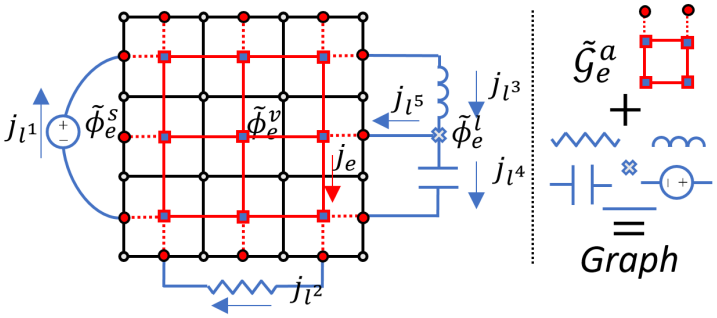

Figure 3.8: Electric Equivalent Circuit, a 2D case exemplification.

the rhs of (3.45) can be also substituted with $\mathbf{j}_{e0}$, which is the vector that stores $j_{0,k}$, i.e. a possible external current injected in the kth dual node of the mesh. Thus, the final electromagnetic problem coupled with lumped circuit elements can be written as

$$\begin{bmatrix} \mathbf{R}_e + i\omega\mathbf{L}_e^e & \tilde{\mathbf{G}}_{\Omega_e}^a & i\omega[\mathbf{L}_m^e, \mathbf{L}_{\Gamma_m}^e]\mathbf{C}_{\Omega_m}^a & \mathbf{0} & \mathbf{0} \\ \mathbf{P}_e\mathbf{D}_{\Omega_e}^a & i\omega\mathbf{1} & \mathbf{0} & \mathbf{P}_e\mathbf{A}_{e,l}^T & \mathbf{0} \\ -\tilde{\mathbf{C}}_{\Omega_m}^a \begin{bmatrix} \mathbf{L}_e^m \\ \mathbf{L}_e^{\Gamma_m} \end{bmatrix} & \mathbf{0} & \mathbf{F} - \tilde{\mathbf{C}}_{\Omega_m}^a\mathbf{L}_m^a\mathbf{C}_{\Omega_m}^a & \mathbf{0} & \mathbf{0} \\ \mathbf{0} & \mathbf{A}_{e,l} & \mathbf{0} & \mathbf{Z}_l & \mathbf{A}_{l,l} \\ \mathbf{0} & \mathbf{0} & \mathbf{0} & \mathbf{A}_{l,l}^T & \mathbf{0} \end{bmatrix} \begin{bmatrix} \mathbf{j}_e \\ \tilde{\boldsymbol{\phi}}_e \\ \mathbf{m} \\ \mathbf{j}_l \\ \tilde{\boldsymbol{\phi}}_{e,l} \end{bmatrix} = \begin{bmatrix} \tilde{\mathbf{e}}_0 \\ \mathbf{j}_{e0} \\ \tilde{\mathbf{b}}_0 \\ \mathbf{u}_{l0} \\ \mathbf{j}_{l0} \end{bmatrix}, \tag{3.47}$$

where $\mathbf{A}_{l,l}$ is the incidence matrix which describes the connections between the lumped branches and lumped nodes, $\mathbf{Z}_l$ is the lumped impedance matrix, $\mathbf{u}_{l0}$ is the array which stores the external voltage excitation of the lumped branches and $\mathbf{j}_{l0}$ is the array which stores the external currents injected in the lumped nodes.

3.2 Discretization of the C–PEEC formulation

This section deals with the unstructured Cell Method discretization of the C–PEEC formulation presented in Section 2.3.

Since the A–PEEC and the C–PEEC formulations are equivalent when magnetic media are not involved, the more general case consisting of conductive, dielectric, and magnetic media is here considered.

As in the A–PEEC method, conductive and dielectric media undergo the same discretization procedure, thus, as in Section 3.1.2, the electric domain $\Omega_e = \Omega_c \cup \Omega_d$ is here considered. All the definitions introduced for Ω_e are still valid for Ω_c and Ω_d by simply changing the subscript e with c and d, respectively.

The electric domain Ω_e is discretized in the same way of Section 3.1.2. Thus, the primal electric grid $\mathcal{G}_{\Omega_e}$ consists of tetrahedral or hexahedral elements and primal electric geometric entities are defined: n_e nodes, e_e edges, f_e faces, and v_e volumes [22]. Then, as in Section 3.1.2, the augmented dual grid $\tilde{\mathcal{G}}_{\Omega_e}^a$ consisting of dual geometric entities ($\tilde{n}_e + \tilde{n}_e^b$, $\tilde{e}_e$, $\tilde{f}_e$, $\tilde{v}_e$) is obtained by taking the barycentric subdivision of $\mathcal{G}_{\Omega_e}$ and adding the dual boundary nodes $\tilde{n}_e^b$ [51]. Again, since the dual grid has been obtained as the barycentric subdivision of the primal one, a one–to–one relationship exists between the entities of the primal and the dual grid: $n_e \leftrightarrow \tilde{v}_e$, $e_e \leftrightarrow \tilde{f}_e$, $f_e \leftrightarrow \tilde{e}_e$, $v_e \leftrightarrow \tilde{n}_e$, $f_e^b \leftrightarrow \tilde{n}_e^b$.

In the C–PEEC formulation, electric and magnetic media are handled with a unified approach. Thus, unlike the A–PEEC method, the same discretization procedure performed for Ω_e is now applied to the magnetic domain Ω_m. However, in order to be consistent with the Tonti's scheme, the role of the primal and dual grids are exchanged in the discretization of the magnetic domain. Indeed, the *dual* magnetic grid $\tilde{\mathcal{G}}_{\Omega_m}$ is now chosen to consist of tetrahedral or hexahedral elements while the *primal* magnetic grid $\mathcal{G}_{\Omega_m}$ is obtained as the barycentric subdivision of $\tilde{\mathcal{G}}_{\Omega_m}$, and thus it consists on general polyhedral (except when a structured case is considered). Therefore, the *dual* magnetic grid $\tilde{\mathcal{G}}_{\Omega_m}$ consists of dual geometric entities ($\tilde{n}_m$, $\tilde{e}_m$, $\tilde{f}_m$, $\tilde{v}_m$) while the *primal* magnetic grid $\mathcal{G}_{\Omega_m}$ consists of primal geometric entities (n_m, e_m, f_m, v_m) and it is augmented by inserting the boundary primal magnetic nodes n_m^b in a one–to–one relationship with the dual boundary faces $\tilde{f}_m^b$. Thus, the augmented primal magnetic matrix $\mathcal{G}_{\Omega_m}^a$ consists of n_m nodes, n_m^b boundary nodes, e_m edges, f_m faces, and v_m volumes.

This choice in the definition of $\tilde{\mathcal{G}}_{\Omega_m}$ and $\mathcal{G}_{\Omega_m}$ allows for a convenient collocation of the DoFs related to the electromagnetic quantities. So, when the C–PEEC formulation is discretized, the primal and dual electric grids (i.e. the ones for Ω_e) are the ones represented in Fig. 3.3. Primal and dual magnetic grids (i.e. the ones for Ω_m) are instead shown in Fig. 3.9, where the only difference with respect to Fig. 3.3 is the changing in the definition of *primal* and *dual*.

The electric current density vector $\mathbf{J}_e$ is now expanded as in (3.22) and the array of DoFs $\mathbf{j}_e$ is introduced with the same definition. In the C–PEEC formulation, the magnetic current density vector $\mathbf{J}_m$ is introduced in (2.59) as equivalent source in the magnetic domains and it is considered as unknown of the electromagnetic problem. $\mathbf{J}_m$ is now expanded by means of vector face shape functions whose supports are the tetrahedral/hexahedral elements of $\tilde{\mathcal{G}}_m$:

$$\mathbf{J}_m(\mathbf{r}) = \sum_{k=1}^{\tilde{f}_m} \mathbf{w}_k^f(\mathbf{r}) \tilde{j}_{m_k}, \tag{3.48}$$

where $\tilde{j}_{m_k}$ represents the flux of $\mathbf{J}_m$ through $\tilde{f}_{m_k}$, i.e. $\tilde{j}_{m_k} = \int_{\tilde{f}_{m_k}} \mathbf{J}_m \cdot d\mathbf{s}$. The fluxes $\tilde{j}_{m_k}$, for $k = 1, \cdots, \tilde{f}_m$, form the array of DoFs $\tilde{\mathbf{j}}_m = (\tilde{j}_{m_k})$ on faces $\tilde{f}_{m_k} \in \tilde{\mathcal{G}}_{\Omega_m}$.

With the same definitions given in Section 3.1.2, the incidence matrices [51] representing discrete gradient, curl, and divergence operators are defined for the primal and dual electric grids: $\mathbf{G}_{\Omega_e}$ (*primal* edges–*primal* nodes), $\mathbf{C}_{\Omega_e}$ (*primal* faces–*primal* edges), and $\mathbf{D}_{\Omega_e}$ (*primal*

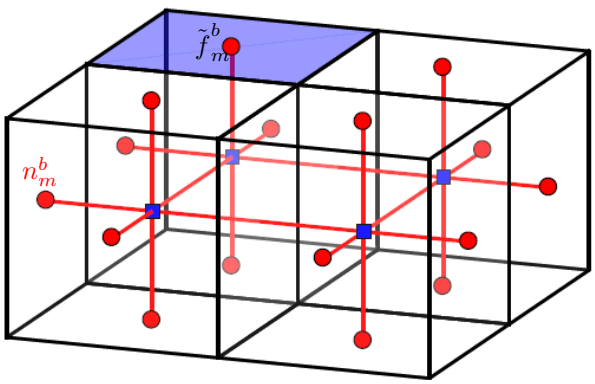

Figure 3.9: Augmented primal ($\mathcal{G}_{\Omega_m}^a$) and dual *magnetic* CM grids ($\tilde{\mathcal{G}}_{\Omega_m}$) for the C–PEEC method. Boundary dual faces $\tilde{f}_m^b$ (blu face) and *primal boundary* nodes n_m^b (red dots) are named in the figure.

volumes–*primal* faces), $\tilde{\mathbf{G}}_{\Omega_e}$ (*dual* edges–*dual* nodes), $\tilde{\mathbf{C}}_{\Omega_e}$ (*dual* faces–*dual* edges), $\tilde{\mathbf{D}}_{\Omega_e}$ (*dual* volumes–*dual* faces).

As done in Section 3.1.2, the $f_e^b \times f_e$ divergence selection matrix $\mathbf{D}_{\Gamma_e}$ which extracts the *boundary* faces f_e^b of $\mathcal{G}_{\Omega_e}$ is introduced; the dual gradient selection matrix $\tilde{\mathbf{G}}_{\Gamma_e} = -\mathbf{D}_{\Gamma_e}^T$ is also introduced and the *augmented* divergence and *augmented* dual gradient matrices are defined as $\mathbf{D}_{\Omega_e}^a = [\mathbf{D}_{\Omega_e}; \mathbf{D}_{\Gamma_e}]$ and $\tilde{\mathbf{G}}_{\Omega_e}^a = -\mathbf{D}_{\Omega_e}^{aT} = [\tilde{\mathbf{G}}_{\Omega_e}, \tilde{\mathbf{G}}_{\Gamma_e}]$, respectively.

Since electric and magnetic media are considered in the same way in the C–PEEC method, the same incidence matrices are now introduced for the magnetic domains. Thus, gradient, curl, and divergence operators are defined for the primal and dual magnetic grids: $\mathbf{G}_{\Omega_m}$ (*primal* edges–*primal* nodes), $\mathbf{C}_{\Omega_m}$ (*primal* faces–*primal* edges), and $\mathbf{D}_{\Omega_m}$ (*primal* volumes–*primal* faces), $\tilde{\mathbf{G}}_{\Omega_m}$ (*dual* edges–*dual* nodes), $\tilde{\mathbf{C}}_{\Omega_m}$ (*dual* faces–*dual* edges), $\tilde{\mathbf{D}}_{\Omega_m}$ (*dual* volumes–*dual* faces). Then, keeping in mind that the role of the *primal* and *dual* grids is exchanged with respect the electric domains, the $\tilde{f}_m^b \times \tilde{f}_m$ *dual* divergence selection matrix $\tilde{\mathbf{D}}_{\Gamma_m}$ which extracts the dual *boundary* faces $\tilde{f}_m^b$ of $\tilde{\mathcal{G}}_{\Omega_m}$ is introduced; the *primal* gradient selection matrix $\mathbf{G}_{\Gamma_m} = -\mathbf{D}_{\Gamma_m}^T$ is also introduced and the *augmented* divergence and *augmented* gradient matrices are defined as $\mathbf{D}_{\Omega_m}^a = [\mathbf{D}_{\Omega_m}; \mathbf{D}_{\Gamma_m}]$ and $\tilde{\mathbf{G}}_{\Omega_m}^a = -\mathbf{D}_{\Omega_m}^{aT} = [\tilde{\mathbf{G}}_{\Omega_m}, \tilde{\mathbf{G}}_{\Gamma_m}]$, respectively.

As in Section 3.1.2, the electromagnetic fields, charges, and potentials are associated to algebraic quantities that are properly associated to the entities of the primal and the dual grids. Thus, the following arrays of DoFs which *live* on the primal and dual entities of the electric domains can be introduced for the C–PEEC formulation:

- $\tilde{\mathbf{e}} = (\tilde{e}_{e_k})$ on dual edges $\tilde{e}_e$, $\tilde{e}_{e_k} = \int_{\tilde{e}_{e_k}} \mathbf{E} \cdot d\mathbf{l}$,
- $\tilde{\mathbf{e}}_0 = (\tilde{e}_{0_k})$ on dual edges $\tilde{e}_e$, $\tilde{e}_{0_k} = \int_{\tilde{e}_{e_k}} \mathbf{E}_{ext} \cdot d\mathbf{l}$,
- $\tilde{\boldsymbol{\phi}}_e = (\tilde{\phi}_{e_k})$ on dual nodes $\tilde{n}_e$ and dual boundary nodes $\tilde{n}_e^b$, $\tilde{\phi}_{e_k} = \varphi_e(\mathbf{r}_{n_{e,k}})$,
- $\mathbf{q}_e^v = (q_{e_k}^v)$ on primal volumes v_e, $q_{e_k}^v = \int_{v_{e_k}} \varrho_e dv$,
- $\mathbf{q}_e^s = (q_{e_k}^s)$ on primal boundary faces f_e^b, $q_{e_k}^s = \int_{f_{e_k}^b} \varsigma_e ds$,
- $\tilde{\mathbf{a}}_e = (\tilde{a}_{e_i})$ on dual edges $\tilde{e}_e$, $\tilde{a}_{e_i} = \int_{\tilde{e}_{e,i}} \mathbf{A}_e \cdot d\mathbf{l}$,
- $\mathbf{a}_m^e = (a_{m_i}^e)$ on primal edges e_e, $a_{m_i}^e = \int_{e_{e,i}} \mathbf{A}_m \cdot d\mathbf{l}$,

whereas, the following arrays of DoFs *living* on the primal and dual entities of the magnetic domains are defined:

- $\mathbf{h} = (h_k)$ on primal edges e_m, $h_k = \int_{e_{m,k}} \mathbf{H} \cdot d\mathbf{l}$,
- $\mathbf{h}_0 = (h_{0_k})$ on primal edges e_m, $h_{0_k} = \int_{e_{m,k}} \mathbf{H}_0 \cdot d\mathbf{l}$,
- $\boldsymbol{\phi}_m = (\phi_{m_k})$ on primal nodes n_m and primal boundary nodes n_m^b, $\phi_{m_k} = \varphi_m(\mathbf{r}_{n_{m,k}})$,
- $\tilde{\mathbf{q}}_m^v = (\tilde{q}_{m_i}^v)$ on dual volumes $\tilde{v}_m$, $\tilde{q}_{m_k}^v = \int_{\tilde{v}_{m,k}} \varrho_m dv$,
- $\tilde{\mathbf{q}}_m^s = (\tilde{q}_{m_k}^s)$ on dual boundary faces $\tilde{f}_m^b$, $\tilde{q}_{m_k}^s = \int_{\tilde{f}_{m,k}^b} \sigma_m ds$.
- $\mathbf{a}_m = (a_{m_k})$ on primal edges e_m, $a_{m_k} = \int_{e_{m,k}} \mathbf{A}_m \cdot d\mathbf{l}$,
- $\tilde{\mathbf{a}}_e^m = (\tilde{a}_{e_k}^m)$ on dual edges $\tilde{e}_m$, $\tilde{a}_{e_k}^m = \int_{\tilde{e}_{m,k}} \mathbf{A}_e \cdot d\mathbf{l}$,

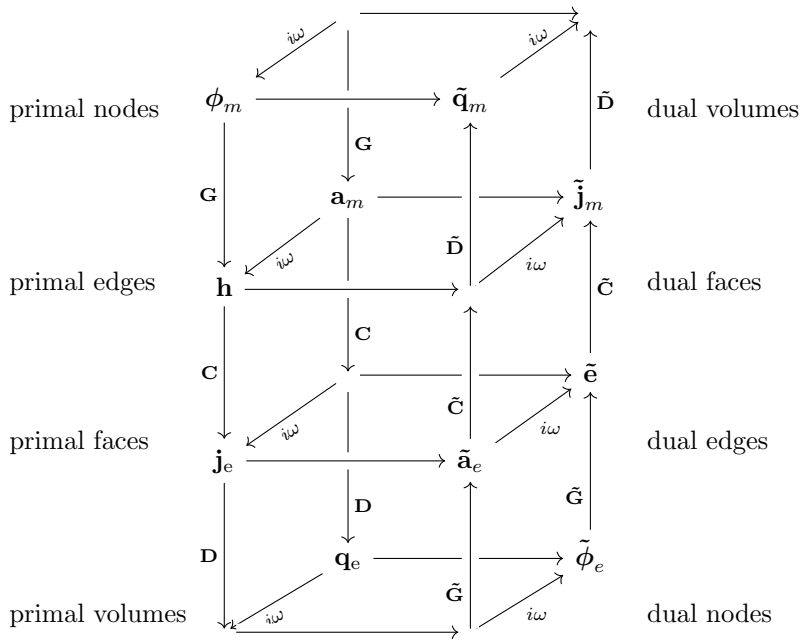

Figure 3.10: Tonti scheme for the C–PEEC method. Arrows without a label refer to resistance, inductance, and potential PEEC matrices.

As one can notice, there are obvious similarities between the DoFs introduced for the electric and the magnetic domains and this reflects the symmetries of the C–PEEC formulation in the handling of electric and magnetic media.

As in Section 3.1.2, the array of DoF $\tilde{\boldsymbol{\phi}}_e$ is subdivided into $\tilde{\boldsymbol{\phi}}_e = [\tilde{\boldsymbol{\phi}}_e^{\,v}; \tilde{\boldsymbol{\phi}}_e^{\,s}]$ and a one–to–one relationship exists between $\tilde{\boldsymbol{\phi}}_e = [\tilde{\boldsymbol{\phi}}_e^{\,v}; \tilde{\boldsymbol{\phi}}_e^{\,s}]$ and $\mathbf{q}_e = [\mathbf{q}_e^v; \mathbf{q}_e^s]$. A completely equivalent argument holds also for $\boldsymbol{\phi}_m = [\boldsymbol{\phi}_m^v; \boldsymbol{\phi}_m^s]$ and $\tilde{\mathbf{q}}_m = [\tilde{\mathbf{q}}_m^v; \tilde{\mathbf{q}}_m^s]$, where $\boldsymbol{\phi}_m^v$ refers to the *interior* nodes n_m of $\mathcal{G}_m$ (in a one–to–one relation with $\tilde{v}_m$) and $\boldsymbol{\phi}_m^s$ refers to the *boundary* nodes n_m^b (in a one–to–one relation with $\tilde{f}_m^b$).

The arrays of DoFs introduced above can be placed in the Tonti's scheme shown Fig. 3.10 and they satisfy algebraic relations equivalent to the differential equations introduced in Section 2.3. For instance, the continuity equation (2.77) (in terms of DoFs) is given by the following

$$\tilde{\mathbf{D}}_{\Omega_m}\tilde{\mathbf{j}}_m = -i\omega\tilde{\mathbf{q}}_m^v, \qquad \tilde{\mathbf{D}}_{\Gamma_m}\tilde{\mathbf{j}}_m = -i\omega\tilde{\mathbf{q}}_m^s, \qquad \tilde{\mathbf{D}}^a_{\Omega_m}\tilde{\mathbf{j}}_m = -i\omega\tilde{\mathbf{q}}_m, \tag{3.49}$$

and (3.24) is still valid for $\mathbf{j}_e$, $\mathbf{q}_e^v$, and $\mathbf{q}_e^s$.

As for the electric currents and charges, the expansion (3.48) adopted for $\mathbf{J}_m$ leads to the following expansions of the magnetic charge densities:

$$\varrho_m(\mathbf{r}) = \sum_k^{\tilde{v}_m} p_k^v(\mathbf{r})\tilde{q}_{m_k}^v, \qquad \varsigma_m(\mathbf{r}) = \sum_k^{\tilde{f}_m^b} p_k^s(\mathbf{r})\tilde{q}_{m_k}^s, \tag{3.50}$$

in which $p_k^v = \frac{1}{V_k}$ and $p_k^s = \frac{1}{S_k^b}$, where V_k is the volume of the kth tetrahedral/hexahedral element of $\tilde{\mathcal{G}}$ and S_k^b if the area of the kth boundary triangular/quadrilateral face.

The expansions (3.22), and (3.48) can now be inserted in the continuum integral equations (2.92) and (2.93) derived in Section 2.3. Moreover, following the Galerkin scheme, the Whitney face elements are adopted as test functions for both the resulting equations. Thus, the discrete forms of (2.92) and (2.93) are given by

$$\mathbf{R}_e\mathbf{j}_e + i\omega\tilde{\mathbf{a}}_e + \tilde{\mathbf{G}}^a_{\Omega_e}\tilde{\boldsymbol{\phi}}_e + \mathbf{M}_{1/\varepsilon_0}\mathbf{C}_{\Omega_e}\mathbf{a}^e_m = \tilde{\mathbf{e}}_0, \tag{3.51}$$

$$\tilde{\mathbf{R}}_m\tilde{\mathbf{j}}_m + i\omega\mathbf{a}_m + \mathbf{G}^a_{\Omega_m}\boldsymbol{\phi}_m - \tilde{\mathbf{M}}_{1/\mu_0}\tilde{\mathbf{C}}_{\Omega_m}\tilde{\mathbf{a}}^m_e = \mathbf{h}_0, \tag{3.52}$$

where

$$\tilde{\mathbf{a}}_e = \mathbf{L}^e_e\mathbf{j}_e, \quad \mathbf{a}_m = \tilde{\mathbf{L}}^m_m\tilde{\mathbf{j}}_m, \quad \tilde{\mathbf{a}}^m_e = \mathbf{N}^m_e\mathbf{j}_e, \quad \mathbf{a}^e_m = \tilde{\mathbf{N}}^e_m\tilde{\mathbf{j}}_m, \tag{3.53}$$

$$\tilde{\boldsymbol{\phi}}_e = \mathbf{P}_e\mathbf{q}_e, \quad \boldsymbol{\phi}_m = \tilde{\mathbf{P}}_m\tilde{\mathbf{q}}_m. \tag{3.54}$$

The definition of the PEEC resistance matrix $\mathbf{R}_e$ is the same one given in (3.33). The electric inductance matrix $\mathbf{L}^e_e$ has also the same definition of the one derived for the discretization of the A–PEEC method and its coefficients are still given by (3.34). The same argument holds for the potential matrix $\mathbf{P}_e$, the definition of which is given in (3.36) and (3.37).

Matrices $\tilde{\mathbf{R}}_m$, $\tilde{\mathbf{L}}^m_m$, and $\tilde{\mathbf{P}}_m$ are instead the resistance, inductance, and potential magnetic PEEC matrices. Their definitions are equivalent to the ones given to the corresponding electric matrices. Thus, the sparse $\tilde{f}_m \times \tilde{f}_m$ PEEC magnetic resistance matrix $\tilde{\mathbf{R}}_m$ represents the discrete form of (2.85) and its coefficients are:

$$\tilde{R}_{m_{uk}} = \int_{\Omega_m} \rho_m(\mathbf{r})\mathbf{w}^f_u(\mathbf{r}) \cdot \mathbf{w}^f_k(\mathbf{r})d\Omega. \tag{3.55}$$

The dense $\tilde{f}_m \times \tilde{f}_m$ PEEC magnetic inductance matrix $\tilde{\mathbf{L}}^m_m$ instead represents the discrete form of equation (2.73) (while $\mathbf{L}^e_e$ is now related to (2.72)) and its coefficients are given by

$$\tilde{L}^m_{m_{ku}} = \tilde{L}^m_{m_{uk}} = \varepsilon_0 \int_{\Omega_m} \mathbf{w}^f_u(\mathbf{r}) \cdot \int_{\Omega_m} \mathbf{w}^f_k(\mathbf{r}')g(\mathbf{r},\mathbf{r}')d\Omega' d\Omega. \tag{3.56}$$

The $((\tilde{v}_m + \tilde{f}^b_m) \times (\tilde{v}_m + \tilde{f}^b_m))$ PEEC potential magnetic matrix $\tilde{\mathbf{P}}_m$ is instead the discrete form of (2.79) and, as the corresponding electric matrix, it can be subdivided into

$$\tilde{\mathbf{P}}_m = \begin{bmatrix} \tilde{\mathbf{P}}^{vv}_m & \tilde{\mathbf{P}}^{vs}_m \\ \tilde{\mathbf{P}}^{sv}_m & \tilde{\mathbf{P}}^{ss}_m \end{bmatrix}, \tag{3.57}$$

where $\tilde{\mathbf{P}}^{vv}_m$, $\tilde{\mathbf{P}}^{ss}_m$, and $\tilde{\mathbf{P}}^{vs}_m = \mathbf{P}^{sv\,T}_m$ are the *volume*, *surface*, and *volume/surface* potential magnetic matrices defined as:

$$\begin{aligned} \tilde{P}^{vv}_{m_{uk}} &= \frac{1}{\mu_0 V_u V_k}\int_{v_{e_u}}\int_{v_{e_k}} g(\mathbf{r},\mathbf{r}')d\Omega' d\Omega, \\ \tilde{P}^{ss}_{m_{uk}} &= \frac{1}{\mu_0 S_u S_k}\int_{f_{e_u}}\int_{f_{e_k}} g(\mathbf{r},\mathbf{r}')d\Gamma' d\Gamma, \\ \tilde{P}^{vs}_{m_{uk}} = \tilde{P}^{sv}_{m_{ku}} &= \frac{1}{\mu_0 V_u S_k}\int_{v_{e_u}}\int_{f_{e_k}} g(\mathbf{r},\mathbf{r}')d\Gamma' d\Omega, \end{aligned} \tag{3.58}$$

in which V_h and S_h indicate the volume and the area of a generic hth volume and surface cell, respectively.

Matrices $\mathbf{N}_e^m$ and $\tilde{\mathbf{N}}_m^e$ represent instead the mutual interaction between the electric and the magnetic domains. In particular, the full $(\tilde{e}_m \times f_e)$ $\mathbf{N}_e^m$ matrix is the discrete form of (2.73) when the magnetic potential $\mathbf{A}_m$ produced by $\mathbf{J}_m$ is evaluated in the electric domain Ω_e. Instead, the $(e_e \times \tilde{f}_m)$ matrix $\tilde{\mathbf{N}}_m^e$ is the discrete form of (2.72) when the electric potential $\mathbf{A}_e$ produced by $\mathbf{J}_e$ is evaluated in the magnetic domain Ω_m. Thanks to the consistency property (3.29), $\mathbf{N}_e^m$ and $\tilde{\mathbf{N}}_m^e$ are defined by evaluating the line integral of the electric and magnetic vector potentials along the primal and dual edges, i.e.

$$N_{e_{wk}}^m = \mu_0 \int_{\tilde{e}_w} \Big(\int_{\Omega_e} \mathbf{w}_k^f(\mathbf{r}') g(\mathbf{r}, \mathbf{r}') d\Omega' \Big) \cdot d\mathbf{l}, \tag{3.59}$$

$$\tilde{N}_{m_{uh}}^e = \varepsilon_0 \int_{e_u} \Big(\int_{\Omega_m} \mathbf{w}_h^f(\mathbf{r}') g(\mathbf{r}, \mathbf{r}') d\Omega' \Big) \cdot d\mathbf{l}. \tag{3.60}$$

Finally, $\mathbf{M}_{1/\varepsilon_0}$ and $\tilde{\mathbf{M}}_{1/\mu_0}$ are mass matrices of dimensions $(f_e \times f_e)$ and $(\tilde{f}_m \times \tilde{f}_m)$, respectively. Their definition is given by

$$\begin{aligned} M_{1/\varepsilon_{0_{uk}}} &= \frac{1}{\varepsilon_0} \int_{\Omega_e} \mathbf{w}_u^f(\mathbf{r}) \cdot \mathbf{w}_k^f(\mathbf{r}) d\Omega, \\ \tilde{M}_{1/\mu_{0_{wh}}} &= \frac{1}{\mu_0} \int_{\Omega_m} \mathbf{w}_w^f(\mathbf{r}) \cdot \mathbf{w}_h^f(\mathbf{r}) d\Omega, \end{aligned} \tag{3.61}$$

and they represent the terms $\frac{1}{\varepsilon_0}$ and $\frac{1}{\mu_0}$ in (2.92) and (2.93), respectively.

Finally, the whole problem can be represented as an algebraic system of equations. Thus, equations (3.54), (3.49), and (3.24) can be combined together resulting in (3.44) and

$$\tilde{\mathbf{D}}_{\Omega_m}^a \tilde{\mathbf{j}}_m + i\omega \tilde{\mathbf{P}}_m^{-1} \boldsymbol{\phi}_m = \mathbf{0}. \tag{3.62}$$

Then, (3.51), (3.52), (3.44), and (3.62) can be written together, resulting in the following system of equations

$$\begin{bmatrix} \mathbf{R}_e + i\omega \mathbf{L}_e^e & \tilde{\mathbf{G}}_{\Omega_e}^a & \tilde{\mathbf{K}}_m^e & \mathbf{0} \\ \mathbf{P}_e \mathbf{D}_{\Omega_e}^a & i\omega \mathbf{1} & \mathbf{0} & \mathbf{0} \\ -\mathbf{K}_e^m & \mathbf{0} & \tilde{\mathbf{R}}_m + i\omega \tilde{\mathbf{L}}_m^m & \mathbf{G}_{\Omega_m}^a \\ \mathbf{0} & \mathbf{0} & \tilde{\mathbf{P}}_m \tilde{\mathbf{D}}_{\Omega_m}^a & i\omega \mathbf{1} \end{bmatrix} \begin{bmatrix} \mathbf{j}_e \\ \tilde{\boldsymbol{\phi}}_e \\ \tilde{\mathbf{j}}_m \\ \boldsymbol{\phi}_m \end{bmatrix} = \begin{bmatrix} \tilde{\mathbf{e}}_0 \\ \mathbf{0} \\ \mathbf{h}_0 \\ \mathbf{0} \end{bmatrix}, \tag{3.63}$$

where

$$\tilde{\mathbf{K}}_m^e = \mathbf{M}_{1/\varepsilon_0} \mathbf{C}_{\Omega_e} \tilde{\mathbf{N}}_m^e, \tag{3.64}$$

and

$$\mathbf{K}_e^m = \tilde{\mathbf{M}}_{1/\mu_0} \tilde{\mathbf{C}}_{\Omega_m} \mathbf{N}_e^m. \tag{3.65}$$

As (3.45), the solution of (3.63) provides also an approximate solution of the continuum electromagnetic problem. Indeed, once obtained $\mathbf{j}_e$ and $\tilde{\mathbf{j}}_m$, the vector arrays $\mathbf{q}_e$ and $\tilde{\mathbf{q}}_m$ are obtained from (3.24) and (3.49), respectively. Then, the distribution of $\mathbf{J}_e$, $\mathbf{J}_m$, ϱ_c, ϱ_m, ς_e, and ς_m are obtained from the expansions (3.22), (3.48), (3.39), and (3.50). Finally the electric and magnetic fields can be evaluated in the whole space by using the integral expressions derived in

Chapter 2.

The numerical features of (3.63) and the strategies to be adopted for its solution are thoroughly discussed in Chapter 4, where (3.63) and (3.45) (i.e. the PEEC system of equation derived from the A– and C–PEEC formulations) are also compared.

3.2.1 Circuit interpretation

When the C–PEEC formulation is discretized, and hence (3.63) is solved, the Cell Method discretization approach offers a natural circuit interpretation of the electromagnetic problem for both the electric and the magnetic domains. Indeed, the nodes $\tilde{n}_e/n_m$ together with the boundary nodes $\tilde{n}_e^b/n_m^b$ can be interpreted as electric circuit nodes, while the edges $\tilde{e}_e/e_m$ can be interpreted as electric circuit branches carrying the electric currents $\mathbf{j}_e/\tilde{\mathbf{j}}_m$. Thus, the first and the third rows of (3.63) can be interpreted as KVLs written for each branch of the equivalent electric circuit (dual edges $\tilde{e}_e$ and primal edges e_m) and $\tilde{\mathcal{G}}_{\Omega_e}/\mathcal{G}_{\Omega_m}$ represent the graph of the equivalent electric circuit. The second and the fourth rows of (3.63) can be instead interpreted as KCLs written for each node of the equivalent electric circuit (dual nodes $\tilde{n}_e$ plus dual boundary nodes $\tilde{n}_e^b$ and primal nodes n_m plus primal boundary nodes n_e^b). Thus, for both the electric and the magnetic domains, the structure of the original PEEC elementary circuit cell shown in Fig. 3.11 can be adopted to represent the equivalent circuit derived from the Cell Method discretization.

It is worth noting that the circuit related to the magnetic domain can be considered as a *magnetic circuit* mutually coupled with the *electric circuit* related to the electric domain. Indeed,

$$\mathbf{R}_e\mathbf{j}_e = \tilde{\mathbf{e}}_0, \tag{3.66}$$

can be considered as the (discrete) matrix version of the Ohm's law, whereas

$$\tilde{\mathbf{R}}_m\tilde{\mathbf{j}}_m = \mathbf{h}_0, \tag{3.67}$$

can be considered as the (discrete) matrix version of the Hopkinson's law.

Thus, the problem can be in principle solved by means of a MNA Spice–like solver (more details concerning this points are given in Section 4.2.1).

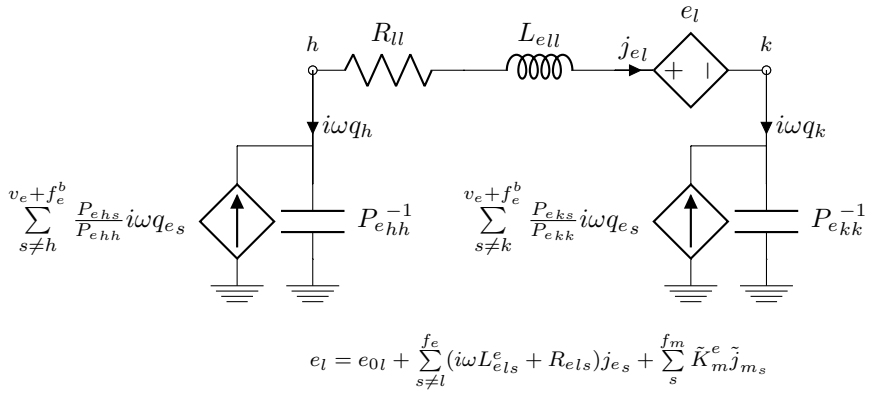

Figure 3.11: Elementary C–PEEC circuit cell for the lth electric face. A completely equivalent cell can be adopted to model the magnetic domains.

Furthermore, as discussed for the A–PEEC formulation, the electromagnetic problem can now be easily coupled with lumped circuit components and, as done in Section 3.1.1, the zero vector in the second row of the rhs of (3.63) can be also substituted with $\mathbf{j}_{e0}$, which is the vector that stores $j_{0,k}$ (a possible external current injected in the kth dual node of the mesh).

Although it may not have a practical interest, *artificial* lumped magnetic elements can be also connected to the equivalent magnetic circuit in order to simulate a hypothetical *amper-turn* generator. Moreover, external magnetic currents can be injected by replacing the fourth row of the rhs in (3.63) with $\tilde{\mathbf{j}}_{m0}$, which is the array of external magnetic currents.

Thus, the final electromagnetic problem coupled with (electric) lumped circuit elements can be written as:

$$\begin{bmatrix} \mathbf{R}_e + i\omega\mathbf{L}_e^e & \tilde{\mathbf{G}}_{\Omega_e}^a & \tilde{\mathbf{K}}_m^e & \mathbf{0} & \mathbf{0} & \mathbf{0} \\ \mathbf{P}_e\mathbf{D}_{\Omega_e}^a & i\omega\mathbf{1} & \mathbf{0} & \mathbf{0} & \mathbf{P}_e\mathbf{A}_{e,l}^T & \mathbf{0} \\ -\mathbf{K}_e^m & \mathbf{0} & \tilde{\mathbf{R}}_m + i\omega\tilde{\mathbf{L}}_m^m & \mathbf{G}_{\Omega_m}^a & \mathbf{0} & \mathbf{0} \\ \mathbf{0} & \mathbf{0} & \tilde{\mathbf{P}}_m\tilde{\mathbf{D}}_{\Omega_m}^a & i\omega\mathbf{1} & \mathbf{0} & \mathbf{0} \\ \mathbf{0} & \mathbf{A}_{e,l} & \mathbf{0} & \mathbf{0} & \mathbf{Z}_l & \mathbf{A}_{l,l}^T \\ \mathbf{0} & \mathbf{0} & \mathbf{0} & \mathbf{0} & \mathbf{A}_{l,l} & \mathbf{0} \end{bmatrix} \begin{bmatrix} \mathbf{j}_e \\ \tilde{\boldsymbol{\phi}}_e \\ \tilde{\mathbf{j}}_m \\ \boldsymbol{\phi}_m \\ \mathbf{j}_l \\ \tilde{\boldsymbol{\phi}}_{e,l} \end{bmatrix} = \begin{bmatrix} \tilde{\mathbf{e}}_0 \\ \mathbf{j}_{e0} \\ \mathbf{h}_0 \\ \mathbf{0} \\ \mathbf{u}_{l0} \\ \mathbf{j}_{l0} \end{bmatrix}, \tag{3.68}$$

where $\mathbf{A}_{e,l}$, $\mathbf{A}_{l,l}$, $\mathbf{Z}_l$, $\mathbf{u}_{l0}$, and $\mathbf{j}_{l0}$ have already been introduced for the A–PEEC system (3.47).

3.3 Extension to inhomogeneous media

In this section, some physical and numerical aspects concerning homogeneous media are first discussed. More details related to this topic can be found in Appendix A (where the presence of the charge density distribution inside conductive, dielectric, and magnetic homogeneous media is discussed) and in Section 4.2.4 where the numerical techniques to be applied for a strong imposition of the properties of the homogeneous media are presented.

Then, the case of inhomogeneous media is discussed and the extension of the discretization schemes introduced in Sections 3.1 and 3.2 are given in order to properly handle inhomogeneous media. In is worth noting that the handling of inhomogeneous media is essential for the extension of the PEEC method to non linear materials. Thus, even if non linear media have not been considered in the context of this thesis, the research concerning inhomogeneous media is also spurred by the interest to extend the PEEC method also to this kind of devices.

Finally, the discretization of the C–PEEC formulation based on total div–free currents presented at the end of Section 2.3 is shortly presented. This particular formulation of the C–PEEC method allows for naturally considering inhomogeneous media without introducing adjustments during the discretization process.

3.3.1 Conservation properties of homogeneous media

Until now, only homogeneous media have been considered in the formulation. For this kind of media, ε_r and μ_r are uniform values (or more generally tensor quantities) inside each (not–touching) sub–domain of Ω_d and Ω_m. As shown in Appendix A, the volume charge densities ϱ_d and ϱ_m are always zero for this kind of media [39] (for the whole frequency range), while in general ς_d and ς_m are not.

When the C–PEEC method is considered, from (2.41) and (2.77), the vanishing of ϱ_d and ϱ_m also implies that

$$\nabla \cdot \mathbf{J}_p = 0, \quad \nabla \cdot \mathbf{J}_m = 0. \tag{3.69}$$

Since the C–PEEC method is a particular form of Volume Integral Equation (VIE) method, these conditions are naturally and implicitly imposed by (3.63), but not in a numerically strong sense [69]. Indeed, all the effects of the full Maxwell's equations are considered in (3.63), including the ones due to the presence of possible bound volume charges ϱ_d and ϱ_m. Thus, since Maxwell's equations imply that $\varrho_d = 0$ and $\varrho_m = 0$ when homogeneous media are considered, the solution of (3.63) must satisfy this property. However, as stated above, this condition is actually imposed, but not in a numerically strong sense. Indeed, as mentioned in [70], when a VIE is solved, the solution will be close to the *right* one, but the volume charge densities ϱ_d and ϱ_m will not be exactly zero inside Ω_d and Ω_m, particularly for the mesh elements close to the boundaries Γ_d and Γ_m. Anyhow, this in general does not particularly affect the global quality of the solution but it could be an issue when high accuracy is required.

In the A–PEEC formulation, the magnetic charges are not considered but the above discussion still holds with regard dielectric media. Instead, amperian currents are introduced as equivalent sources in the magnetic domains. As more widely discussed in the following, also the electromagnetic properties of the amperian currents (i.e. the magnetization) are implicitly satisfied by system (3.45), but again not in a numerically strong sense. For instance, in steady state condition and for non–conductive homogeneous magnetic media, only the surface amperian currents exist while the volume amperian currents are zero. This condition is not strongly enforced by (3.45) and a distribution of $\mathbf{J}_a$ close to the boundary Γ_m is obtained also when a zero frequency problem is solved. Anyhow, again this does not particularly affect the global quality of the solution but it could be an issue when high accuracy is required or when the actual distribution of the magnetization is important. Numerical techniques to be applied in order to strongly impose $\varrho_d = 0$, $\varrho_m = 0$ (i.e. $\nabla \cdot \mathbf{J}_d = 0$, $\nabla \cdot \mathbf{J}_m = 0$) and the electromagnetic properties of $\mathbf{M}$ are presented in Section 4.2.4.

In the above discussion, only dielectric and magnetic media have been mentioned. Instead, the presence of free charge density inside conductive media is a sensitive issue which is discussed in appendix A [71]. However, from an engineering point of view, ϱ_c is almost negligible for the whole frequency range [70], while $\varsigma_c \simeq 0$ only when the frequency is sufficient low. Thus, the above discussion concerning dielectric and magnetic media holds also for the conductive media and in Section 4.2.4 also the case of conductive media is treated.

3.3.2 Inhomogeneous media

In this section, the case of inhomogeneous media [72] is considered. The extension of the C–PEEC method is first considered. Then, the case of the A–PEEC method is discussed and finally the discretization of the C–PEEC formulation proposed at the end of Section 2.3 which involves the use of total div–free currents is presented.

C–PEEC method for inhomogeneous media

When inhomogeneous dielectric and magnetic media are involved, ε_r and μ_r must be considered as functions of the position, i.e. $\varepsilon_r(\mathbf{r})$ and $\mu_r(\mathbf{r})$. For the sake of clarity and simplicity, conductive

domains are not considered in this section, thus the electric domain Ω_e coincides with the dielectric domain Ω_d. Therefore, since we will refers to *dielectric* media and not to *conductive* media, the subscript d is used instead of e.

Thus, starting from the following relations derived from the constitutive equations introduced in Chapter 2,

$$\mathbf{P} = (1 - \frac{1}{\varepsilon_r})\mathbf{D}, \tag{3.70}$$

$$\mu_0\mathbf{M} = (1 - \frac{1}{\mu_r})\mathbf{B}, \tag{3.71}$$

and applying the divergence operator to both the equations, the following expressions are obtained:

$$\nabla \cdot \mathbf{P} = \nabla \cdot \Big((1 - \frac{1}{\varepsilon_r})\mathbf{D}\Big) = (1 - \frac{1}{\varepsilon_r})\nabla \cdot \mathbf{D} + \mathbf{D} \cdot \nabla(1 - \frac{1}{\varepsilon_r}), \tag{3.72}$$

$$\nabla \cdot (\mu_0\mathbf{M}) = \nabla \cdot \Big((1 - \frac{1}{\mu_r})\mathbf{B}\Big) = (1 - \frac{1}{\mu_r})\nabla \cdot \mathbf{B} + \mathbf{B} \cdot \nabla(1 - \frac{1}{\mu_r}). \tag{3.73}$$

Moreover, since $\varrho_d = -\nabla \cdot \mathbf{P}$ and $\varrho_m = -\nabla \cdot (\mu_0\mathbf{M})$, we finally obtain:

$$-\varrho_d = \nabla \cdot \mathbf{P} = (1 - \frac{1}{\varepsilon_r})\nabla \cdot \mathbf{D} + \mathbf{D} \cdot \nabla(1 - \frac{1}{\varepsilon_r}), \tag{3.74}$$

$$-\varrho_m = \nabla \cdot (\mu_0\mathbf{M}) = \mathbf{B} \cdot \nabla(1 - \frac{1}{\mu_r}). \tag{3.75}$$

When ideal dielectric media are considered (i.e. no free charges are presented in Ω_d), equation (3.74) reduces to

$$-\varrho_d = \nabla \cdot \mathbf{P} = \mathbf{D} \cdot \nabla(1 - \frac{1}{\varepsilon_r}), \tag{3.76}$$

since $\nabla \cdot \mathbf{D} = 0$.

Thus, unlike homogeneous media, volume bound charges are actually present when inhomogeneous dielectric and magnetic media are considered. Indeed, the rhs of (3.74), (3.75), and (3.76) are non–vanishing quantities.

For the sake of clarity, let's now distinguish two different cases:

(a) $\varepsilon_r(\mathbf{r})$ and $\mu_r(\mathbf{r})$ are piecewise continuous functions, i.e. Ω_d and Ω_m consist of (homogeneous) sub–domains within which the permittivity and the permeability have unique values. Thus, $\varepsilon_r(\mathbf{r})$ and $\mu_r(\mathbf{r})$ show a discontinuity on the surfaces which divide the sub–domains;

(b) $\varepsilon_r(\mathbf{r})$ and $\mu_r(\mathbf{r})$ are continuous smoothly varying functions in Ω_d and Ω_m.

Case (a) When $\varepsilon_r(\mathbf{r})$ and $\mu_r(\mathbf{r})$ are piecewise continuous functions, equations (3.74) and (3.75) must be handled in the *distribution theory* sense [39], since the computation of the gradient of a noncontinuous function is required. Thus, considering that Ω_d consists of two sub–domains Ω_{d_1} and Ω_{d_2} divided by the interface face $\bar{\Gamma}_{d^*}$, and that Ω_m consists of two sub–domains Ω_{m_1} and Ω_{m_2} divided by the interface face $\bar{\Gamma}_{m^*}$, we obtain

$$-\varsigma_d = (\mathbf{P}_1 - \mathbf{P}_2) \cdot \mathbf{n} = ((1 - \varepsilon_{r_1}^{-1}) - (1 - \varepsilon_{r_2}^{-1}))\mathbf{D} \cdot \mathbf{n}, \tag{3.77}$$

$$-\varsigma_m = \mu_0(\mathbf{M}_1 - \mathbf{M}_2) \cdot \mathbf{n} = ((1 - \mu_{r_1}^{-1}) - (1 - \mu_{r_2}^{-1}))\mathbf{B} \cdot \mathbf{n}, \tag{3.78}$$

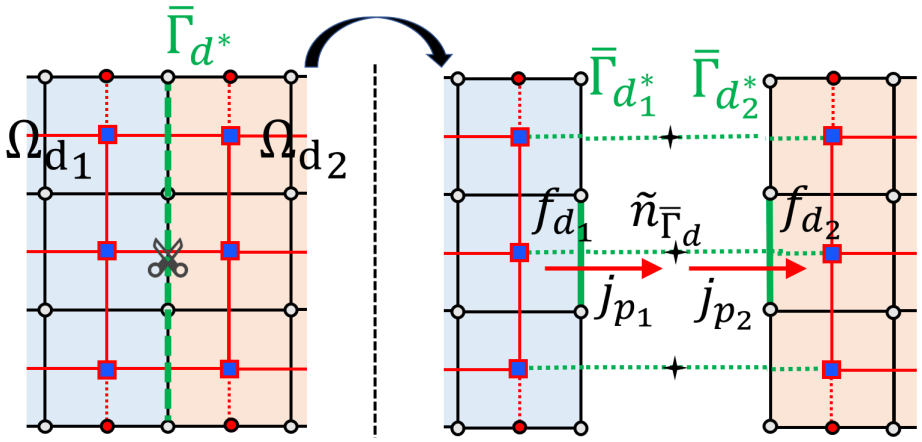

Figure 3.12: Graph adjustments for piecewise inhomogeneous dielectric media in C–PEEC method.

where the subscripts 1 and 2 indicate the left and the right side of the interface region between the two (dielectric or magnetic) sub–domains, respectively, and $\mathbf{n}$ is the unit normal vector of $\bar{\Gamma}_{d^*}$ and $\bar{\Gamma}_{m^*}$. Thus, for a piecewise homogeneous material, the volume charge densities ϱ_d and ϱ_m are zero in Ω_d and Ω_m, while electric and magnetic surface charge densities ς_d and ς_m appear in $\bar{\Gamma}_{d^*}$ and $\bar{\Gamma}_{m^*}$, respectively.

It is clear now that the normal components of $\mathbf{P}$ and $\mathbf{M}$ (i.e. $\mathbf{J}_p$ and $\mathbf{J}_m$) are discontinuous in $\bar{\Gamma}_{d^*}$ and $\bar{\Gamma}_{m^*}$. However, the Whitney face elements $\mathbf{w}^f$ adopted in (3.22) and (3.48) for the expansion of $\mathbf{J}_p$ and $\mathbf{J}_m$ impose the continuity of the normal component. Thus, if no adjustment is done to the girds, no surface charge can lay on $\bar{\Gamma}_{d^*}$ and $\bar{\Gamma}_{m^*}$.

To solve this problem (i.e. to allow a surface charge distribution on the interfaces between different materials), the primal dielectric grid $\mathcal{G}_d$ and the dual magnetic grid $\tilde{\mathcal{G}}_m$ are slightly changed. For simplicity reasons, since in the C–PEEC formulation dielectric and magnetic media are handled in a completely equivalent manner, the following discussion is carried out for the dielectric media only.

First, the set of the interface faces which discretizes $\bar{\Gamma}_{d^*}$ is defined as $\bar{f}_d$. Thus, each triangular/quadrilateral face $\bar{f}_{d_k} \in \bar{f}_d$ must be *virtually* divided into two faces, a left one $f_{d_{k,1}}$ and a right one $f_{d_{k,2}}$. So, two distinct current DoFs $j_{p_{k,1}}$ and $j_{p_{k,2}}$ must be considered: $j_{p_{k,1}}$ related to $f_{d_{k,1}}$, and $j_{p_{k,2}}$ related to $f_{d_{k,2}}$, as shown in Fig. 3.12 for an equivalent 2–D case. The support of the Whitney face function associated to $j_{p_{k,1}}$ is (only) the volume element which belongs to Ω_{d_1} while the support of the Whitney face function associated to $j_{p_{k,2}}$ is (only) the volume element which belongs to Ω_{d_2}.

Then, *interface* (dual) nodes $\tilde{n}_{\bar{\Gamma}_{d,k}}$ are added to the grid, as exemplified in Fig. 3.12. Moreover, $\mathbf{D}^a_{\Omega_d}$ and $\tilde{\mathbf{G}}^a_{\Omega_d}$ (i.e. the incidence matrix of the equivalent electric circuit) must be properly modified in order to consider $f_{d_{k,1}}$ and $f_{d_{k,2}}$ instead of $\bar{f}_{d_k}$ and their connections with $\tilde{n}_{\bar{\Gamma}_{d,k}}$. These *modified* incidence matrices are defined as $\mathbf{D}^{\bar{a}}_{\Omega_d}$ and $\tilde{\mathbf{G}}^{\bar{a}}_{\Omega_d}$ and they also satisfy $\mathbf{D}^{\bar{a}}_{\Omega_d} = -\tilde{\mathbf{G}}^{\bar{a}T}_{\Omega_d}$.

Moreover, the contribution of the charge that lays on the *interface* faces $\bar{f}_{d_k}$ must be taken into account. Therefore, the array of DoFs $\mathbf{q}^{\bar{s}}_d = (q^{\bar{s}}_{d_k})$ which stores the charges laying on $\bar{f}_{d_k}$, with $k = 1, \cdots, \bar{f}_d$, must be defined. Each DoF, $q^{\bar{s}}_{d_k}$, related to the charge which lays on the interface face $\bar{f}_{d_k}$, must satisfy the continuity relation:

$$j_{p_{k,1}} - j_{p_{k,2}} = -i\omega q^{\bar{s}}_{d_k}. \tag{3.79}$$

Thus, the discrete continuity equation for the general case of inhomogeneous dielectric media becomes

$$\mathbf{D}^{\bar{a}}_{\Omega_d}\mathbf{j}_d = -i\omega\mathbf{q}^{\bar{a}}_d, \tag{3.80}$$

where $\mathbf{q}^{\bar{a}}_d = [\mathbf{q}^v_d; \mathbf{q}^s_d; \mathbf{q}^{\bar{s}}_d]$ and with a proper re–ordered of the entities of the mesh.

The array of DoFs $\tilde{\boldsymbol{\phi}}^{\bar{s}}_d$, in a one–to–one relation with $\mathbf{q}^{\bar{s}}_d$, must also be introduced, where $\tilde{\phi}^{\bar{s}}_{d_k}$ is related to the kth interface face $\bar{f}_{d_k}$. Subsequently, the electric potential matrix must be properly augmented:

$$\mathbf{P}^{\bar{a}}_d = \begin{bmatrix} \mathbf{P}^{vv}_d & \mathbf{P}^{vs}_d & \mathbf{P}^{v\bar{s}}_d \\ \mathbf{P}^{sv}_d & \mathbf{P}^{ss}_d & \mathbf{P}^{s\bar{s}}_d \\ \mathbf{P}^{\bar{s}v}_d & \mathbf{P}^{\bar{s}s}_d & \mathbf{P}^{\bar{s}\bar{s}}_d \end{bmatrix}, \tag{3.81}$$

where $\mathbf{P}^{v\bar{s}}_e = \mathbf{P}^{\bar{s}vT}_e$, $\mathbf{P}^{s\bar{s}}_e = \mathbf{P}^{\bar{s}sT}_e$, and $\mathbf{P}^{\bar{s}\bar{s}}_d$ are *volume/surface* and *surface* potential matrices whose coefficients are given by (3.37). With the introduction of $\mathbf{P}^{\bar{a}}_d$, the discrete relation between the scalar electric potential and the electric charges is finally given by

$$\tilde{\boldsymbol{\phi}}^{\bar{a}}_d = \mathbf{P}^{\bar{a}}_d\mathbf{q}^{\bar{a}}_d. \tag{3.82}$$

where $\tilde{\boldsymbol{\phi}}^{\bar{a}}_d = [\tilde{\boldsymbol{\phi}}^v_d, \tilde{\boldsymbol{\phi}}^s_d, \tilde{\boldsymbol{\phi}}^{\bar{s}}_d]$.

So, finally, (3.80) and (3.82), are combined together resulting in

$$\mathbf{D}^{\bar{a}}_{\Omega_d}\tilde{\mathbf{j}}_d + i\omega\mathbf{P}^{\bar{a}-1}_d\tilde{\boldsymbol{\phi}}^{\bar{a}}_d = \mathbf{0}. \tag{3.83}$$

A completely equivalent procedure can be applied to the case of inhomogeneous magnetic media resulting in

$$\tilde{\mathbf{D}}^{\bar{a}}_{\bar{\Omega}_m}\tilde{\mathbf{j}}_m = -i\omega\tilde{\mathbf{q}}^{\bar{a}}_m, \tag{3.84}$$

$$\boldsymbol{\phi}^{\bar{a}}_m = \tilde{\mathbf{P}}^{\bar{a}}_m\tilde{\mathbf{q}}^{\bar{a}}_m, \tag{3.85}$$

where $\tilde{\mathbf{D}}^{\bar{a}}_{\bar{\Omega}_m}$, $\boldsymbol{\phi}^{\bar{a}}_m$, $\tilde{\mathbf{P}}^{\bar{a}}_m$, and $\tilde{\mathbf{q}}^{\bar{a}}_m$ have definitions equivalent to the corresponding dielectric ones.

Thus, the final system of equation for the case of inhomogeneous dielectric and magnetic media is given by

$$\begin{bmatrix} \mathbf{R}_d + i\omega\mathbf{L}^d_d & \tilde{\mathbf{G}}^{\bar{a}}_{\Omega_d} & \mathbf{M}_{1/\varepsilon_0}\mathbf{C}_{\Omega_d}\tilde{\mathbf{N}}^d_m & \mathbf{0} \\ \mathbf{P}^{\bar{a}}_d\mathbf{D}^{\bar{a}}_{\Omega_d} & i\omega\mathbf{1} & \mathbf{0} & \mathbf{0} \\ -\tilde{\mathbf{M}}_{1/\mu_0}\tilde{\mathbf{C}}_{\Omega_m}\mathbf{N}^m_d & \mathbf{0} & \tilde{\mathbf{R}}_m + i\omega\tilde{\mathbf{L}}^m_m & \mathbf{G}^{\bar{a}}_{\Omega_m} \\ \mathbf{0} & \mathbf{0} & \tilde{\mathbf{P}}^{\bar{a}}_m\tilde{\mathbf{D}}^{\bar{a}}_{\Omega_m} & i\omega\mathbf{1} \end{bmatrix} \begin{bmatrix} \mathbf{j}_d \\ \tilde{\boldsymbol{\phi}}^{\bar{a}}_d \\ \tilde{\mathbf{j}}_m \\ \boldsymbol{\phi}^{\bar{a}}_m \end{bmatrix} = \begin{bmatrix} \tilde{\mathbf{e}}_0 \\ \mathbf{0} \\ \mathbf{h}_0 \\ \mathbf{0} \end{bmatrix}. \tag{3.86}$$

When this procedure is adopted, and thus (3.86) is solved, (3.77) and (3.78) are strongly imposed.

Alternatively, the *interface* faces $f_{d_{k,1}}$ and $f_{d_{k,2}}$ can be interpreted as boundary faces (as the ones on Γ_d), so $\tilde{n}_{\bar{\Gamma}_d}$ has not to be defined and the graph remains actually divided, as exemplified in Fig. 3.13. With this choice, the value of σ_d which lays on f_d is implicitly imposed by the integral formulation as the sum of two charge densities that lay on $f_{d_{k,1}}$ and $f_{d_{k,2}}$, but not in a numerically strong sense. The same for the magnetic case.

Summarizing, following the circuit interpretation, the solution is given by replacing each

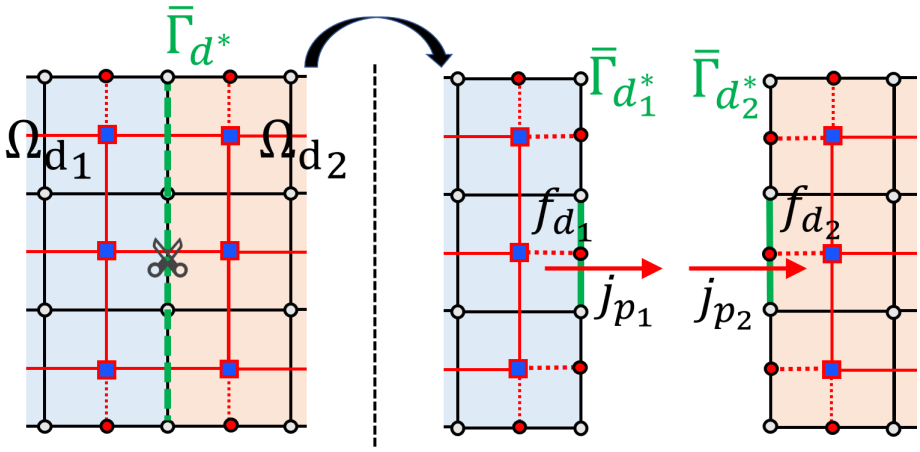

Figure 3.13: Graph adjustments for piecewise inhomogeneous dielectric media in C–PEEC method. Implicit imposition.

circuit branch representing an interface face with two distinct branches connected to two floating nodes. The two floating nodes can be merged into a single *interface* node or remain distinct and considered as *normal* boundary faces. For both cases, each one of the two distinct branches can be represented by means of the traditional PEEC elementary circuit cell: one circuit node is the interior node (i.e. the barycenter of one of the two tetrahedral/hexahedral elements sharing the interface face), while the second circuit node is one of the two floating nodes placed in $f_{d_{k,1}}$ and $f_{d_{k,2}}$. Then, the two floating nodes can be merged into a single *interface* node (Fig. 3.12) or remain distinct (Fig. 3.13).

Case (b) When $\varepsilon_r(\mathbf{r})$ and $\mu_r(\mathbf{r})$ are continuous functions which smoothly vary in Ω_d and Ω_m, $\mathbf{J}_p$ and $\mathbf{J}_m$ are continuous inside Ω_d and Ω_m.

Then, from (3.74) and (3.75), volume charge densities ϱ_d and ϱ_m appear inside Ω_d and Ω_m. This case can be simply considered without forcing the divergence of $\mathbf{J}_p$ and $\mathbf{J}_m$ to be zero and evaluating the entries of $\mathbf{R}_d$ $\mathbf{R}_m$ as shown in (3.33), and (3.55), where the value of $\rho_d(\mathbf{r})$ and $\rho_m(\mathbf{r})$ depends from $\varepsilon_r(\mathbf{r})$ and $\mu_r(\mathbf{r})$ point–by–point, respectively.

Alternatively, once the discretization of Ω_d and Ω_m is obtained, a given value of $\varepsilon_r(\mathbf{r})$ and $\mu_r(\mathbf{r})$ (e.g. the mean value or the barycentric value) can be associated to each mesh element, leading to a piecewise constant approximation of the functions $\varepsilon_r(\mathbf{r})$ and $\mu_r(\mathbf{r})$. Then, each mesh face that separates two elements with different value of ε_r and μ_r must be treated as discussed in **Case (a)**. Thus, strongly inhomogeneous media can be handled by systematically treating all the internal faces as *interface* faces.

A–PEEC method for inhomogeneous media

Since A–PEEC and C–PEEC methods are formally equivalent when magnetic media are not involved, inhomogeneous dielectric media in the A–PEEC formulation can be handled in the same way of the C–PEEC formulation, as discussed above.

These methods behave differently when magnetic domains are involved. Thus, the handling of inhomogeneous magnetic media for the A–PEEC method is here discussed.

The magnetization is related to the magnetic field as

$$\mathbf{M} = \frac{\mathbf{H}}{\mu_r - 1}, \tag{3.87}$$

Thus, by applying the curl operator to the above equation one obtains

$$\nabla \times \mathbf{M} = \frac{1}{\mu_r - 1} \nabla \times \mathbf{H} + \nabla\left(\frac{1}{\mu_r - 1}\right) \times \mathbf{H}. \tag{3.88}$$

Moreover, since $\mathbf{J}_a = \nabla \times \mathbf{M}$ and $\nabla \times \mathbf{H} = \mathbf{J}_c + i\omega\mathbf{D}$, the following relations are obtained:

$$\mathbf{J}_a = \nabla \times \mathbf{M} = \frac{1}{\mu_r - 1} \nabla \times \mathbf{H} + \nabla\left(\frac{1}{\mu_r - 1}\right) \times \mathbf{H}, \tag{3.89}$$

$$\mathbf{J}_a = \nabla \times \mathbf{M} = \frac{\mathbf{J}_c + i\omega\mathbf{D}}{\mu_r - 1} + \nabla\left(\frac{1}{\mu_r - 1}\right) \times \mathbf{H}. \tag{3.90}$$

Thus, when homogeneous media are considered (i.e. μ_r is uniform inside each disconnected sub–domain of Ω_m), the volume amperian currents are not zero when the magnetic domain has a conductivity greater than zero or when the frequency of the problem is not zero. When non–conductive homogeneous magnetic media are considered, and when the frequency is low, $\mathbf{J}_a$ is instead a negligible quantity.

When inhomogeneous magnetic media are considered, the term $\nabla\left(\frac{1}{\mu_r - 1}\right) \times \mathbf{H}$ in (3.90) is in general a non–vanishing quantity which contributes to the value of $\mathbf{J}_a$.

Two different cases are considered as above:

(i) $\mu_r(\mathbf{r})$ is a piecewise continuous function, i.e. Ω_m consists of (homogeneous) sub–domains within which the permeability has unique value and thus $\mu_r(\mathbf{r})$ shows a discontinuity on the surfaces which divide the sub–domains;

(ii) $\mu_r(\mathbf{r})$ is a continuous smoothly varying function Ω_m.

Case i When $\mu_r(\mathbf{r})$ is a piecewise continuous function, (3.90) must be handled in the *distribution theory sense*. Thus, considering that Ω_m consists of two sub–domains Ω_{m_1} and Ω_{m_2} divided by the interface face $\bar{\Gamma}^*_m$, we obtain

$$\mathbf{K}_a = (\mathbf{M}_1 - \mathbf{M}_2) \times \mathbf{n} = \left(\frac{1}{\mu_{r_1} - 1} - \frac{1}{\mu_{r_2} - 1}\right)\mathbf{H} \times \mathbf{n}, \tag{3.91}$$

where the subscripts 1 and 2 indicate the left and the right side of the interface region between the two magnetic sub–domains, respectively, and $\mathbf{n}$ is the unit normal vector of $\bar{\Gamma}_{m^*}$. Thus, surface amperian currents $\mathbf{K}_a$ appear in $\bar{\Gamma}_{m^*}$.

It is clear now that the tangential component of $\mathbf{M}$ is discontinuous in $\bar{\Gamma}_{m^*}$. However, the Whitney edge elements $\mathbf{w}^e$ adopted in (3.23) for the expansion of $\mathbf{M}$ impose the continuity of the tangential component. Thus, if no adjustment is done to the magnetic gird, no surface amperian current can lay on $\bar{\Gamma}_{m^*}$.

To solve this problem, the primal magnetic grid $\mathcal{G}_m$ is slightly changed. First, the set of the interface edges which discretizes $\bar{\Gamma}_{m^*}$ is defined as $\bar{e}_m$. Thus, each edge $\bar{e}_{m_k} \in \bar{e}_m$ must be *virtually* divided into two edges, a left one $e_{m_{k,1}}$ and a right one $e_{m_{k,2}}$. So, two distinct magnetization DoFs $m_{k,1}$ and $m_{k,2}$ must be considered: $m_{k,1}$ related to $e_{m_{k,1}}$ and $m_{k,2}$ related to $e_{m_{k,2}}$, as exemplified in Fig 3.14. The support of the Whitney edge function associated to

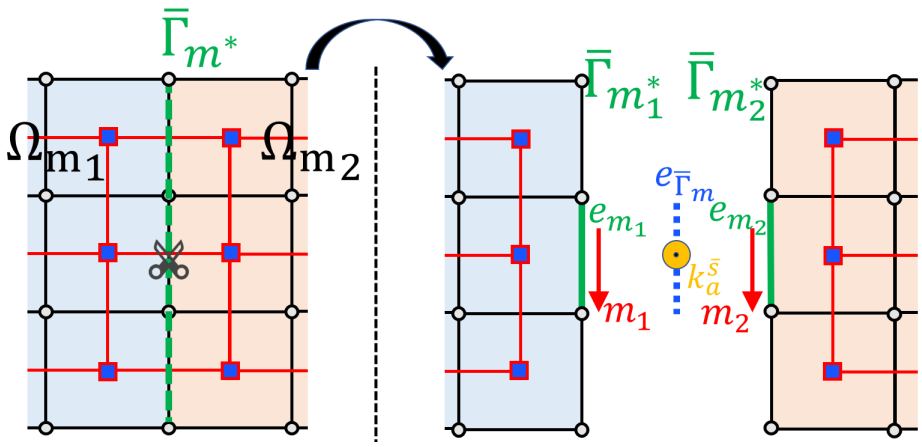

Figure 3.14: Graph adjustments for piecewise inhomogeneous magnetic media in the A–PEEC method.

$m_{k,1}$ are (only) the volume elements which belong to Ω_{m_1} while the support of the Whitney edge function associated to $m_{k,2}$ are (only) the volume elements which belong to Ω_{m_2}.

Then, an *interface* edge $\tilde{e}_{\bar{\Gamma}_{m,k}}$ is added to the grid, as exemplified in Fig. 3.14. Moreover, the contribution of the amperian surface current related to the *interface* edge $\tilde{e}_{\bar{\Gamma}_{m,k}}$ must be taken into account. Therefore, the array of DoFs $\mathbf{k}_a^{\bar{s}} = (k_{a_k}^{\bar{s}})$ which stores the amperian currents related to $\tilde{e}_{\bar{\Gamma}_{m,k}}$, with $k = 1, \cdots, \bar{e}_m$, must be defined. Each DoF must fulfill the relation:

$$m_{k,1} - m_{k,2} = k_{a_k}^{\bar{s}}. \tag{3.92}$$

Thus, the discrete relations between the magnetization and amperian currents for the general case of inhomogeneous magnetic media become

$$\mathbf{j}_a = \mathbf{C}_{\Omega_m}\mathbf{m}, \qquad \mathbf{k}_a = \mathbf{C}_{\Gamma_m}\mathbf{m}, \qquad \mathbf{k}_a^{\bar{s}} = \mathbf{C}_{\bar{\Gamma}_m}^{\bar{s}}\mathbf{m}, \tag{3.93}$$

where $\mathbf{C}_{\bar{\Gamma}_m}^{\bar{s}}$ is the curl selection matrix which extracts the DoFs related to the *left* and *right* magnetizations unknowns $m_{k,1}$ and $m_{k,2}$ resulting from the *virtual* splitting of the interface face $\bar{\Gamma}_{m^*}$. Thus, the third equation in (3.93) is the matrix form of (3.92).

With a proper re–ordering of the entities of the mesh, relations (3.93) can be written in a compact form as:

$$[\mathbf{j}_a; \mathbf{k}_a; \mathbf{k}_a^{\bar{s}}] = \mathbf{C}_{\Omega_m}^{\bar{a}}\mathbf{m} \tag{3.94}$$

where $\mathbf{C}_{\Omega_m}^{\bar{a}} = [\mathbf{C}_{\Omega_m}; \mathbf{C}_{\Gamma_m}; \mathbf{C}_{\bar{\Gamma}_m}^{\bar{s}}]$ is the *modified* augmented curl matrix for inhomogeneous magnetic media. $\tilde{\mathbf{C}}_{\Omega_m}^{\bar{a}} = \mathbf{C}_{\Omega_m}^{\bar{a},T}$.

The array of DoFs $\tilde{\mathbf{a}}^{m,\bar{s}}$, in a one–to–one relation with $\mathbf{k}_a^{\bar{s}}$, must also be introduced, where $\tilde{a}^{m,\bar{s}}$ is related to the kth interface edge $\bar{e}_{m_k}$. Subsequently, the effects of the surface amperian currents flowing in $\bar{\Gamma}_{m^*}$ must be taken into account. Thus, the *volume/surface* inductance matrices $\mathbf{L}_{\bar{\Gamma}_m}^{e}$ and $\mathbf{L}_{e}^{\bar{\Gamma}_m}$ ($\mathbf{L}_{\bar{\Gamma}_m}^{e,T} = \mathbf{L}_{e}^{\bar{\Gamma}_m}$), which represents the mutual effects between the electric domain and $\mathbf{k}_a^{\bar{s}}$, must be added. Moreover, the *amperian* inductance matrix (3.46) must be properly augmented:

$$\mathbf{L}_m^{\bar{a}} = \begin{bmatrix} \mathbf{L}_m^m & \mathbf{L}_{\Gamma_m}^m & \mathbf{L}_{\bar{\Gamma}_m}^m \\ \mathbf{L}_m^{\Gamma_m} & \mathbf{L}_{\Gamma_m}^{\Gamma_m} & \mathbf{L}_{\bar{\Gamma}_m}^{\Gamma_m} \\ \mathbf{L}_m^{\bar{\Gamma}_m} & \mathbf{L}_{\Gamma_m}^{\bar{\Gamma}_m} & \mathbf{L}_{\bar{\Gamma}_m}^{\bar{\Gamma}_m} \end{bmatrix}. \tag{3.95}$$

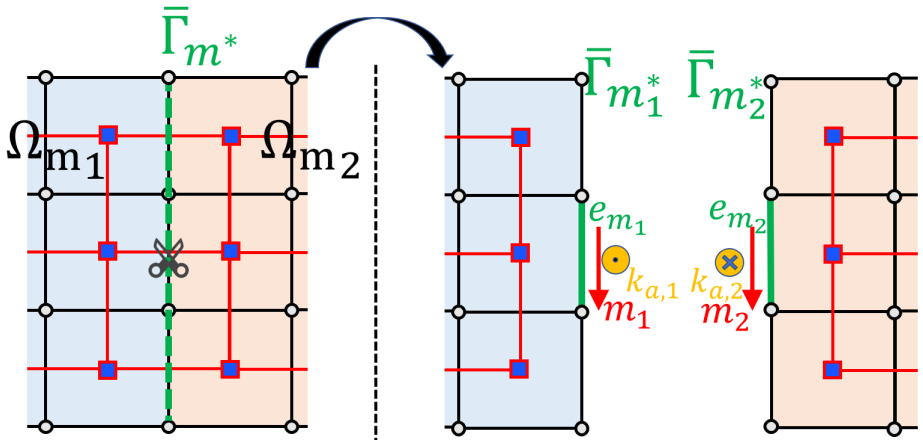

Figure 3.15: Graph adjustments for piecewise inhomogeneous magnetic media in the A–PEEC method. implicit imposition.

Thus, the final EB-PEEC system of equation for the case of inhomogeneous magnetic media is given by

$$\begin{bmatrix} \mathbf{R}_e + i\omega\mathbf{L}^e_e & \tilde{\mathbf{G}}^a_{\Omega_e} & i\omega[\mathbf{L}^e_m, \mathbf{L}^e_{\bar{\Gamma}_m}, \mathbf{L}^e_{\bar{\Gamma}_m}]\mathbf{C}^{\bar{a}}_{\Omega_m} \\ \mathbf{P}_e\mathbf{D}^a_{\Omega_e} & i\omega\mathbf{1} & \mathbf{0} \\ -\tilde{\mathbf{C}}^{\bar{a}}_{\Omega_m} \begin{bmatrix} \mathbf{L}^m_e \\ \mathbf{L}^{\Gamma_m}_e \\ \mathbf{L}^{\bar{\Gamma}_m}_e \end{bmatrix} & \mathbf{0} & \mathbf{F} - \tilde{\mathbf{C}}^{\bar{a}}_{\Omega_m}\mathbf{L}^{\bar{a}}_m\mathbf{C}^{\bar{a}}_{\Omega_m} \end{bmatrix} \begin{bmatrix} \mathbf{j}_e \\ \tilde{\phi}_e \\ \mathbf{m} \end{bmatrix} = \begin{bmatrix} \tilde{\mathbf{e}}_0 \\ \mathbf{0} \\ \tilde{\mathbf{b}}_0 \end{bmatrix}. \tag{3.96}$$

When this procedure is adopted, and thus (3.96) is solved, (3.91) are strongly imposed.

Alternatively, the *interface* edges $e_{m_{k,1}}$ and $e_{m_{k,2}}$ can be interpreted as a boundary edges, so $\tilde{e}_{\bar{\Gamma}_{m,k}}$ has not to be defined and the graph remains there divided, as exemplified in Fig. 3.15. With this choice, the value of $\mathbf{K}_a$ which flows in $\bar{\Gamma}_{m^*}$ is implicitly imposed by the integral formulation as the sum of two amperian currents that flow on the right and left side of $\bar{\Gamma}_{m^*}$.

Summarizing, the solution is given by replacing each edge which discretizes $\bar{\Gamma}_{m^*}$ with two distinct edges. The difference between the two magnetizations DoFs related to these edges gives the value of the amperian surface current DoF, the effects of which must be considered by augmenting the inductance matrices. By doing so, equation (3.91) is explicitly enforced.

Alternatively, Ω_m can be actually cut in $\bar{\Gamma}_{m^*}$. Thus, the two sides of $\bar{\Gamma}_{m^*}$ are considered as normal boundaries, and then two distinct amperian currents are considered, one for the left part and one for the right part. By doing this, equation (3.91) is implicitly enforced by the integral formulation, but not in a numerically strong sense.

Case ii When $\mu_r(\mathbf{r})$ is a continuous function which smoothly varies in Ω_m, $\mathbf{M}$ is continuous inside Ω_m. Then, from (3.90), volume amperian currents $\mathbf{J}_a$ appear inside Ω_m. This case can be simply considered by evaluating the entries of $\mathbf{F}$ as shown in (3.42), where the value of $\alpha_m(\mathbf{r})$ depends on $\mu_r(\mathbf{r})$ point–by–point.

Alternatively, once the discretization Ω_m is obtained, a given value of $\mu_r(\mathbf{r})$ (e.g. the mean value or the barycentric value) can be associated to each mesh element, leading to a piecewise constant approximation of the function $\mu_r(\mathbf{r})$. Then, each mesh edge that separates two elements with different value of μ_r must be treated as discussed in **Case (i)**. Thus, strongly inhomogeneous magnetic media can be handled in the A–PEEC method by systematically treating all the internal edges as *interface* edges.

Discretization of C–PEEC formulation based on total div–free currents

The procedure presented in Section 3.3.2 for the handling of inhomogeneous media, which consists in modifying the equivalent graph, leads to a duplication of the unknowns related to the interface faces between domains with different values of ε_r and μ_r. Thus, when strongly inhomogeneous media are handled with the procedure described in **Case (a)**, the dimension of the final system of equations to be solved may grow significantly.

The C–PEEC formulation introduced in Section 2.3.1 (presented in [23] for the case of conductive and dielectric media and extended to the case of magnetic media in [27] by the author) allows reducing the computational cost when inhomogeneous media are considered. This method indeed can be interpreted as an extension of the method proposed in [73] for the study of electromagnetic scattering by arbitrarily shaped inhomogeneous dielectric bodies.

Indeed, the unknowns adopted in this formulation are the total electric and magnetic currents densities, $\mathbf{J}_e^{tot}$ and $\mathbf{J}_m^{tot}$, introduced in (2.96), which are diverge free for both homogeneous and inhomogeneous media. Thus, thanks to this choice of unknowns, no adjustment must be done when inhomogeneous media are considered, and the DoFs on the interfaces between materials are not duplicated.

$\mathbf{J}_e^{tot}$ and $\mathbf{J}_m^{tot}$ are expanded with the same procedure adopted in (3.22) and (3.48), resulting in

$$\mathbf{J}_e^{tot}(\mathbf{r}) = \sum_{k}^{f_e} \mathbf{w}_k^f(\mathbf{r}) j_{e_k}^{tot}, \tag{3.97}$$

$$\mathbf{J}_m^{tot}(\mathbf{r}) = \sum_{k}^{\tilde{f}_m} \mathbf{w}_k^f(\mathbf{r}) \tilde{j}_{m_k}^{tot}, \tag{3.98}$$

where $j_{e_k}^{tot}$ represent the flux of $\mathbf{J}_e^{tot}$ through f_{e_k}: $j_{e_k}^{tot} = \int_{f_{e_k}} \mathbf{J}_e^{tot} \cdot d\mathbf{s}$. The fluxes $j_{e_k}^{tot}$, for $k = 1, \cdots, f_e$, are stored in the array of degrees of freedom (DoF) $\mathbf{j}_e^{tot} = (j_{e_k}^{tot})$ on faces $f_{e_k} \in \mathcal{G}_{\Omega_e}$. An equivalent argument holds for $j_{m_k}^{tot}$ and the corresponding array of DoFs $\tilde{\mathbf{j}}_m^{tot}$ is introduced.

The rest of the discretization follows the procedure described in Section 3.2 and the same arrays of DoFs are introduced.

Finally, the expansions (3.97) and (3.98) are introduced in equations (2.100), (2.101), (2.102), and (2.103). Then, following the Galerkin scheme, the resulting equations are tested with the same Whitney face functions. Thus, the final algebraic system of equations to be solved is

$$\begin{bmatrix} \mathbf{R}_e^{tot} + i\omega\mathbf{L}_e^{tot} & \tilde{\mathbf{G}}_{\Omega_e}^a & \mathbf{K}_e^{m,tot} & \mathbf{0} \\ \mathbf{P}_e^{tot} & -i\omega\mathbf{1} & \mathbf{0} & \mathbf{0} \\ -\mathbf{K}_e^{m,tot} & \mathbf{0} & \tilde{\mathbf{R}}_m^{tot} + i\omega\tilde{\mathbf{L}}_m^{tot} & \mathbf{G}_{\Omega_m}^a \\ \mathbf{0} & \mathbf{0} & \tilde{\mathbf{P}}_m^{tot} & -i\omega\mathbf{1} \end{bmatrix} \begin{bmatrix} \mathbf{j}_e^{tot} \\ \tilde{\boldsymbol{\phi}}_e \\ \tilde{\mathbf{j}}_m^{tot} \\ \boldsymbol{\phi}_m \end{bmatrix} = \begin{bmatrix} \tilde{\mathbf{e}}_0 \\ \mathbf{0} \\ \mathbf{h}_0 \\ \mathbf{0} \end{bmatrix}, \tag{3.99}$$

where

$$\tilde{\mathbf{K}}_m^{e,tot} = \mathbf{M}_{1/\varepsilon_0}\mathbf{C}_{\Omega_e}\tilde{\mathbf{N}}_m^{e,tot}, \tag{3.100}$$

$$\mathbf{K}_e^{m,tot} = \tilde{\mathbf{M}}_{1/\mu_0}\tilde{\mathbf{C}}_{\Omega_m}\mathbf{N}_e^{m,tot}, \tag{3.101}$$

and $\mathbf{j}_e^{tot}$, $\tilde{\boldsymbol{\phi}}_e$, $\tilde{\mathbf{j}}_m^{tot}$, and $\tilde{\mathbf{j}}_m^{tot}$ are the unknowns.

In (3.99), unlike (3.63), the electric and magnetic potentials are directly related to the electric and magnetic currents, respectively. Indeed, $\mathbf{P}_e^{tot}$ and $\tilde{\mathbf{P}}_m^{tot}$ are rectangular matrices with dimensions $\big((v_e + f_e^b) \times f_e\big)$ and $\big((\tilde{v}_m + \tilde{f}_m^b) \times \tilde{f}_m\big)$, respectively, and they can be subdivided into $\mathbf{P}_e^{tot} = [\mathbf{P}_e^{v,tot}; \mathbf{P}_e^{s,tot}]$ and $\tilde{\mathbf{P}}_m^{tot} = [\tilde{\mathbf{P}}_m^{v,tot}; \tilde{\mathbf{P}}_m^{s,tot}]$.

The definitions of the (new) matrices in (3.99) (derived from the Galerkin testing of (2.100), (2.101), (2.102), and (2.103)) are given by the following:

$$R_{e_{uk}}^{tot} = \int_{\Omega_e} \frac{1}{\sigma_e^*(\mathbf{r})}\mathbf{w}_u^f(\mathbf{r}) \cdot \mathbf{w}_k^f(\mathbf{r}) d\Omega, \tag{3.102}$$

$$\tilde{R}_{m_{wh}}^{tot} = \int_{\Omega_m} \frac{1}{\sigma_m^*(\mathbf{r})}\mathbf{w}_w^f(\mathbf{r}) \cdot \mathbf{w}_h^f(\mathbf{r}) d\Omega, \tag{3.103}$$

$$L_{e_{ku}}^{tot} = L_{e_{uk}}^{tot} = \mu_0 \int_{\Omega_e} \mathbf{w}_u^f(\mathbf{r}) \cdot \int_{\Omega_e} \frac{\sigma_e(\mathbf{r}')}{\sigma_e^*(\mathbf{r}')}\mathbf{w}_k^f(\mathbf{r}') g(\mathbf{r}, \mathbf{r}') d\Omega' d\Omega, \tag{3.104}$$

$$\tilde{L}_{m_{ku}}^{tot} = \tilde{L}_{m_{uk}}^{tot} = \varepsilon_0 \int_{\Omega_m} \mathbf{w}_u^f(\mathbf{r}) \cdot \int_{\Omega_m} \frac{\sigma_m(\mathbf{r}')}{\sigma_m^*(\mathbf{r}')}\mathbf{w}_k^f(\mathbf{r}') g(\mathbf{r}, \mathbf{r}') d\Omega' d\Omega, \tag{3.105}$$

$$P_{e_{h,k}}^{v,tot} = \frac{1}{\varepsilon_0 V_{v_{e_h}}} \int_{v_{e_h}} \int_{\Omega_e} \frac{\sigma_e(\mathbf{r}')}{\sigma_e^*(\mathbf{r}')}\mathbf{w}_k(\mathbf{r}') \cdot \nabla' g(\mathbf{r}, \mathbf{r}') \; d\Omega' d\Omega, \tag{3.106}$$

$$P_{e_{h,k}}^{s,tot} = \frac{1}{\varepsilon_0 S_{f_{e_h}}} \int_{f_{e_h}} \int_{\Omega_e} \frac{\sigma_e(\mathbf{r}')}{\sigma_e^*(\mathbf{r}')}\mathbf{w}_k(\mathbf{r}') \cdot \nabla' g(\mathbf{r}, \mathbf{r}') \; d\Omega' d\Gamma, \tag{3.107}$$

$$\tilde{P}_{m_{h,k}}^{v,tot} = \frac{1}{\mu_0 V_{v_{m_h}}} \int_{v_{m_h}} \int_{\Omega_m} \frac{\sigma_m(\mathbf{r}')}{\sigma_m^*(\mathbf{r}')}\mathbf{w}_k(\mathbf{r}') \cdot \nabla' g(\mathbf{r}, \mathbf{r}') \; d\Omega' d\Omega, \tag{3.108}$$

$$\tilde{P}_{m_{h,k}}^{s,tot} = \frac{1}{\mu_0 S_{f_{m_h}}} \int_{\tilde{f}_{m_h}} \int_{\Omega_m} \frac{\sigma_m(\mathbf{r}')}{\sigma_m^*(\mathbf{r}')}\mathbf{w}_k(\mathbf{r}') \cdot \nabla' g(\mathbf{r}, \mathbf{r}') \; d\Omega' d\Gamma, \tag{3.109}$$

$$N_{e_{wk}}^{m,tot} = \mu_0 \int_{\tilde{e}_{m_w}} \Big(\int_{\Omega_e} \frac{\sigma_e(\mathbf{r}')}{\sigma_e^*(\mathbf{r}')}\mathbf{w}_k^f(\mathbf{r}') g(\mathbf{r}, \mathbf{r}') d\Omega' \Big) \cdot d\mathbf{l}, \tag{3.110}$$

$$\tilde{N}_{m_{uh}}^{e,tot} = \varepsilon_0 \int_{e_{e_u}} \Big(\int_{\Omega_m} \frac{\sigma_m(\mathbf{r}')}{\sigma_m^*(\mathbf{r}')}\mathbf{w}_h^f(\mathbf{r}') g(\mathbf{r}, \mathbf{r}') d\Omega' \Big) \cdot d\mathbf{l}, \tag{3.111}$$

where σ_e^* and σ_m^* are defined in (2.98) and (2.99), respectively.

This formulation offers a circuit interpretation similar to the one of Section 3.2.1. Moreover, inhomogeneous media can be naturally considered without any adjustment of the equivalent circuit and increasing of the number of unknowns.

Unlike the C–PEEC formulation of Section 3.2, in this method the coefficients of the *integral* inductance and potential matrices depend on the material parameter that are frequency dependent. Thus, when *frequency sweep* problem are considered, all matrices must be recomputed for each value of the frequency. Moreover, the coefficients of $\mathbf{P}_e^{tot}$ and $\tilde{\mathbf{P}}_m^{tot}$ depend on the gradient

of the Green's function, which has a strong singularity that must be properly handled.

In the PEEC methods that use the *traditional* currents and the magnetization as unknowns (i.e. $\mathbf{J}_e$, $\mathbf{J}_m$, and $\mathbf{M}$), the inductance and potential matrices exhibit useful numerical properties, i.e. they are related to the concepts of *magnetic* and *electric* energy [21] (i.e. positive definite). In this particular C–PEEC method, instead, because of the dependence of the integral matrices on the material parameters, these properties are less evident, since the inductance and potential matrices depend on the material properties of the media involved. For instance, when inhomogeneous media are considered, inductance and potential matrices are mo more complex symmetric.

It is worth noting that the total currents are divergence free in Ω_e and Ω_m and they have non–zero normal component in Γ_e and Γ_m, in general. Thus, the arrays of DoFs related to $\mathbf{J}_e^{tot}$ and $\mathbf{J}_m^{tot}$ exhibit equivalent (discrete) properties, i.e.:

$$\mathbf{D}_{\Omega_e}\mathbf{j}_e^{tot} = \mathbf{0}, \quad \tilde{\mathbf{D}}_{\Omega_m}\tilde{\mathbf{j}}_m^{tot} = \mathbf{0}. \tag{3.112}$$

These properties are implicitly imposed by (3.99), but again not in a numerically strong sense. In Section 4.2.4, the methods to be applied in order to strongly enforce the zero divergence of $\mathbf{J}_e^{tot}$ and $\mathbf{J}_m^{tot}$ are presented.

3.4 Equivalent 2–D and 1–D PEEC models

When the shape of the devices or the electromagnetic problem provide an *a priori knowledge* of the distribution of the unknowns, equivalent 2–D or 1–D models can be adopted. It is worth noting that in this thesis 2–D and 1–D models refer to equivalent surface and linear models, respectively, which are used to represent a 3–D device (with small thickness of small cross section). Thus, even if the equivalent models are surfaces (2–D) or stick elements (1–D) the problem is actually 3–D.

Typically, these equivalent models are adopted for the study of conductive media devices, but they can also be adopted for the study of dielectric and magnetic media which allow the use of these simplified models.

3.4.1 2–D models

When thin conductive devices are considered (e.g. antennas, printed circuits, etc.), equivalent surface models can be adopted. Indeed, when the current is uniformly distributed along the thickness of the device, the model can be meshed with only one element along the thickness [74, 75]. Thus, the 3–D model can be replaced with an equivalent 2–D model, i.e. a surface placed in the middle of the thickness of the 3–D model [76].

For the sake of simplicity, a purely conductive case is considered (i.e. dielectric and magnetic media are not involved). When an equivalent surface model is adopted, the volume conductive domain Ω_c is replaced with the equivalent surface domain Γ_c^{2D}. This domain is first discretized into a triangular or quadrilateral grid $\mathcal{G}_{\Gamma_c^{2D}}$ consisting of f_c^{2D} faces, e_c^{2D} edges, and n_c^{2D} nodes. Then, a dual grid $\tilde{\mathcal{G}}_{\Gamma_c^{2D}}$ consisting of dual geometric entities ($\tilde{f}_c^{2D}$, $\tilde{e}_c^{2D}$, $\tilde{n}_c^{2D}$) can be obtained by taking the barycentric subdivision of $\mathcal{G}_{\Gamma_c^{2D}}$. As for the 3–D case, the entities of the primal and dual grids are in a one–to–one relation: $f_c^{2D} \leftrightarrow \tilde{n}_c^{2D}$, $e_c^{2D} \leftrightarrow \tilde{e}_c^{2D}$, $n_c^{2D} \leftrightarrow \tilde{f}_c^{2D}$. Moreover, the following incidence matrices are defined for the primal grid $\mathcal{G}_{\Gamma_c^{2D}}$: $\mathbf{G}_{\Gamma_c^{2D}}$ (*primal* edges–*primal*

nodes) and $\mathbf{C}_{\Gamma_c^{2D}}$ (*primal* faces–*primal* edges). The same can be done for the dual grid $\tilde{\mathcal{G}}_{\Gamma_c^{2D}}$ defining the following incidence matrices: $\tilde{\mathbf{G}}_{\Gamma_c^{2D}}$ (*dual* edges–*dual* nodes) and $\tilde{\mathbf{C}}_{\Gamma_c^{2D}}$ (*dual* faces–*dual* edges). These matrices satisfy the following properties: $\mathbf{C}_{\Gamma_c^{2D}}\mathbf{G}_{\Gamma_c^{2D}} = \mathbf{0}$, $\tilde{\mathbf{C}}_{\Gamma_c^{2D}}\tilde{\mathbf{G}}_{\Gamma_c^{2D}} = \mathbf{0}$, $\mathbf{C}_{\Gamma_c^{2D}} = -\tilde{\mathbf{G}}^T_{\Gamma_c^{2D}}$, and $\mathbf{G}_{\Gamma_c^{2D}} = \tilde{\mathbf{C}}^T_{\Gamma_c^{2D}}$.

It is worth noting that, because of the introduction of the equivalent surface model, the incidence matrices are now related to different mathematical operators. For instance, matrix $\mathbf{C}_{\Gamma_c^{2D}}$ is now related to the divergence operator.

Although a surface model is adopted, a thickness is still associated to $\mathcal{G}_{\Gamma_c^{2D}}$. Thus, faces f_c^{2D} are the 2–D equivalent of (3–D) volumes, edges e_c^{2D} are the 2–D equivalent of (3–D) faces, and nodes n_c^{2D} are the 2–D equivalent of (3–D) edges. The conduction current is then expanded as:

$$\mathbf{J}_c(\mathbf{r}) = \sum_k^{e_c^{2D}} \mathbf{w}_k^{f_\Gamma}(\mathbf{r}) \frac{1}{\delta} j_{e_k}^{2D}, \tag{3.113}$$

where $j_{e_k}^{2D}$ is the current DoF related to the kth edge (3–D face) of the mesh $e_{c_k}^{2D}$ and δ is the thickness associated to the equivalent 2–D model Γ_c^{2D}. Thus, the array of DoFs $\mathbf{j}_e^{2D}$ which stores $j_{e_k}^{2D}$, for $k = 1, \cdots, e_c^{2D}$ is introduced.

In analogy with the 3–D case, dual *boundary* nodes $\tilde{n}_c^{b,2d}$ are added to $\tilde{\mathcal{G}}_{\Gamma_c^{2D}}$, thus the augmented dual grid is defined as $\tilde{\mathcal{G}}^a_{\Gamma_c^{2D}}$. These nodes are in one–to–one relation with the *boundary* edges $e_c^{b,2D}$ which discretize the contour of Γ_c^{2D} defined as $\Lambda_c^{2D} = \partial\Gamma_c^{2D}$. Moreover, the selection matrix $\mathbf{C}_{\Lambda_c^{2D}}$ which extracts the *boundary* edges $e_c^{b,2D}$ of $\mathcal{G}_{\Gamma_c^{2D}}$ is introduced. The gradient selection matrix $\tilde{\mathbf{G}}_{\Lambda_c^{2D}} = -\mathbf{C}^T_{\Lambda_c^{2D}}$ and the *augmented* matrices $\mathbf{C}^a_{\Gamma_c^{2D}} = [\mathbf{C}_{\Gamma_c^{2D}}; \mathbf{C}_{\Lambda_c^{2D}}]$, $\tilde{\mathbf{G}}^a_{\Lambda_c^{2D}} = -\mathbf{C}^{aT}_{\Gamma_c^{2D}} = [\tilde{\mathbf{G}}_{\Gamma_c^{2D}}, \tilde{\mathbf{G}}_{\Lambda_c^{2D}}]$ are also introduced:

Then, in analogy with the 3–D case, the following arrays of DoFs are introduced:

- $\tilde{\mathbf{e}}^{2D} = (\tilde{e}_{e_k}^{2D})$ on dual edges $\tilde{e}_c^{2D}$, $\tilde{e}^s_{e_k} = \int_{\tilde{e}_{c_k}^{2D}} \mathbf{E} \cdot d\mathbf{l}$,
- $\tilde{\mathbf{e}}_0^{2D} = (\tilde{e}_{0_k}^{2D})$ on dual edges $\tilde{e}_c^{2D}$, $\tilde{e}_{0_k}^{2D} = \int_{\tilde{e}_{c_k}^{2D}} \mathbf{E}_{ext} \cdot d\mathbf{l}$,
- $\tilde{\boldsymbol{\phi}}_e^{v,2D} = (\tilde{\phi}_{e_k}^{v,2D})$ on dual nodes $\tilde{n}_c^{2D}$, $\tilde{\phi}_{e_k}^{v,2D} = \varphi_e(\mathbf{r}_{\tilde{n}_{c,k}^{2D}})$,
- $\tilde{\boldsymbol{\phi}}_e^{s,2D} = (\tilde{\phi}_{e_k}^{s,2D})$ on dual boundary nodes $\tilde{n}_c^{b,2D}$, $\tilde{\phi}_{e_k}^{s,2D} = \varphi_e(\mathbf{r}_{\tilde{n}_{c,k}^{b,2D}})$,
- $\mathbf{q}_c^{v,2D} = (q_{c_k}^{2D})$ on primal faces f_c^{2D}, $q_{c_k}^{2D} = \delta \int_{f_{c_k}^{2D}} \varrho_c ds$,
- $\mathbf{q}_c^{s,2D} = (q_{c_k}^{2D})$ on boundary edges $e_c^{b,2D}$, $q_{c_k}^{s,2D} = \int_{e_{c_k}^{b,2D}} \varsigma_c ds$,
- $\tilde{\mathbf{a}}^{e,2D} = (\tilde{a}_k^{e,2D})$ on dual edges $\tilde{e}_c^{2D}$, $\tilde{a}_k^{e,2D} = \delta \int_{\tilde{e}_{c_k}^{2D}} \mathbf{A} \cdot d\mathbf{l}$.

The vector arrays related to the electric potential can be grouped in $\tilde{\boldsymbol{\phi}}_e^{2D} = [\tilde{\boldsymbol{\phi}}_e^{v,2D}, \tilde{\boldsymbol{\phi}}_e^{s,2D}]$ in a one to one relation with $\mathbf{q}_c^{2D} = [\mathbf{q}_c^{v,2D}, \mathbf{q}_c^{s,2D}]$.

Such as the 3–D case, the arrays of DoFs introduced above satisfy algebraic relations equivalent to the differential equations introduced in Chapter 2.

For instance, the discrete continuity equation is now given by:

$$\mathbf{C}_{\Gamma_c^{2D}}\mathbf{j}_e^{2D} = -i\omega\mathbf{q}_e^{v,2D}, \qquad \mathbf{C}_{\Lambda_c^{2D}}\mathbf{j}_e^{2D} = -i\omega\mathbf{q}_e^{s,2D}, \qquad \mathbf{C}^a_{\Gamma_c^{2D}}\mathbf{j}_e^{2D} = -i\omega\mathbf{q}_e^{2D}, \tag{3.114}$$

while the discrete relation between the potentials and the electric field is given by

$$\tilde{\mathbf{e}}^{2D} = -i\omega\tilde{\mathbf{a}}^{e,2D} - \tilde{\mathbf{G}}_{\Gamma_c^{2D}}\tilde{\boldsymbol{\phi}}_e^{2D} + \tilde{\mathbf{e}}_0^{2D}. \tag{3.115}$$

The expansion (3.113) is now inserted in the continuum equations (2.34) and (2.35). Then, the resulting equations are tested by using a Galerkin approach. Thus, the discrete form of (2.34) and (2.35) is finally given by:

$$\mathbf{R}_c^{2D}\mathbf{j}_e^{2D} + i\omega\tilde{\mathbf{a}}^{e,2D} + \tilde{\mathbf{G}}^a_{\Gamma_c^{2D}}\tilde{\boldsymbol{\phi}}_e^{2D} = \tilde{\mathbf{e}}_0^{2D}, \tag{3.116}$$

where

$$\tilde{\mathbf{a}}^{e,2D} = \mathbf{L}_c^{c,2D}\mathbf{j}_e^{2D}, \tag{3.117}$$

$$\tilde{\boldsymbol{\phi}}_e^{2D} = \mathbf{P}_c^{2D}\mathbf{q}_e^{2D}. \tag{3.118}$$

The $e_c \times e_c$ resistance matrix of a 2–D equivalent conductive model is given by

$$R_{c_{uk}}^{2D} = \int_{\Gamma_e^{2D}} \frac{\rho_c(\mathbf{r})}{\delta}\mathbf{w}_u^{f_\Gamma}(\mathbf{r})\cdot\mathbf{w}_k^{f_\Gamma}(\mathbf{r})d\Gamma, \tag{3.119}$$

while the expression of the coefficients of $\mathbf{L}_c^{c,2D}$ is the same of the *surface* inductance matrix in (3.43). The dimension of $\mathbf{L}_c^{c,2D}$ is $e_c \times e_c$.

Matrix $\mathbf{P}_c^{2D}$, with dimension $\left((f_c^{2D} + e_c^{b,2D}) \times (f_c^{2D} + e_c^{b,2D})\right)$, is instead subdivided as

$$\mathbf{P}_c^{2D} = \begin{bmatrix} \mathbf{P}_c^{ss,2D} & \mathbf{P}_c^{sl,2D} \\ \mathbf{P}_c^{ls,2D} & \mathbf{P}_c^{ll,2D} \end{bmatrix}, \tag{3.120}$$

where $\mathbf{P}_c^{ss,2D}$, $\mathbf{P}_c^{ll,2D}$, and $\mathbf{P}_c^{sl,2D} = \mathbf{P}_c^{ls,2D^T}$ are the *surface*, *linear*, and *surface/linear* potential matrices defined as:

$$\begin{aligned} P_{c_{uk}}^{ss} &= \frac{1}{\varepsilon_0 S_u S_k}\int_{f_{e_u}^{2D}}\int_{f_{e_k}^{2D}} g(\mathbf{r},\mathbf{r}')d\Gamma' d\Gamma, \\ P_{c_{uk}}^{ll} &= \frac{1}{\varepsilon_0 L_u L_k}\int_{e_{e_u}^{b,2D}}\int_{e_{e_k}^{b,2D}} g(\mathbf{r},\mathbf{r}')d\Lambda' d\Lambda, \\ P_{c_{uk}}^{sl} = P_{e_{ku}}^{ls} &= \frac{1}{\varepsilon_0 S_u L_k}\int_{f_{e_u}^{2D}}\int_{e_{e_k}^{b,2D}} g(\mathbf{r},\mathbf{r}')d\Lambda' d\Gamma, \end{aligned} \tag{3.121}$$

in which S_h and L_h indicate the area and the length of a generic h–th face and boundary edge, respectively.

Finally, combining (3.114) and (3.118), the whole problem can be written as

$$\begin{bmatrix} \mathbf{R}_c^{2D} + i\omega\mathbf{L}_c^{c,2D} & \tilde{\mathbf{G}}^a_{\Gamma_c^{2D}} \\ \mathbf{P}_c^{2D}\mathbf{C}^a_{\Gamma_c^{2D}} & i\omega\mathbf{1} \end{bmatrix} \begin{bmatrix} \mathbf{j}_e^{2D} \\ \tilde{\boldsymbol{\phi}}_e^{2D} \end{bmatrix} = \begin{bmatrix} \tilde{\mathbf{e}}_0^{2D} \\ \mathbf{0} \end{bmatrix}. \tag{3.122}$$

In the above discussion, the more general discretization of an equivalent 2–D conductive model has been presented. However, often the model is simplified, i.e. the boundary charges $\mathbf{q}_c^{s,2D}$ and the boundary potentials $\tilde{\boldsymbol{\phi}}_e^{s,2D}$ are not defined. Thus, the primal and the dual grids are not augmented, as well the incidence matrices. In general, for practical cases this further

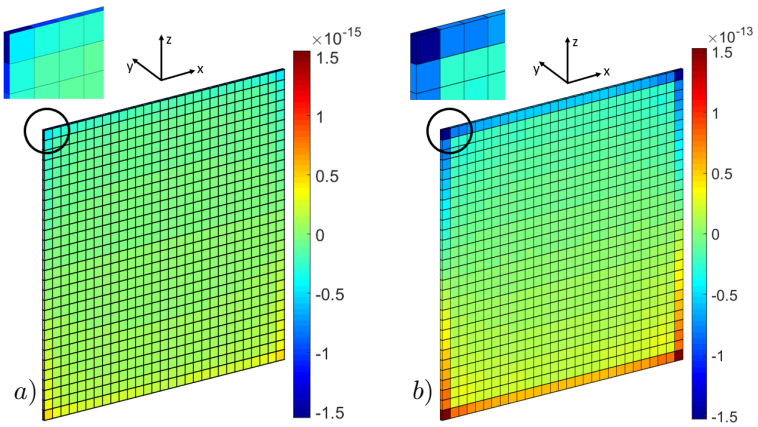

Figure 3.16: Charge distribution for an equivalent 2–D model of a conductive plate excited by an external electric field along the z direction. *a*) 2–D model with surface charges, values in C/m^2. *b*) Simplified 2–D model without surface charges C/m^3.

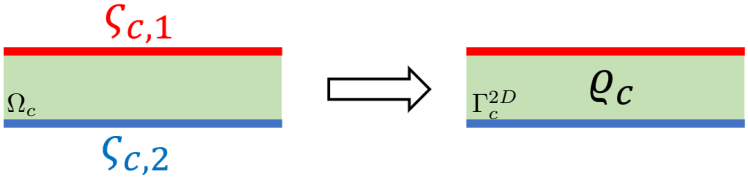

Figure 3.17: Charge distribution from 3–D to equivalent 2–D model.

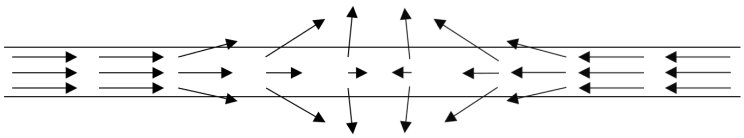

Figure 3.18: Current flow exemplification: leakage case.

simplification does not affect the quality of the solution. Indeed, when this simplification is performed, the effects of the surface charges which lay on the boundary Λ_c (i.e. the surface obtained by the extrusion of Λ_c along the thickness of the equivalent surface model) are neglected. However, an approximate solution is obtained where the effects of the missing boundary charges are replaced by the volume charges which lay on the faces (i.e. 3–D volumes) connected to the boundary edges. In Fig. 3.16, the results obtained from a (complete) 2–D model (i.e. the boudary charges are considered) and a simplified 2–D model (i.e. the boudary charges are neglected) are shown for the case of a conductive plate excited by a vertical electric field. In order to allow a clear visualization, the results obtained with the 2–D equivalent models are reported to the original 3–D model. As one can notices, the values are scaled by a factor 0.01 which is the thickness of the plate ($\delta = 0.01$ m). Indeed, in Fig. 3.16.*a* the color scale is related to the surface charge density C/m^2 while in Fig. 3.16.*a* the color scale is related to the volume charge density C/m^3.

Even if the two charge distributions in the two cases of Fig. 3.16 are different, the electromagnetic fields evaluated in the points of the 3–D space are almost identical, except for the points very close to the boundary of the conductive domain.

When a 2–D equivalent model is adopted (complete or simplified), an obvious approximation is introduced. Indeed, $\mathbf{J}_c$ is approximated as a vector which flows with tangential direction with

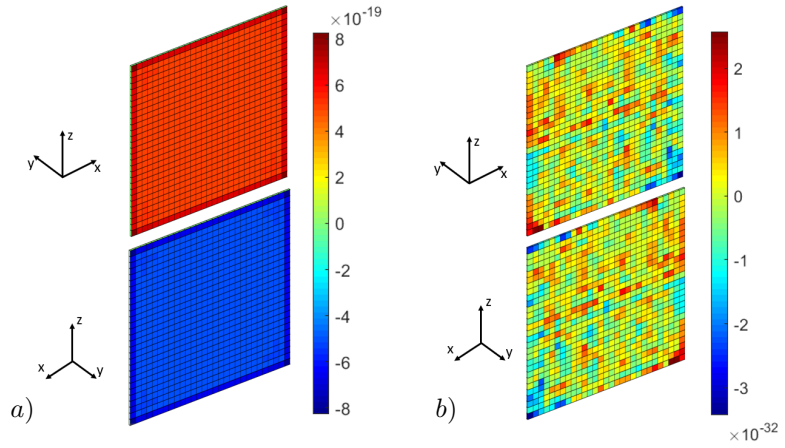

Figure 3.19: Charge distribution in a conductive plate excited by an external electric field along the y direction. *a*) 3–D model with surface charges. *b*) 2–D model with equivalent volume charges.

respect to Γ_c^{2D}. Thus, the normal component of $\mathbf{J}_c$ (with respect of Γ_c^{2D}) is completely neglected. Furthermore, also the potentials $\mathbf{A}$ and $\mathbf{A}_e$ produced by the *approximated* $\mathbf{J}_c$ are neglected. In volume conductive media, the volume charge density ϱ_c is in general truly negligible (see Appendix A) while the boundary charge ς_c must be taken into account when the frequency is sufficiently high or when the capacitive effects are significant. From the continuity equation (2.23), ς_c is related to the normal component of $\mathbf{J}_c$. When the complete simplified 2–D model is adopted, the surface charge ς_c is considered only on the boundary Λ_c, whereas the charge which lies on the other two sides of the boundaries of the real 3–D domain are replaced by a charge which lies on the (only) surface Γ_c^{2D}, as exemplified in Fig. 3.17.

This approximation is appropriate when in the real 3–D problem $\mathbf{J}_c$ flows outside (or inside) the 3–D domain from both the two sides, as exemplified in Fig. 3.18. Indeed, in this case a surface charge distribution *of the same sign* lays on both the sides of the domain. Thus, this two charge layers can be approximated by a volume charge of the same sign placed in Γ_c^{2D}.

Instead, when the surface charge distributions have opposite signs in the two sides (for instance, $\varsigma_{c,1} > 0$ and $\varsigma_{c,2} < 0$ in Fig. 3.17) the equivalent 2–D approximation could be totally inappropriate, most of all when $\varsigma_{c,1} = -\varsigma_{c,2}$. Indeed, no equivalent 2–D distribution can produce the same effects of the real 3–D one.

In Fig. 3.19, the case of a square conductive plate excited by an external electric field along the y direction is considered. Fig. 3.19.*a* shows the results obtained from a 3–D model of the problem while Fig. 3.19.*b* shows the results obtained form the equivalent 2–D model, that are clearly wrong.

The case considered in Fig. 3.19 is a very specific case, where the external field is purely normal to the equivalent 2–D model (and so $\mathbf{J}_c$ too). Although this case is maybe not so significant in the practice, it is clear that an equivalent 2–D model may not be capable of properly reproduce all the electromagnetic effects of a real 3–D problem. Thus, the equivalent 2–D approximation must be properly adopted (i.e. when the tangential direction of $\mathbf{J}_c$ can actually be imposed) or proper adjustments must be applied.

It is worth noting that the equivalent 2–D models are usually adopted when high frequency problems involving conductive media are considered [77]. Indeed, when the frequency is sufficiently high, the current is mainly distributed in the proximity of the boundaries of the conductive device. However, although the current is concentrated in a very thin layer, its distribution is far

from being uniform and indeed its distribution can be described by means of Bessel functions. If the uniform distribution of the current is still enforced, a *mean* value of the current will be obtained as solution of the electromagnetic problem. The solution in terms of electromagnetic fields evaluated outside the device may be close to the real one but the quantities related to the actual distribution of the conduction current density will be strongly affected because of the approximation. For instance, if the interest is in the accurate evaluation of the Joule losses, that are strongly affected by the actual distribution of the conduction current, the use of an equivalent 2–D model will be probably inappropriate.

A solution to this problem can be the one proposed in [76], where the conduction current is expanded by imposing an exponentially decay along the thickness. However, this solution may extend the applicability of the use of equivalent 2–D models but it is not general. Indeed, as stated in [76], a more general solution to this problem would require the adoption of higher order Surface Impedance Boundary Conditions (SIBCs) [78, 79, 80], which is actually a sensitive topic.

The above discussion is related to a purely conductive case. However, when the C–PEEC formulation is adopted, the same procedure can be applied to obtain an equivalent 2–D model of the dielectric and the magnetic domains. Nonetheless, as shown for the case of the conductive plate above, the equivalent 2–D model can be properly adopted when the currents ($\mathbf{J}_e$ and $\mathbf{J}_m$) mainly flow in the tangential direction (as for the case of Fig. 3.16) or when they flow likewise Fig. 3.18. The condition shown in Fig. 3.18 may represent the flow of the conduction current along a transmission line (when the frequency is sufficiently high).

However, a similar condition is not common for the polarization and the magnetic currents $\mathbf{J}_p$ and $\mathbf{J}_m$. For instance, for thin magnetic media this condition could be fulfilled when the permeability is sufficiently high. Thus, the magnetization tends to flow in the tangential direction and the two surface charge distributions laying in the two sides of the thin object may not be purely *mirror images* (with reverse sign). Thus, an equivalent 2–D model as the one described above can in principle be adopted also for dielectric and magnetic media. However, for some practical case, the model for thin dielectric or magnetic media should be properly adjusted in order to have an appropriate approximation of the real 3–D problem.

It is worth noting that with problems consisting of equivalent 2–D conductive models and magnetic media, the mutual coupling between the two domains must be properly considered. In the 3–D problem, the effects of the magnetic media on the electric domain are given by the block term $(1,3)$ of system (3.63):

$$\mathbf{M}_{1/\varepsilon_0}\mathbf{C}_{\Omega_e}\tilde{\mathbf{N}}^e_m\tilde{\mathbf{j}}_m, \tag{3.123}$$

where $\mathbf{a}^e_m = \tilde{\mathbf{N}}^e_m\tilde{\mathbf{j}}_m$ is the array of DoFs related to the edges of the tetrahedral/hexahedral mesh of Ω_e. Or more specifically, $\mathbf{a}^e_m$ stores the line integrals of $\mathbf{A}_m$ along the edges of the tetrahedral/hexahedral mesh of Ω_e. Then, when $\mathbf{a}^e_m$ is multiplied by the curl matrix $\mathbf{C}_{\Omega_e}$ the resulting array of DoFs is related to the fluxes of $\nabla\times\mathbf{A}_m$ trough the faces of the tetrahedral/hexahedral mesh f_e. Then, matrix $\mathbf{M}_{1/\varepsilon_0}$ projects these fluxes from the primal faces f_e to the dual edges $\tilde{e}_e$ of the electric grids. However, when an equivalent 2–D model is adopted, the faces of the mesh are collapsed to edges. Thus, the evaluation of the mutual coupling between the electric and the magnetic domains must be properly handled.

From the implementation point of view, one possibility is to *virtually* restore the *real* 3–D *structure* of the electric domain. Thus, the term $\mathbf{C}_{\Omega_e}\tilde{\mathbf{N}}^e_m$ can be replaced by the $(e^{2d}_c\times\tilde{f}_m)$

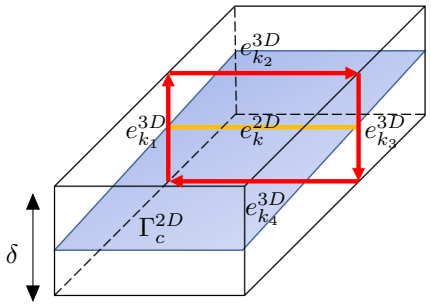

Figure 3.20: Restoring the 3–D model for the evaluation of the mutual coupling between the 2–D electric and 3–D magnetic domains.

matrix $\tilde{\mathbf{T}}^{e,2D}_{m}$ evaluated as:

$$\tilde{T}^{e,2D}_{m_{kh}} = \tilde{N}^{e}_{m,k_1h} + \tilde{N}^{e}_{m,k_2h} + \tilde{N}^{e}_{m,k_3h} + \tilde{N}^{e}_{m,k_4h}, \tag{3.124}$$

knowing that $\mathbf{C}_{\Omega_e}$ is a sparse matrix the coefficient of which are only -1, 1, and 0. The *restored* 3–D geometrical entities are shown in Fig. 3.20; $\tilde{N}^{e}_{m,k_uh}$, with $u = 1, \cdots, 4$ is evaluated likewise (3.60) for the four (restored 3–D) edges $e^{3D}_{k_u}$ shown in Fig. 3.20.

Then, the matrix $\mathbf{M}_{1/\varepsilon_0}$ is replaced by the corresponding equivalent 2–D one defined as $\mathbf{M}^{2D}_{1/\varepsilon_0}$. The dimension of $\mathbf{M}^{2D}_{1/\varepsilon_0}$ is $e^{2D}_{c} \times e^{2D}_{c}$ and its coefficients are given by:

$$M^{2D}_{1/\varepsilon_{0_{uk}}} = \frac{1}{\varepsilon_0 \delta} \int_{\Gamma^{2D}_{e}} \mathbf{w}^{f_\Gamma}_{u}(\mathbf{r}) \cdot \mathbf{w}^{f_\Gamma}_{k}(\mathbf{r}) d\Gamma. \tag{3.125}$$

Finally, when the electromagnetic problem consists of equivalent 2–D conductive models and 3–D magnetic models, the final system to be solved can be written as

$$\begin{bmatrix} \mathbf{R}^{2D}_{c} + i\omega \mathbf{L}^{c,2D}_{c} & \tilde{\mathbf{G}}^{a}_{\Gamma^{2D}_{c}} & \mathbf{M}^{2D}_{1/\varepsilon_0} \tilde{\mathbf{T}}^{e,2D}_{m} & \mathbf{0} \\ \mathbf{P}^{2D}_{c} \mathbf{C}^{a}_{\Gamma^{2D}_{c}} & i\omega \mathbf{1} & \mathbf{0} & \mathbf{0} \\ -\tilde{\mathbf{M}}_{1/\mu_0} \tilde{\mathbf{C}}_{\Omega_m} \mathbf{N}^{m}_{e,2D} & \mathbf{0} & \tilde{\mathbf{R}}_{m} + i\omega \tilde{\mathbf{L}}^{m}_{m} & \mathbf{G}^{a}_{\Omega_m} \\ \mathbf{0} & \mathbf{0} & \tilde{\mathbf{P}}_{m} \tilde{\mathbf{D}}^{a}_{\Omega_m} & i\omega \mathbf{1} \end{bmatrix} \begin{bmatrix} \mathbf{j}^{2D}_{e} \\ \tilde{\boldsymbol{\phi}}^{2D}_{e} \\ \tilde{\mathbf{j}}_{m} \\ \boldsymbol{\phi}_{m} \end{bmatrix} = \begin{bmatrix} \tilde{\mathbf{e}}^{2D}_{0} \\ \mathbf{0} \\ \mathbf{h}_0 \\ \mathbf{0} \end{bmatrix}, \tag{3.126}$$

where a generic coefficient of the $\tilde{e}_m \times e^{2D}_{c}$ matrix $\mathbf{N}^{m}_{e,2D}$ is given by

$$N^{m}_{e,2D_{wk}} = \mu_0 \int_{\tilde{e}_w} \left(\int_{\Gamma^{2D}_{c}} \mathbf{w}^{f_\Gamma}_{u}(\mathbf{r}') g(\mathbf{r}, \mathbf{r}') d\Gamma' \right) \cdot d\mathbf{l}. \tag{3.127}$$

The general case consisting of a mixture of equivalent 2–D models and 3–D models for both electric and magnetic domains can be derived by performing similar adjustments on the equivalent electric and magnetic 2–D models.

Finally, some consideration on the A–PEEC method. Clearly, since C–PEEC and A–PEEC handle electric media in the same ways, an equivalent 2–D model can be constructed exactly as above for the electric domains. For the magnetic domains instead it is not possible to define an equivalent 2–D model based on the A–PEEC formulation (or at least its construction is not straightforward). Indeed, when the 3–D models is collapsed to the equivalent 2–D one, the definition of the amperian currents is partially lost and it may be restored by using distribution

theory concepts.

3.4.2 1–D models

When electric or magnetic thin wires are considered, equivalent 1–D models can be adopted. Likewise the case of equivalent 2–D models, when an equivalent 1–D model is adopted the distribution of the currents is considered uniform (or at least known) in the cross section of the wire. Thus, a discretization process similar to the one proposed above for the 2–D models can be applied for the 1–D ones. More details concerning equivalent 1–D models can be found in the work proposed by the author [19] where an equivalent 1–D PEEC model has been adopted for the study of the Toroidal Field coils system of a thermonuclear fusion reactor magnets.

Clearly, as for the case of 2–D models, the adoption of equivalent 1–D models introduces some simplifications and thus it may not be capable of properly reproducing all the electromagnetic effects of a real 3–D problem. Thus, likewise the 2–D case, the equivalent 1–D approximation must be properly adopted (i.e. when the currents mainly flow along the direction of the wire). However, dedicated equivalent 1–D models which restore the real 3–D geometry can be developed as the one proposed in [81] for the study of array magnetic wires.

In the context of an ongoing collaboration with Prof. Thomas Bauernfeind from the Technical University of Graz, Austria, a PEEC code for equivalent 1–D models has been developed during the PhD thesis. Such code has been adopted for the design and the optimization of high frequency electromagnetic devices (e.g. Near Field Communication Antennas) and the results are disseminated in several joint publications [82], [83], [84], [85].

Chapter 4

Solution of the PEEC system of equations

In Chapter 2, the A–PEEC and C–PEEC formulations have been presented. Then, in Chapter 3, both the formulations have been discretized by means of the Cell Method scheme leading to the final algebraic system of equations (3.45) and (3.63) (or their variants when lumped circuits elements or inhomogeneous media are considered).

In this chapter, the PEEC algebraic system of equations derived from the Cell Method discretization of the A–PEEC and C–PEEC formulation are discussed. Indeed, depending on the kind of problem to be solved (e.g. low and high frequency), the system of equations can be properly handled and different solution strategies can be adopted in order to efficiently solve the electromagnetic problem. Thus, in the following, the numerical properties of the A–PEEC and the C–PEEC system of equations are discussed and different way to re–write the system are proposed. Then, different solution strategies are proposed and discussed. The numerical issues arising from the solution of the final system of equations (e.g. break down in frequency) are discussed and the techniques to avoid this problem are presented.

It is worth noting that the storage and the computational effort required for the solution of system of equations derived from VIE methods (as the PEEC method) grow rapidly with the number of the unknowns. Thus, its solution may becomes unfeasible on standard workstations when large problem are considered. Low–rank approximation techniques can be indeed adopted to increase problem size while maintaining the same computing research. Although this topic is indeed a *solution strategy*, due to its importance in the context of this PhD work, this argument is not considered in this chapter while Chapter 5 is completely dedicated to that.

At the end of this chapter, academic and industrial numerical test cases are considered.

4.1 PEEC system of equations

The system of equations (3.45) and (3.63) (i.e. the ones obtained from the A–PEEC and C–PEEC methods) are the final PEEC system of equations, where the unknowns are the currents, the magnetization, and the potentials (as in the the *traditional* PEEC method where currents and potentials were considered as unknowns).

Systems (3.45) and (3.63) show good numerical properties. However, they cannot be directly solved when zero frequency problems are considered. Moreover, when objects with a relatively fine discretization are considered, the storage and the computational effort required for the solution of (3.45) and (3.63) may be unfeasible. Thus, in the following, the two system of

equations are handled in order to allow a DC solution. Furthermore, they are also re–written in a more compact form, i.e. by using a reduced number of unknowns.

In the following, for the sake of simplicity, the case of homogeneous media is considered and the presence of the external lumped circuits elements is neglected. Indeed, the following discussion can be easily extended to the case of inhomogeneous media and external lumped circuit elements.

4.1.1 A–PEEC system of equations

The system of equations obtained from the Cell Method discretization of the A–PEEC formulation for the case of homogeneous media is reported in (3.45), where lumped circuit elements are not considered. By performing simple algebraic manipulations, (3.45) can be rewritten as

$$\begin{bmatrix} \mathbf{R}_e + i\omega\mathbf{L}_e^e & \tilde{\mathbf{G}}_{\Omega_e}^a & i\omega[\mathbf{L}_m^e, \mathbf{L}_{\Gamma_m}^e]\mathbf{C}_{\Omega_m}^a \\ -\mathbf{D}_{\Omega_e}^a & -i\omega\mathbf{P}_e^{-1} & \mathbf{0} \\ i\omega\tilde{\mathbf{C}}_{\Omega_m}^a \begin{bmatrix} \mathbf{L}_e^m \\ \mathbf{L}_e^{\Gamma_m} \end{bmatrix} & \mathbf{0} & -i\omega\mathbf{F} + i\omega\tilde{\mathbf{C}}_{\Omega_m}^a \mathbf{L}_m^a \mathbf{C}_{\Omega_m}^a \end{bmatrix} \begin{bmatrix} \mathbf{j}_e \\ \tilde{\phi}_e \\ \mathbf{m} \end{bmatrix} = \begin{bmatrix} \tilde{\mathbf{e}}_0 \\ \mathbf{0} \\ -i\omega\tilde{\mathbf{b}}_0 \end{bmatrix}. \tag{4.1}$$

Thanks to the relation between the primal and dual incidence matrices, the above system of equations is symmetric. However, the inversion of $\mathbf{P}_e$ is required, which could be actually unfeasible or really computationally expensive.

When the frequency is zero, the magnetic media do not affect the electric ones and the electric and magnetic problems can be decoupled [86]. Moreover, conductive and dielectric media act differently when the frequency is zero, thus they must be considered separately. Therefore, the zero–frequency problem (4.1) can be written as

$$\begin{bmatrix} \mathbf{R}_c & \tilde{\mathbf{G}}_{\Omega_c}^a \\ -\mathbf{D}_{\Omega_c}^a & \mathbf{0} \end{bmatrix} \begin{bmatrix} \mathbf{j}_c \\ \tilde{\phi}_e \end{bmatrix} = \begin{bmatrix} \tilde{\mathbf{e}}_0 \\ \mathbf{0} \end{bmatrix}, \tag{4.2}$$

for the conductive media, where coefficients of $\mathbf{R}_c$ are

$$R_{c_{uk}} = \int_{\Omega_c} \rho_c(\mathbf{r}) \mathbf{w}_u^f(\mathbf{r}) \cdot \mathbf{w}_k^f(\mathbf{r}) d\Omega. \tag{4.3}$$

The solution of the magnetostatic problem is instead given by

$$\left[\mathbf{F} - \tilde{\mathbf{C}}_{\Omega_m}^a \mathbf{L}_m^a \mathbf{C}_{\Omega_m}^a\right] \mathbf{m} = \tilde{\mathbf{b}}_0 + \tilde{\mathbf{C}}_{\Omega_m}^a \begin{bmatrix} \mathbf{L}_e^m \\ \mathbf{L}_e^{\Gamma_m} \end{bmatrix} \mathbf{j}_c. \tag{4.4}$$

The electrostatic problem for dielectric media instead needs a little more of discussion. Indeed, when the frequency is zero the polarization currents $\mathbf{J}_p = i\omega\mathbf{P}$ are obviously zero. Thus, the polarization $\mathbf{P}$ must be now considered as the problem unknown and the array $\mathbf{p} = (p_i)$, with $i = 1, \cdots, f_d$, which stores the fluxes of $\mathbf{P}$ through the primal faces of the mesh is introduced. Therefore, the electrostatic problem for dielectric media can be written as:

$$\begin{bmatrix} \mathbf{R}_{d0} & \tilde{\mathbf{G}}_{\Omega_d}^a \\ -\mathbf{P}_e \mathbf{D}_{\Omega_d}^a & \mathbf{1} \end{bmatrix} \begin{bmatrix} \mathbf{p} \\ \tilde{\phi}_e \end{bmatrix} = \begin{bmatrix} \tilde{\mathbf{e}}_0 \\ \mathbf{0} \end{bmatrix}, \tag{4.5}$$

where coefficients of $\mathbf{R}_{d0}$ are

$$R_{d0_{uk}} = \int_{\Omega_d} \frac{\mathbf{w}_u^f(\mathbf{r}) \cdot \mathbf{w}_k^f(\mathbf{r})}{\varepsilon_0(\varepsilon_r(\mathbf{r}) - 1)} d\Omega. \tag{4.6}$$

The above systems are obtained from the *traditional* form of the A–PEEC system of equations, where the potentials are considered as unknowns. Except for the discrete magnetic equation, the electric equations are in a form suitable for the Modified Nodal Analysis (MNA). Indeed, the unknowns are the nodal potentials of the equivalent electric circuit (the reference node is the infinite node) and the currents of the circuit branches with voltage sources (i.e. all the circuit branches). Indeed, all the electric circuit branches can be modeled with the elementary PEEC circuit branch shown in Fig. 3.7. Thus, each branch of the equivalent circuit is made of current–controlled voltage sources, therefore each current must be considered as unknown. The choice of write the final system of equations in MNA form is useful for Spice–like solvers. However, as more widely discussed in Section 4.2.1, this choice is actually useful only for some specific case.

On the other hand, when problems of industrial interest are considered, it is convenient to reduce the size of the final system of equations. Starting from system (3.45) and applying the Schur complement it is possible to delete the presence of the electric potential from the unknowns. Thus, the following system of equations is obtained:

$$\begin{bmatrix} \mathbf{R}_e + i\omega\mathbf{L}_e^e + \frac{1}{i\omega}\tilde{\mathbf{G}}_{\Omega_e}^a \mathbf{P}_e \mathbf{D}_{\Omega_e}^a & i\omega[\mathbf{L}_m^e, \mathbf{L}_{\Gamma_m}^e]\mathbf{C}_{\Omega_m}^a \\ -\tilde{\mathbf{C}}_{\Omega_m}^a \begin{bmatrix} \mathbf{L}_e^m \\ \mathbf{L}_e^{\Gamma_m} \end{bmatrix} & \mathbf{F} - \tilde{\mathbf{C}}_{\Omega_m}^a \mathbf{L}_m^a \mathbf{C}_{\Omega_m}^a \end{bmatrix} \begin{bmatrix} \mathbf{j}_e \\ \mathbf{m} \end{bmatrix} = \begin{bmatrix} \tilde{\mathbf{e}}_0 \\ \tilde{\mathbf{b}}_0 \end{bmatrix}. \tag{4.7}$$

This system of equations has a smaller dimension compared to (3.45) and by multiply the second row for $-i\omega$ it can be made symmetric. However, as discussed in Section 4.2.3, (4.7) may suffer from numerical issues common to Integral Equation Method, e.g. the breakdown in frequency [87]. Nevertheless, *change of basis* techniques can be applied to (4.7) in order to improve its numerical properties and avoid the breakdown in frequency problem. These techniques are presented in Section 4.2.4.

It is worth noting that even if $\tilde{\boldsymbol{\phi}}_e$ has been deleted from the unknowns of (4.7), when the problem is solved $\tilde{\boldsymbol{\phi}}_e$ can be still evaluated by

$$\tilde{\boldsymbol{\phi}}_e = \frac{1}{i\omega}\mathbf{P}_e \mathbf{D}_{\Omega_e}^a \mathbf{j}_e. \tag{4.8}$$

Moreover, the electromagnetic problem offers the same circuit interpretation and lumped circuit elements can be still considered. When lumped circuit elements are involved, the Schur

complement can be applied to system (3.47) leading to

$$\begin{bmatrix} \mathbf{R}_e + i\omega\mathbf{L}_e^e + \frac{1}{i\omega}\tilde{\mathbf{G}}^a_{\Omega_e}\mathbf{P}_e\mathbf{D}^a_{\Omega_e} & i\omega[\mathbf{L}_m^e, \mathbf{L}_{\Gamma_m}^e]\mathbf{C}^a_{\Omega_m} & \frac{1}{i\omega}\tilde{\mathbf{G}}^a_{\Omega_e}\mathbf{P}_e\mathbf{A}^T_{e,l} & \mathbf{0} \\ -\tilde{\mathbf{C}}^a_{\Omega_m}\begin{bmatrix}\mathbf{L}_e^m \\ \mathbf{L}_e^{\Gamma_m}\end{bmatrix} & \mathbf{F} - \tilde{\mathbf{C}}^a_{\Omega_m}\mathbf{L}^a_m\mathbf{C}^a_{\Omega_m} & \mathbf{0} & \mathbf{0} \\ \frac{1}{i\omega}\mathbf{A}_{e,l}\mathbf{P}_e\mathbf{D}^a_{\Omega_e} & \mathbf{0} & \mathbf{Z}_l & \mathbf{A}_{l,l} \\ \mathbf{0} & \mathbf{0} & \mathbf{A}^T_{l,l} & \mathbf{0} \end{bmatrix} \begin{bmatrix} \mathbf{j}_e \\ \mathbf{m} \\ \mathbf{j}_l \\ \tilde{\boldsymbol{\phi}}_{e,l} \end{bmatrix} = \begin{bmatrix} \tilde{\mathbf{e}}_0 + \frac{1}{i\omega}\tilde{\mathbf{G}}^a_{\Omega_e}\mathbf{P}_e\mathbf{j}_{e0} \\ \tilde{\mathbf{b}}_0 \\ \mathbf{u}_{l0} \\ \mathbf{j}_{l0} \end{bmatrix}, \tag{4.9}$$

which can be made symmetric (by multiplying the second row for $-i\omega$). The electric potentials $\tilde{\boldsymbol{\phi}}_{e,l}$ related to the lumped nodes cannot be removed from the system. Indeed, they are not in a one–to–one relationship with the electric charges.

The Schur complement can be also adopted to reduce the dimension of (4.5) leading to

$$\left[\mathbf{R}_{d0} + \tilde{\mathbf{G}}^a_{\Omega_d}\mathbf{P}_e\mathbf{D}^a_{\Omega_d}\right]\mathbf{p} = \tilde{\mathbf{e}}_0. \tag{4.10}$$

Finally, similar considerations can be carried out for the case of inhomogeneous media starting from system (3.96).

4.1.2 C–PEEC system of equations

When the Cell Method discretization is applied to the C–PEEC formulation, the system of equations (3.63) is obtained, where homogeneous media are considered and lumped circuit elements are not involved. By performing simple algebraic manipulations, (3.63) can be rewritten as

$$\begin{bmatrix} \mathbf{R}_e + i\omega\mathbf{L}_e^e & \tilde{\mathbf{G}}^a_{\Omega_e} & \tilde{\mathbf{K}}^e_m & \mathbf{0} \\ -\mathbf{D}^a_{\Omega_e} & -i\omega\mathbf{P}_e^{-1} & \mathbf{0} & \mathbf{0} \\ \mathbf{K}_e^m & \mathbf{0} & -\tilde{\mathbf{R}}_m - i\omega\tilde{\mathbf{L}}_m^m & -\mathbf{G}^a_{\Omega_m} \\ \mathbf{0} & \mathbf{0} & \tilde{\mathbf{D}}^a_{\Omega_m} & i\omega\tilde{\mathbf{P}}_m^{-1} \end{bmatrix} \begin{bmatrix} \mathbf{j}_e \\ \tilde{\boldsymbol{\phi}}_e \\ \tilde{\mathbf{j}}_m \\ \boldsymbol{\phi}_m \end{bmatrix} = \begin{bmatrix} \tilde{\mathbf{e}}_0 \\ \mathbf{0} \\ -\mathbf{h}_0 \\ \mathbf{0} \end{bmatrix}. \tag{4.11}$$

The symmetry property of this system depends on matrices:

$$\tilde{\mathbf{K}}^e_m = \mathbf{M}_{1/\varepsilon_0}\mathbf{C}_{\Omega_e}\tilde{\mathbf{N}}^e_m, \tag{4.12}$$

$$\mathbf{K}^m_e = \tilde{\mathbf{M}}_{1/\mu_0}\tilde{\mathbf{C}}_{\Omega_m}\mathbf{N}^m_e. \tag{4.13}$$

From a physical point of view, $\tilde{\mathbf{K}}^e_m$ and $\mathbf{K}^m_e$ represent the mutual effects between electric and magnetic media and they should satisfy $\tilde{\mathbf{K}}^e_m = \mathbf{K}^{mT}_e$. However, unless sophisticated singularity extraction techniques are adopted, the coefficients of $\tilde{\mathbf{N}}^e_m$ and $\mathbf{N}^m_e$ are evaluated numerically and an unavoidable approximation is introduced. Moreover, $\tilde{\mathbf{N}}^e_m$ and $\mathbf{N}^m_e$ are obtained by integrating the vector potentials along the edges, which also introduces an approximation; indeed the electromagnetic potentials are obtained from the Green's function and thus they are not linear varying quantities in the 3–D space. Therefore, if $\tilde{\mathbf{K}}^e_m$ and $\mathbf{K}^m_e$ are explicitly evaluated, the resulting matrices do not exactly satisfy $\tilde{\mathbf{K}}^e_m = \mathbf{K}^{mT}_e$. Indeed, both $\tilde{\mathbf{K}}^e_m$ and $\mathbf{K}^m_e$ are two

different (equivalent) numerical *approximations* of an *exact* integral operator. However, once $\tilde{\mathbf{K}}_m^e$ is evaluated, the symmetry can be actually enforced by replacing $\mathbf{K}_e^m$ with $\tilde{\mathbf{K}}_m^{eT}$. Thus, matrices $\tilde{\mathbf{M}}_{1/\mu_0}$ and $\mathbf{N}_e^m$ are not calculated.

Likewise the A–PEEC formulation, when the frequency is zero the electric and magnetic problems can be decoupled. The resulting system for the case of conductive and dielectric media are again given by (4.2) and (4.5). The magnetostatic problem instead is given by

$$\begin{bmatrix} \tilde{\mathbf{R}}_{m0} & \mathbf{G}_{\Omega_m}^a \\ -\tilde{\mathbf{P}}_m \tilde{\mathbf{D}}_{\Omega_m}^m & \mathbf{1} \end{bmatrix} \begin{bmatrix} \tilde{\mathbf{p}}_m \\ \boldsymbol{\phi}_m \end{bmatrix} = \begin{bmatrix} \mathbf{h}_0 + \tilde{\mathbf{M}}_{1/\mu_0} \tilde{\mathbf{C}}_{\Omega_m} \mathbf{N}_e^m \mathbf{j}_e \\ \mathbf{0} \end{bmatrix}, \tag{4.14}$$

where $\tilde{\mathbf{p}}_m = (\tilde{p}_{m_i})$, with $i = 1, \cdots, \tilde{f}_m$ is the array of fluxes of $\mu_0 \mathbf{M}$ through the dual faces of Ω_m and coefficients of $\tilde{\mathbf{R}}_{m0}$ are

$$\tilde{R}_{m0_{uk}} = \int_{\Omega_m} \frac{\mathbf{w}_u^f(\mathbf{r}) \cdot \mathbf{w}_k^f(\mathbf{r})}{\mu_0(\mu_r(\mathbf{r}) - 1)} d\Omega. \tag{4.15}$$

The system above is in the MNA form. Unlike the A–PEEC method, in the C–PEEC method also the magnetic equation is written in the MNA form. Thus, the electromagnetic problem can be theoretically solved by means of a MNA Spice–like solver. More details concerning this topic are given in Section 4.2.1.

However, for most of the problems of industrial interest, it is convenient to reduce the size of the final system of equations. Starting from (3.63) and applying a Schur complement it is possible to delete the presence of the electric and magnetic scalar potentials from the system unknowns. Thus, the following system of equations can be obtained:

$$\begin{bmatrix} \mathbf{R}_e + i\omega \mathbf{L}_e^e + \frac{1}{i\omega} \tilde{\mathbf{G}}_{\Omega_e}^a \mathbf{P}_e \mathbf{D}_{\Omega_e}^a & \tilde{\mathbf{K}}_m^e \\ -\mathbf{K}_e^m & \tilde{\mathbf{R}}_m + i\omega \tilde{\mathbf{L}}_m^m + \frac{1}{i\omega} \mathbf{G}_{\Omega_m}^a \tilde{\mathbf{P}}_m \tilde{\mathbf{D}}_{\Omega_m}^a \end{bmatrix} \begin{bmatrix} \mathbf{j}_e \\ \tilde{\mathbf{j}}_m \end{bmatrix} = \begin{bmatrix} \tilde{\mathbf{e}}_0 \\ \mathbf{h}_0 \end{bmatrix}. \tag{4.16}$$

This system has a smaller dimension compared to (3.63) and by multiplying the second row for -1 it can be made symmetric. However, such as the A–PEEC method, this system may suffer from numerical issues. This topic is discussed more in detail in Section 4.2.3.

The Schur complement can be also applied to (4.14), (3.68) (where lumped circuit elements are considered), and also (3.86) for the case of inhomogeneous media, as above for A–PEEC. Thus, the electric and the magnetic scalar potentials can be always removed from the unknowns of the C–PEEC system of equations.

When the C–PEEC formulation based on the total div–free current is adopted, a completely equivalent discussion can be provided and systems of equations similar to the ones presented above can be obtained.

4.2 Techniques for the solution of the final algebraic system of equations

As discussed in the previous section, the final algebraic system of equations can be written in many different forms. Indeed, depending on the kind of problem to be solved, one of the previous forms of the system should be more convenient that the others. Therefore, different solution

strategies can be applied and, depending on the form of the final system of equations, different solvers can be applied.

In the following, different possible solution strategies are discussed. Moreover, the numerical properties and the numerical issues arising from the solution of final system are presented. Finally, *change of basis* techniques which allow for strongly imposing the properties of the unknowns and improve the numerical properties of the final system are presented.

4.2.1 MNA Spice–like solver

In the 70s, when the PEEC method was first proposed, due to the limited computing power the studied systems were mainly small interconnects or PCB traces with very crude meshes. Indeed, at that time the main interest on the PEEC method was the possibility to couple the full Maxwell electromagnetic problem with the circuit problems (even huge ones) consisting of lumped components with limited connectivity between ports.

When this kind of problems is considered, since the final coupled electromagnetic–circuit problem mainly consists of lumped components, it is natural to consider the problem in the context of *electric circuits*, rather than of electromagnetic fields. Thus, the more natural way to solve the final problem is to adopt a Spice–like solver. Typically, the input file required by this kind of solvers is the *net list* of the electric circuit to be solved and then the problem is written in the MNA form by the software itself. In the most of the cases, the connections between the components are limited, thus the resulting system of equations is a very sparse matrix (even of huge dimension). Indeed, the solvers adopted in Spice softwares are usually direct solvers which operate efficiently when the system is a sparse matrix, e.g. T. Davis's KLU [88]. Therefore, when this solution strategy is chosen, the final PEEC system of equations to be solved is (3.47) for the case of the A–PEEC method, and (3.68) for the case of C–PEEC method. Actually, the *net list* of the equivalent circuit (obtained from the Cell Method discretization of the PEEC method coupled with the lumped elements) must be constructed and the resulting file is the input of the Spice software. Thus, the final system of equations is actually assembled by the software. One of the main advantage on the use of a Spice solver is that a lot of passive and active circuit component models are already implemented in the Spice software. Thus, the user can use them as *black box* components during the construction of the *net list*, which is a very attractive feature for some kind of applications.

As already stated, it is worth noting that system (3.47) derived from the A–PEEC method is not directly suitable to be written in MNA form. Indeed, the magnetic domains cannot be represented by means of the PEEC elementary circuit branch and thus they must be further handled [13]. Instead, the C–PEEC formulation proposed by the author offers the same circuit interpretation of both electric and magnetic domains by means of the traditional PEEC elementary circuit cell.

Different ways to construct the *net list* from the equivalent PEEC circuit are shown in [89] and [18]. However, as very clearly stated in these papers, with the current computing power the use of a MNA Spice–like solver for solving the final electromagnetic–circuit problem is actually feasible only when the discretized objects are represented with a small number of equivalent electric branches (a few hundred). Indeed, the equivalent circuit components obtained from the PEEC discretization are fully mutually coupled. Thus, with the increase of the number of mesh elements the sparsity ratio of (3.47) and (3.68) decreases and the efficiency on the use of sparse solvers is drastically reduced. Moreover, with most of the Spice solvers a very limited number

of mutual connections between the lumped components is allowed. Furthermore, when a lot of mutual connections are considered, the *net list* itself would require a considerable amount of disk space and computational time for file reading.

Finally, it is worth noting that when Spice–like solvers are considered both frequency and time domains simulations can be performed by using the same equivalent circuit (i.e. the same *net list*). However, when the dynamic Green's function is adopted (i.e. retarded effects are considered) time domain analysis cannot be studied with traditional Spice software. Indeed, as widely presented in Chapter 6, Marching On–in–Time (MOT) scheme should be applied to the PEEC method in order to perform transient simulations considering the time delay effects in the propagation of the electromagnetic fields.

4.2.2 Direct and iterative solvers for dense PEEC matrices

With the massive increase of the computing power and available RAM for the standard workstations, the interest in performing increasingly complex and computationally expensive electromagnetic simulations has grown up. For the applications where the air meshing is computational expensive, integral equation methods are usually preferable to the Finite Element Method. The PEEC method offers all the advantages of integral equation methods together with a useful circuit interpretation of the electromagnetic problem. Thus, when complex electromagnetic devices are coupled with lumped circuit components, the PEEC method is competitive.

As discussed in Section 4.2.1, when the meshing of the electromagnetic devices requires a relative high number of equivalent circuit branches, it is convenient to consider the problem in the context of electromagnetic fields, rather than *electric circuits*. Thus, since MNA Spice–like solvers cannot be efficiently used for the solution of coupled electromagnetic–circuit PEEC problems, different solution strategies must be adopted.

As discussed in detail in Section 4.2.3, systems (3.47) and (3.68) show good numerical properties. Therefore, when the storage of the system matrix is not prohibitive in terms of memory consumption, (3.47) and (3.68) can be solved by means of an LU matrix decomposition. It is worth noting that, since the system of equations are symmetric (or they can be made symmetric), only the lower triangular L matrix of the LU decomposition must be evaluated. The *zgesv* routine of Intel®Math Kernel Library LAPACK can be adopted for an efficient solution of the final system of equations by means of the LU decomposition. However, since $\frac{2}{3}N^3$ floating–point operations ar required (where N is the matrix system dimension), it is convenient to operate on a system as small as possible. Therefore, when this solution strategy is adopted, the compact systems (4.9) and (4.16) are more desirable.

In recent years, the interest in using iterative solvers for the solution of the final PEEC system of equations has been increasing. Indeed, the final purpose is to provide a method which allows for an accurate approximation of the solution with a computational cost reasonably smaller than that one required by LU decomposition. However, good results can be obtained only when an appropriate preconditioner is adopted, which is currently a very sensitive issue. Interesting results and discussions have been presented in [6] (a PhD work carried out by a former PhD student in the G2Elab research group) where different preconditioning approaches have been investigated for different PEEC formulations. In the literature concerning Volume Integral Equation methods, the sparse *resistive* matrices are usually adopted as preconditioners [90, 91]. However, all these solutions are far from being general and more sophisticated preconditioning approaches

should be adopted [92]. For instance, incomplete–LU (ILU) preconditioning has been investigated in the literature in the context of scattering problems [93, 94]. Thus, the *preconditioning* topic still requires a lot of research and a completely general solution is probably not possible since the numerical nature of the final PEEC system is highly problem dependent.

Besides the problem of the computational cost required for the solution of the final system of equations, the storage of the matrix itself is a sensitive issue which must be considered. For all these reasons, in the context of this PhD thesis, the *preconditioning* topic has not been directly investigated. Instead, the application of low–rank approximation techniques to the PEEC method has been examined and the use of iterative solvers has been mainly considered in the context of low–rank approximations. Indeed, for problems of practical interest, low–rank approximation approaches are often mandatory. Thus, iterative solvers combined with appropriate *preconditioning* techniques would be actually useful only when combined with low–rank approximation methods. Some numerical experience are presented in Chapter 5.

Finally, the *preconditioning* topic is also affected by the conditioning number and the numerical properties of the final system. In the following sections, the numerical issues emerging during the solution of the final PEEC system are discussed and subsequently some techniques to avoid these numerical problems are presented.

4.2.3 Numerical issues

The literature concerning the numerical issues arising when integral equation methods are solved is very broad. In this section, the *round–off / breakdown in frequency* issue (which is probably the most important and basic issue) is considered and the author refers the interested readers to specific works for a more comprehensive discussion [95, 96, 97]. Moreover, another numerical issue caused by the material coefficients of the A– and C–PEEC formulations is first discussed.

These two numerical issues (i.e. breakdown in frequency and the one due to the material coefficients) are chosen for the discussion since they have been actually encountered during the PhD thesis.

Material coefficients of the A–PEEC and the C–PEEC methods

In the A–PEEC formulation, dielectric and magnetic media are differently considered. The resistance dielectric matrix, $\mathbf{R}_d$, depends on the coefficient

$$\rho_d = \frac{1}{i\omega\varepsilon_0(\varepsilon_r - 1)}, \tag{4.17}$$

whereas the constitutive magnetic matrix, $\mathbf{F}$, depends on

$$\alpha_m = \frac{\mu_0\mu_r}{\mu_r - 1}. \tag{4.18}$$

In the C–PEEC formulation, dielectric media are considered as in the A–PEEC formulation while the resistance magnetic matrix, $\mathbf{R}_m$, depends on

$$\rho_m = \frac{1}{i\omega\mu_0(\mu_r - 1)}. \tag{4.19}$$

The A–PEEC method, which is based on the amperian interpretation of the electromagnetic phenomena, suffers from a numerical issue when magnetic media with high permeability are actually involved. Indeed, when increasing the relative permeability, the coefficient α_m in (4.18) tends to μ_0 (i.e. $\alpha_m \to \mu_0$ with the increasing of μ_r). For instance, numerically speaking, the difference between $\mu_r = 100$ and $\mu_r = 1000$ is left to the last significant figures of α_m and this *numerical information* can be completely lost when floating–point arithmetic is used. Especially when matrix $\mathbf{F}$ is added to other integral matrices which (due to the integration of the Green's function) are affected by numerical approximations orders of magnitude grater than the last significant figures of α_m (most of all for the non–zero entries of $\mathbf{F}$ which correspond to the *self* and *close–mutual* coefficients of the integral matrices that are subject to the most significant approximations).

It is worth noting that a similar numerical issue may arise also when coefficients (4.17) and (4.19) are involved (i.e. when dielectric media are involved in the A–PEEC method or when dielectric and magnetic media are considered in the C–PEEC method). However, the numerical experiments during this PhD thesis showed that such issue is much less severe with respect the one due to coefficient (4.18).

C–PEEC method is usually preferable to the A–PEEC formulation also for this reason. Numerical test cases which show such numerical issues are reported in Section 4.3 and in Section 5.4 (in the context of low–rank approximation techniques).

Breakdown in frequency

When MNA Spice–Like solvers cannot be used, systems (4.9), for A–PEEC, and (4.16), for C–PEEC, are preferable for their smaller dimension. For the sake of simplicity, magnetic media are not considered in this discussion. Thus, under this assumption, (4.9) and (4.16) lead to the same matrix system:

$$[\mathbf{R}_e + i\omega\mathbf{L}_e^e + \frac{1}{i\omega}\tilde{\mathbf{G}}^a_{\Omega_e}\mathbf{P}_e\mathbf{D}^a_{\Omega_e}]\mathbf{j}_e = \tilde{\mathbf{e}}_0. \tag{4.20}$$

From a physical point of view, the three matrix terms at the left hand side of the equation are related to the *resistive*, *inductive*, and *capacitive* interactions. The inductive and the capacitive terms, in accordance with their physical interpretation, act differently with the varying of the frequency. In order to provide an useful interpretation of the different terms, one can state that the capacitive term $\frac{1}{i\omega}\tilde{\mathbf{G}}^a_{\Omega_e}\mathbf{P}_e\mathbf{D}^a_{\Omega_e}$ enforces the *divergence* of $\mathbf{j}_e$ while the inductive term $i\omega\mathbf{L}_e^e$ enforces the *curl* of $\mathbf{j}_e$.

When the frequency is low, due to the different dependence on ω, the magnitude of the capacitive term increases while the magnitude of the inductive term decreases. This different dependence on the frequency leads to the well–known *breakdown in frequency*. Indeed, in low frequency problems both the inductive and the capacitive terms act an important role. However, when (4.20) is assembled, the capacitive term is orders of magnitude larger than the inductive one. Thus, because of the use of floating point numbers, the *information* related to $i\omega\mathbf{L}_e^e$ can be completely lost when the inductive and the capacitive terms are summed together. When this occurs, the solution of (4.20) is completely inconsistent because of severe system ill–conditioning. This numerical issue can be related to the well defined *round–off* problem [98, 99] which arises when two very different numerical quantities are added together in floating–point arithmetic.

It is worth noting that with the increase of the frequency a similar problem may arise since the information related to the capacitive term can be canceled out by the increasing of the

inductive term. However, with the increasing of the frequency others predominant numerical issues may arise [100].

A naive approach to avoid this problem is to solve systems (3.47) or (3.68) instead (i.e. that ones with the scalar potentials as unknowns). Indeed, in this larger system the capacitive and the inductive effects are separated by keeping the scalar potentials as unknowns. Thus, the breakdown in frequency problem does not arise. However, other approaches can be adopted in order to avoid the breakdown in frequency while maintaining a small size of the final system. In the following section, these approaches are described.

4.2.4 Change of basis

In this section, different *change of basis* techniques are presented. As stated in the previous chapters, the final PEEC system of equations derived from the CM discretization of the A–PEEC and C–PEEC formulations correctly enforce the electromagnetic properties of the unknowns, but not in a numerically strong sense. Indeed, the final discretized equations are obtained from the full Maxwell's equations; therefore, all the electromagnetic effects are considered. However, due to the discretization scheme, some of the properties of the unknowns (e.g. the divergence of the currents) are imposed by the integral matrices, which are affected by unavoidable numerical approximations.

As already discussed in Section 3.3.1, the *numerically weak* imposition of the electromagnetic conservation properties usually does not affect the global quality of the solution, but it could be an issue when high accuracy is required or when the actual distribution of the electromagnetic fields is important. Moreover, when some specific property want to be enforced (e.g. div–free), it is possible to adopt a *change of basis* in order to strongly impose such property and also reduce the number of the unknowns, i.e. the dimension of the final system to be solved. Furthermore, the change of basis techniques can be adopted to avoid the problem of the breakdown in frequency.

In the following, the case of C–PEEC formulation is first considered. Then, the case of magnetic media for the A–PEEC formulation is discussed.

C–PEEC

From a mathematical point of view, *conductive* and *dielectric* media have been considered together during the discretization of the formulations under the definition of *electric* media. However, the conduction and the polarization currents, from the physical point of view, show different behaviors. Concerning conductive media, the following cases can be considered:

1. for low frequency problems and when capacitive effects are completely neglected, the conduction current $\mathbf{J}_c$ can be considered divergence free and with zero normal component on Γ_c: $\nabla \cdot \mathbf{J}_c = 0$ and $\mathbf{J}_c \cdot \mathbf{n} = 0$;

2. for high frequency problems the effect of the boundary electric charges can be considered whereas the volume charge are neglected, thus the conduction current $\mathbf{J}_c$ can be considered divergence free in Ω_c but with a non–zero normal component on Γ_c: $\nabla \cdot \mathbf{J}_c = 0$ and $\mathbf{J}_c \cdot \mathbf{n} \neq 0$;

3. both the volume and surface charges are considered to be possible non–vanishing quantities, thus $\nabla \cdot \mathbf{J}_c \neq 0$ and $\mathbf{J}_c \cdot \mathbf{n} \neq 0$.

For the case of dielectric media, the following cases are considered instead

1. for homogeneous media, the polarization current $\mathbf{J}_p$ is always divergence free in Ω_d (bound volume electric charges are null) whereas the normal component of $\mathbf{J}_p$ on Γ_d is generally different from zero (bound surface electric charges are not null): $\nabla \cdot \mathbf{J}_d = 0$ and $\mathbf{J}_d \cdot \mathbf{n} \neq 0$;

2. both the volume and surface charges are considered to be possible non–vanishing quantities (which is the case of inhomogeneous media with smoothly varying permittivity), thus $\nabla \cdot \mathbf{J}_p \neq 0$ and $\mathbf{J}_d \cdot \mathbf{n} \neq 0$.

Dielectric and magnetic media are considered with a unified approach in the C–PEEC method, thus, completely equivalent considerations hold for $\mathbf{J}_m$.

For the sake of simplicity, in the following the discussion is carried out considering the electric current density $\mathbf{j}_e$ and no distinction is made between conductive and dielectric media. Indeed, even if the physical reasons are different, conductive and dielectric media can be treated equivalently. Moreover, a completely equivalent discussion can be done for the magnetic media.

It is worth noting that the same considerations can be provided when the total div–free electric and magnetic currents are chosen as unknowns. These currents indeed always satisfy: $\nabla \cdot \mathbf{J}_e^{tot} = 0$, $\mathbf{J}_e^{tot} \cdot \mathbf{n} \neq 0$ (and $\nabla \cdot \mathbf{J}_m^{tot} = 0$, $\mathbf{J}_m^{tot} \cdot \mathbf{n} \neq 0$). Thus, when the C–PEEC method based on the discretization presented at the end of Section 3.3.2 is adopted, those properties can be strongly imposed as discussed in the following.

When the divergence free conditions want to be strongly imposed on $\mathbf{J}_e$, two main possibilities are considered:

(i) A first possibility to enforce $\nabla \cdot \mathbf{J}_e = 0$ and $\mathbf{J}_e \cdot \mathbf{n} \neq 0$ is to impose $\mathbf{J}_e = \nabla \times \mathbf{T}_c$, where $\mathbf{T}_e$ is an electric vector potential in Ω_e. In matrix form, by means of the Cell Method, this condition is given by

$$\mathbf{j}_e = \mathbf{C}_{\Omega_e} \mathbf{t}_e, \tag{4.21}$$

where $\mathbf{t}_e = (t_{e_k})$ are the array of DoFs related to $\mathbf{T}_e$, i.e. $t_{e_k} = \int_{e_e} \mathbf{T}_e \cdot d\mathbf{l}$. Anyhow, to guarantee the uniqueness of $\mathbf{T}_e$, a gauge should be introduced. Different ways to impose this gauge can be adopted [101]. One of the most common technique is the *Tree–Cotree Gauging* described in [102]. First, the tree edges e_e^{tree} of the graph made up by the edges $e_e \in \mathcal{G}_{\Omega_e}$ are defined. Then, matrix $\mathbf{C}_{\Omega_e}^{red}$ is defined as a reduced matrix $\mathbf{C}_{\Omega_e}$ where the columns related to the tree edges have been deleted. Thus, $\mathbf{J}_e = \nabla \times \mathbf{T}_e$ is now given by

$$\mathbf{j}_e = \mathbf{C}_{\Omega_e}^{red} \mathbf{t}_e^{cotree}, \tag{4.22}$$

whereas $\mathbf{t}_e^{tree}$ is automatically set to zero imposing a gauge on $\mathbf{T}_e$. In order to impose $\mathbf{J}_e \cdot \mathbf{n} = 0$ together with $\nabla \cdot \mathbf{J}_e = 0$, the tree–cotree decomposition must be performed building the tree in such a way that each cotree edge on Γ_e forms an independent loop consisting of tree edges still located on Γ_e only. Then, also the cotree boundary edges are eliminated from $\mathbf{C}_{\Omega_e}^{red}$ leading to the *new* reduced matrix $\mathbf{C}_{\Omega_e}^{red^*}$. Thus, $\nabla \cdot \mathbf{J}_e = 0$ and $\mathbf{J}_e \cdot \mathbf{n} = 0$ is now given by

$$\mathbf{j}_e = \mathbf{C}_{\Omega_e}^{red^*} \mathbf{t}_e^{cotree^*}. \tag{4.23}$$

This procedure is computationally simple. However, it is not valid when Ω_e is a non–simply connected region, unless some extra equations are added to the system [103].

(ii) Another procedure based on the *basis reduction scheme* can be instead used. This procedure is widely discussed in [104], where also a comparison with method (i) is presented. Following this idea, a tree–cotree decomposition is first applied to the dual graph consisting on dual edges $\tilde{e}_e \in \tilde{\mathcal{G}}_e$ (i.e. the circuit branches crossed by the currents $\mathbf{j}_e$ in a one–to–one relation with the primal faces of the mesh f_e). So, $\mathbf{j}_e$ can be subdivided into $\mathbf{j}_e = [\mathbf{j}_e^{tree}; \mathbf{j}_e^{cotree}]$. Now, in order to impose $\mathbf{D}_{\Omega_e}\mathbf{j}_e = \mathbf{0}$ (i.e. $\nabla \cdot \mathbf{J}_e = 0$), a relation between $\mathbf{j}_e$ and $\mathbf{j}_e^{cotree}$ must be obtained such that

$$\mathbf{j}_e = \begin{bmatrix} \mathbf{j}_e^{tree} \\ \mathbf{j}_e^{cotree} \end{bmatrix} = \begin{bmatrix} \mathbf{V} \\ \mathbf{1} \end{bmatrix} \mathbf{j}_e^{cotree} = \mathbf{M}^{\circ}\mathbf{j}_e^{cotree}. \tag{4.24}$$

In [104], a depth–first method to construct the proper $\mathbf{V}$ is suggested. An efficient alternative method (which can be derived by following [105]) for obtaining $\mathbf{V}$ is by computing the *reduced row echelon form* (RREF) of matrix $\mathbf{D}^*_{\Omega_e}$, where

$$\mathbf{D}^*_{\Omega_e} = [\mathbf{D}^{cotree}_{\Omega_e}, \mathbf{D}^{tree}_{\Omega_e}]$$

is a reordered $\mathbf{D}_{\Omega_e}$ matrix where the columns that multiply $\mathbf{j}_e^{tree}$ are positioned as first and the ones that multiply $\mathbf{j}_e^{cotree}$ as last. Since $\mathbf{D}^*_{\Omega_e}$ is very sparse and it consists of 0, 1, and -1 entries, its RREF can be evaluated by performing a QR decomposition, leading to a very efficient algorithm (a fast MATLAB® algorithm for that can be found in [106]). Finally, since

$$\mathrm{RREF}(\mathbf{D}^*_{\Omega_e}) = [\mathbf{1}, -\mathbf{V}],$$

the change of basis matrix $\mathbf{M}^{\circ}$ is easily obtained and the condition $\nabla \cdot \mathbf{J}_e = 0$ and $\mathbf{J}_e \cdot \mathbf{n} \neq 0$ is given by imposing $\mathbf{j}_e = \mathbf{M}^{\circ}\mathbf{j}_e^{cotree}$. It is worth noting that this procedure is similar to the one proposed in [107] where a set of independent loop current is selected as *new* unknowns. Indeed, from a symbolic point of view, in (4.24) $\mathbf{j}_e^{cotree}$ can be substituted with $\mathbf{j}_e^{\circ}$, where $j_{e_k}^{\circ}$ is the kth loop current defined by the $+1$ and -1 coefficients of the kth column of $\mathbf{M}^{\circ}$. The condition $\mathbf{J}_e \cdot \mathbf{n} = 0$ is simply imposed by neglecting the presence of the boundary faces from the equivalent graph. Instead, the *global surface neutrality* condition

$$\int_{\Gamma_e} \mathbf{J}_e \cdot \mathbf{n} d\Gamma = 0, \tag{4.25}$$

can be naturally imposed by considering the exterior region as a node of the graph in which all the (dual) branches related to the boundary faces converge. This procedure holds for both simply and non–simply connected domains.

Finally, with the aim of reducing the non–zero entries of $\mathbf{M}^{\circ}$ (which is useful for reducing the memory allocation and for the application of low–rank approximation, see Section 5.3) it is useful to perform a reordering of the unknowns before the tree–cotree decomposition. Indeed, with the aim of reducing the incidences between fundamental cut–sets and the cotree edges, the faces of the mesh should be reordered by using the nested dissection algorithm implemented in METIS libraries [108]. Then, the tree–cotree decomposition is performed by selecting all the edges of the graph (faces of the mesh) following the reordered order and, when possible, add them to the tree of the graph. Then, the construction of $\mathbf{M}^{\circ}$ proceeds from equation (4.24). In Fig. 4.1, matrix $\mathrm{RREF}(\mathbf{D}^*_{\Omega_e})^T$ obtained with and

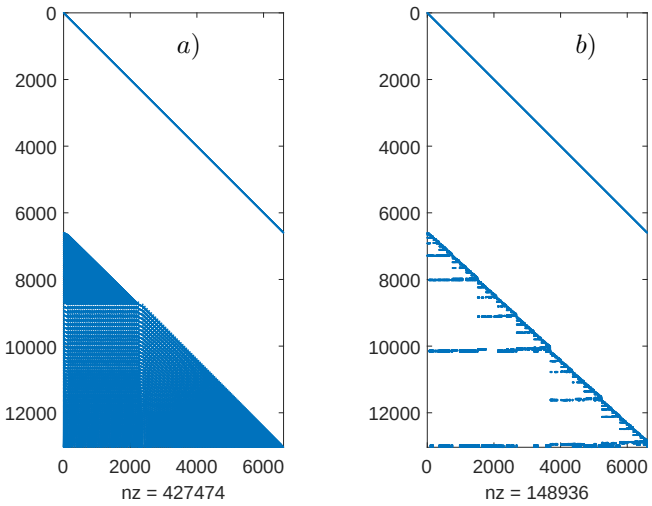

Figure 4.1: RREF$(\mathbf{D}^{*}_{\Omega_e})^T$ obtained without (a) and with (b) the reordering technique.

without the use of this technique are shown.

As discussed in [6], method (i) can be considered as a particular case of method (ii) where the *independent loop currents* are the smallest possible loops (the ones flowing around the edges of the mesh, i.e. minimum support fundamental loops). Thus, in the following $\mathbf{M}^{\circ}$ is only considered and $\mathbf{C}^{red^{*}}_{\Omega_e}$ is considered as a particular case of $\mathbf{M}^{\circ}$.

The above discussion is adopted to strongly impose the div-free condition on the current unknowns. However, the proposed methods can be also used to apply a *discrete quasi–Helmholtz decomposition* of $\mathbf{j}_e$ [109], i.e. to separate the div–free and not div–free components of $\mathbf{j}_e$. Indeed, this topic which refers to the *Loop–Star* and *Loop–Tree* quasi–Helmholtz decomposition, has been historically introduced to solve the breakdown in frequency related to the EFIE equation [110, 111]. In the following, this topic is only marginally discussed and the author refers interested readers to more specific and exhaustive works in the literature [97].

The electric current density $\mathbf{j}_e$ (or equivalently $\tilde{\mathbf{j}}_m$) can be decomposed as

$$\mathbf{j}_e = \mathbf{M}^{\circ}\mathbf{j}^{\circ}_e + \mathbf{M}^{\star}\mathbf{j}^{\star}_e, \tag{4.26}$$

where $\mathbf{M}^{\circ}$ is the *loop* matrix and $\mathbf{j}^{\circ}_e$ is the array of the independent currents defined above. The vector array $\mathbf{j}^{\star}_e$ stores the *star currents* and $\mathbf{M}^{\star}$ is the the *star* matrix. The kth star current $j^{\star}_{e_k}$ is instead defined as a linear combination of $\mathbf{j}_c$, where the $+1$ and -1 coefficients of the kth column of $\mathbf{M}^{\star}$ define the coefficient of that linear combination.

Matrices $\mathbf{M}^{\circ}$ and $\mathbf{M}^{\star}$ must satisfy

$$\mathbf{M}^{\star T}\mathbf{M}^{\circ} = \mathbf{0}. \tag{4.27}$$

Thus, from (4.27) and from the properties of the Cell Method incidence matrices, a possible choice for $\mathbf{M}^{\star}$ is

$$\mathbf{M}^{\star} = \mathbf{D}^{red\ T}_{\Omega_e}, \tag{4.28}$$

where $\mathbf{D}^{red}_{\Omega_e}$ is the $\mathbf{D}_{\Omega_e}$ matrix without one row for each sub–domain Ω_{e_k}.

When (4.26) is applied, the capacitive effects are ruled by the term $\mathbf{M}^\star \mathbf{j}_e^\star$. The inductive effects instead are mainly produced by $\mathbf{M}^\circ \mathbf{j}_e^\circ$. Indeed, since (4.26) is a *quasi*–Helmholtz decomposition, inductive effects are also produced by $\mathbf{M}^\star \mathbf{j}_e^\star$.

The square *change of basis* matrix

$$\mathbf{Q}_e = [\mathbf{M}^\circ, \mathbf{M}^\star], \tag{4.29}$$

can now be applied to the system (4.20) where, for the sake of simplicity, only electric media are considered. Thus, applying (4.26) and using $\mathbf{Q}_e^T$ as a projection matrix, system (4.20) becomes

$$\begin{bmatrix} \mathbf{M}^{\circ T}[\mathbf{R}_e + i\omega \mathbf{L}_e^e]\mathbf{M}^\circ & \mathbf{M}^{\circ T}[\mathbf{R}_e + i\omega \mathbf{L}_e^e]\mathbf{M}^\star \\ \mathbf{M}^{\star T}[\mathbf{R}_e + i\omega \mathbf{L}_e^e]\mathbf{M}^\circ & \mathbf{M}^{\star T}[\mathbf{R}_e + i\omega \mathbf{L}_e^e + \frac{1}{i\omega}\tilde{\mathbf{G}}^a_{\Omega_e}\mathbf{P}_e\mathbf{D}^a_{\Omega_e}]\mathbf{M}^\star \end{bmatrix} \begin{bmatrix} \mathbf{j}_e^\circ \\ \mathbf{j}_e^\star \end{bmatrix} = \begin{bmatrix} \mathbf{M}^{\circ T}\tilde{\mathbf{e}}_0 \\ \mathbf{M}^{\star T}\tilde{\mathbf{e}}_0 \end{bmatrix}. \tag{4.30}$$

In the system above, the capacitive term is only present in the matrix block $(2,2)$. Indeed, due to the properties (4.27) and (4.28), the capacitive term vanishing in all the other matrix blocks.

One can notice that in the matrix block $(2,2)$ of (4.30), we still have two terms which shows opposite behavior with the frequency. However, the term $\mathbf{M}^\star[i\omega \mathbf{L}_e^e]\mathbf{M}^\star$ is much less significant compared to $\mathbf{M}^\star[\frac{1}{i\omega}\tilde{\mathbf{G}}^a_{\Omega_e}\mathbf{P}_e\mathbf{D}^a_{\Omega_e}]\mathbf{M}^\star$ and, when the frequency is low, it can be also completely removed (indeed, it models the *negligible* inductive effects due to the star unknowns).

Finally, by scaling the second row of (4.30) for $\omega^2\mu_0\varepsilon_0$, the breakdown in frequency issue can be removed and (with a further scaling of the polarization currents) the problem can be solved till $\omega = 0$.

Obviously, a completely equivalent procedure can be applied when magnetic media are considered. Thus, thanks to this change of basis technique, a system of the same dimension of (4.16) (much smaller than (4.11) where the scalar potentials are kept as unknowns) can be adopted also for the study of low frequency electromagnetic problems avoiding the breakdown in frequency issue.

When for some physical reason the divergence free condition $\nabla \cdot \mathbf{J}_e = 0$ and $\mathbf{J}_e \cdot \mathbf{n} = 0$ have to be enforced, the star matrix $\mathbf{M}^\star$ and the star unknowns $\mathbf{j}_e^\star$ are not needed anymore. Thus, the system to be solved becomes

$$\mathbf{M}^{\circ T}[\mathbf{R}_e + i\omega \mathbf{L}_e^e]\mathbf{M}^\circ \mathbf{j}_e^\circ = \mathbf{M}^{\circ T}\tilde{\mathbf{e}}_0. \tag{4.31}$$

It is worth noting that the equation above could have been directly derived from the formulation of Chapter 2 by assuming the quasi–static assumption. Indeed, in (4.31), the effects of displacement currents is not taken into account.

The dimension of the system (4.31) is $\big(f_e - (v_e - N_e)\big) \times \big(f_e - (v_e - N_e)\big)$, where N_e is the number of disconnected electric domains $\Omega_e = \Omega_{e_1} \sqcup \Omega_{e_2} \sqcup \cdots \sqcup \Omega_{e_{N_e}}$. Thus, when the property $\nabla \cdot \mathbf{J}_e = 0$ and $\mathbf{J}_e \cdot \mathbf{n} = 0$ holds, it is convenient to solve (4.31) instead of (4.20) which has a larger dimension.

When for some physical reason the condition $\nabla \cdot \mathbf{J}_e = 0$ and $\mathbf{J}_e \cdot \mathbf{n} \neq 0$ have to be instead enforced, a proper $\mathbf{M}^\circ$ matrix (e.g. $\mathbf{M}^\circ = \mathbf{C}^{red}_{\Omega_e}$) can be directly adopted as a change of basis of

(4.20). Thus, the following system holds

$$\mathbf{M}^{\circ T}[\mathbf{R}_e + i\omega\mathbf{L}_e^e + \frac{1}{i\omega}\tilde{\mathbf{G}}^a_{\Omega_e}\mathbf{P}_e\mathbf{D}^a_{\Omega_e}]\mathbf{M}^{\circ}\mathbf{j}_e^{\circ} = \mathbf{M}^{\circ T}\tilde{\mathbf{e}}_0. \tag{4.32}$$

However, since $\mathbf{C}^{redT}_{\Omega_e}\tilde{\mathbf{G}}_{\Omega_e} = \mathbf{0}$ and $\mathbf{D}_{\Omega_e}\mathbf{C}^{red}_{\Omega_e} = \mathbf{0}$, (4.32) becomes

$$\mathbf{M}^{\circ T}[\mathbf{R}_e + i\omega\mathbf{L}_e^e + \frac{1}{i\omega}\tilde{\mathbf{G}}_{\Gamma_e}\mathbf{P}_e^{ss}\mathbf{D}_{\Gamma_e}]\mathbf{M}^{\circ}\mathbf{j}_e^{\circ} = \mathbf{M}^{\circ T}\tilde{\mathbf{e}}_0. \tag{4.33}$$

Indeed, when $\nabla\cdot\mathbf{J}_e = 0$ the volume charge density is zero, thus only the surface potential matrix is needed.

System (4.33) may suffer of the breakdown in frequency issue. However, only the currents related to the boundary faces contribute to the capacitive effects. Thus, that unknowns can be separated from the others and properly scaled. Thus, the breakdown in frequency can be avoided also when (4.33) is adopted.

Finally, for the sake of completeness, when an electrostatic problem is considered, the loop currents vanishing. Indeed, no electric conduction or polarization current flows and only free or bound electric charges are present. This problem is represented by

$$\mathbf{M}^{\star T}[\mathbf{R}_{e0} + \tilde{\mathbf{G}}^a_{\Omega_e}\mathbf{P}_e\mathbf{D}^a_{\Omega_e}]\mathbf{M}^{\star}\mathbf{p}_e^{\star} = \mathbf{M}^{\star T}\tilde{\mathbf{e}}_0, \tag{4.34}$$

where $\mathbf{R}_{e0}$ is equal to $\mathbf{R}_{d0}$ in (4.6) for the case of dielectric media and $\mathbf{R}_{e0}$ is equal to the null matrix for the case of conductive media. The array $\mathbf{p}_e^{\star}$ of *star* electric polarization fluxes obtained from (4.34) then provides $\mathbf{p}_e = \mathbf{M}^{\star}\mathbf{p}_e^{\star}$ and $\mathbf{q}_e = \mathbf{D}^a_{\Omega_e}\mathbf{p}_e$.

When a change of basis is applied (e.g. (4.30)), the resistance, inductance, and potential matrices are evaluated. Then, the change of basis matrices are applied and matrix–matrix products must be carried out. The change of basis matrices are in general very sparse, however the matrix–matrix products may still require a considerable computational effort. Furthermore, both the *old* and the *new* matrices must be stored for a given time. Alternatively, the system of equations can be directly assembled in the form (4.30). This is equivalent to use different basis functions for the expansion of $\mathbf{J}_e$, i.e.

$$\mathbf{J}_e(\mathbf{r}) = \sum_{k=1}^{N_\circ}\mathbf{w}_k^{\circ}(\mathbf{r})j_{e_k}^{\circ} + \sum_{k=1}^{N_\star}\mathbf{w}_k^{\star}(\mathbf{r})j_{e_k}^{\star}, \tag{4.35}$$

where $N_\circ$ is the number of loop basis function and $N_\star$ is the number of the star basis functions. The kth loop basis function $\mathbf{w}_k^{\circ}$ and the kth star basis function $\mathbf{w}_k^{\star}$ are obtained as a linear combination of $\mathbf{w}_k^f$, i.e. (in MATLAB® notation)

$$\mathbf{w}_k^{\circ} = \mathbf{M}^{\circ}(:,k)\mathbf{w}_k^f, \qquad \mathbf{w}_k^{\star} = \mathbf{M}^{\star}(:,k)\mathbf{w}_k^f. \tag{4.36}$$

For instance, when $\mathbf{M}^{\circ} = \mathbf{C}_{\Omega_c}$, $\mathbf{w}_k^{\circ}$ becomes the *curl–edge* basis function related to the kth edge of the mesh.

Thus, (4.30) can be alternatively written as

$$\begin{bmatrix}\mathbf{R}_e^{\circ\circ} + i\omega\mathbf{L}_e^{e,\circ\circ} & \mathbf{R}_e^{\circ\star} + i\omega\mathbf{L}_e^{e,\circ\star} \\ \mathbf{R}_e^{\star\circ} + i\omega\mathbf{L}_e^{e,\star\circ} & \mathbf{R}_e^{\star\star} + i\omega\mathbf{L}_e^{e,\star\star} + \frac{1}{i\omega}\mathbf{\Sigma}^T_{\Omega_e}\mathbf{P}_e\mathbf{\Sigma}_{\Omega_e}\end{bmatrix}\begin{bmatrix}\mathbf{j}_e^{\circ} \\ \mathbf{j}_e^{\star}\end{bmatrix} = \begin{bmatrix}\mathbf{M}^{\circ T}\tilde{\mathbf{e}}_0 \\ \mathbf{M}^{\star T}\tilde{\mathbf{e}}_0\end{bmatrix}. \tag{4.37}$$

where $\mathbf{\Sigma}_{\Omega_e} = \mathbf{D}^a_{\Omega_e}\mathbf{M}^\star$, the *loop–star* resistance matrices are given by

$$R^{\circ\circ}_{e_{uk}} = \int_{\Omega_e} \rho_e(\mathbf{r})\mathbf{w}^\circ_u(\mathbf{r}) \cdot \mathbf{w}^\circ_k(\mathbf{r})d\Omega, \qquad R^{\star\star}_{e_{uk}} = \int_{\Omega_e} \rho_e(\mathbf{r})\mathbf{w}^\star_u(\mathbf{r}) \cdot \mathbf{w}^\star_k(\mathbf{r})d\Omega,$$
$$R^{\circ\star}_{e_{uk}} = R^{\star\circ}_{e_{ku}} = \int_{\Omega_e} \rho_e(\mathbf{r})\mathbf{w}^\circ_u(\mathbf{r}) \cdot \mathbf{w}^\star_k(\mathbf{r})d\Omega, \tag{4.38}$$

and the *loop-star* inductance matrices are given by

$$\begin{aligned} L^{e,\circ\circ}_{uk} &= \mu_0 \int_\Omega \mathbf{w}^\circ_u(\mathbf{r}) \cdot \int_\Omega \mathbf{w}^\circ_k(\mathbf{r}')g(\mathbf{r},\mathbf{r}')d\Omega' d\Omega, \\ L^{e,\star\star}_{uk} &= \mu_0 \int_\Omega \mathbf{w}^\star_u(\mathbf{r}) \cdot \int_\Omega \mathbf{w}^\star_k(\mathbf{r}')g(\mathbf{r},\mathbf{r}')d\Omega' d\Omega, \\ L^{e,\circ\star}_{uk} = L^{e,\star\circ}_{ku} &= \mu_0 \int_\Omega \mathbf{w}^\circ_u(\mathbf{r}) \cdot \int_\Omega \mathbf{w}^\star_k(\mathbf{r}')g(\mathbf{r},\mathbf{r}')d\Omega' d\Omega. \end{aligned} \tag{4.39}$$

It is worth noting that when $\mathbf{w}^\circ_k$ has a *limited* support (e.g. when $\mathbf{M}^\circ = \mathbf{C}_{\Omega_c}$) the coefficients of the *loop–star* inductance coefficients can be evaluated without an excessive computational effort. Instead, when longer independent loops are adopted (i.e. when the sparsity ratio of $\mathbf{M}^\circ$ decreases), the support of $\mathbf{w}^\circ_k$ can be considerably large and the computational cost required for the evaluation of the inductance coefficients grows.

Some considerations can now be done for the case of the C–PEEC method with div–free total currents. When this method is adopted, the unknown currents always satisfy $\nabla \cdot \mathbf{J}^{tot}_e = 0$ while in general $\mathbf{J}^{tot}_e \cdot \mathbf{n} \neq 0$ (the same for $\mathbf{J}^{tot}_m$). Thus, the above discussion still holds and the loop matrix $\mathbf{M}^\circ$ can be applied as a change of basis and projection matrix in order to strongly impose the div–free condition of $\mathbf{J}^{tot}_e$ and $\mathbf{J}^{tot}_m$ as shown in [27] by the author.

Finally,it should be also noted that the change of basis procedure (complemented by an appropriate scaling) allows for improving the condition number of the system to be solved and they can be combined with *ad–hoc* preconditioning techniques [112].

A–PEEC

When the A–PEEC method is applied, electric media can be handled as shown in the previous section. In the case of magnetic media instead the final system must be treated in a different way.

In the A–PEEC method, the magnetization is introduced as unknown and it is expanded by means of edge shape functions. Thus, whereas for the C–PEEC method the divergence of the currents is investigated, for the A–PEEC the curl of the magnetization must be considered.

From the Maxwell's equations and from constitutive relationship for magnetic media the following relation can be derived:

$$\nabla \times \left(\frac{\mathbf{M}}{\mu_r - 1}\right) = \mathbf{J}_c + i\omega\mathbf{D}. \tag{4.40}$$

For a non–conductive and homogeneous magnetic media (4.40) becomes

$$\nabla \times \mathbf{M} = i\omega\varepsilon_0(\mu_r - 1)\mathbf{E}. \tag{4.41}$$

Thus, when the frequency is sufficiently small, $\mathbf{M}$ can be considered to be curl–free. More in general, as proposed by the author in [26], the magnetization can be decomposed as:

$$\mathbf{M} = \nabla\psi_m + i\omega\mathbf{P}_m, \tag{4.42}$$

where ψ_m is a magnetic potential defined in Ω_m and $\mathbf{P}_m$ is a magnetic polarization in Ω_m.

Thus, an equivalent decomposition can be introduced for the discrete form [26]:

$$\mathbf{m} = \mathbf{G}^{red}_{\Omega_m}\boldsymbol{\psi}_m + i\omega\mathbf{p}_m, \tag{4.43}$$

where $\mathbf{G}^{red}_{\Omega_m}$ is a $\mathbf{G}_{\Omega_m}$ without one column for each sub–domain Ω_{mk}, $\boldsymbol{\psi}_m = (\psi_{m_k})$ is defined for each node n_m of the mesh (except one for each sub–domain Ω_{mk} considered as reference potential) and $\mathbf{p}_m$ is defined for each edge of the mesh.

Then, unlike what has been proposed in [26], the discrete decomposition (4.43) can be further developed and it can be made a complete *discrete* Helmholtz decomposition (i.e. imposing the dive–free property of $\mathbf{p}_m$) by imposing

$$\mathbf{p}_m = \mathbf{C}^{red\ T}_{\Omega_m}\mathbf{d}_m, \tag{4.44}$$

where a $\mathbf{C}^{red}_{\Omega_m}$ is a $\mathbf{C}_{\Omega_m}$ matrix without a set of faces related to a (dual) tree. Indeed, as for the loop–star decomposition, $\mathbf{C}^{red\ T}_{\Omega_m}$ and $\mathbf{G}^{red}_{\Omega_m}$ satisfy

$$(\mathbf{C}^{red\ T}_{\Omega_m})^T\mathbf{G}^{red}_{\Omega_m} = \mathbf{0}. \tag{4.45}$$

Then, the change of basis

$$\mathbf{m} = [\mathbf{G}^{red}, i\omega\mathbf{C}^{red\ T}]\begin{bmatrix}\boldsymbol{\psi}_m\\ \mathbf{d}_m\end{bmatrix} = \mathbf{Q}^A_m\begin{bmatrix}\boldsymbol{\psi}_m\\ \mathbf{d}_m\end{bmatrix}, \tag{4.46}$$

can be applied to (4.7) (or to any system where $\mathbf{m}$ is considered as unknown) and $\mathbf{Q}^{A,T}_m$ is adopted as projection matrix for the magnetic A–PEEC discrete equation.

When only magnetic media are considered, the discrete magnetic equation of the A–PEEC method (reported here for the sake of clarity):

$$[\mathbf{F} - \tilde{\mathbf{C}}^a_{\Omega_m}\mathbf{L}^a_m\mathbf{C}^a_{\Omega_m}]\mathbf{m} = \tilde{\mathbf{b}}_0, \tag{4.47}$$

does not suffer from the breakdown in frequency issue. Thus, the problem can be solved without adopting the change of basis presented above. However, as already stated in the previous chapter, when (4.7) is solved, the property of the unknowns are imposed, but not in a numerically strong sense. For instance, when the frequency is low the volume amperian currents vanish, i.e. $\nabla\times\mathbf{M}\approx 0$. However, this condition is not strongly satisfied by (4.47) and an inaccurate distribution of $\mathbf{M}$ is obtained. Applying the change of basis (4.46), the property of $\mathbf{M}$ can be instead strongly imposed. Moreover, it is worth noting that when the frequency is zero (or close to zero) $\mathbf{Q}^A_m$ can be chosen as $\mathbf{Q}^A_m = \mathbf{G}^{red}_{\Omega_m}$. In this way the dimension of the system to be solved is also decreased.

4.3 Case studies and numerical examples

In this section, academic and industrial numerical test cases are considered. These studies allow for comparisons between the A– and C–PEEC formulations. Moreover, the change of basis solution strategies are shown. The numerical cases reported in this section have been obtained without using low–rank approximation techniques and the MATLAB® *backslash* has been adopted to solve the system of equations. Thus, a LU decomposition has been adopted resulting in a considerable computational cost for simulating industrial cases. However, other numerical results obtained by using low–rank compression techniques are presented in Section 5.4 where computational costs are drastically reduced.

It is worth noting that most of the presented test cases are low frequency/medium frequency problems and retardation effects have been rarely considered. Indeed, considering the framework of the group of research of the University of Padova and Grenoble, the industrial applications considered during the PhD thesis have been mostly related to this range of frequency (i.e. when both inductive and capacitive effects must be considered and retardation effects can be neglected). Nonetheless, the developed codes and the proposed methods can be also used for the study of high frequency problems. However, it is worth noting that when retardation effects are considered, the computation of the dense matrix coefficients is generally more complicated with respect to the not–retarded case. Moreover, generally speaking, with the increase of the frequency a finer mesh should be used, thus leading to a increase of the memory requirement.

Several 3–D, 2–D, and 1–D codes based on the A–PEEC and C–PEEC have been developed during the PhD thesis. MATLAB® has been used for the system assembly and data handling, while MEX–FORTRAN functions combined with OpenMP libraries have been adopted for the computation of the matrix coefficients and post–processing. Both tetrahedral and hexahedral elements can be adopted for the mesh discretization of 3–D objects and both triangular and quadrilateral elements can be adopted for the mesh discretization of equivalent 2–D models. Thin wires can also be used for the discretization of equivalent 1–D models. Furthermore, both external electromagnetic fields and lumped elements can be considered for the problem excitation. The codes have been validated on several benchmarks including the cases shown here.

4.3.1 Academic cases

Breakdown in frequency and loop–star decomposition With the aim of showing the effects of the breakdown in frequency issue, the simple case of a 1 m × 1 m square conductive plate with thickness 0.025 m is here considered. The plate in centered at the origin of the x–y plane and it is excited by a uniform magnetic flux field directed in the z direction, i.e. $\mathbf{B}_{ext} = \mathbf{u}_z$, $\mathbf{H}_{ext} = \frac{1}{\mu_0}\mathbf{u}_z$, $\mathbf{E}_{ext} = \frac{1}{2}i\omega y\mathbf{u}_x - \frac{1}{2}i\omega x\mathbf{u}_y$. The conductivity of the plate is $57 \cdot 10^6$ S/m and the frequency of the problem is $f = 10$ Hz. The PEEC model of the plate consists of 841 quadrilateral elements (i.e. the equivalent surface model described in Section 3.4.1 is adopted).

The problem is solved by using four different solution strategies (for the sake of clarity, the 4 system of equations actually solved are also reported):

1. the direct solution of (4.16) (which is equivalent to (4.7) since magnetic media are not considered) without any change of basis:

$$\left[\mathbf{R}_e + i\omega\mathbf{L}_e^e + \tfrac{1}{i\omega}\tilde{\mathbf{G}}^a_{\Omega_e}\mathbf{P}_e\mathbf{D}^a_{\Omega_e}\right]\left[\mathbf{j}_e\right] = \left[\tilde{\mathbf{e}}_0\right], \tag{4.48}$$

2. the application of the loop–star change of basis discussed in Section 4.2.4, i.e. $\mathbf{j}_e = \mathbf{M}^{\circ}\mathbf{j}_e^{\circ} + \mathbf{M}^{\star}\mathbf{j}_e^{\star}$:

$$\begin{bmatrix} \mathbf{M}^{\circ T}[\mathbf{R}_e + i\omega\mathbf{L}_e^e]\mathbf{M}^{\circ} & \mathbf{M}^{\circ T}[\mathbf{R}_e + i\omega\mathbf{L}_e^e]\mathbf{M}^{\star}\tau \\ \tau\mathbf{M}^{\star T}[\mathbf{R}_e + i\omega\mathbf{L}_e^e]\mathbf{M}^{\circ} & \tau\mathbf{M}^{\star T}[\mathbf{R}_e + i\omega\mathbf{L}_e^e + \frac{1}{i\omega}\tilde{\mathbf{G}}^a_{\Omega_e}\mathbf{P}_e\mathbf{D}^a_{\Omega_e}]\mathbf{M}^{\star}\tau \end{bmatrix} \begin{bmatrix} \mathbf{j}_e^{\circ} \\ \mathbf{j}_e^{\star} \end{bmatrix} = \begin{bmatrix} \mathbf{M}^{\circ T}\tilde{\mathbf{e}}_0 \\ \tau\mathbf{M}^{\star T}\tilde{\mathbf{e}}_0 \end{bmatrix}, \tag{4.49}$$

   where τ is the scaling factor $\tau = \omega\sqrt{\mu_0\varepsilon_0}$,

3. the application of the loop change of basis (star unknowns are set to zero), i.e. $\mathbf{j}_e = \mathbf{M}^{\circ}\mathbf{j}_e^{\circ}$:

$$\left[\mathbf{M}^{\circ T}[\mathbf{R}_e + i\omega\mathbf{L}_e^e]\mathbf{M}^{\circ}\right]\left[\mathbf{j}_e^{\circ}\right] = \left[\mathbf{M}^{\circ T}\tilde{\mathbf{e}}_0\right], \tag{4.50}$$

4. the application of the star change of basis (loop unknowns are set to zero) , i.e. $\mathbf{j}_e = \mathbf{M}^{\star}\mathbf{j}_e^{\star}$:

$$\left[\mathbf{M}^{\star T}[\mathbf{R}_e + i\omega\mathbf{L}_e^e + \tfrac{1}{i\omega}\tilde{\mathbf{G}}^a_{\Omega_e}\mathbf{P}_e\mathbf{D}^a_{\Omega_e}]\mathbf{M}^{\star}\right]\left[\mathbf{j}_e^{\star}\right] = \left[\mathbf{M}^{\star T}\tilde{\mathbf{e}}_0\right]. \tag{4.51}$$

It is worth noting that, due to the kind of the problem excitation (magnetoquasistatic), method 4 (i.e. system (4.51)) is not be capable to provide the right solution. Indeed, the application of $\mathbf{M}^{\star}$ neglects the rotational component of the fields, i.e. the rhs of the system (4.51) is zero (or almost zero).

Moreover, due to the low frequency of the problem and the high conductivity of the plate, the breakdown in frequency issue is very severe for this numerical study. Indeed, the norm of $\mathbf{R}_e$ (resistive effects), the norm of $i\omega\mathbf{L}_e^e$ (inductive effects), and the norm of $\frac{1}{i\omega}\tilde{\mathbf{G}}^a_{\Omega_e}\mathbf{P}_e\mathbf{D}^a_{\Omega_e}$ (capacitive effects) are $2.917 \cdot 10^{-6}$ Ω, $2.025 \cdot 10^{-6}$ Ω, and $1.254 \cdot 10^{11}$ Ω, respectively. Thus, it is clear that round–off errors appear when system (4.48) is assembled and solved.

The results in term of Joule losses W_j where and the conditioning numbers of the final system of equations (4.48)–(4.51) are reported in Table 4.1. Moreover, Fig. 4.2 shows the current density vector distribution obtained from the four methods in a corner of the conductive plate.

As already stated, due to the low frequency and the kind of excitation of the problem, the contribution to the solution of star unknowns is truly negligible. Indeed, results obtained from the loop–star and the loop techniques are practically the same.

Even if the star change of basis strategy is actually not applicable to this kind of problem, it is interesting to note that the conditioning number of the loop system (4.50) is much better than the one of the star system (4.51). However, both the conditioning numbers are good.

Table 4.1: Joule losses for the conductive plate

	W_j $[W]$	Conditioning number
Direct solution of (4.16)	$3.475712203115757 \cdot 10^{9}$	$3.745284122585657 \cdot 10^{18}$
Loop–star	$1.909349947442374 \cdot 10^{6}$	$8.323919981160288 \cdot 10^{4}$
Loop	$1.909349947442374 \cdot 10^{6}$	17.283831696619270
Star	$3.972944765077949 \cdot 10^{-29}$	$8.323919981198369 \cdot 10^{4}$

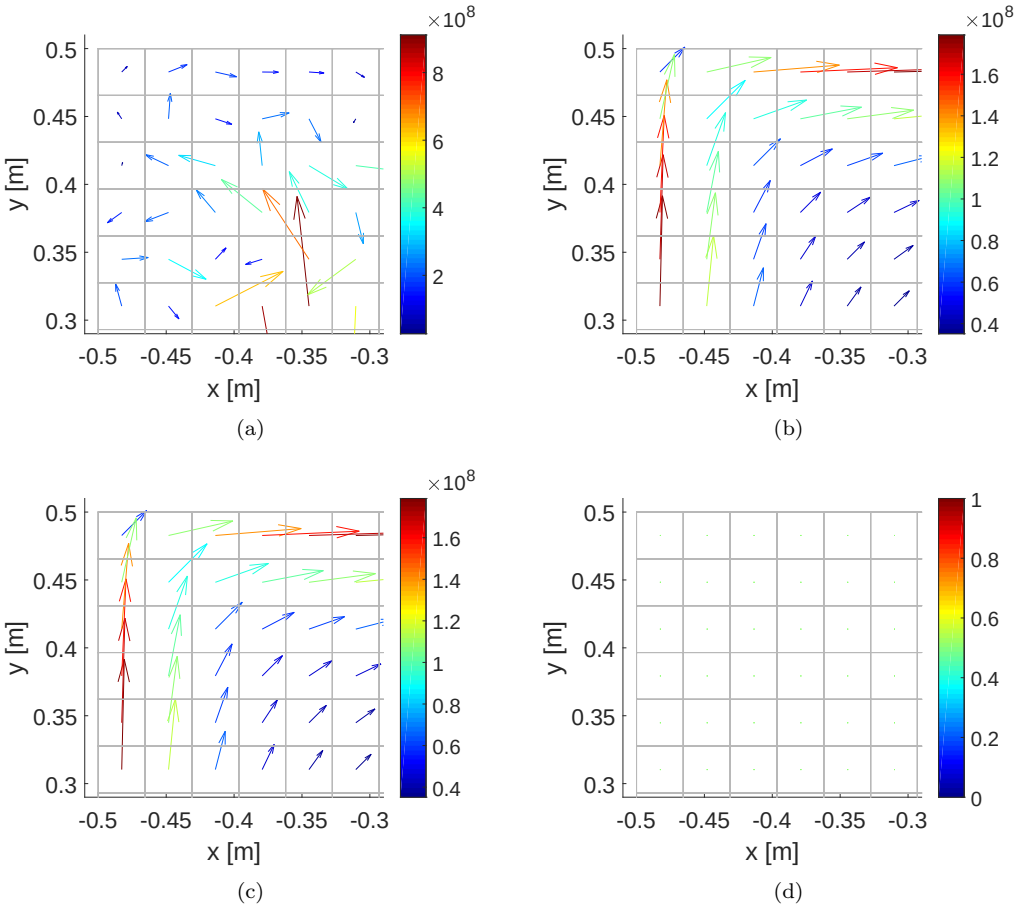

Figure 4.2: Current density (real part) distribution obtained from: *a*) the direct solution of (4.16), *b*) the loop–star change of basis strategy, *c*) the loop change of basis strategy, and *d*) the star change of basis strategy. Values in A/mm^{-2}.

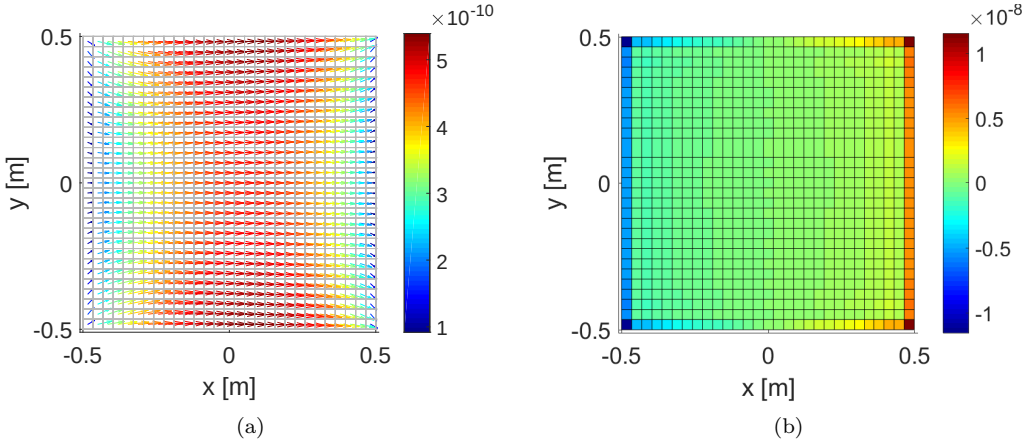

Figure 4.3: *a*) Electric polarization (real part) distribution, (C/m^{-2}. *b*)) Electric charge density distribution (C/m^{-3}).

Finally, the same plate model is simulated by imposing an electrostatic excitation: $\mathbf{E}_{ext} = \mathbf{u}_x$, $f = 0$ Hz. Complementary to the previous magnetoquasistatic problem, for this electrostatic case the loop–star and the star solution strategies are able to provide the right solution. The loop strategy would produce a null solution instead and (4.48) cannot be solved instead since

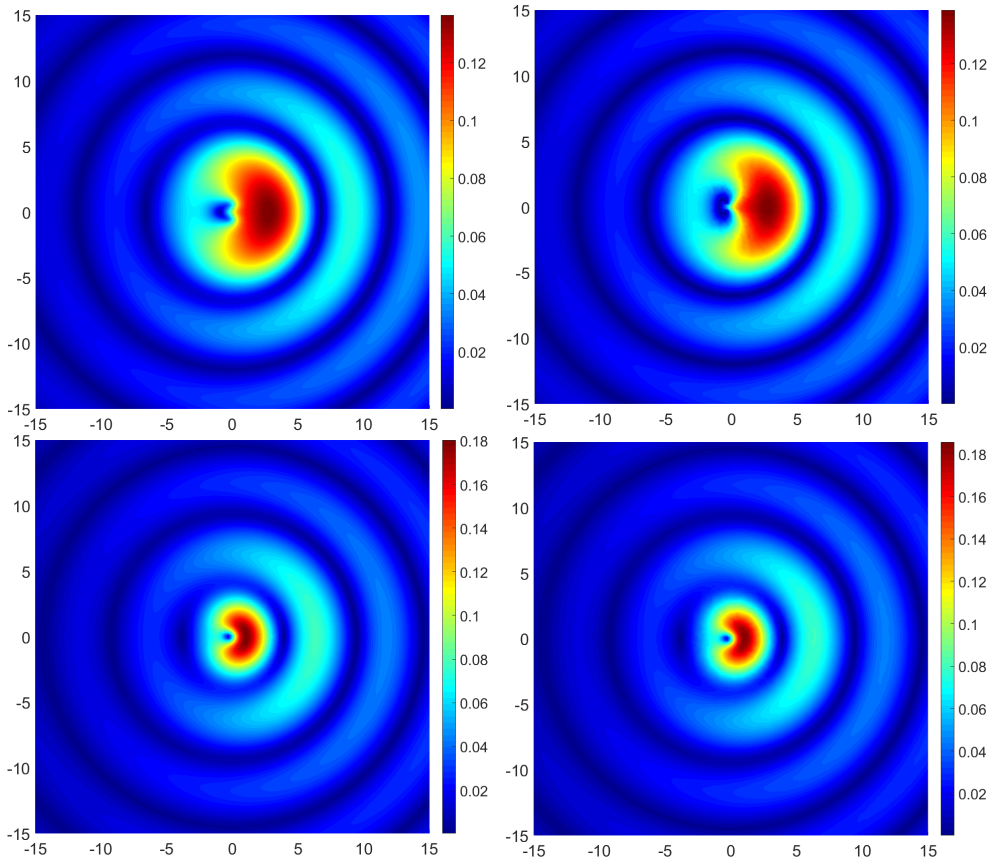

Figure 4.4: Scattered electric field magnitude (V/m) on the xz-plane, dimensions in m. Left: 3-D PEEC-Hertz. Right: COMSOL®. Top: $\Re$ part. Bottom: $\Im$ part.

$\omega = 0$. The results in terms of electric polarization vector distribution $\mathbf{P}_e$ (i.e. $\mathbf{J}_e = i\omega\mathbf{P}_e$, which is not the dielectric polarization, see [30], Chapter 8, Section 8.3) and electric charges are shown in Fig. 4.3

Dielectric and magnetic spheres Two spheres with 1 m radius, a dielectric one ($\varepsilon_r = 2$) and a magnetic one ($\mu_r = 10$) placed 3 m apart on the y–axis and excited by a linearly polarized plane wave $\mathbf{E_0} = e^{-ik_0 x}\mathbf{u}_z$. Where $k_0 = 2\pi f\sqrt{\varepsilon_0\mu_0}$, $f = 30$ MHz. The magnitude of the real and imaginary part of the scattered electric field has been compared with the Radio-Frequency module of COMSOL® with good agreement (Fig. 4.4). Small discrepancies are due to the sphere meshes required by C–PEEC and FEM, the intrinsic differences of the two approaches, and the numerical post processing adopted for C–PEEC.

Homogeneous anisotropic magnetic sphere The academic case of a homogeneous and anisotropic magnetic sphere, $\mu_r = \begin{bmatrix} 7 & 2 & 3 \\ 2 & 8 & 4 \\ 3 & 4 & 9 \end{bmatrix}$, excited by a plane wave $\mathbf{E}_0 = e^{-i\omega x/c_0}\mathbf{u}_z$, with $f = 10^7$ Hz, is considered. The radius of the sphere is 1 m and it is centered in $[0, 1.5, 0]$ m.

Fig. 4.5 shows the scattered magnetic field evaluated by the C–PEEC code along a 16 m straight line in the z direction, centered in the origin.

The results are compared with ones obtained with a commercial FEM software (COMSOL Multiphysics®, RF module). In the FEM simulation a third order discretization with tetrahedral support has been adopted ($\sim 11 \cdot 10^6$ DoFs) and FGMRES method with a relative tolerance of 10^{-10} has been chosen for the solution of the resulting linear system.

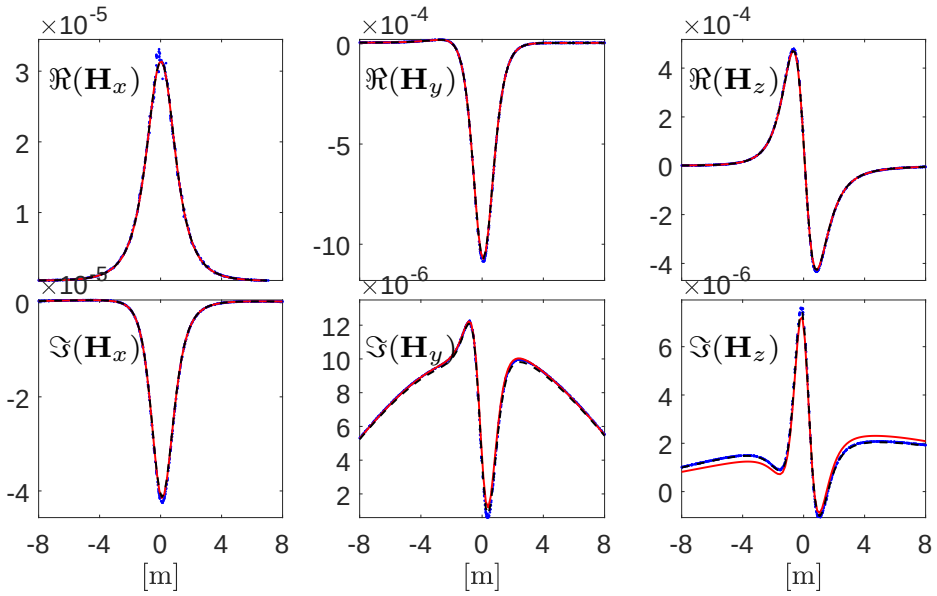

Figure 4.5: Scattered magnetic field (real and imaginary part), (A/m). FEM: blue dots, PEEC–no–ch: red solid line, PEEC–ch: black dashed line.

For the C–PEEC method, two solution strategies have been used: 1) the direct solution of (4.16) without any change of basis (PEEC–no–ch), and 2) the change of basis procedure proposed in Section 4.2.4 to apply the condition $\nabla \cdot \mathbf{J}_m = 0$, $\mathbf{J}_m \cdot \mathbf{n} \neq 0$ (PEEC–ch). Thus, for PEEC–ch the change of basis matrix $\mathbf{Q}_m$ (i.e. $\tilde{\mathbf{j}}_m = \mathbf{Q}_m \mathbf{j}_m^{\circ}$) is chosen to be $\mathbf{Q}_m = \tilde{\mathbf{C}}_{\Omega_m}^{red}$ (PEEC–ch), where $\tilde{\mathbf{C}}_{\Omega_m}^{red}$ is the *reduced* curl incidence matrix of the magnetic region.

The results of Fig. 4.5 show an excellent agreement between FEM and the C–PEEC method. As previously discussed, as it can been seen from the imaginary part of the z component of $\mathbf{H}$, the accuracy of PEEC–ch is greater than the one of PEEC–no–ch; however, the both methods are very accurate.

Inhomogeneous magnetic cube An inhomogeneous magnetic cube (1 m side) centered in the origin and excited by a plane wave $\mathbf{E}_0 = e^{-i\omega x/c_0}\mathbf{u}_z$ with $f = 10^6$ Hz is now considered. The permeability of the cube is defined as $\mu_r(\mathbf{r}) = 41 - 40|\mathbf{r}|/(1\text{ m})$.

Fig. 4.6 shows the more significant components of the scattered magnetic fields evaluated along a circular line (1 m radius) surrounding the cube in the yz–plane. The inhomogeneous media is treated by the C–PEEC method in two different ways as explained in **Case (b)** in Section 3.3.2, i.e. without the use of the *interface* faces (PEEC–no–int) and with the use of the *interface* faces (PEEC–int) for all the internal faces. For PEEC–int, the barycentric value of μ_r is assigned to each hexahedral element.

The solution is compared with the one obtained from the already mentioned FEM software. Both PEEC–no–int and PEEC–int show an excellent agreement with FEM results.

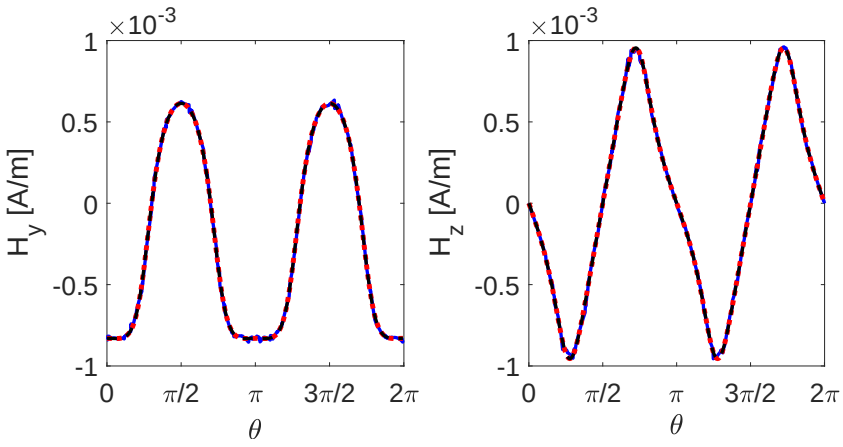

Figure 4.6: Scattered magnetic field (real part). FEM: blue solid line, PEEC–no–int: red dotted line, PEEC–int: black dashed line.

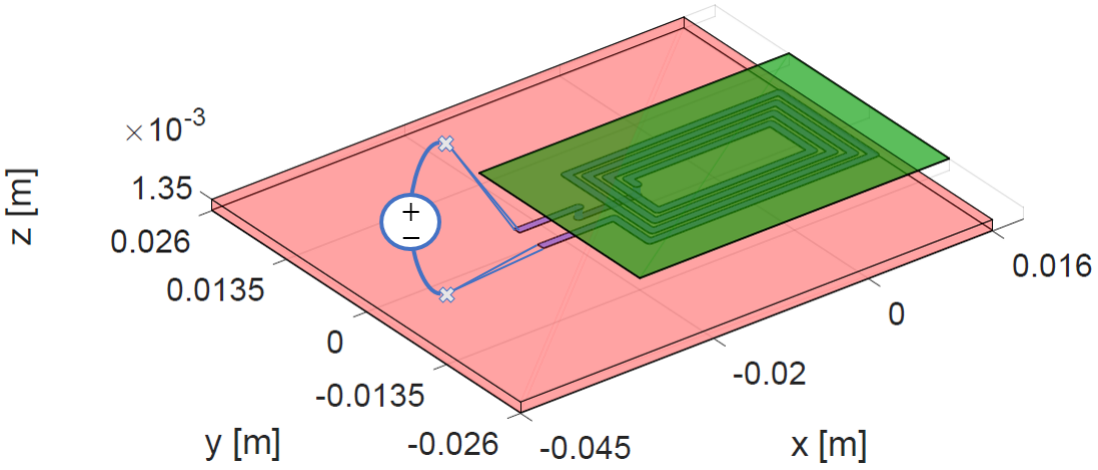

Figure 4.7: NFC antenna model. Antenna: blue, FR4: red, ferrite foil: green.

4.3.2 Industrial cases

NFC Antenna

For this case, simulations were run on a Linux machine equipped with a dual 6-core/12-thread processors (Xeon E5-2643 v4 @3.40GHz) and 512 GB of RAM.

The case of a real NFC antenna is now considered [113]. The device consists of a copper trace ($\sigma_c = 57 \cdot 10^6$ S/m, 35 μm thick, 1 mm wide) placed on a FR4 dielectric substrate ($\varepsilon_r = 4.3$). The coil has outer dimensions of 30 mm×17 mm, while the FR4 substrate is 61 mm×52 mm wide, with a 1.35 mm thickness. A ferrite foil ($\mu_r = 163$), 40 mm×27 mm wide and with 100 μm thickness, is mounted on top of the copper trace in order to reduce the detuning effects because of the eddy currents. The operating frequency is $f = 13.56$ MHz.

The device is discretized into hexahedral elements and a lumped voltage source is connected to the quadrilateral faces that discretize the terminals of the conductive antenna by means of short circuit branches, as shown in Fig. 4.7.

The value of the equivalent impedance Z_{eq} obtained from the simulations by means of the A–PEEC and C–PEEC codes is compared with measurements [113], with the values obtained from the already mentioned FEM software, and a well known commercial software based on

Table 4.2: Equivalent Impedance NFC Antenna

	Z_{eq} *mod.*1 [Ω]	Z_{eq} *mod.*2 [Ω]
Measured	$0.4589 + i55.3896$	$0.3630 + i34.8196$
C–PEEC	$0.4498 + i55.1837$	$0.3654 + i34.3945$
FEM	$0.4446 + i55.0611$	$0.3605 + i34.4629$
IE	$0.3302 + i57.6515$	$0.3299 + i35.5193$
A–PEEC	$0.3933 + i35.9283$	$0.3654 + i34.3945^*$

* C–PEEC and A–PEEC are equivalent when magnetic media are not involved.

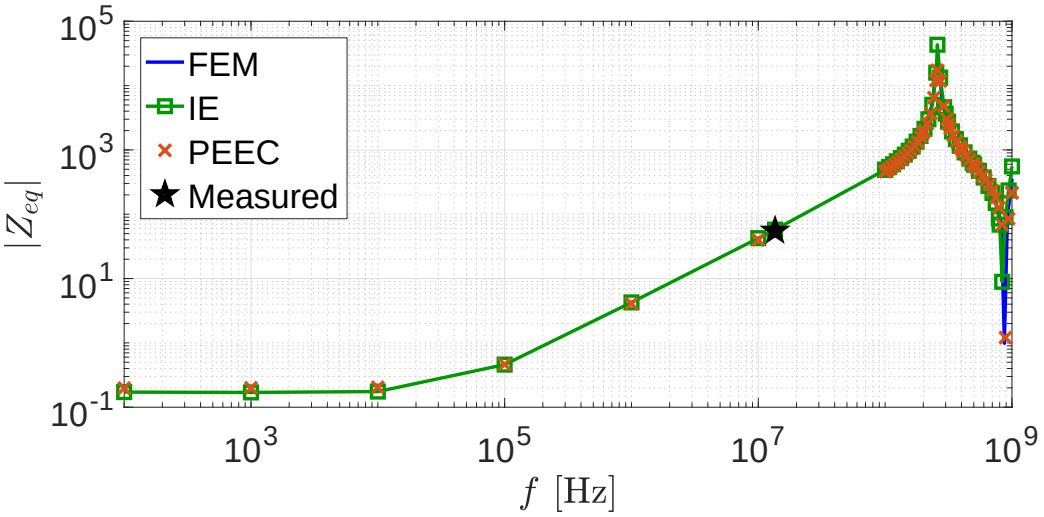

Figure 4.8: $|Z_{eq}|$ *mod.*1 vs. frequency. Values in [Ω].

IEM (IE). The results are shown in Table 4.2; for this study the device has been considered with (*mod.*1) and without (*mod.*2) the presence of the ferrite foil.

From Table 4.2, it can be noticed that the results obtained from C–PEEC are in good agreement with measured values and that C–PEEC method is capable to capture the influence of the thin magnetic foil on the value of the active losses (i.e. real part of Z_{eq}). A–PEEC, instead, seems to be not capable of obtaining an accurate value of Z_{eq}. This behavior often emerges when thin magnetic objects are placed very closed to conductive media probably due to the numerical issues discussed in Section 4.2.3 and to the numerically weak imposition of the amperian currents distribution. Indeed, an inaccurate distribution of $\mathbf{J}_a$ and $\mathbf{K}_a$ locally perturbs the values of the electromagnetic fields, thus therefore also the value of Z_{eq}. However, in order to allows a fair comparison between the A– and the C–PEEC methods, the same mesh and the same precision for the evaluation of the matrix coefficients have been adopted for A–PEEC and C–PEEC codes.

Fig. 4.8 shows the magnitude of Z_{eq} in the frequency range computed by the implemented C–PEEC code and commercial software. Moreover, the electric and magnetic fields produced

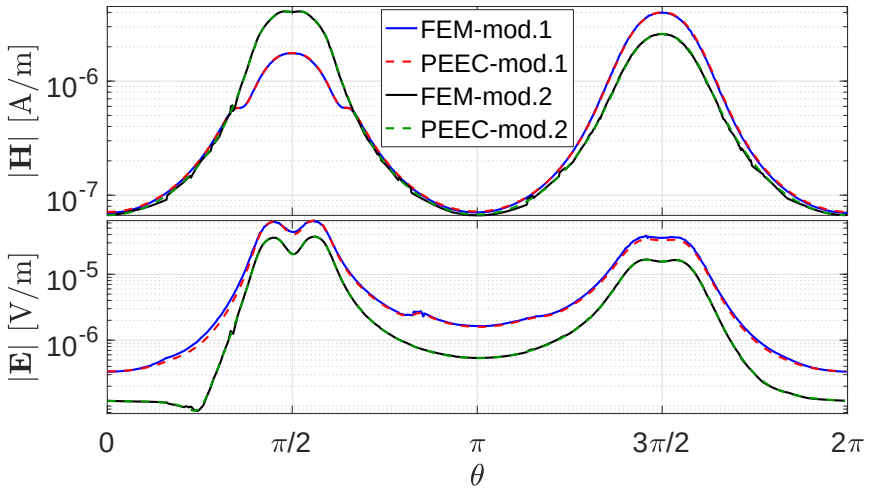

Figure 4.9: Complex magnitude of **H** and **E** along the elliptical line.

by the device along an elliptical line surrounding the NFC antenna are evaluated and compared with the results obtained from FEM software. The support of the elliptical line is $p_x = 0$ mm, $p_y = 30$ mm·cosθ, $p_z = 4$ mm·sinθ, with $\theta \in [0, 2\pi]$, and also for this analysis *mod.*1 and *mod.*2 are considered. The results of the magnetic and electric fields magnitude are shown in Fig. 4.9. The computation of the electric and magnetic fields along the elliptical line has been efficiently performed in parallel with Mex-OpenMP Fortran functions. For that case, such computation time was truly negligible with respect to the time required for the system assembling and solution. However, it is worth noting that such computation time may become significant when the electromagnetic fields are evaluated in a great amount of target points. Table I, Fig. 4.8, and Fig. 4.9 show a good agreement between the results obtained from the implemented C–PEEC code, measurements, and commercial software.

Concerning the computational cost, the model adopted for FEM simulations consists of a large amount of elements since very thin volumetric objects, such as the copper trace and the magnetic foil, have been discretized. In particular the FEM model consists of $\sim 6.2 \cdot 10^6$ tetrahedral elements and 5,508 prisms (for the Perfectly Match Layer condition), leading to $\sim 39.3 \cdot 10^6$ DoFs, and required 4,230 s simulation time and 235 GB peak memory usage (PMU). FGMRES solver with a relative tolerance of 10^{-7} has been chosen.

On the contrary, the C–PEEC method requires a small number of hexahedral elements for the discretization of the conductive, dielectric, and magnetic domains. In particular, a very coarse mesh consisting of 322 conducting, 1,374 dielectric, and 2,852 magnetic hexahedral elements is sufficient to attain a very good accuracy in terms of the produced electromagnetic fields. Indeed, concerning the evaluation of the electromagnetic fields, one element carrying a (mean) value of the conduction current density is sufficient for the discretization of the cross section of the copper trace. The number of DoFs of the final system is 17,335.

Since only homogeneous media have been considered, the change of basis procedure discussed in Section 4.2.4 is adopted (i.e. $\nabla \cdot \mathbf{J}_c = 0$, $\mathbf{J}_c \cdot \mathbf{n} \neq 0$, $\nabla \cdot \mathbf{J}_d = 0$, $\mathbf{J}_d \cdot \mathbf{n} \neq 0$, $\nabla \cdot \mathbf{J}_m = 0$, and $\mathbf{J}_m \cdot \mathbf{n} \neq 0$), leading to 12,789 DoFs for the system to be solved in the reduced basis. The simulation time is 98 s and the PMU is 10.7 GB.

On the other hand, the evaluation of the real part of the equivalent impedance (related to the energy losses) requires a larger amount of elements for the discretization of the copper trace,

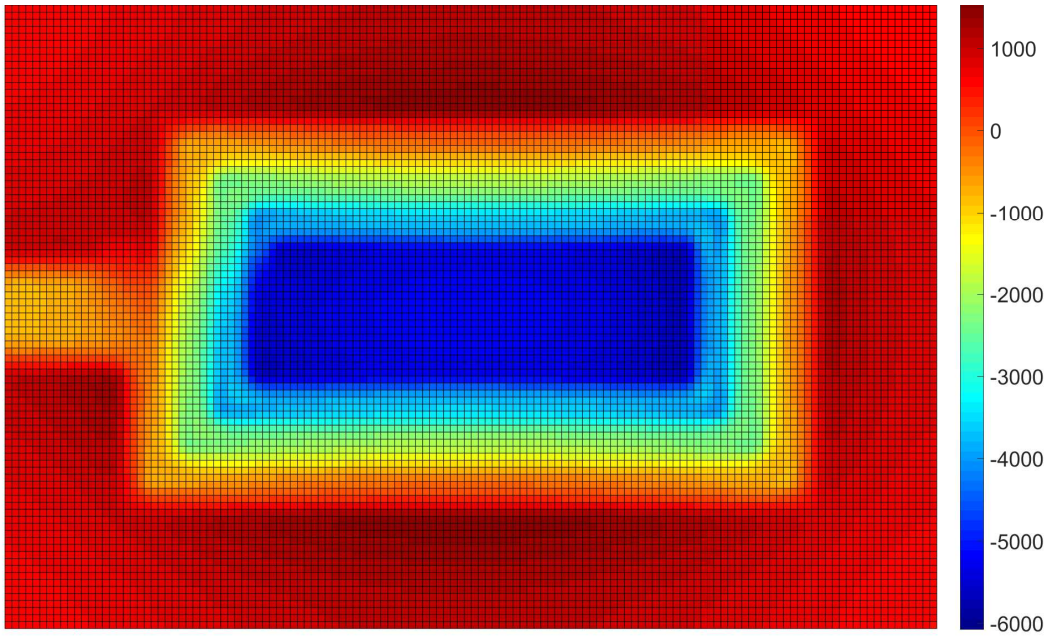

Figure 4.10: Magnetic potential evaluated with C–PEEC code on the magnetic foil of the NFC antenna. Values in A.

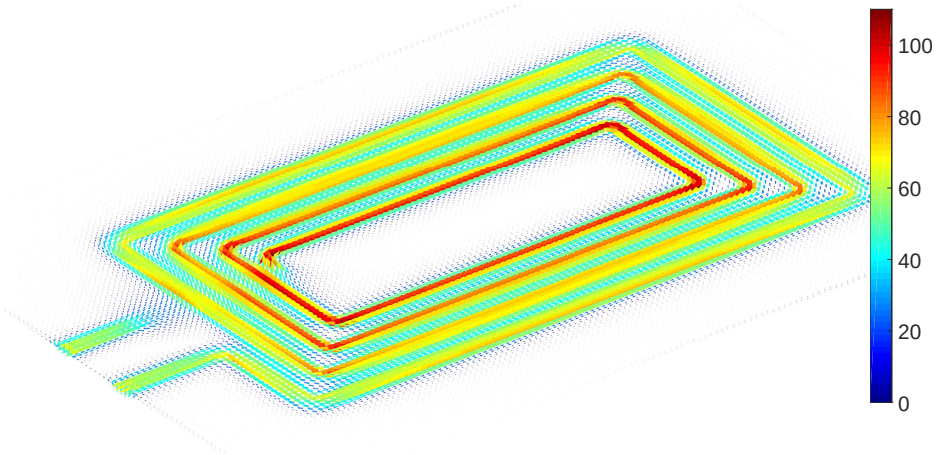

Figure 4.11: Surface amperian currents evaluated with A–PEEC code on the magnetic foil of the NFC antenna. Values in Am^{-1}.

since it is necessary to obtain a good approximation of the real distribution of the conduction current density vector, that is strongly affected by proximity effects. Thus, the model adopted for A–PEEC and C–PEEC codes for the evaluation of Z_{eq} consists of 6,480 conducting, 1,374 dielectric, and 12,060 magnetic hexahedral elements, leading to a total amount of DoFs equal to 81,059 for the assembled system, 59,669 for the system to be solved, 4,817 s simulation time, and 184 GB PMU (which, by appropriate optimization, can be reduced to $\sim$ 56 GB, i.e. the memory required by the storage of the system to be solved). The C–PEEC system was solved by an LU decomposition.

For the commercial IE software, since lumped voltage sources can be applied only to the interior edges of surface models, an equivalent surface model has been adopted for the copper trace and the two terminals of the antenna have been *physically* connected. The computational

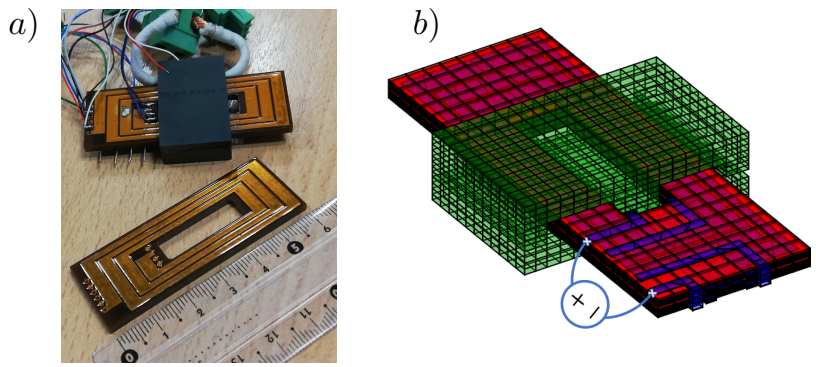

Figure 4.12: *a*) L–C–T prototype. *b*) L–C–T Model.

cost is comparable with the PEEC one (coarse case). However, probably because of the use of a too simplistic equivalent surface model, the real part of Z_{eq} seems not to be influenced by the presence of the magnetic foil, even when finer meshes are adopted. This can be an issue when computing joule losses. Instead, with the 3–D C–PEEC code, volume models can be naturally connected to lumped circuit elements allowing for properly evaluate the value of the active losses of the NFC antenna, which is an important quantity to be considered during the design process.

Fig. 4.10 shows the magnetic scalar potential evaluated on the magnetic foil by C–PEEC code. Fig. 4.11 shows the amperian surface current distribution, $\mathbf{K}_a$, evaluated by the A–PEEC code.

LCT transformer

The Unstructured–PEEC method based on the C–formulation with total div–free currents developed with MATLAB® and parallel MEX–FORTRAN functions based on OpenMP libraries is here adopted. The simulations were run on a Windows machine equipped with 6-core/24-thread processors (Intel E5645 @2.40GHz) and 104 GB RAM.

The L–C–T component proposed in [2] is here considered. All geometrical and material details of the device are reported in [114] (Appendix 4). The device is made by 16 copper layers (70 μm thickness each) that compose the first and the second part of the primary winding of the transformer. Any copper layer is printed on a dielectric substrate made of Kapton ($\varepsilon_r = 3.3$, 50 μm thick) or Preg ($\varepsilon_r = 4.5$, 140 μm thick). The magnetic core is made of Ferrite 3F3. Fig. 4.12 shows a picture of the L–C–T component and its corresponding model. Note that neither the dielectric nor the magnetic media are simply connected regions. The device is fed by a voltage source connected to only two of the four terminals of the primary winding (Fig. 4.12).

Fig. 4.13 shows the model of the conductive domain of the L–C–T device, scaled along the z–axis.

At low frequency, the device behaves as a capacitor. The primary winding is an open circuit and the current flows from the first part to the second part of the winding thanks to capacitive effects [2]. The working frequency of the device is close to the first resonance frequency, thus the components acts like a transformer and a filter too. In Fig. 4.14 the magnitude and the argument of the equivalent impedance (Z_{eq}) obtained from the PEEC code are compared with measurements and with the numerical results obtained from FEM and an Integral Equation Method (IEM) commercial software. Fig. 4.15 shows the cases of the device without the the magnetic core (no–core) and the case with the conductive media only (con-only). The PEEC

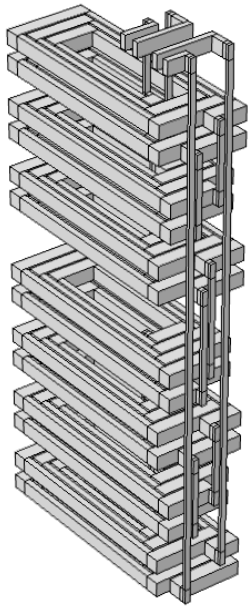

Figure 4.13: LCT model, conductive domain scaled along the z direction. .

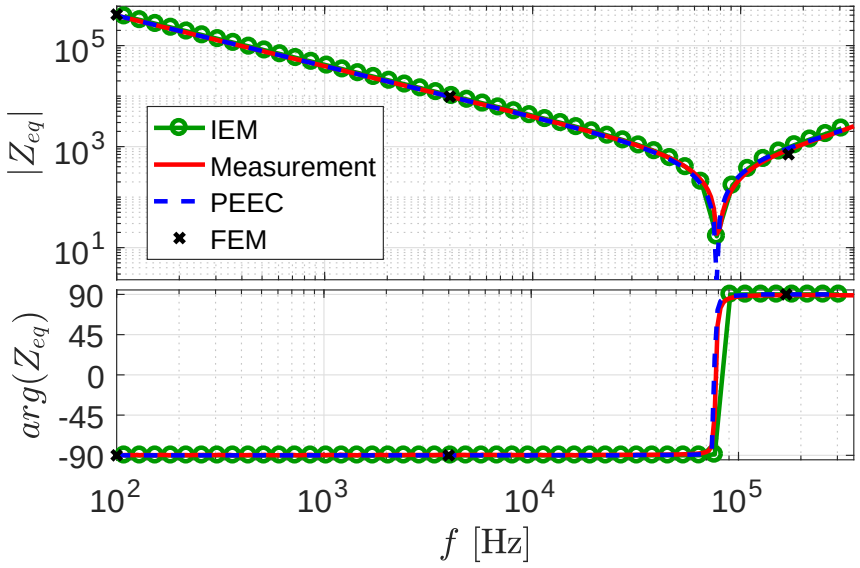

Figure 4.14: Z_{eq} absolute value and argument of the L–C–T component.

model of the (entire) L–C–T component is made by hexahedral elements and consists of 18,429 DoFs. The time required for the computation of the matrices is 545 s. The matrix system is solved by means of LU decomposition and the solution time for a single frequency value is 733 s with 15 GB PMU.

For a frequency sweep analysis, the PEEC matrices can be computed only once. Then, for each frequency value, the system (4.16) is assembled and solved.

In order to assess the computational cost required by FEM for the study of the L–C–T component, three simulations have been run. Due to the small thickness of the layers a great amount of elements is needed for the discretization. The FEM problem is first solved by adopting liner basis functions (4,956,667 DoFs) and using a direct solver (MUMPS). This required 8,914

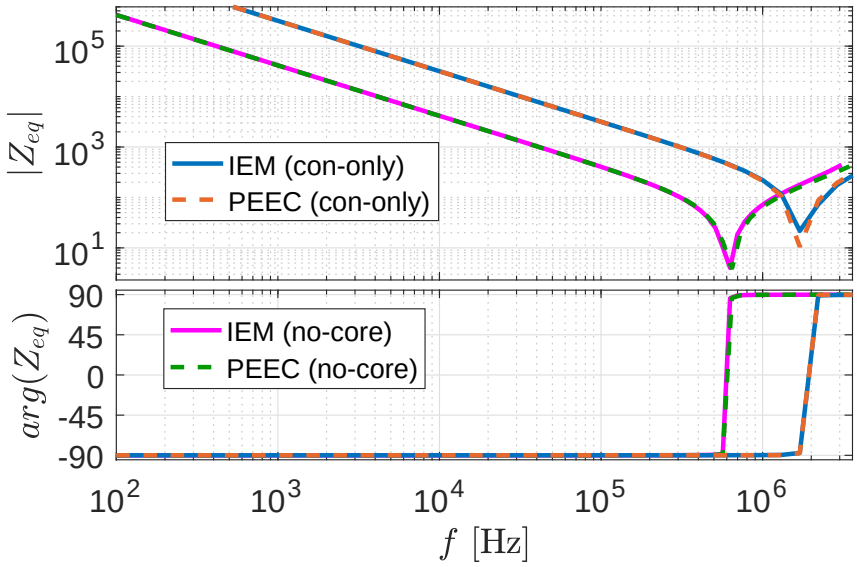

Figure 4.15: Z_{eq} absolute value and argument, no–core and con-only cases.

s and 380 GB PMU. Then, starting from the obtained solution, an iterative solver (FGMRES) and quadratic basis functions are adopted to increase the solution accuracy (29,582,652 DoFs, 9,799 s, PMU of 430 GB).

The model adopted for the commercial IEM software consists of 35,243 DoFs and the mesh is made by tetrahedral and triangular elements. An equivalent surface model is used for the copper layers to include in the model the voltage excitation. The simulations requires 1,892 s and a 19 GB PMU for each frequency value.

Chapter 5

Low–rank approximation applied to PEEC

In Section 4.2, different approaches for the solution of the final PEEC system of equations have been discussed. However, such as all integral equation methods, the storage and the computational effort required for the solution of the PEEC system of equations rapidly increase along with the number of unknowns and its solution becomes unfeasible on standard workstations. Alternatively, low–rank approximation techniques can be adopted to increase the size of the largest solvable problem and, in most of the cases, they become mandatory numerical tools. Thus, all the discussions of Section 4.2 should be considered under the context of compression techniques allowing a great speed up in algebraic operations, such as matrix multiplication and solution of linear systems.

During the last years, several low–rank compression techniques based on Hierarchical ($\mathcal{H}$)–matrices [7] and Adaptive–Cross–Approximations (ACA) [10] or Hybrid–Cross–Approximations (HCA) [6] have been developed and successfully applied to integral equation methods [77].

In the context of this PhD thesis, the author decided to not develop new or ad–hoc low–rank approximation approaches (which is a sensitive topic in applied mathematic context and image processing but probably outside the area of expertise of computational electromagnetic engineers). Instead, the use of different low–rank compression methods available in free and highly optimized libraries has been investigated in the context of PEEC method for low and high frequency problems. Moreover, the use of several numerical techniques previously described (e.g. loop–star decomposition) have been investigated with the aim of improving the compression performances of these libraries.

In this chapter, the HLIBPro library [115] (which relies on $\mathcal{H}$– and $\mathcal{H}^2$–matrix representation coupled with ACA) and STRUMPACK Dense Package (SDP) [116] (which relies on Hierarchically Semi–Separable (HSS) matrices) are investigated in the context of their application to PEEC method. Thus, the theory beyond $\mathcal{H}$–matrix, HSS matrices, and ACA is shortly introduced. Then, the application of those methods to different PEEC problems is investigated and the performances of $\mathcal{H}$– and HSS matrices are also compared. Moreover, some numerical procedures which allow improving the compression performances of such libraries are discussed in the context of numerical simulations of industrial devices.

5.1 PEEC and low-rank approximation

In this PhD thesis, in accordance with several groups of research and works in the literature, the PEEC method is interpreted as a particular form of Integral Equation method which allows a natural and useful circuit interpretation of the full Maxwell electromagnetic problem [20].

In Chapter 2, two different PEEC formulations are derived based on the Amperian and Coulombian interpretation of the magnetization phenomena, respectively. Then, in Chapter 3 these two PEEC formulations are discretized following the Unstructured discretization based on the Cell Method. The final results of such discretization process are the algebraic system of equations (3.47) and (3.68) where, as commonly done in the context of standard PEEC methods, currents and potentials are considered as independent unknowns.

However, as discussed in Chapter 4, scalar potentials can be removed from the independent unknowns resulting in a more compact PEEC system of equations (i.e. with a reduced number of unknowns): (4.7) and (4.16). These systems of reduced size present some numerical issues (which however can be prevented by using loop–star or other change of basis techniques) but they are more suitable for the application of low–rank approximation techniques. Indeed, contrary to (3.47) and (3.68) which are block structured matrices consisting of sparse (topology) and dense (mutual interaction) matrix blocks, systems (4.7) and (4.16) have only (potentially low–rank) dense matrix blocks. This *more homogeneous* composition of (4.7) and (4.16) allows for an easier application of low–rank compression techniques and therefore they have been selected when HLIBPro and SDP libraries have been adopted. However, it is worth noting that, at the expense of a more complicated algorithm, low–rank compression techniques can also be applied to the dense matrix blocks of (3.47) and (3.68) while keeping uncompressed the other sparse matrix blocks. However, this possibility has not yet been investigated in the context of this PhD thesis and is a possible future research topic.

For the sake of clarity and simplicity, in this chapter the reduced size PEEC system is adopted. The PEEC system is indicated as $\bar{\mathbf{M}}$. A generic entry of the system matrix $\bar{\mathbf{M}}$ involves the double integration of the Green's function (2.17) which, for the sake of clarity, is here reported:

$$g(\omega, r) = \frac{e^{-ik_0 r}}{r}, \tag{5.1}$$

where r is the geometric distance and $k_0 = \omega/c_0$, in which c_0 is the speed of light in vacuum.

In the next section, the basic theory concerning low low–rank approximation techniques applied to matrix $\bar{\mathbf{M}}$ is discussed. However, even if the PEEC system is firstly represented with $\bar{\mathbf{M}}$, it is worth noting that its actual structure (which depends on the media involved in the problem, the frequency, change of basis, etc.) highly influences the compression performances, how shown by the numerical test cases.

5.2 Low-Rank approximation

Although fully populated, the $N \times N$ matrix $\bar{\mathbf{M}}$ arising from the PEEC formulation contains low–rank blocks (typically the ones far from the diagonal) that make $\bar{\mathbf{M}}$ suitable for the compression. Thus, $\bar{\mathbf{M}}$ is commonly defined as a hierarchical off–diagonal low–rank (HODLR) matrix [117]. We recall that a complex valued matrix $\mathbf{A} \in \mathbb{C}^{m \times n}$ (e.g. a off–diagonal block of $\bar{\mathbf{M}}$) is low–rank

if there exists a pair of matrices $\mathbf{U} \in \mathbb{C}^{m\times k}$ and $\mathbf{V} \in \mathbb{C}^{n\times k}$, with $k(m+n) < mn$, such that [7]:

$$\mathbf{A} = \mathbf{U}\mathbf{V}^{*}, \tag{5.2}$$

where * indicates the conjugate transpose operator and k is the *exact* rank of $\mathbf{A}$. Therefore, $\bar{\mathbf{M}}$ can be expressed by a suitable data–sparse representation, that stores its rank–deficient blocks by computing a reduced number of entries only. The remaining (high–rank blocks) are entirely stored as dense matrices. Moreover, the use of a data–sparse representation allows a great speed up in algebraic operations, e.g. matrix multiplication and solution of linear systems. It is worth noting that the exact rank k of each low–rank block is not known a priori. Hence, the factors in (5.2) are computed in approximate way by a rank–revealing factorization [118]:

$$\|\mathbf{A} - \mathbf{U}_{k'}\mathbf{V}_{k'}^{*}\|_F < \varepsilon, \tag{5.3}$$

where $\|\cdot\|_F$ indicates the Frobenius norm, $\mathbf{U}_{k'} \in \mathbb{C}^{m\times k'}$, $\mathbf{V}_{k'} \in \mathbb{C}^{n\times k'}$, and k' is the minimal rank such that the approximation error is lower than a prescribed tolerance ε. The above truncated factorization defines a low–rank approximation of the block $\mathbf{A}$.

Different techniques may be applied to compute the low–rank approximation of a matrix. A truncated SVD may be the easiest choice. However, since the cost of SVD is roughly $\mathcal{O}(mnk')$, when the size of $\mathbf{A}$ is not *small enough*, other factorization methods should be applied, avoiding the access to all the matrix entries. Among different data–sparse representations, $\mathcal{H}$–matrices, $\mathcal{H}^2$–matrices, and Hierarchically Semi–Separable (HSS) matrices are commonly used.

Each one relies on a binary cluster tree that identifies the hierarchical partitioning of the row and column indices of the matrix to compress, i.e. $\bar{\mathbf{M}}$. Once the matrix is partitioned, the high and low–rank blocks are distinguished according to the chosen representation. Let $I_0 = \{1, ..., N\}$ be the set of row/column indices of the matrix. The whole interval I_0 identifies the *root* node (cluster) τ_0 that corresponds to the first level of the tree. A second level is obtained halving I_0 into two parts, for example in equal subintervals $I_1 = \{1, ...\frac{N}{2}\}$ and $I_2 = \{\frac{N}{2} + 1, ..., N\}$, that correspond to *children* nodes (clusters) τ_1 and τ_2, respectively. If at each level all the nodes are recursively halved, the last p level contains 2^{p-1} nodes (clusters) without any children (these nodes are also called *leafs* of the tree).

When discretizing operators involving kernel functions with geometric dependency as in (5.1), each row/column index of the matrix is related to a specific unknown having one or more geometric elements of the mesh as support (i.e. volumes, faces, edges, or nodes of the mesh). Thus, each row/column index can be associated to a geometric coordinate in the 3–D space, e.g. the barycenter of the support. In this regard, the tree construction can be managed by a geometrical clustering, that splits the mesh with the aim of obtaining leaf nodes corresponding to evenly populated mesh clusters. The described process leads to more general trees, where not all the nodes may have been halved. This clustering process is exemplified in Fig. 5.1.

In the next two sections, on the basis of the previous general description of low–rank approximation of dense matrices, the theory of $\mathcal{H}$– and HSS matrix representation (which are the theoretical background of HLIBPro and STRUMPACK Dense Package libraries) is shortly presented. It is worth noting that the discussion of the next section is far from being an exhaustive and comprehensive presentation of that topic. Thus, the author refers the interested readers to dedicated references such as [119] for HSS matrix representation, [120] for $\mathcal{H}^2$ matrix representation, [11] for a comparison between HSS and $\mathcal{H}^2$ matrix representation.

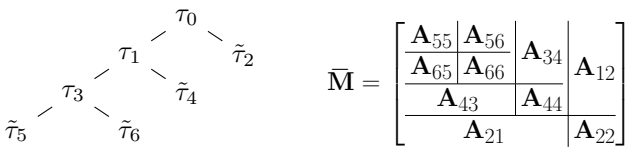

Figure 5.1: Binary cluster tree with 4 leaf nodes $\tilde{\tau}$ and related matrix partition.

5.2.1 HLIBPro, $\mathcal{H}$– and $\mathcal{H}^2$–matrices

Once the row/column index coordinates are provided, a partitioning algorithm, based on geometric bisection, splits the mesh into disjoint clusters and builds a binary tree which ends as soon as a prescribed condition is reached (e.g. when leaf nodes contain at most a fixed number of elements). It should be noted that each kth row/column index corresponds to the kth DoF, which has a geometrical collocation in the space. For instance, if the DoFs are associated to the faces of the mesh, the position of each kth DoF can be associated to the barycenter of the kth face, i.e. $\mathbf{r}_k$. Thus, the kth row/column index is in turn associated to $\mathbf{r}_k$.

It is worth noting that, if the clusters contain suitably numbered unknowns, the off–diagonal matrix blocks represent the electromagnetic coupling between unknowns belonging to pairs of distant clusters. HLIBPro natively provides this functionality (i.e. partitioning algorithm). Therefore, because of the decay of Green's kernel with the relative distance between the clusters, blocks compatible with a low–rank representation can be identified.

Let be (τ_k, τ_h) a generic pair of clusters belonging to the same tree level. The following definitions are then introduced [121]:

$$diam(\tau_k) := max\left\{\|\mathbf{r}_k - \mathbf{r}_h\|_2 : \mathbf{r}_k, \mathbf{r}_h \in \tau_k\right\}, \tag{5.4}$$

$$dist(\tau_k, \tau_h) := min\left\{\|\mathbf{r}_k - \mathbf{r}_h\|_2 : \mathbf{r}_k \in \tau_k, \mathbf{r}_h \in \tau_h\right\}, \tag{5.5}$$

where $\mathbf{r}_k$ and $\mathbf{r}_h$ are the coordinates related to the row/column indices belonging to the clusters τ_k and τ_h. Then, the tree is traversed from top to bottom and each pair of disjoint clusters belonging to the same level are tested against the following admissibility criterion:

$$min\{diam(\tau_k), diam(\tau_h)\} \leq \eta\, dist(\tau_k, \tau_h), \tag{5.6}$$

where η is the admissibility parameter ($0 < \eta < 2$). The criterion identifies the $\mathcal{H}$–matrix format in which the system matrix $\bar{\mathbf{M}}$ will be compressed. If true, the corresponding blocks $\mathbf{A}_{kh} = \bar{\mathbf{M}}(I_{\tau_k}, I_{\tau_h})$ and $\mathbf{A}_{hk} = \bar{\mathbf{M}}(I_{\tau_h}, I_{\tau_k})$ are expressed by a low-rank approximation, otherwise the blocks are split in their sons following the tree structure and the procedure is repeated down to the deepest level of the tree. The final hierarchical matrix structure includes non–admissible high–rank blocks, stored as dense sub–matrices, and low–rank ones factorized by ACA or other suitable methods. Indeed, HLIBPro allows for the use of different kind of compression techniques such as: SVD, ACA, Advanced ACA, ACA with full pivot search, HCA, and rank revealing QR. If $\mathbf{A}$ is a low–rank candidate to be stored, at each step ν, ACA computes a pivot row u_ν and column v_ν of $\mathbf{A}$ in order to obtain a rank–1 approximation of the remainder matrix $\mathbf{A} - \sum_{\mu=1}^{\nu-1} u_\mu v_\mu^T$ [10]. The algorithm adaptively increases the number of pivot rows and columns until, after k'

steps, a prescribed relative tolerance ε_{ACA} is obtained such that:

$$\frac{\|\mathbf{A} - \sum_{\mu=1}^{k'} u_\mu v_\mu^T\|_F}{\|\mathbf{A}\|_F} < \varepsilon_{ACA}. \tag{5.7}$$

ACA and Advanced ACA do not require to access all matrix entries, hence the approach is completely *matrix–free*, i.e. no matrix blocks satisfying (5.6) are actually stored. User has only to provide an element–access routine, able to compute each single entry required by ACA. Once $\bar{\mathbf{M}}$ is compressed, a $\mathcal{H}$–LU factorization is performed in $\mathcal{H}$–matrix arithmetic and used as preconditioner for a GMRES solver.

The experience gained from numerical experiments (partially reported in Section 5.4) indicates that the use of $\mathcal{H}$–LU preconditioner allows for a very efficient solution of the PEEC system of equations by means of GMRES solver. An easy and general introduction to the construction of $\mathcal{H}$–LU preconditioner starting from $\mathcal{H}$–matrices can be found in [6] (i.e. the PhD thesis of a former PhD student of G2ELab). Other specific references concerning the solution and the preconditioning of $\mathcal{H}$–matrix system of equations can be found in [122], [123], [124], and [125].

5.2.2 STRUMPACK Dense Package, HSS–matrices

The approach of SDP library, based on HSS–matrix representation, is less conservative, since a low–rank approximation is applied to *all* the off–diagonal blocks without any geometrical admissibility criterion test.

The matrix is partitioned according to a binary tree which is constructed by recursively halving the index interval. Its depth can be controlled by the user setting the number of levels or the maximum size of leaf clusters. In the HSS representation, off–diagonal matrix blocks $\mathbf{A}_{kh}$ and $\mathbf{A}_{hk}$, corresponding to tree nodes τ_k and τ_h, are factorized as [126]:

$$\mathbf{A}_{kh} = \mathbf{U}_{\tau_k}^{big} \mathbf{B}_{\tau_k,\tau_h} \mathbf{V}_{\tau_h}^{big\,*}, \quad \mathbf{A}_{hk} = \mathbf{U}_{\tau_h}^{big} \mathbf{B}_{\tau_h,\tau_k} \mathbf{V}_{\tau_k}^{big\,*}. \tag{5.8}$$

In HSS format the bases $\mathbf{U}_{\tau_k}^{big}$ and $\mathbf{V}_{\tau_k}^{big}$ that identify the previous factorization are nested.

Namely, let τ_k be a parent node with children τ_1 and τ_2, the following property holds:

$$\mathbf{U}_{\tau_k}^{big} = \begin{bmatrix} \mathbf{U}_{\tau_1}^{big} & 0 \\ 0 & \mathbf{U}_{\tau_2}^{big} \end{bmatrix} \mathbf{U}_{\tau_k}, \quad \mathbf{V}_{\tau_k}^{big} = \begin{bmatrix} \mathbf{V}_{\tau_1}^{big} & 0 \\ 0 & \mathbf{V}_{\tau_2}^{big} \end{bmatrix} \mathbf{V}_{\tau_k}. \tag{5.9}$$

Otherwise, at leaf nodes $\mathbf{U}_{\tau_k}^{big} \equiv \mathbf{U}_{\tau_k}$ and $\mathbf{V}_{\tau_k}^{big} \equiv \mathbf{V}_{\tau_k}$. The SDP low–rank approximation algorithm is based on randomized sampling [127] combined with an Iterative Decomposition (ID) factorization method [126]. Given a matrix $\mathbf{A} \in \mathbb{C}^{m\times n}$, the ID finds a vector J of k' column indices of $\mathbf{A}$ and a matrix $\mathbf{X} \in \mathbb{C}^{k'\times n}$ such that:

$$\frac{\|\mathbf{A} - \mathbf{A}(:,J)\mathbf{X}\|_F}{\|\mathbf{A}\|_F} < \varepsilon_{ID}, \tag{5.10}$$

where ε_{ID} is a prescribed tolerance. Let $\mathbf{R}^r, \mathbf{R}^c \in \mathbb{C}^{N\times k''}$ be random matrices, in which k'' is an integer number fixed by the user. Then, row and column samples of the bases of $\bar{\mathbf{M}}$ are defined as:

$$\mathbf{S}^r = \bar{\mathbf{M}}\mathbf{R}^r, \qquad \mathbf{S}^c = \bar{\mathbf{M}}^*\mathbf{R}^c. \tag{5.11}$$

Opposite to HLIBPro, in SDP the tree is traversed in a bottom–up order. For each node τ_k, the following matrices are defined:

$$\mathbf{S}^r_{\tau_k} = \mathbf{S}^r(I_{\tau_k}, :) - \mathbf{D}_{\tau_k}\mathbf{R}^r(I_{\tau_k}, :), \tag{5.12}$$

$$\mathbf{S}^c_{\tau_k} = \mathbf{S}^c(I_{\tau_k}, :) - \mathbf{D}^*_{\tau_k}\mathbf{R}^c(I_{\tau_k}, :), \tag{5.13}$$

where $\mathbf{D}_{\tau_k}$ is the diagonal block $\bar{\mathbf{M}}(I_{\tau_k}, I_{\tau_k})$. $\mathbf{S}^r_{\tau_k}$ and $\mathbf{S}^c_{\tau_k}$ represent the action of the product between the off–diagonal blocks $\bar{\mathbf{M}}(I_{\tau_k}, I_0 \setminus I_{\tau_k})$, $\bar{\mathbf{M}}(I_0 \setminus I_{\tau_k}, I_{\tau_k})$ with the given set of random matrices [126].

If the selected τ_k is a leaf node, the diagonal block $\mathbf{D}_{\tau_k}$ is stored as a dense matrix. Then, the ID factorization of samples $\mathbf{S}^r_{\tau_k}$ and $\mathbf{S}^c_{\tau_k}$ yields to factors $\mathbf{U}_{\tau_k}$, $\mathbf{V}_{\tau_k}$ and to vectors $J^r_{\tau_k}$, $J^c_{\tau_k}$ that are subsets of I_{τ_k}. Otherwise, if τ_k has children τ_1 and τ_2, $\mathbf{U}_{\tau_k}$ and $\mathbf{V}_{\tau_k}$ together with $J^r_{\tau_k}$ and $J^c_{\tau_k}$ are computed by ID. Then, $\mathbf{U}^{big}_{\tau_k}$ and $\mathbf{V}^{big}_{\tau_k}$ are evaluated with (5.9) by using $\mathbf{U}^{big}_{\tau_1}$ and $\mathbf{V}^{big}_{\tau_2}$ coming from the computation on the lower levels. A consequence of using ID is that $\mathbf{B}_{\tau_1,\tau_2} = \bar{\mathbf{M}}(J^r_{\tau_1}, J^c_{\tau_2})$, and this completes the low–rank approximation.

The randomized sampling avoids the direct access to all the off-diagonal block entries. Nevertheless, the SDP approach cannot be considered entirely matrix–free. Thus, together with an element–access routine, the user has to provide a multiplication routine able to compute sample matrices without storing the whole $\bar{\mathbf{M}}$ matrix. Since ID works on sample matrices, it is able to find the right truncated rank k' that verifies (5.10) only if random matrices contain a sufficient number of columns. Therefore, the user has to generate random matrices such that $k'' > k'$, where the k' is the maximum rank found by ID of low–rank blocks (HSS rank). Furthermore, in contrast to HLIBPro, SDP does not include any clustering algorithm. Thus, a mesh partitioning routine has to be provided by the user in order to split the mesh following the tree structure and then reorder the clusters with the aim to have low–rank off–diagonal blocks.

Once $\bar{\mathbf{M}}$ is obtained in a low–rank form, the problem is solved by means of a fast Cholesky or ULV factorization of the HSS matrix and backward substitution [119, 126], without any refinement of the solution. This solution strategy does not require any preconditioning and is generally very fast and efficient. Instead, the time required for the compression of $\bar{\mathbf{M}}$, due to the nested factorization, is generally greater than the one of HLIBPro. However, considerations concerning the time and the efficiency of the compression are highly problem dependent.

5.3 Challenges in the use of low–rank compression techniques for the PEEC method

Regardless of the method chosen for the compression, when low–rank compression techniques are applied to system of equations derived from PEEC method some issues must be properly addressed.

Even though the coefficients of inductance, potential, and integral interaction PEEC matrices depend on the Green's function (5.1), the PEEC matrix $\bar{\mathbf{M}}$ is generally obtained by combining together all these matrices with projection and incidence matrices. Thus, $\bar{\mathbf{M}}$ may lose its off–diagonal low–rank behavior if some particular issues are not properly addressed.

With the aim of improving the efficiency and the accuracy of the compression techniques, the off–diagonal blocks of $\bar{\mathbf{M}}$ must be actually low–rank. In this regard, HLIBpro library provides a reordering and partitioning algorithm based on geometric bisection which would provide an

excellent HODLR structure of $\bar{\mathbf{M}}$, assuming that the general khth coefficient of $\bar{\mathbf{M}}$ only depends on the inverse of the distance between DoFs kth and hth. However, in the practice, coefficients of $\bar{\mathbf{M}}$ do not only depend on the mutual distances between DoFs. Thus, a reordering and partitioning algorithm based on a pure geometric bisection may be too simplistic and may produce non–optimal HODLR structure of $\bar{\mathbf{M}}$.

When compression techniques based on HODLR structures are applied to PEEC, the choice of the PEEC formulation (e.g. Amperian or Columbian), the choice of the discretization method and unknowns, the use of change of basis techniques, and other arguments which affect the final structure of $\bar{\mathbf{M}}$ must be properly taken into account.

In this regard, some issues to be addressed in the context of low–rank compression techniques applied to PEEC are:

Reordering When different kind of media are considered the partitioning of the unknowns should be performed by forcing the first clustering subdivision collecting all the variables *of the same kind* in a dedicated cluster. Thus, when for instance conductive, dielectric, magnetic media, and lumped circuit elements are considered, the first clustering partition should be carried out with respect of these 4 kind of variables. Then, the clustering partition proceeds by following a geometrical bisection. The same discussion holds when, in the context of structured mesh, vector basis functions with orthogonal directions are used or when boundary and internal unknowns are differently handled. This issue is actually addressed in the *Induction heating pot* and *Embedded Wireless Power Transfer* cases of Section 5.4.

Breakdown in frequency and non–simply connected domains The breakdown in frequency issue discussed in Section 4.2.3 is more severe when compression techniques are applied. Indeed, the compression procedure based on ACA may delete essential information which accounts for the last significant digits of the matrix coefficients. Thus, round–off issues may appear for higher values of the frequency with respect PEEC problems solved with standard direct solvers (i.e. without the use of compression techniques). However, this problem can be overcome by using the loop–star decomposition or other change of basis procedures proposed in Section 4.2.4. However, such techniques must be properly applied in order to maintain a proper HODLR structure of the resulting PEEC system in the new basis. At this aim, when change of basis methods based on independent loop currents are adopted, it is important to ensure a small support of the loop shape functions [6]. This can be achieved in different ways:

a) by using the curl matrix as loop change of basis (see discussion on equation (4.21)) and add extra equations when non–simply connected domains are considered [103],

b) following the approach in [107] where the independent loops search algorithm gives priority to loops with small support,

c) applied the procedure described in Section 4.2.4 based on the use of METIS libraries.

It is worth noting that, while methods *a*) and *b*) provide an optimal or semi–optimal selection of small loops, method *c*) (which allows for an easier implementation) has lower performances. Finally, the breakdown in frequency issue should be avoided also by selecting PEEC systems (3.47) or (3.68) for the compression (ones with scalar potential as unknowns). However, this choice would lead to others issues to be addressed as described in the following paragraphs. The

breakdown in frequency issue is actually addressed *Embedded Wireless Power Transfer* case of Section 5.4.

High frequency and oscillating kernel When high frequency problems are considered (i.e. when retardation effects are significant and the dynamic Green's function is used), due to the oscillating kernel of $\bar{\mathbf{M}}$, standard ACA approaches may fail. Thus, alternative approaches should be adopted for the matrix compression. Numerical results of Section 5.4 (*Dielectric sphere* and *Ion Cyclotron Resonance Heating* cases) shown that the use of an ACA with full pivot search avoids this kind of problem. However, this kind of ACA requires the computation of all the matrix coefficients of $\bar{\mathbf{M}}$ and thus a longer time for the matrix compression with respect traditional ACA methods.

Complex–structure HODLR matrices When matrix $\bar{\mathbf{M}}$ consists of dense off–diagonal blocks and also sparse off–diagonal blocks describing connections between elements (e.g. when lumped circuit elements are considered or when PEEC systems (3.47) and (3.68) are selected for the compression) it is important to do not apply compression techniques to sparse off–diagonal blocks. Thus, a complex–structure HODLR matrix with compressed and sparse (topological) uncompressed off–diagonal blocks must be handled. This is actually possible with the general and highly optimized HLIBPro library. However, such complex–structure HODLR matrix affects the performances in the creation of the $\mathcal{H}$–LU preconditioner.

High–rank matrix blocks When non–simply connected domains are considered and loop unknowns are used, a set of loops with an extended support is inevitably created (the number of this *long* loops is almost equal to the number of holes). This set of loops with extended support (long loops) must be properly treated when compression techniques are actually applied. A first possibility is to group them in a independent cluster. However, this operation may slow down the final construction of the $\mathcal{H}$–LU since, as discussed in the previous paragraph, a complex–structure HODLR matrix must be handled. Indeed, the block matrices which describe the interactions with long loops may be not low–rank. A second possibility proposed by the author during this PhD thesis is to apply the Schur complement to matrix $\bar{\mathbf{M}}$ with the aim to completely neglect the presence of long loops form the unknowns of the system. Thus, subdividing $\bar{\mathbf{M}}$ as

$$\bar{\mathbf{M}} = \begin{bmatrix} \bar{\mathbf{M}}_{11} & \bar{\mathbf{M}}_{12} \\ \bar{\mathbf{M}}_{21} & \bar{\mathbf{M}}_{22} \end{bmatrix}, \tag{5.14}$$

where $\bar{\mathbf{M}}_{22}$ describes the interactions between long–loops unknowns, the Schur complement applied to the PEEC system of equations

$$\begin{bmatrix} \bar{\mathbf{M}}_{11} & \bar{\mathbf{M}}_{12} \\ \bar{\mathbf{M}}_{21} & \bar{\mathbf{M}}_{22} \end{bmatrix} \begin{bmatrix} \mathbf{x}_1 \\ \mathbf{x}_2 \end{bmatrix} = \begin{bmatrix} \mathbf{b}_1 \\ \mathbf{b}_2 \end{bmatrix} \tag{5.15}$$

results in

$$(\bar{\mathbf{M}}_{11} + \bar{\mathbf{M}}_{12}\bar{\mathbf{M}}_{22}^{-1}\bar{\mathbf{M}}_{21})\mathbf{x}_1 = \mathbf{b}_1 - \bar{\mathbf{M}}_{12}\bar{\mathbf{M}}_{22}^{-1}\mathbf{b}_2, \tag{5.16}$$

where $\mathbf{x}_2$ (long–loops unknowns) are not present. It is worth noting that for practical industrial application the number of holes in non–simply connected domains is generally very small. Thus, $\bar{\mathbf{M}}_{22}$ is a small square matrix which can be easily inverted. Moreover, $\bar{\mathbf{M}}_{12}\bar{\mathbf{M}}_{22}^{-1}\bar{\mathbf{M}}_{21}$ is

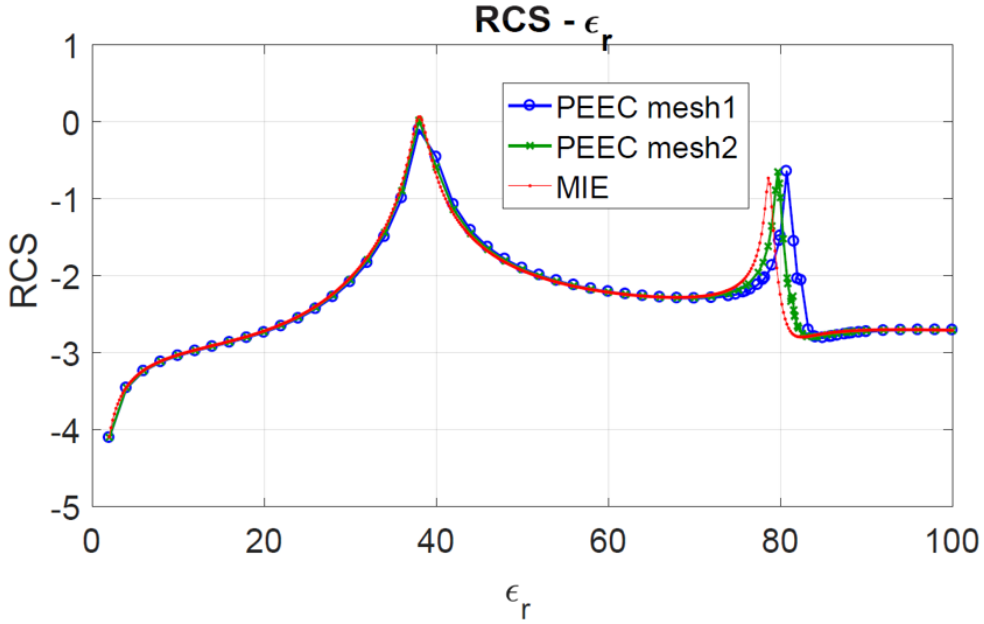

Figure 5.2: RCS of a dielectric sphere excited by a plane wave at 30 MHz vs the permittivity value.

a low–rank matrix of rank equal to the rows of $\bar{\mathbf{M}}_{22}$ since it satisfies (5.2). Thus, if $\bar{\mathbf{M}}_{11}$ is a low–rank matrix, system (5.16) has still low–rank off–diagonal blocks. Furthermore, low–rank compression techniques can be applied to $\bar{\mathbf{M}}_{11} + \bar{\mathbf{M}}_{12}\bar{\mathbf{M}}_{22}^{-1}\bar{\mathbf{M}}_{21}$ in two possible ways: 1) by directly considering $(\bar{\mathbf{M}}_{11} + \bar{\mathbf{M}}_{12}\bar{\mathbf{M}}_{22}^{-1}\bar{\mathbf{M}}_{21})$, or 2) by compressing $\bar{\mathbf{M}}_{11}$ and $\bar{\mathbf{M}}_{12}\bar{\mathbf{M}}_{22}^{-1}\bar{\mathbf{M}}_{21}$ and then efficiently performing the matrix summation in $\mathcal{H}$–matrix algebra. Finally, it is worth noting that when the support of the long loops is actually relatively small (which is the case of devices with relatively small holes), long loops can be treated as small loops without any particular attention.

5.4 Numerical results

In this Section, HLIBPro v2.7 and SDP v1.1.1 are applied to the PEEC method for the study of different test cases. The simulations were run on a Linux machine equipped with dual 6-core/24-thread processors (Xeon E2543 v4 @3.40GHz) and 500 GB of RAM.

Dielectric sphere

When the scattering from dielectric and magnetic media is considered, the frequency values are higher than typical values fpr the breakdown in frequency. Thus, the PEEC system of equations (4.16) can be used. However, when high frequency problems involving dielectric or magnetic media with high values of permittivity and permeability are considered, VIE methods (such as the PEEC method) require a very fine mesh. This issue, shortly discussed in *Material coefficients of A–PEEC and C–PEEC methods* in Section 4.2.3, is widely discussed in [128, 100, 129]. Indeed, with the increasing of the permittivity (or permeability) and the frequency, the polarization current density distribution inside the media shows a really complicated behavior and internal resonances appear. Thus, the adopted shape functions cannot easily capture the

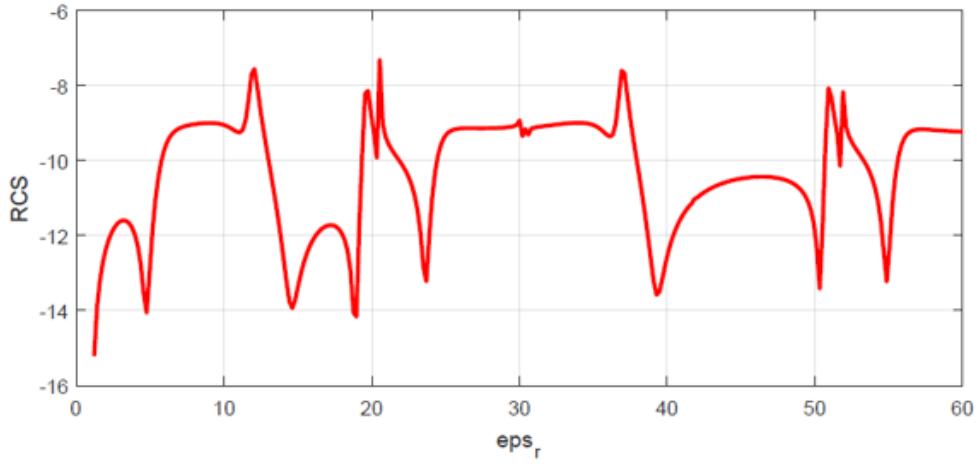

Figure 5.3: RCS of a dielectric sphere excited by a plane wave at 60 MHz vs the permittivity value.

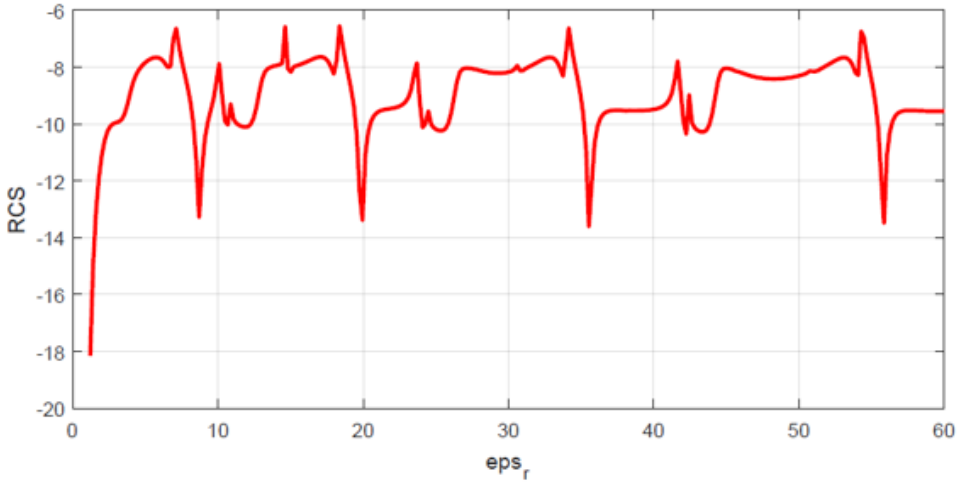

Figure 5.4: RCS of a dielectric sphere excited by a plane wave at 100 MHz vs the permittivity value.

oscillation of the electromagnetic fields. Therefore, a very fine mesh should be adopted when high permittivity (or permeability) and frequency values are considered.

In this regard, Fig. 5.2 shows the Radar Cross Section (RCS) of a 1 m dielectric sphere excited by a plane wave at 30 MHz versus the value of the permittivity. Results obtained form the MIE solution and from the (uncompressed) PEEC method with a mesh of $\sim$ 8,300 tetrahedral elements (PEEC mesh1) and $\sim$ 16,400 tetrahedral elements (PEEC mesh2) are compared.

Instead, Fig. 5.3 and Fig. 5.4 show the results obtained from the MIE solution of the same dielectric sphere excited by a plane wave at 60 MHz and 100 MHz, respectively. As can been seen, many internal resonances appears with the increasing of the frequency. Such discussion motivates the use of compression techniques when scattering from high contrast dielectric and magnetic media is considered, since a high number of DoFs is required to capture the internal resonances.

The academic case of the RCS of a high–contrast homogeneous dielectric sphere (radius 1 m, $\varepsilon_r = 80$), excited by a linearly polarized wave $\mathbf{E}_0 = e^{-ik_0 x}\mathbf{u}_z$, $f = 10$ MHz, is now considered in the context of compression techniques. This case is also reported in [130] in the context of a collaboration with a a group of researcher from the RFX Consortium, Padova. A fine mesh

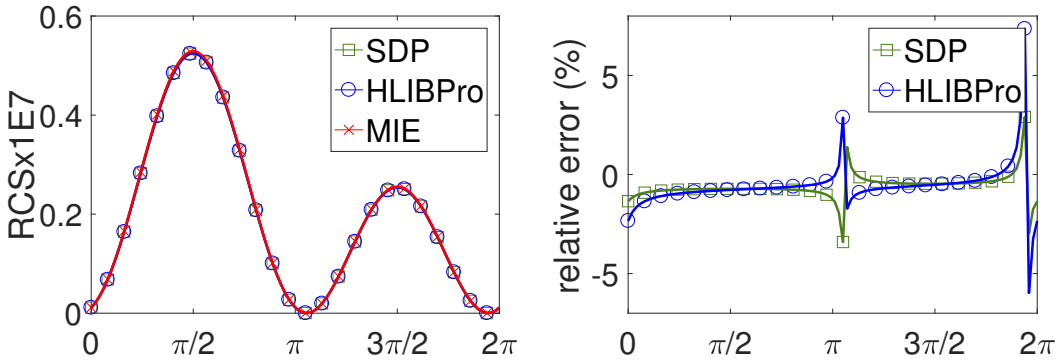

Figure 5.5: RCS along a yz–circular target, distance 500 m.

Table 5.1: CR and TRs of the Sphere case — HLIBPro & SDP

	HLIBPro	SDP	Dense
ε	10^{-3}	10^{-6}	-
TR compression (%)	184	209	13,851 (s)
TR solution (%)	75	5.1	12,394 (s)
TR tot. (%)	132	112	26,245 (s)
CR (%)	11	9.1	–
HSS rank (k')	–	6,578	–
PMU (%)	22	19.6	287 (GB)

with 133,921 unknowns with volumetric support is adopted, leading to a dense matrix of 287 GB RAM for its storage.

HLIBPro and SDP are adopted to solve the PEEC system of equations (4.16) with the aim of comparing their performances when oscillating kernels are considered.

Fig. 5.5 compares the RCS evaluated by using the two libraries with the MIE [131] analytical solution implemented in the open–source MATLAB® toolbox [132].

In Table 5.1 the computational performances obtained by applying HLIBPro and SDP libraries are shown and compared with those required by the solution of the original (uncompressed) system (4.16) by means of an LU decomposition. The compression ratio (CR), which expresses the memory ratio between the approximate and the dense versions of the PEEC matrix $\bar{\mathbf{M}}$, and the peak memory usage (PMU) are also given. Moreover, the time ratios (TR) for the matrix computation and the system solution, with respect to the ones for the dense case, are reported.

During the compression phase, SDP requires the storage of random and sample matrices, with dimension at least $N \times k'$, together with the approximate version of $\bar{\mathbf{M}}$. On the contrary, HLIBPro has to store in addition the LU factors of the compressed matrix for the solver preconditioner, that leads to almost comparable PMU.

Due to the high frequency of the problem and the oscillating kernel of $\bar{\mathbf{M}}$, an ACA with full pivot search has been adopted for improving the convergence of the HLIBPro compression process. It is worth noting that, at the expense of a greater computation time due to the randomized sampling, SDP allows for a very fast solution of the final system of equations thanks

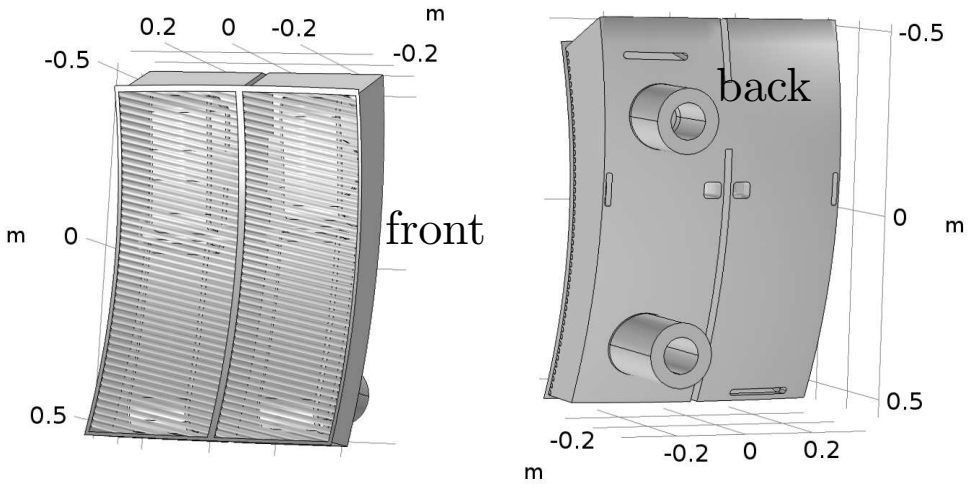

Figure 5.6: ICRH device geometry (dimensions in m). Courtesy of ICRH group, Max–Plank Institute for Plasmaphysics, Garching, Germany.

to the efficiency of the ULV factorization of the HSS matrix.

Ion Cyclotron Resonance Heating

The second test case consists in a more complex device used for the Ion Cyclotron Resonance Heating (ICRH) of plasma in fusion machines, see Fig. 5.6 [133]. The Faraday screen in the frontal part of the device is used as a scatterer of the electromagnetic wave emitted by the internal antennas. These results are also reported in [130].

The device is fed by two lumped ports, placed on the back, with $|\mathbf{J}| = 1$ A/m^2 at a 100 MHz frequency. The model consists of 141,031 unknowns with surface support (i.e. an equivalent 2–D PEEC model discussed in Section 3.4.1 has been adopted), leading to a full matrix of 318.24 GB. Thus, the PEEC system obtained by Schur complement of (3.122) with only electric currents as unknowns has been selected. Also for this case, HLIBPro and SDP are adopted to solve the PEEC system of equations.

With the aim to compare the performances of the two libraries, the compression tolerance are varied from 10^{-3} to 10^{-5} for HLIBPro and from 10^{-6} to 10^{-8} for SDP. Results are also compared with the computational cost required for the solution of the uncompressed PEEC system. In Fig. 5.7 the magnitude of the imaginary part of $\mathbf{E}$, evaluated along a line perpendicular to the antenna surface, is compared with the results obtained by solving the uncompressed system (REF).

Table 5.2 summarizes the most significant computational performances of HLIBPro and SDP, respectively. The Root Mean Square Error (RMSE) of the solution vectors with respect the one obtained from the dense system is also given in the table. In spite of obtaining very accurate solutions with small and comparable CR, the two libraries work on a different range of compression tolerances. In SDP, the absence of a solution refinement requires a sufficiently accurate approximation of $\bar{\mathbf{M}}$. On the other hand, the iterative solver used in HLIBPro, admits a worst low–rank approximation, but it requires a longer time for the system solution.

Comparing the results obtained for the *Dielectric sphere* case and the *ICRH* case, it appears that, although having almost the same number of unknowns, in the sphere case the time required

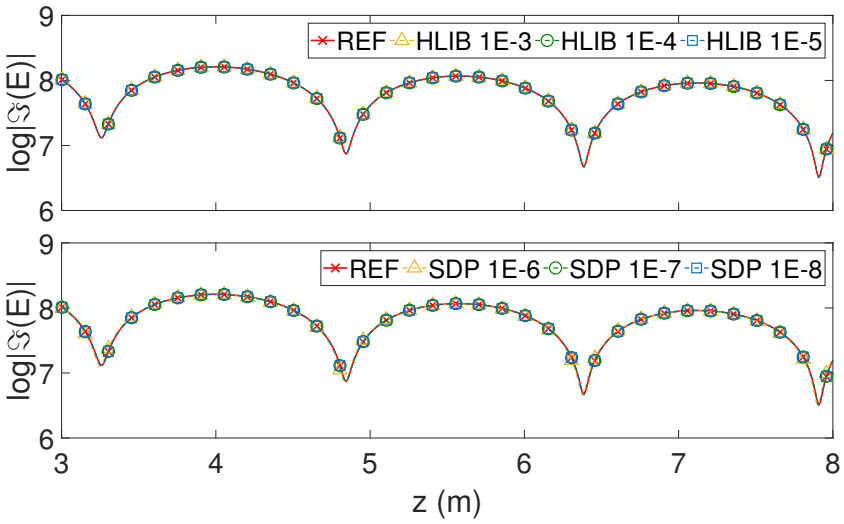

Figure 5.7: $log|\Im(\mathbf{E})|$ along a line (top: HLIBPro, bottom: SDP)

Table 5.2: CR and TRs of the ICRH case — HLIBPro & SDP

HLIBPro ε_{ACA}	10^{-3}	10^{-4}	10^{-5}	Dense
TR compression (%)	183	185	187	4,338 (s)
TR solution (%)	41	67.6	120	14,546 (s)
TR tot. (%)	74	95	135	18,884 (s)
CR (%)	5.3	7.8	10.5	–
PMU (%)	10.6	15.5	21	318.24 (GB)
RMSE ($\cdot 10^{-4}$)	7.31	0.72	0.12	–
SDP ε_{ID}	10^{-6}	10^{-7}	10^{-8}	Dense
TR compression (%)	339	352	535	4,338 (s)
TR solution (%)	2.0	3.4	5.5	14,546 (s)
TR tot. (%)	79	83	127	18,884 (s)
CR (%)	4.5	6	9.5	–
HSS rank (k')	3,998	4,842	5,860	–
PMU (%)	15.9	19.8	26.1	318.24 (GB)
RMSE ($\cdot 10^{-4}$)	18.1	1.8	0.3	–

for compression is much larger. This is mainly due to the different computational efficiency of the element–access routines (i.e. volumetric vs. superficial). It is worth mentioning that high–frequency problems are not easily compressible because of the oscillatory behavior of the retarded Green's kernel. Hence some blocks, labeled by either library as rank–deficient, may actually be almost full–rank. In HLIBPro, improved ACA methods may fail in rapidly converging to a small set of pivoting rows and columns for such blocks, hence a full pivoting ACA could give better performances. Moreover, to avoid ACA working on big clusters that may have very high ranks, the η parameter can be set to small values (e.g. $0.5 \div 1$) that makes only the smaller blocks admissible.

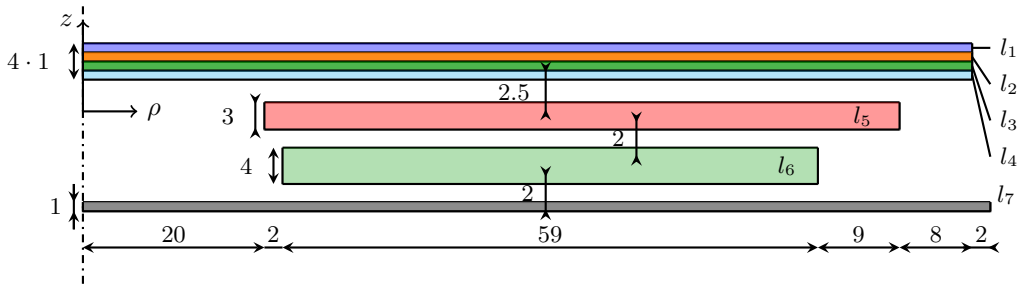

Figure 5.8: Axisymmetric model of the induction cookware. Dimensions are in mm. l_1) Stainless Steel, l_2) Aluminum, l_3) Magnetic Steel, l_4) Stainless Steel, l_5) External coil, l_6) Ferrite (flux concentrator), l_7) Aluminum (shield).

Table 5.3: Material parameters of the induction heating pot.

	l_1	l_2	l_3	l_4	l_6	l_7
σ [MS/m]	1.04	29.1	$a)0$ $b)2$	1.04	0	29.1
μ_r	1	1	$400 - i175$	1	2300	1

The accuracy of the results, as well as the CR and TR, shows that the PEEC formulation for high frequency problems can be effectively coupled with low-rank approximations. The performances are highly problem–dependent and, because of the oscillatory kernel, may not be so promising like in low–frequency problems [134]. Nevertheless, the application of the PEEC formulation to devices with complex geometries would not be possible without compression. HLIBPro and SDP demonstrated to be the powerful tools also when high frequency problems are considered that require a careful setting of their parameters to obtain the best performances. Finally, the development of more efficient element-access routines would reduce the absolute times in matrix assembling, and the compression times would scale with almost the same TRs presented.

Induction heating pot

With the aim of showing the performances of HLIBPro when applied for the solution of matrix systems with smooth kernels, the case of the Induction Heating Pot presented in [135] is here considered by means of the Axisymmetric PEEC methods presented in Appendix B and based on the Amperian and Coulombian interpretation of the magnetization phenomena.

Two algorithms based on the two proposed integral axisymmetric formulations have been implemented in MATLAB® and parallel MEX–FORTRAN functions based on OpenMP libraries. Moreover, the code has been also combined with HLIBpro library in a *matrix–free* logic. Thus, when HLIBPro is adopted, PEEC systems (B.41) (Amperian) and (B.82) (Coulombian) are never actually assembled and stored. In the following, the (axisymmetric) code based on the formulation of Section B.1 is defined as *A–code* (Amperian code) while the one based on Section B.2 is defined as *C–code* (Coulombian code). Thus, such numerical test case also allows for comparing the two axisymmetric PEEC formulations proposed in appendix B and based on the two PEEC formulations proposed in Chapter 2 (i.e. Amperian vs Coulombian).

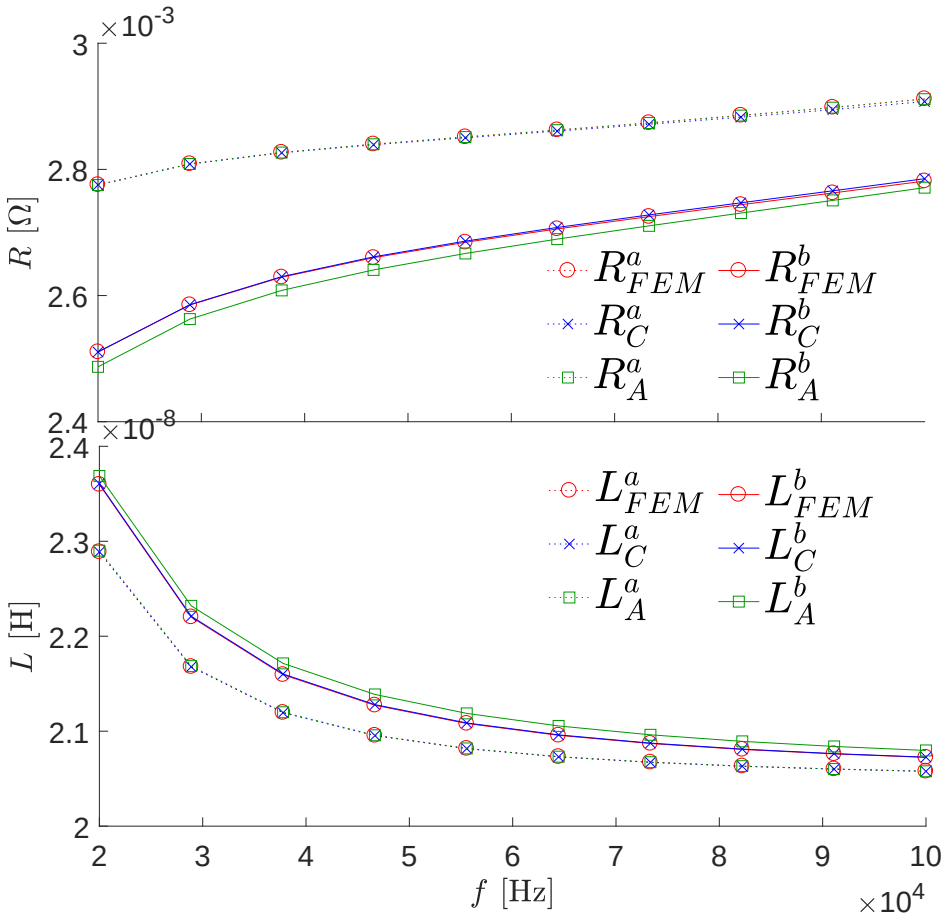

Figure 5.9: Z_{eq} of the induction cookware. Results obtained from A–code, C–code, and FEM for cases (a) and (b).

The geometry of the problem is completely described by Fig. 5.8. With respect of Fig. 5.8, layers l_1, l_2, l_3, and l_4 constitute the bottom part of the pot, layer l_5 is the external current–driven coil (the problem excitation), l_6 is the magnetic flux concentrator, and l_7 is the shield for th electronic components. The material parameters of the pot layers are the ones in Table 5.3. With the aim of investigating the numerical behavior of the A– and C–codes under different conditions, the magnetic steel (layer l_3 in Fig. 5.8) is modeled in two different ways: a) by non conductive magnetic media, and b) by conductive magnetic media with a conductivity of 2 MS/m. The frequency of the problem, f, is swept from 20 kHz to 100 kHz. The equivalent impedance of the device, with respect to a uniform (external) current flowing in the external coil, is modeled as $Z_{eq} = R + i\omega L$ and evaluated with the two proposed methods. Due to the strong skin effects (skin depth of $\delta \approx 0.06$ mm for the worst case), a great amount of mesh elements is required for the discretization of the conductive layers. Thus, the mesh of the induction cookware model consists of 54,120 conductive quadrilateral faces and 16,680 magnetic quadrilateral faces. With the aim of allowing a fair comparison, the same mesh is adopted for the A– and C–codes.

In Fig. 5.9, the results obtained from A–code and C–code are compared with the ones from the commercial Finite Element Method software COMSOL®, which allows for a very efficient solution of this kind of device and therefore is considered as a reference. The axisymmetric FEM model consists of 64,847 mesh elements and third order basis function.

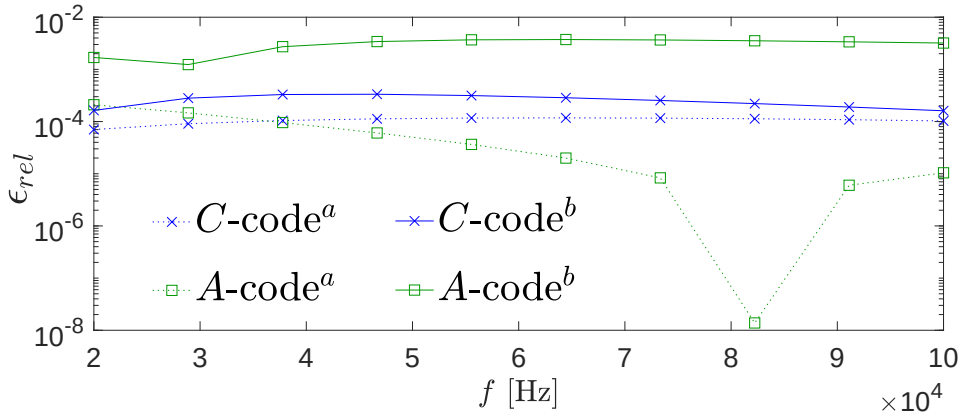

Figure 5.10: Relative error of $|Z_{eq}|$ for A–code and C–code for cases (a) and (b).

Table 5.4: Induction cookware: Computational Data

	N_{DoFs}	Time [s]	PMU [GB]
FEM	1,029,074	55	4.36
Uncompressed A–code*	88,307	432^a+$3{,}408^s$	238
Compressed A–code$^\#$	88,307	7^a+43^s	2.8
Uncompressed C–code*	88,307	335^a+$3{,}308^s$	238
Compressed C–code$^\#$	88,307	7^a+44^s	3.0

^{a}Assembling. ^{s}Solution.

Fig. 5.10 shows the relative error of the magnitude of Z_{eq} obtained from A–code and C–code with respect to FEM for both cases (a) and (b).

Results in Fig. 5.9 and Fig. 5.10 show an excellent agreement when case (a) is considered. For case (a), the simulations have been carried out with and without the imposition of (B.42) and (B.84), i.e. (axisymmetric change of basis). However, as expected, even if a little distortion on the distribution of $\mathbf{M}$ is obtained when (B.42) and (B.84) are not enforced, the results in terms of Z_{eq} differ less than 0.05%.

For case (b), C–code still shows an excellent agreement with FEM. A–code instead shows a lower accuracy, especially for the real part of Z_{eq} which is more affected by the actual distribution of $\mathbf{M}$, that is not enforced in a numerically strong sense (in accordance with the discussion in Section 4.2.3 and Section 4.2.4). Indeed, it is worth noting that for case (b), since a conductive magnetic media is considered, (B.42) cannot be enforced since $\mathbf{M}$ is not curl free.

Moreover, due to round–off errors, the A–code is very sensitive to the accuracy of the numerical integrations. However, due to the numerical nature of round–off errors, a higher accuracy in the computation of the integral matrices does not ensure to avoid this numerical issue. For the sake of comparison, the same number of Gauss points has been chosen for the A– and C–codes.

In Table 5.4 the computational details of the two methods are reported for case (b) and $f = 100$ kHz. For the A and the C–codes, the computational time and the Peak Memory Usage (PMU) are reported with and without the adoption of low–rank approximation techniques. The

results of Table 5.4 have been obtained *without* the imposition of (B.42) and (B.84) (axisymmetric change of basis), the compression tolerance described in Section 5.2.1 is set to $\varepsilon_{ACA} = 10^{-3}$ (much lower than the ones adopted for the 3–D cases of the dielectric sphere and the ICRH previously considered) and the admissibility parameter is $\eta = 2$. With this choice of ε_{ACA}, the relative error introduced by the low–rank approximation on the solution is less than 1%. Thus, it is safe to say that the errors introduced by the low–rank approximation do not noticeably affect the accuracy (results shown in Fig. 5.9 are the ones obtained from HLIBpro).

With respect Table 5.4, for the uncompressed case the problem is solved with an LU decomposition of the matrix system. Instead, as discussed in Section 5.2.1, the compressed case is solved by means of GMRES solver with an $\mathcal{H}$–LU preconditioner. Thus, the solution time includes both the $\mathcal{H}$–LU and the GMRES solution. For both the uncompressed and compressed cases, the PMU almost coincides with the memory required for the storage of the system matrices and LU factorizations. The $\mathcal{H}$–LU is generated by imposing the same tolerance ε_{ACA} and its storage requires almost the same memory of the compressed system. As can been seen from Table 5.4, due to the big size of the problem, the use of low–rank approximation techniques is mandatory. Indeed, thanks to the remarkable smoothness of axisymmetric Green's function (i.e. the kernel of the PEEC matrix $\bar{\mathbf{M}}$), the adoption of HLIBpro library allows for a drastic reduction of the computational cost required by the PEEC methods which become comparable with the highly optimized FEM commercial software for this kind of application.

Embedded Wireless Power Transfer

This section is the result of a collaboration with the Department of Energy "G. Ferraris", Politecnico di Torino, Italy, in the context of the numerical modeling of road embedded transmitting wireless power transfer coil. Results reported here are the ones in [136].

Several research projects are demonstrating that the wireless power transfer (WPT) for the charge of electric vehicles (EVs) can represent an effective technology to boost their widespread adoption. The system developed by the Politecnico di Torino, named PoliTO Charge While Driving, has been oriented to the direct embedment of the transmitters in the road pavement for an easier installation and a reduction of the maintenance. However, the direct embedment of the coils in the road pavement incurred in significant technical issues since the behavior of the embedded coil strongly deviated from the expected one. Measurements only did not allow for fully understanding and quantifying the physical phenomena causing these modifications.

In this regard, with the aim of understanding and quantifying how the electromagnetic parameters of the concrete and the geometrical parameters of the WPT influence the overall device behavior, an ad–hoc numerical method which couples the PEEC method with low–rank compression techniques has been developed.

Embedded WPT coil experiment The first experiment of embedment was with the transmitter depicted in Fig. 5.11, having inner dimensions 1.25 m $\times$ 0.5 m and consisting of 9 turns of litz wire with a diameter of 4 mm. The coil was buried between two layers of non–reinforced concrete, i.e. without rebar in order to prevent any possible alteration of the distribution of magnetic field produced by the coil. The equivalent impedance Z_{eq} of the coil was preliminary measured in laboratory conditions (i.e. far from metallic objects) at 85 kHz by means of an LCR meter. The measured Z_{eq} was interpreted as the series of a lumped resistance R and an inductance L having values of 303 mΩ and 211.8 μH, respectively.

Figure 5.11: Road–embedment of the 9–turns WPT in dry concrete.

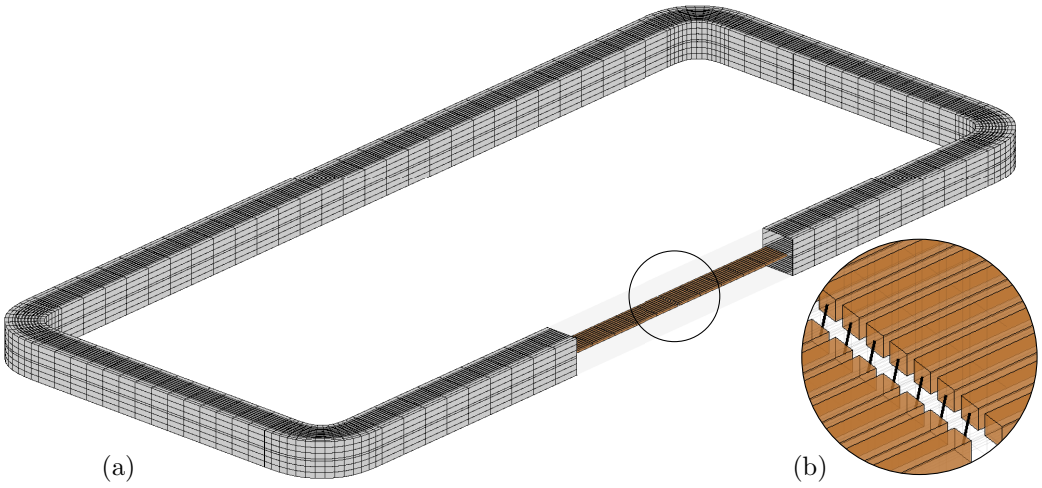

Figure 5.12: PEEC model of the embedded coil. (a) Full model. (b) Detail of the connection between the 9 coil turns and the lumped shorts.

Measurements carried out after the embedment in dry concrete revealed a strong non–linear dependence of Z_{eq} on the frequency above 60 kHz. This behavior showed that the embedded coil cannot be properly modelled as an equivalent R–L circuit with constant lumped parameters. Moreover, capacitive stray currents strongly limiting the effectiveness of the wireless transmission occurred.

With the aim of quantifying the effects of the electromagnetic parameters of the concrete on the overall coil behavior, a dedicated PEEC model of the embedded device was constructed. Resistivity and permittivity of standard concretes may vary in a very wide range and they are strongly affected by the water content and external environmental parameters. Thus, a dedicated measurement arrangement for the characterization of the concrete adopted for the embedment of the coil was carried out. Such study identified a range from 10 Ωm to 1000 Ωm for the concrete resistivity ρ_c, and from 5 to 50 for the concrete permittivity ε_{r_c}.

Parametric sweep and Low–Rank compression In this section, the numerical procedure developed to optimize the parametric analysis by means of PEEC is described. For the case of the embedded WPT device described above, only conductive and dielectric media are involved.

In order to reduce the complexity of the mesh (i.e. the number of unknowns), the 9 turns of the WPT are modelled as 9 independent open turns which are connected with lumped short circuits, as shown in Fig. 5.12. The coil is fed by a lumped voltage source connected to the terminals of the most internal and external turns. Since the litz wires guarantee an almost uniform current distribution at the frequency range of interest, the 9 turns are modelled with only one mesh element in the cross section adopting a conductivity of $\sigma_t = 57{\cdot}10^6$ S/m.

Thus, identifying the 9 turns (plus lumped elements) and the concrete with subscripts t and c, respectively, the algebraic system of equations (4.16) derived by applying PEEC method to the embedded WPT model can be written as

$$\begin{bmatrix} \mathbf{R}_t + \mathbf{B}_{tt} & \mathbf{B}_{tc} \\ \mathbf{B}_{ct} & \mathbf{R}_c + \mathbf{B}_{cc} \end{bmatrix} \begin{bmatrix} \mathbf{j}_t \\ \mathbf{j}_c \end{bmatrix} = \begin{bmatrix} \mathbf{e}_t \\ \mathbf{0} \end{bmatrix}, \tag{5.17}$$

where $\mathbf{B}_{\alpha\beta} = i\omega\mathbf{L}_{\alpha\beta} + \frac{1}{i\omega}\mathbf{D}_\alpha^{aT}\mathbf{P}_{\alpha\beta}\mathbf{D}_\beta^a$ (with $\alpha = t, c$ and $\beta = t, c$).

Before applying low–rank compression techniques, the problem must be properly handled in order to improve the compression performances. In this regard, following the discussion of Section 5.3, two main issues must be addressed: 1) the well–known breakdown in frequency issue would lead to severe round–off errors which would make compression techniques very inaccurate, and 2) both the concrete and turns are non–simply connected regions which require to be properly handled.

To solve the breakdown in frequency issue, the loop–star decomposition method is adopted. Thus, following the discussion in 4.2.4, change of basis matrices $\mathbf{M}_\alpha^\circ$ (loop to currents) and $\mathbf{M}_\alpha^\star$ (star to currents) are evaluated. Since both the concrete and the turns models are non–simply connected regions, the independent loops search algorithm proposed in [137] is adopted in order to generate independent loops giving priority to that ones with small support. This technique generates a small number of loops with large support (i.e. almost equal to the number of holes) ensuring a good low–rank behavior of the resulting system of equations [6]. Matrix $\mathbf{M}_\alpha^\star$ instead is easily obtained from the incidence matrix $\mathbf{D}_\alpha^a$ by removing one column and taking its transpose.

Once obtained $\mathbf{M}_\alpha^\circ$ and $\mathbf{M}_\alpha^\star$, the Loop–Star quasi–Helmholtz decomposition (4.26) can be applied to $\mathbf{j}_t$ and $\mathbf{j}_c$, i.e. $\mathbf{j}_c = \mathbf{M}_c^c\mathbf{j}_c^\circ + \mathbf{M}_c^\star\mathbf{j}_c^\star$, where $\mathbf{j}_c^\circ$ and $\mathbf{j}_c^\star$ are the loop and star unknowns, respectively (the same holds for $\mathbf{j}_c$). Therefore, matrix rows of (5.17) can be projected into a new set of equations by left multiplying them by $[\mathbf{M}_\alpha^\circ, \mathbf{M}_\alpha^\star]^T$. This results in (4.37). Thanks to the Loop–Star quasi–Helmholtz decomposition, the resulting new system of equations, in the unknowns $\mathbf{j}_t^\circ$, $\mathbf{j}_t^\star$, $\mathbf{j}_c^\circ$ and $\mathbf{j}_c^\star$, does not suffer the breakdown in frequency.

The resulting system in the loop–star basis is now suitable for the application of low–rank approximation techniques. In the context of parametric analysis, when the material parameters of the concrete change, only matrix $\mathbf{R}_c$ in (5.17) changes while all the other matrices remain unchanged. Thus, differently from the previous numerical cases considered in this section where the entire PEEC system has been compressed, the system of equations to be solved (i.e. (4.37)) is here written as

$$\left[\bar{\mathbf{M}}_1 + \bar{\mathbf{M}}_2\right]\left[\mathbf{j}_t^{\circ\star}, \mathbf{j}_c^{\circ\star}\right]^T = \left[\mathbf{e}_t^{\circ\star}, \mathbf{0}\right]^T, \tag{5.18}$$

where $\mathbf{j}_c^{\circ\star} = [\mathbf{j}_c^\circ, \mathbf{j}_c^\star]$, $\mathbf{j}_t^{\circ\star} = [\mathbf{j}_t^\circ, \mathbf{j}_t^\star]$, $\mathbf{e}_t^{\circ\star} = [\mathbf{e}_t^\circ, \mathbf{e}_t^\star]$, and

$$\bar{\mathbf{M}}_1 = \begin{bmatrix} \mathbf{0} & \mathbf{0} \\ \mathbf{0} & \mathbf{R}_c^{\circ\star} \end{bmatrix}, \quad \bar{\mathbf{M}}_2 = \begin{bmatrix} \mathbf{R}_t^{\circ\star} + \mathbf{B}_{tt}^{\circ\star} & \mathbf{B}_{tc}^{\circ\star} \\ \mathbf{B}_{ct}^{\circ\star} & \mathbf{B}_{cc}^{\circ\star} \end{bmatrix}, \tag{5.19}$$

and superscript "$\circ\star$" denotes the projection onto the loop–star basis. Thus, to drastically minimize the computational effort required by the parametric analysis, the low–rank dense matrix $\bar{\mathbf{M}}_2$ can be compressed only once at the beginning of the parametric analysis by applying the low–rank approximation method described in Section 5.2.1 and based on $\mathcal{H}$–matrices and ACA implemented in the HLIBPro library [115]. It is worth noting that, how stated in Section 5.2.1, $\bar{\mathbf{M}}_2$ is evaluated in a *matrix–free* logic thanks to the functionality of HLIBPro. Thus, the dense matrix is never stored and, thanks to ACA, only a set of its coefficients is actually evaluated.

Sparse matrix $\bar{\mathbf{M}}_1$ (converted in $\mathcal{H}$–matrix thanks to the functionality of HLIBPro) is instead updated at each parametric evaluation by setting the value of the equivalent electric resistivity of the concrete ρ_{eq_c} (i.e. ρ_c and ε_{rc}), with a negligible computational effort (indeed, the concrete is considered as an homogeneous material). Thus, compressed matrices $\mathcal{H}$–$\bar{\mathbf{M}}_1$ and $\mathcal{H}$–$\bar{\mathbf{M}}_2$ are added together in $\mathcal{H}$-matrix algebra, i.e. $\mathcal{H}$–$\bar{\mathbf{M}} = \mathcal{H}$–$\bar{\mathbf{M}}_1 + \mathcal{H}$–$\bar{\mathbf{M}}_2$.

System $\mathcal{H}$–$\bar{\mathbf{M}}$ is finally solved for each value of the parameter ρ_{eq_c} by means of a GMRES solver (implemented in HLIBPro) and preconditioned with an incomplete $\mathcal{H}$–LU decomposition. In this regard, there are two possibilities: 1) evaluate the $\mathcal{H}$–LU preconditioner of $\mathcal{H}$–$\bar{\mathbf{M}}$ at each parametric evaluation, and 2) using a pre–evaluated $\mathcal{H}$–LU preconditioner obtained by imposing a mean value of the parameter ρ_{eq_c}. At the expense of a greater computational effort due to the need of evaluating the $\mathcal{H}$–LU at each parametric evaluation, the first choice allows for a very robust solver which requires only few GMRES iterations. However, numerical simulations showed that the use of a pre–evaluated $\mathcal{H}$–LU preconditioner is sufficient to guarantee a very good convergence of the GMRES, drastically reducing the overall computation time.

Finally, from the discussion in Section 5.3, it is worth noting that, in order to obtain $\mathcal{H}$–matrices with actually low–rank off–diagonal blocks (i.e. HODLR matrices), it is important to force the first clustering partition of the unknowns by subdividing $\mathbf{j}_t^\circ$, $\mathbf{j}_t^\star$, $\mathbf{j}_c^\circ$ and $\mathbf{j}_c^\star$ into different clusters. Moreover, loop unknowns should be further subdivided into two clusters: the ones with local support (small loops), and the ones with extended support (long loops). Then, as described in Section 5.2.1, the partitioning algorithm proceeds with the construction of the cluster tree starting from these master cluster nodes.

The above procedure is summarized in Algorithm 1, which implements both the preconditioning possibilities. The inputs of such algorithm are *fun-GetEntry*-$\bar{\mathbf{M}}_1$ and *fun-GetEntry*-$\bar{\mathbf{M}}_2$ which evaluates a generic entry of $\bar{\mathbf{M}}_1$ and $\bar{\mathbf{M}}_2$, respectively.

It is worth noting that, when a single simulation is considered, the long loops unknowns can also be removed by means of the Schur complement method (5.16) proposed in Section 5.3. However, this solution is not convenient in the context of parametric analysis since at each parametric evaluation the Schur complement must be re–evaluated.

Results In this paragraph, the results obtained from the numerical method proposed above applied to the embedded WPT coil described above are reported.

Before performing the parametric analysis, for validation purposes and to construct an efficient PEEC model of the embedded WPT device, the results of the simulations have been compared with those obtained from measurements considering a concrete having measured resistivity and permittivity of 11.8 Ωm and 26.7, respectively. Such comparison is reported in Fig. 5.13, showing a good accordance. Then, the thickness of concrete which is actually significant for the PEEC model has been investigated. In this regard, the frequency sweep simulation was repeated with a progressively smaller concrete model cross section until a difference of about

Algorithm 1 Parametric Analysis of the embedded WPT coil

Input: *fun-GetEntry-*$\bar{\mathbf{M}}_1$, *fun-GetEntry-*$\bar{\mathbf{M}}_2$
Output: $Z_{eq}(\rho_{eq_c})$ of the embedded WPT coil
Initialisation
Compute and store $\mathcal{H}$–$\bar{\mathbf{M}}_2$
Set the mean value of ρ_{eq_c}, i.e. $\bar{\rho}_{eq_c}$
Compute $\mathcal{H}$–$\bar{\mathbf{M}}_1(\bar{\rho}_{eq_c})$
Compute $\mathcal{H}$–$\bar{\mathbf{M}}(\bar{\rho}_{eq_c}) = \mathcal{H}$–$\bar{\mathbf{M}}_1(\bar{\rho}_{eq_c}) + \mathcal{H}$–$\bar{\mathbf{M}}_2$
Compute and store $\mathcal{H}$–LU$(\bar{\rho}_{eq_c})$ of $\mathcal{H}$–$\bar{\mathbf{M}}(\bar{\rho}_{eq_c})$
Parametric analysis
for all the selected values of ρ_{eq_c} **do**
  Compute $\mathcal{H}$–$\bar{\mathbf{M}}_1(\rho_{eq_c})$
  Compute $\mathcal{H}$–$\bar{\mathbf{M}}(\rho_{eq_c}) = \mathcal{H}$–$\bar{\mathbf{M}}_1(\rho_{eq_c}) + \mathcal{H}$–$\bar{\mathbf{M}}_2$
  Solve (5.18) with GMRES and $\mathcal{H}$–LU$(\bar{\rho}_{eq_c})$ precond.
  if GMRES does not converge **then**
    Compute $\mathcal{H}$–LU(ρ_{eq_c}) of $\mathcal{H}$–$\bar{\mathbf{M}}(\rho_{eq_c})$
    Solve (5.18) with GMRES and $\mathcal{H}$–LU(ρ_{eq_c}) precond.
  end if
  From Loop–Star to currents: $\mathbf{j}_\alpha = \mathbf{M}_\alpha^\circ \mathbf{j}_\alpha^\circ + \mathbf{M}_\alpha^\star \mathbf{j}_\alpha^\star$
  Evaluate $Z_{eq}(\rho_{eq_c})$ of the embedded WPT coil
end for
return Z_{eq} for all the selected values of ρ_{eq_c}

Table 5.5: Computation time and memory requirement of Algorithm 1 for the case of WPT PEEC model.

	Time [s]	Memory [GB]
$\mathcal{H}$–$\bar{\mathbf{M}}_2$	88.9	2.0
$\mathcal{H}$–$\bar{\mathbf{M}}_1(\bar{\rho}_c)$ and $\mathcal{H}$–$\bar{\mathbf{M}}_1(\rho_c)$	1.1	$12 \cdot 10^{-3}$
$\mathcal{H}$–$\mathbf{A}(\bar{\rho}_c) = \mathcal{H}$–$\bar{\mathbf{M}}_1(\bar{\rho}_c) + \mathcal{H}$–$\bar{\mathbf{M}}_2$	1.3	2.0
$\mathcal{H}$–LU$(\bar{\rho}_c)$ of $\mathcal{H}$–$\bar{\mathbf{M}}(\bar{\rho}_c)$	57.7	1.9
GMRES solution of $\mathcal{H}$–$\bar{\mathbf{M}}(\rho_c)$	11.2	–

3% in the amplitude of Z_{eq} was reached. This study showed that only the concrete close to the turns actually affects the overall coil behavior. Thus, the PEEC model of the concrete can be substantially reduced and only the material in close proximity to the copper turns must be actually discretized. Indeed, results of Fig. 5.13 are obtained with a concrete thickness of about 5×5 cm cross section, i.e. the one represented in Fig. 5.12.

As a further result of such analysis, it has been noticed that the electric current density in the concrete has two main components: one which flows parallel to the current inside the winding (inductive component) and a second one which flows from the external turn to the internal one (capacitive component), accumulating charge at the interfaces between the concrete and the turns. Fig. 5.14.(a) and Fig. 5.14.(b) show the qualitative behavior of the current in the concrete (in logarithmic scale) at 10 kHz and 100 kHz, respectively. As can been seen, when the frequency is low, the inductive component is predominant whereas, with the increase of the frequency, the capacitive component becomes more relevant, significantly affecting the overall coil behavior.

Finally, the constructed model of the embedded WPT coil is simulated varying ρ_c and ε_{rc}

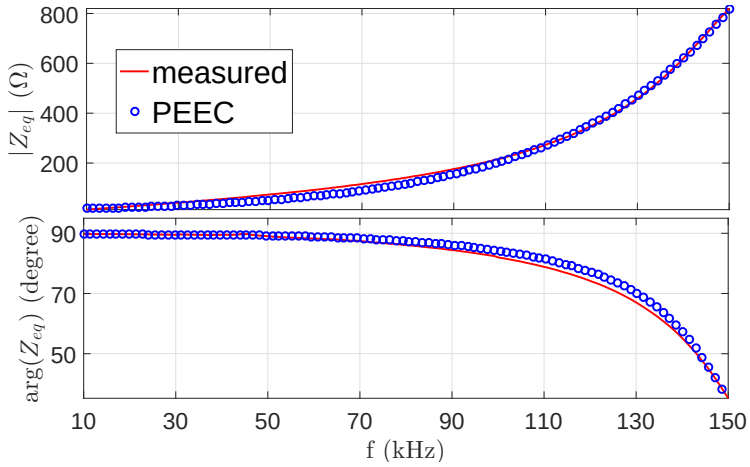

Figure 5.13: Absolute value of Z_{eq} of the embedded coil (measures vs PEEC results).

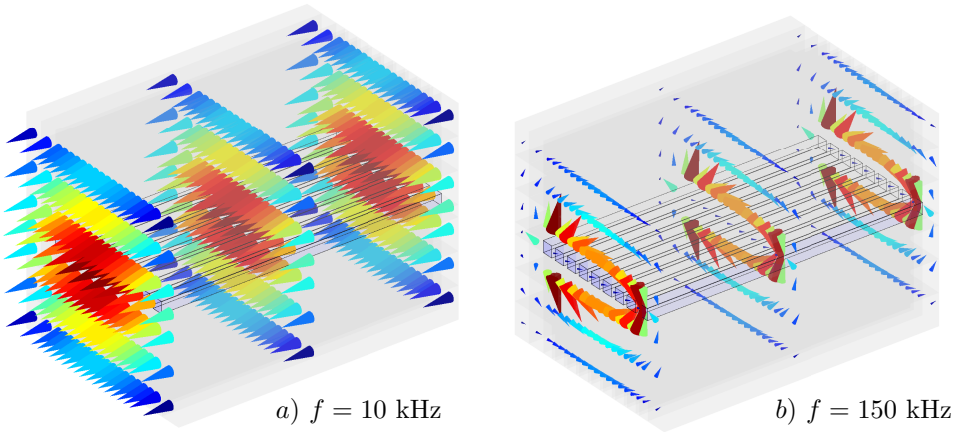

Figure 5.14: PEEC model simulation: distribution of $\mathbf{J}_e$ (real part) in the concrete (arbitrary units). *a*) Inductive component predominant. *b*) Capacitive component predominant. *a*) and *b*) not in the same scale.

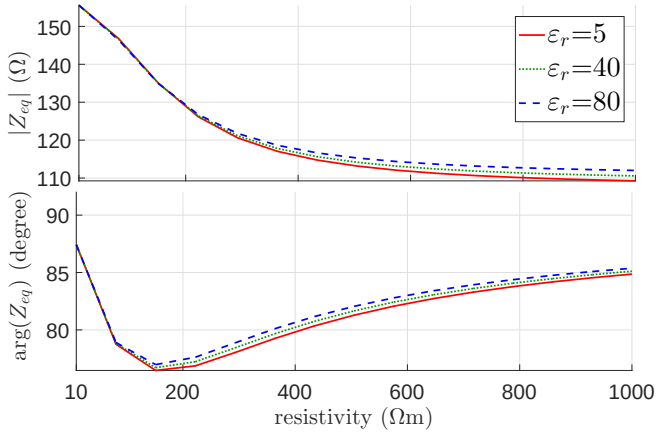

Figure 5.15: Z_{eq} of the embedded coil for a concrete resistivity from 10 Ωm to 1000 Ωm, parametrized for ε_{r_c} equal to 5, 40, and 80.

from 10 Ωm to 1000 Ωm by applying Algorithm 1. Such model is made by 1,368 hexahedral elements for the turns model and 14,592 hexahedral elements for the concrete model plus 9

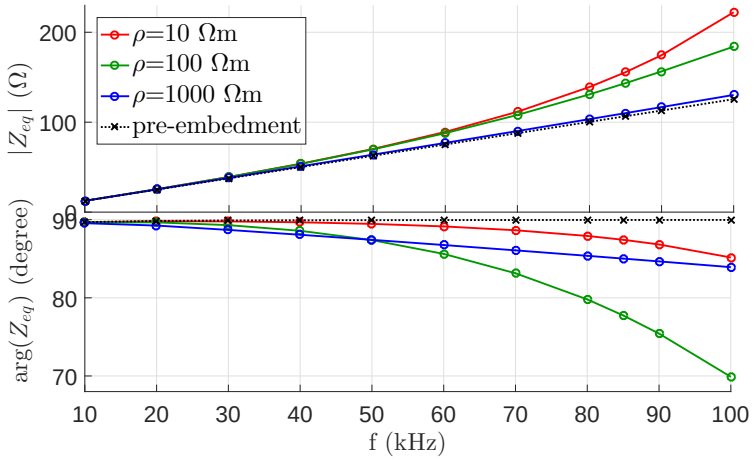

Figure 5.16: Z_{eq} (absolute value and argument) of the embedded WPT vs frequency parametrized for a resistivity equal to 10 Ωm, 100 Ωm, and 1000 Ωm.

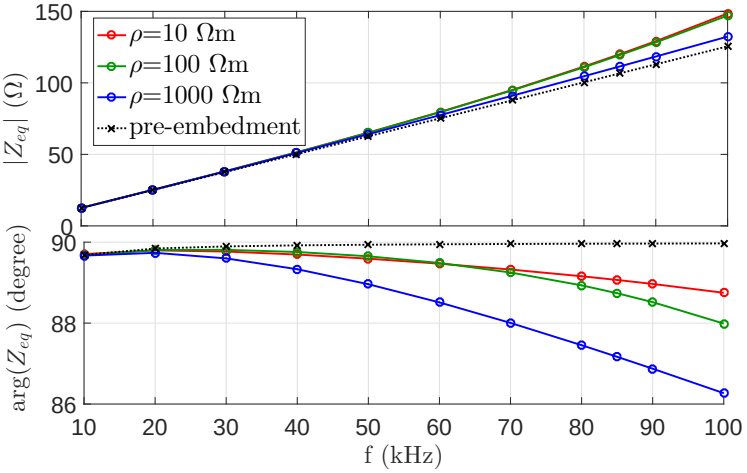

Figure 5.17: Z_{eq} (absolute value and argument) of the embedded WPT with increased insulation vs frequency parametrized for a resistivity equal to 10 Ωm, 100 Ωm, and 1000 Ωm.

lumped circuit elements which connect the 9 turns. This results in 57,322 DoFs which (without the use of Algorithm 1) would require 52.6 GB of RAM for the storage of system (5.17) and a computation time of $\sim$ 2,657 s for each parametric solution with a Peak Memory Usage of $\sim$ 105 GB (due to the storage of the LU decomposition during the solution).

In Table 5.5, the computation time and memory requirement resulting from the adoption of Algorithm 1 are reported. Timings and memory refer to a selected parametric evaluation. However, all the parametric evaluations showed similar results.

It is worth noting that the "**if**" statement of Algorithm 1 (reached after 20 GMRES iterations) was satisfied only for the extrema values of the range of ρ_c and normally only $\sim$ 6 GMRES iteration are sufficient to reach a residual of 10^{-17}.

The results obtained from this analysis are shown in Fig. 5.15 and Fig. 5.16. Moreover, to study the effects of the coil geometry, such analysis is repeated with a different model having an increased insulation thickness between turns and concrete. The results obtained from such analysis are shown in Fig. 5.17 and, more in detail, in [136].

Chapter 6

Marching On–in–Time PEEC method

6.1 Short overview on time domain PEEC approaches

The PEEC methods discussed in Chapters 2–4 are based on the electromagnetic harmonic assumption, i.e. Frequency Domain (FD) assumption.

When a transient phenomena (i.e. time domain) want to be analyzed instead, at least three procedures are possibles [138]:

1. Apply the well–known θ–method [139] to the PEEC systems (3.47) and (3.68), (or other traditional procedures such as: forward Euler, backward Euler, Crank–Nicolson, and Runge Kutta methods),

2. Apply the Inverse Discrete Fourier Transform (IDFT) to frequency domain simulations and extract the time domain simulation results for a given temporal window,

3. Apply the Marching On–in–Time (MOT) scheme [140].

It is worth noting that, the application of the θ–method to PEEC systems (3.47) and (3.68) is straightforward only under the assumption of electrically small devices, i.e. when the propagation effects are neglected [141, 142, 143, 15]. Indeed, when electrically long devices are considered, the dynamic Green function (2.17) must be adopted, which means that the electromagnetic interactions between the DoFs of the mesh are not instantaneous. Thus, fast transient phenomena can not be studied with such method.

Instead, the application of IDFT allows for considering the time delay effects on the propagation of the electromagnetic fields. However, when time domain analysis with a rich harmonic content are analyzed, this method easily results in a considerable computational cost. Indeed, for each frequency simulation the PEEC problem must be solved. Moreover, when the selected frequencies to be simulated do not allow neglecting the time delay propagation effects, the integral PEEC matrices must be properly updated considering the dependence of the dynamic Green function with the frequency. Since retardation effects must be considered, the dense integral matrices of FD–PEEC must be updated at each frequency simulation. However, to avoid prohibitive computation time, the exponential term of the dynamic Green's function can be considered to be constant within every single cell (with a good approximation) in order to avoid the re–evaluation of the integrals at each frequency step. Thus, the integral PEEC matrices are updated at each frequency value by multiplying each matrix entry with the related (retardation)

coefficient. Moreover, a further limitation of the IDFT method is the non natural handling of media which exhibit a non–linear behaviour with the electric and magnetic fields.

In the context of this PhD thesis, with the aim of overcoming the shortcomings of the application of the θ–method and IDFT in the context of PEEC method, the application of the MOT scheme to the Unstructured C–PEEC formulation derived in section 2.3 has been investigated.

The MOT scheme has been first applied to integral equation methods in [140]. Such numerical method allows for naturally considering the time delay propagation effects and non–linear properties of the electromagnetic media.

The possibility to combine the MOT procedure with the structured (standard) version of PEEC has been shortly discussed in [9] and [144], while in literature time–domain PEEC methods under the assumption of electrically short structures have been mostly proposed. Very recently, a MOT–PEEC method based on the standard PEEC discretization approach has been presented in [145, 146] for the study of conductive and dielectric media.

Compared to the aforementioned work, the MOT–PEEC formulation presented in the following section is based on the Unstructured version of PEEC, and the MOT procedure is differently applied to the PEEC formulation. Moreover, magnetic media are also treated by the proposed MOT–PEEC method and, with respect to [145], a reduced amount of unknowns is required. Furthermore, the proposed formulation provides the same well–known circuit interpretation of the harmonic PEEC method, easily allowing for coupling discretized devices and lumped circuits components. Non–homogeneous and anisotropic media can be considered as well and numerical results show good stability properties of the proposed method.

6.2 Unstructured Marching On–in–Time PEEC method for conductive, dielectric, and magnetic media

In this section, the Unstructured MOT–PEEC method developed during the PhD thesis is proposed. The method here proposed is intended as a basic and general formulation which is however suitable to be combined with more sophisticated approaches [147] and parallelization techniques [148] widely proposed in the literature in the context of MOT integral equation methods. The PEEC formulation based on the Coulombian interpretation of the magnetization phenomena has been selected for the derivation of the unstructured MOT–PEEC method. However, an analogous procedure can be easily derived for the PEEC formulation based on the Amperian interpretation of the magnetization phenomena by following the space and time discretization proposed in the next sections.

6.2.1 Formulation

For the sake of completeness and self consistence, the definition of some quantity given in the previous chapters is here shortly repeated.

Thus, Ω_c, Ω_d, and Ω_m are the conductive ($\sigma > 0$), dielectric ($\varepsilon_r \neq 1$), the magnetic ($\mu_r \neq 1$) domains, respectively, where σ is the electric conductivity, ε_r is the relative electric permittivity, and μ_r is the relative magnetic permeability.

The electric domain is also $\Omega_e = \Omega_c \cup \Omega_d$ and the following boundaries are defined: $\Gamma_c = \partial\Omega_c$, $\Gamma_d = \partial\Omega_d$, $\Gamma_m = \partial\Omega_m$, and $\Gamma_e = \partial\Omega_e$. The computational domain is $\Omega = \Omega_e \cup \Omega_m$.

As introduced in section 2.3, where a time harmonic PEEC method is proposed, the electric, $\mathbf{E}$, and magnetic, $\mathbf{H}$, fields can be written in terms of electric and magnetic potentials, i.e.

$$\mathbf{E} = -\frac{\partial}{\partial t}\mathbf{A}_e - \nabla\varphi_e - \varepsilon_0^{-1}\nabla\times\mathbf{A}_m + \mathbf{E}_0, \tag{6.1}$$

$$\mathbf{H} = -\frac{\partial}{\partial t}\mathbf{A}_m - \nabla\varphi_m + \mu_0^{-1}\nabla\times\mathbf{A}_e + \mathbf{H}_0, \tag{6.2}$$

where $\mathbf{A}_e$ and $\mathbf{A}_m$ are electric and magnetic vector potentials, φ_e and φ_m are electric and magnetic scalar potentials, and $\mathbf{E}_0$ and $\mathbf{H}_0$ are external electric and magnetic fields produced by some source domain. Electromagnetic quantities in (6.1) and (6.2) are evaluated in the field point $\mathbf{r}$ and at the *present* time instant t.

Moreover, as in Section 2.3, $\mathbf{J}_c$, $\mathbf{J}_d$, and $\mathbf{J}_m$ (i.e. the conduction, polarization, and magnetic current, respectively) can be introduced. Time domain constitutive relations which links $\mathbf{E}$ and $\mathbf{H}$ with current densities $\mathbf{J}_c$, $\mathbf{J}_d$, and $\mathbf{J}_m$ are also derived from (2.30), (2.45), and (2.85):

$$\mathbf{E}(\mathbf{r},t) = \rho_c(\mathbf{r},t)\mathbf{J}_c(\mathbf{r},t),\ \ \mathbf{r}\in\Omega_c, \tag{6.3}$$

$$\mathbf{E}(\mathbf{r},t) = \rho_d(\mathbf{r},t)\int_0^t \mathbf{J}_d(\mathbf{r},\tau)d\tau,\ \ \mathbf{r}\in\Omega_d, \tag{6.4}$$

$$\mathbf{H}(\mathbf{r},t) = \rho_m(\mathbf{r},t)\int_0^t \mathbf{J}_m(\mathbf{r},\tau)d\tau,\ \ \mathbf{r}\in\Omega_m, \tag{6.5}$$

where ρ_c is the electric resistivity, $\rho_d = \frac{1}{\varepsilon_0(\varepsilon_r-1)}$, and $\rho_m = \frac{1}{\mu_0(\mu_r-1)}$, where ε_0 and μ_0 are the vacuum permittivity and permeability, respectively.

The time domain expressions of vector potentials $\mathbf{A}_e$ and $\mathbf{A}_m$ are given by:

$$\mathbf{A}_e(\mathbf{r},t) = \frac{\mu_0}{4\pi}\int_{\Omega_e}\frac{\mathbf{J}_e(\mathbf{r}',t')}{|\mathbf{r}-\mathbf{r}'|}d\Omega, \tag{6.6}$$

$$\mathbf{A}_m(\mathbf{r},t) = \frac{\varepsilon_0}{4\pi}\int_{\Omega_m}\frac{\mathbf{J}_m(\mathbf{r}',t')}{|\mathbf{r}-\mathbf{r}'|}d\Omega, \tag{6.7}$$

where $\mathbf{J}_e = \mathbf{J}_c + \mathbf{J}_d$, $\mathbf{r}'$ is the integration point, and $t' = t - \frac{|\mathbf{r}-\mathbf{r}'|}{c_0}$ is the retarded time; c_0 is the velocity of light in vacuum.

Analogously, the time derivatives of $\mathbf{A}_e$ and $\mathbf{A}_m$ which appear in (6.1) and (6.2) are given by:

$$\frac{\partial}{\partial t}\mathbf{A}_e(\mathbf{r},t) = \frac{\mu_0}{4\pi}\int_{\Omega_e}\frac{\frac{\partial}{\partial t'}\mathbf{J}_e(\mathbf{r}',t')}{|\mathbf{r}-\mathbf{r}'|}d\Omega, \tag{6.8}$$

$$\frac{\partial}{\partial t}\mathbf{A}_m(\mathbf{r},t) = \frac{\varepsilon_0}{4\pi}\int_{\Omega_m}\frac{\frac{\partial}{\partial t'}\mathbf{J}_m(\mathbf{r}',t')}{|\mathbf{r}-\mathbf{r}'|}d\Omega. \tag{6.9}$$

The integral expressions of scalar electric and magnetic potentials in time domain are instead given by:

$$\varphi_e(\mathbf{r},t) = \frac{1}{4\pi\varepsilon_0}\Big[\int_{\Omega_e}\frac{\varrho_e(\mathbf{r}',t')}{|\mathbf{r}-\mathbf{r}'|}d\Omega + \int_{\Gamma_e}\frac{\varsigma_e(\mathbf{r}',t')}{|\mathbf{r}-\mathbf{r}'|}d\Gamma\Big], \tag{6.10}$$

$$\varphi_m(\mathbf{r},t) = \frac{1}{4\pi\mu_0}\Big[\int_{\Omega_m}\frac{\varrho_m(\mathbf{r}',t')}{|\mathbf{r}-\mathbf{r}'|}d\Omega + \int_{\Gamma_m}\frac{\varsigma_m(\mathbf{r}',t')}{|\mathbf{r}-\mathbf{r}'|}d\Gamma\Big], \tag{6.11}$$

where ϱ_e and ς_e are the volume and surface electric charges, respectively, while ϱ_m and ς_m are the volume and surface magnetic charges.

Electric and magnetic charges are related to $\mathbf{J}_e$ and $\mathbf{J}_m$ by means of continuity relations:

$$\varrho_e(\mathbf{r},t) = -\int_0^t \nabla\cdot\mathbf{J}_e(\mathbf{r},\tau)d\tau, \qquad \varsigma_e(\mathbf{r},t) = -\int_0^t \mathbf{J}_e(\mathbf{r},\tau)\cdot\mathbf{n}d\tau, \tag{6.12}$$

$$\varrho_m(\mathbf{r},t) = -\int_0^t \nabla\cdot\mathbf{J}_m(\mathbf{r},\tau)d\tau, \qquad \varsigma_m(\mathbf{r},t) = -\int_0^t \mathbf{J}_m(\mathbf{r},\tau)\cdot\mathbf{n}d\tau, \tag{6.13}$$

where $\mathbf{n}$ is the outward unit normal vector of Γ_e and Γ_m.

6.2.2 Spatial and temporal discretization

Given a spatial discretization $\mathcal{G}$ of Ω and a temporal discretization $\mathcal{T}$ of the time interval of interest, $\mathbf{J}_c$ is expanded in terms of degrees of freedoms (DoFs) by using Whitney face shape functions $\mathbf{w}$ and temporal basis functions T [147]:

$$\mathbf{J}_c(\mathbf{r},t) = \sum_{k=1}^{N_f}\sum_{s=0}^{N_t}\mathbf{w}_k(\mathbf{r})T_s(t)j_{c_{k,s}} \tag{6.14}$$

where $j_{c_{k,s}}$ is the flux of $\mathbf{J}_c$ through the kth face of the mesh (i.e. the kth branch of the equivalent circuit) at the sth time step, N_f and N_t are the number of space (i.e. faces of the mesh) and temporal basis functions, respectively. At each time instant s (i.e. $t = s\Delta_T$), the DoFs are stored in the array $\mathbf{j}_{\mathbf{c}\,s}$. $\mathbf{J}_d$ and $\mathbf{J}_m$ are expanded likewise, leading to the vector arrays $\mathbf{j}_{\mathbf{d}\,s}$ and $\mathbf{j}_{\mathbf{m}\,s}$.

From now on T is considered as the well–known *hat* shape function with support $[-\Delta_T, \Delta_T]$, where Δ_T is the chosen time step. This leads to a causal MOT scheme. However, how discussed in the following, a different choice of the basis function can be made, leading to a non–causal MOT system [147].

As in the pioneering work [140], a Galerkin approach for the spatial expansion and a collocation method for each sth time instant for the time discretization are applied to (6.1) and (6.2) combined with (6.3)–(6.13). For each sth time step, this operation leads to the following matrix equations:

$$\mathbf{e}_{\mathbf{c}_s} = \mathbf{R}_\mathbf{c}\mathbf{j}_{\mathbf{c}\,s} + \tilde{\mathbf{G}}^{a}_{\Omega_c}\boldsymbol{\phi}_{\mathbf{c}\,s} + \sum_{u=0}^{H_T}\Big(\mathbf{L}_{\mathbf{cc}\,u}\mathbf{j}_{\mathbf{c}\,s-u} + \mathbf{L}_{\mathbf{cd}\,u}\mathbf{j}_{\mathbf{d}\,s-u} + \mathbf{K}_{\mathbf{cm}\,u}\mathbf{j}_{\mathbf{m}\,s-u}\Big), \tag{6.15}$$

for the conductive media,

$$\mathbf{e}_{\mathbf{d}_s} = \Delta_T\mathbf{R}_\mathbf{d}\Big(\frac{\mathbf{j}_{\mathbf{d}\,s}}{2} + \sum_{u=1}^{N_T}\mathbf{j}_{\mathbf{d}\,s-u}\Big) + \tilde{\mathbf{G}}^{a}_{\Omega_d}\boldsymbol{\phi}_{\mathbf{d}\,s} + \sum_{u=0}^{H_T}\Big(\mathbf{L}_{\mathbf{dd}\,u}\mathbf{j}_{\mathbf{d}\,s-u} + \mu_0\mathbf{L}_{\mathbf{dc}\,u}\mathbf{j}_{\mathbf{c}\,s-u} + \mathbf{K}_{\mathbf{dm}\,u}\mathbf{j}_{\mathbf{m}\,s-u}\Big), \tag{6.16}$$

for the dielectric media, and

$$\mathbf{h}_s = \Delta_T\mathbf{R}_\mathbf{m}\Big(\frac{\mathbf{j}_{\mathbf{m}\,s}}{2} + \sum_{u=1}^{N_T}\mathbf{j}_{\mathbf{m}\,s-u}\Big) + \mathbf{G}^{a}_{\Omega_m}\boldsymbol{\phi}_{\mathbf{m}\,s} + \sum_{u=0}^{H_T}\Big(\mathbf{L}_{\mathbf{mm}\,u}\mathbf{j}_{\mathbf{m}\,s-u} + \mathbf{K}_{\mathbf{mc}\,u}\mathbf{j}_{\mathbf{c}\,s-u} + \mathbf{K}_{\mathbf{md}\,u}\mathbf{j}_{\mathbf{d}\,s-u}\Big), \tag{6.17}$$

for the magnetic media.

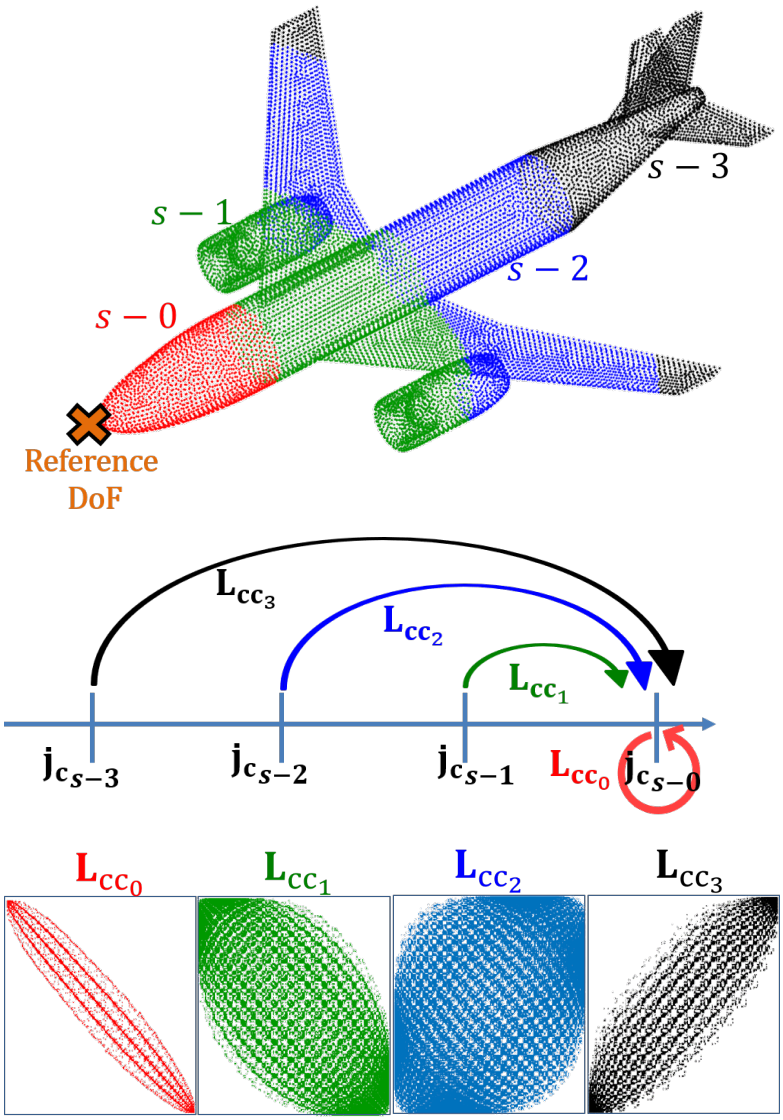

Figure 6.1: Marching matrices interactions exemplification.

Matrices and vector arrays in (6.15)–(6.17) are the corresponding time domain version of the frequency domain quantities defined in section 3.2 with the Cell Method discretization approaches. Also the same concepts of *primal* and *dual* grids are maintained. However, for the sake of simplicity, "∼" symbol is not adopted to distinguish between primal and dual arrays of DoFs and matrices (with the except of the gradient incidence matrices). Moreover, for the sake of conciseness, these quantities are defined without dwelling on their interpretation.

In (6.15)–(6.17), $\mathbf{e}_{\mathbf{c}_s}$ and $\mathbf{e}_{\mathbf{d}_s}$ are the array of DoFs related to $\mathbf{E}_0$ in Ω_c and Ω_d, respectively, and $\mathbf{h}_s$ is the array of DoFs related to $\mathbf{H}_0$ in Ω_m. The other matrices and vector arrays are defined in the following, and, for the sake of clarity, subscripts c, d, and m are introduced to indicate the conductive, dielectric, and magnetic domains and material quantities, respectively. When a double subscript is used, the first indicates the *target* domain, while the second the *source* domain. Thus, similar to Section 2.3, the coefficients of time domain MOT–PEEC matrices

which appear in (6.15)–(6.17) are given by

$$R_{ckh} = \int_{\Omega_c} \rho_c(\mathbf{r},t)\mathbf{w}_k(\mathbf{r})\cdot\mathbf{w}_h(\mathbf{r})T(0)d\Omega, \tag{6.18}$$

$$R_{dkh} = \int_{\Omega_d} \rho_d(\mathbf{r},t)\mathbf{w}_k(\mathbf{r})\cdot\mathbf{w}_h(\mathbf{r})T(0)d\Omega, \tag{6.19}$$

$$R_{m_{kh}} = \int_{\Omega_m} \rho_m(\mathbf{r},t)\mathbf{w}_k(\mathbf{r})\cdot\mathbf{w}_h(\mathbf{r})T(0)d\Omega, \tag{6.20}$$

for the resistance matrices (note that $T(0)=1$ when hat temporal shape functions are used),

$$L_{cc_{u,kh}} = \mu_0 \int_{\Omega_c}\int_{\Omega_c} \frac{\mathbf{w}_k(\mathbf{r})\cdot\mathbf{w}_h(\mathbf{r}')\frac{\partial}{\partial t'}T(t_u)}{4\pi|\mathbf{r}-\mathbf{r}'|}d\Omega d\Omega, \tag{6.21}$$

$$L_{dd_{u,kh}} = \mu_0 \int_{\Omega_d}\int_{\Omega_d} \frac{\mathbf{w}_k(\mathbf{r})\cdot\mathbf{w}_h(\mathbf{r}')\frac{\partial}{\partial t'}T(t_u)}{4\pi|\mathbf{r}-\mathbf{r}'|}d\Omega d\Omega, \tag{6.22}$$

$$L_{cd_{u,kh}} = \mu_0 \int_{\Omega_c}\int_{\Omega_d} \frac{\mathbf{w}_k(\mathbf{r})\cdot\mathbf{w}_h(\mathbf{r}')\frac{\partial}{\partial t'}T(t_u)}{4\pi|\mathbf{r}-\mathbf{r}'|}d\Omega d\Omega, \tag{6.23}$$

$$L_{dc_{u,kh}} = \mu_0 \int_{\Omega_d}\int_{\Omega_c} \frac{\mathbf{w}_k(\mathbf{r})\cdot\mathbf{w}_h(\mathbf{r}')\frac{\partial}{\partial t'}T(t_u)}{4\pi|\mathbf{r}-\mathbf{r}'|}d\Omega d\Omega, \tag{6.24}$$

$$L_{mm_{u,kh}} = \varepsilon_0 \int_{\Omega_m}\int_{\Omega_m} \frac{\mathbf{w}_k(\mathbf{r})\cdot\mathbf{w}_h(\mathbf{r}')\frac{\partial}{\partial t'}T(t_u)}{4\pi|\mathbf{r}-\mathbf{r}'|}d\Omega d\Omega, \tag{6.25}$$

for the inductance matrices, and

$$K_{cm_{u,kh}} = \frac{1}{4\pi}\int_{\Omega_c}\mathbf{w}_k(\mathbf{r})\cdot\int_{\Omega_m}\mathbf{w}_h(\mathbf{r}')\times(\mathbf{r}-\mathbf{r}')\left(\frac{T(t_u)}{|\mathbf{r}-\mathbf{r}'|^3}+\frac{\frac{\partial}{\partial t'}T(t_u)}{c_0|\mathbf{r}-\mathbf{r}'|^2}\right)d\Omega d\Omega, \tag{6.26}$$

$$K_{mc_{u,kh}} = \frac{1}{4\pi}\int_{\Omega_m}\mathbf{w}_k(\mathbf{r})\cdot\int_{\Omega_c}\mathbf{w}_h(\mathbf{r}')\times(\mathbf{r}-\mathbf{r}')\left(\frac{T(t_u)}{|\mathbf{r}-\mathbf{r}'|^3}+\frac{\frac{\partial}{\partial t'}T(t_u)}{c_0|\mathbf{r}-\mathbf{r}'|^2}\right)d\Omega d\Omega, \tag{6.27}$$

$$K_{dm_{u,kh}} = \frac{1}{4\pi}\int_{\Omega_d}\mathbf{w}_k(\mathbf{r})\cdot\int_{\Omega_m}\mathbf{w}_h(\mathbf{r}')\times(\mathbf{r}-\mathbf{r}')\left(\frac{T(t_u)}{|\mathbf{r}-\mathbf{r}'|^3}+\frac{\frac{\partial}{\partial t'}T(t_u)}{c_0|\mathbf{r}-\mathbf{r}'|^2}\right)d\Omega d\Omega, \tag{6.28}$$

$$K_{md_{u,kh}} = \frac{1}{4\pi}\int_{\Omega_m}\mathbf{w}_k(\mathbf{r})\cdot\int_{\Omega_d}\mathbf{w}_h(\mathbf{r}')\times(\mathbf{r}-\mathbf{r}')\left(\frac{T(t_u)}{|\mathbf{r}-\mathbf{r}'|^3}+\frac{\frac{\partial}{\partial t'}T(t_u)}{c_0|\mathbf{r}-\mathbf{r}'|^2}\right)d\Omega d\Omega, \tag{6.29}$$

for the interaction integral matrices between electric and magnetic domains. It is worth noting that, for the sake of conciseness, differently to Section 3.2, the interaction matrices between electric and magnetic domains (i.e. **K**–matrices) are here differently derived. However, the approach of Section 3.2 can be also used to derived the interaction matrices.

All the resistance, inductance, and interaction matrices have dimension $N_{f_\alpha}\times N_{f_\beta}$, with $\alpha=c,d,m$ and $\beta=c,d,m$. In (6.21)–(6.29), $t_u = u\Delta_T - |\mathbf{r}-\mathbf{r}'|/c_0$.

$\tilde{\mathbf{G}}^a_{\Omega_c}$, $\tilde{\mathbf{G}}^a_{\Omega_d}$, and $\mathbf{G}^a_{\Omega_m}$, are (augmented) gradient matrices defined in Section 3.1.2 with dimension $N_{f_c}\times(N_{v\alpha}+N_{fb_\alpha})$, where $N_{v\alpha}$ and N_{fb_α} are the number of volume and boundary faces of the mesh of Ω_α, with $\alpha=c,d,m$.

Matrices $\mathbf{L}_{\boldsymbol{\alpha\beta}_u}$ and $\mathbf{K}_{\boldsymbol{\alpha\beta}_u}$ ($\alpha=c,d,m$ and $\beta=c,d,m$), with $u=0,\cdots,H_T$, represent the electromagnetic interactions between the unknowns at the time instant s and those at the previous time instant $s-u$ (when $u=0$ they represent *instantaneous* interactions between unknowns at the same time instant). In (6.15)–(6.17), $H_T=\lceil 1+D_{max}/(\Delta_T c_0)\rceil$ indicates *how many previous time steps* actually *interact* with the present solution, where D_{max} is the maximum distance between two mesh elements of Ω and $\lceil\bullet\rceil$ is the *ceiling* operator (see Fig. 6.1).

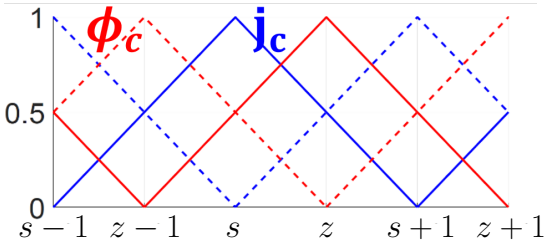

Figure 6.2: Primal ($\mathcal{T}$) and dual ($\tilde{\mathcal{T}}$) temporal discretization.

As in section 3.2, arrays of DoFs $\boldsymbol{\phi_{c}}_s$, $\boldsymbol{\phi_{d}}_s$, and $\boldsymbol{\phi_{m}}_s$ store the averaged scalar electric and magnetic potentials related to $N_{vc}+N_{fb_c}$, $N_{vd}+N_{fb_d}$, and $N_{vm}+N_{fb_m}$ (i.e. the nodes of the equivalent circuit), respectively, at the instant $t = s\Delta_T$.

Indeed $\boldsymbol{\phi_{c}}_s$ and $\boldsymbol{\phi_{d}}_s$ are related to the electric scalar potential in domains Ω_c and Ω_d, whereas $\boldsymbol{\phi_{m}}_s$ is related to the scalar magnetic potential in Ω_m.

In the same fashion of the frequency domain PEEC method, the time derivative of $\boldsymbol{\phi_{c}}_s$, $\boldsymbol{\phi_{d}}_s$, and $\boldsymbol{\phi_{m}}_s$ is related to the divergence of the electric and magnetic current array of DoFs (i.e. the electric and magnetic charge array of DoFs) by means of integral potential matrices, i.e.:

$$\frac{\partial}{\partial t}\boldsymbol{\phi}_{\mathbf{c}s} = \frac{1}{\varepsilon_0}\sum_{u=0}^{H_T}\left(\mathbf{P}_{\mathbf{cc}u}\tilde{\mathbf{G}}^{aT}_{\Omega_c}\mathbf{j}_{\mathbf{c}s-u} + \mathbf{P}_{\mathbf{cd}u}\tilde{\mathbf{G}}^{aT}_{\Omega_d}\mathbf{j}_{\mathbf{d}s-u}\right), \tag{6.30}$$

$$\frac{\partial}{\partial t}\boldsymbol{\phi}_{\mathbf{d}s} = \frac{1}{\varepsilon_0}\sum_{u=0}^{H_T}\left(\mathbf{P}_{\mathbf{dd}u}\tilde{\mathbf{G}}^{aT}_{\Omega_d}\mathbf{j}_{\mathbf{d}s-u} + \mathbf{P}_{\mathbf{dc}u}\tilde{\mathbf{G}}^{aT}_{\Omega_c}\mathbf{j}_{\mathbf{c}s-u}\right), \tag{6.31}$$

$$\frac{\partial}{\partial t}\boldsymbol{\phi}_{\mathbf{m}s} = \frac{1}{\mu_0}\sum_{u=0}^{H_T}\left(\mathbf{P}_{\mathbf{mm}u}\mathbf{G}^{aT}_{\Omega_m}\mathbf{j}_{\mathbf{m}s-u}\right), \tag{6.32}$$

where, as in Section 3.2, potential matrices $\mathbf{P}_{\boldsymbol{\alpha\beta}_u}$ (with $\alpha = c, d, m$ and $\beta = c, d, m$) of dimension $(N_{v\alpha}+N_{fb_\alpha})\times(N_{v\beta}+N_{fb_\beta})$ are subdivided into *volume*, *surface*, and *volume–surface* matrices, i.e.

$$\mathbf{P}_{\boldsymbol{\alpha\beta}_u} = \begin{bmatrix} \mathbf{P}^{vv}_{\boldsymbol{\alpha\beta}_u} & \mathbf{P}^{vs}_{\boldsymbol{\alpha\beta}_u} \\ \mathbf{P}^{sv}_{\boldsymbol{\alpha\beta}_u} & \mathbf{P}^{ss}_{\boldsymbol{\alpha\beta}_u} \end{bmatrix},$$

and their coefficients are given by

$$P^{vv}_{\boldsymbol{\alpha\beta}_u,kh} = \frac{1}{\|v_k\|\|v_h\|}\int_{v_k}\int_{v_h}\frac{T(t_u)}{4\pi|\mathbf{r}-\mathbf{r}'|}d\Omega d\Omega, \tag{6.33}$$

$$P^{ss}_{\boldsymbol{\alpha\beta}_u,kh} = \frac{1}{\|fb_k\|\|fb_h\|}\int_{fb_k}\int_{fb_h}\frac{T(t_u)}{4\pi|\mathbf{r}-\mathbf{r}'|}d\Gamma d\Gamma, \tag{6.34}$$

$$P^{vs}_{\boldsymbol{\alpha\beta}_u,kh} = \frac{1}{\|v_k\|\|fb_h\|}\int_{v_k}\int_{fb_h}\frac{T(t_u)}{4\pi|\mathbf{r}-\mathbf{r}'|}d\Omega d\Gamma, \tag{6.35}$$

$$P^{sv}_{\boldsymbol{\alpha\beta}_u,kh} = \frac{1}{\|fb_k\|\|v_h\|}\int_{fb_k}\int_{v_h}\frac{T(t_u)}{4\pi|\mathbf{r}-\mathbf{r}'|}d\Gamma d\Omega, \tag{6.36}$$

where $\|\cdot\|$ indicates the measure (i.e. volume or area) of the kth, hth volume and surface elements. For the sake of conciseness, with respect to frequency domain methods, the electric and magnetic PEEC potential matrices are scaled by ε_0 and μ_0, respectively. Thus, electric and magnetic potential matrix coefficients have the same expression.

Following a leap–frog scheme [144] and according to the classical Tonti diagram, $\boldsymbol{\varphi_e}$ and $\boldsymbol{\varphi_m}$ are expanded onto the dual spatial and temporal grids $\tilde{\mathcal{G}}$ and $\tilde{\mathcal{T}}$ obtained by the barycentric subdivision of $\mathcal{G}$ and $\mathcal{T}$, respectively (see Fig. 6.2). Thus, $\frac{\partial}{\partial t}\boldsymbol{\phi_{cs}}$, $\frac{\partial}{\partial t}\boldsymbol{\phi_{ds}}$, and $\frac{\partial}{\partial t}\boldsymbol{\phi_{ms}}$ are also given by

$$\frac{\partial}{\partial t}\boldsymbol{\phi_{cs}} = \frac{\boldsymbol{\phi_{cl}} - \boldsymbol{\phi_{cl-1}}}{\Delta_T}, \tag{6.37}$$

$$\frac{\partial}{\partial t}\boldsymbol{\phi_{ds}} = \frac{\boldsymbol{\phi_{dl}} - \boldsymbol{\phi_{dl-1}}}{\Delta_T}, \tag{6.38}$$

$$\frac{\partial}{\partial t}\boldsymbol{\phi_{ms}} = \frac{\boldsymbol{\phi_{ml}} - \boldsymbol{\phi_{ml-1}}}{\Delta_T}, \tag{6.39}$$

where subscript l in (6.37)–(6.39) refers to the time instant $t_l = t_s + \Delta_T/2$, while $\boldsymbol{\phi_{cs}}$, $\boldsymbol{\phi_{ds}}$, and $\boldsymbol{\phi_{ms}}$ are given by

$$\boldsymbol{\phi_{cs}} = \frac{\boldsymbol{\phi_{cl}} + \boldsymbol{\phi_{cl-1}}}{2}, \tag{6.40}$$

$$\boldsymbol{\phi_{ds}} = \frac{\boldsymbol{\phi_{dl}} + \boldsymbol{\phi_{dl-1}}}{2}, \tag{6.41}$$

$$\boldsymbol{\phi_{ms}} = \frac{\boldsymbol{\phi_{ml}} + \boldsymbol{\phi_{ml-1}}}{2}. \tag{6.42}$$

Finally, combining (6.30)–(6.32) with (6.40)–(6.42), one obtains:

$$\frac{\boldsymbol{\phi_{cl}} - \boldsymbol{\phi_{cl-1}}}{\Delta_T} = \frac{1}{\varepsilon_0}\sum_{u=0}^{H_T}\left(\mathbf{P_{cc}}_u\tilde{\mathbf{G}}^{aT}_{\Omega_c}\mathbf{j_c}_{s-u} + \mathbf{P_{cd}}_u\tilde{\mathbf{G}}^{aT}_{\Omega_d}\mathbf{j_d}_{s-u}\right), \tag{6.43}$$

$$\frac{\boldsymbol{\phi_{dl}} - \boldsymbol{\phi_{dl-1}}}{\Delta_T} = \frac{1}{\varepsilon_0}\sum_{u=0}^{H_T}\left(\mathbf{P_{dd}}_u\tilde{\mathbf{G}}^{aT}_{\Omega_d}\mathbf{j_d}_{s-u} + \mathbf{P_{dc}}_u\tilde{\mathbf{G}}^{aT}_{\Omega_d}\mathbf{j_c}_{s-u}\right), \tag{6.44}$$

$$\frac{\boldsymbol{\phi_{ml}} - \boldsymbol{\phi_{ml-1}}}{\Delta_T} = \frac{1}{\mu_0}\sum_{u=0}^{H_T}\left(\mathbf{P_{mm}}_u\mathbf{G}^{aT}_{\Omega_m}\mathbf{j_m}_{s-u}\right). \tag{6.45}$$

Equations (6.15)–(6.17) and (6.43)–(6.45) (scaled by Δ_T to improve the conditioning) are finally combined leading to the MOT–PEEC scheme where (for each time step sth and lth) the unknowns are $\mathbf{j_c}_s$, $\mathbf{j_d}_s$, $\mathbf{j_m}_s$, $\boldsymbol{\phi_{cl}}$, $\boldsymbol{\phi_{dl}}$, and $\boldsymbol{\phi_{ml}}$. The system of equations to be solved is given by

$$\begin{bmatrix}
\mathbf{R_c} + \mathbf{L_{cc}}_0 & \mathbf{L_{cd}}_0 & \mathbf{K_{cm}}_0 & \frac{1}{2}\tilde{\mathbf{G}}^{a}_{\Omega_c} & \mathbf{0} & \mathbf{0} \\
\mathbf{L_{dc}}_0 & \frac{\Delta_T}{2}\mathbf{R_d} + \mathbf{L_{dd}}_0 & \mathbf{K_{dm}}_0 & \mathbf{0} & \frac{1}{2}\tilde{\mathbf{G}}^{a}_{\Omega_d} & \mathbf{0} \\
\mathbf{K_{mc}}_0 & \mathbf{K_{md}}_0 & \frac{\Delta_T}{2}\mathbf{R_m} + \mathbf{L_{mm}}_0 & \mathbf{0} & \mathbf{0} & \frac{1}{2}\mathbf{G}^{a}_{\Omega_m} \\
\Delta_T\mathbf{P_{cc}}_0\tilde{\mathbf{G}}^{aT}_{\Omega_c} & \Delta_T\mathbf{P_{cd}}_0\tilde{\mathbf{G}}^{aT}_{\Omega_d} & \mathbf{0} & -\Delta_T\mathbf{1} & \mathbf{0} & \mathbf{0} \\
\Delta_T\mathbf{P_{dc}}_0\tilde{\mathbf{G}}^{aT}_{d} & \Delta_T\mathbf{P_{dd}}_0\tilde{\mathbf{G}}^{aT}_{\Omega_c} & \mathbf{0} & \mathbf{0} & -\Delta_T\mathbf{1} & \mathbf{0} \\
\mathbf{0} & \mathbf{0} & \Delta_T\mathbf{P_{mm}}_0\mathbf{G}^{aT}_{m} & \mathbf{0} & \mathbf{0} & -\Delta_T\mathbf{1}
\end{bmatrix}
\begin{bmatrix}
\mathbf{j_c}_s \\ \mathbf{j_d}_s \\ \mathbf{j_m}_s \\ \boldsymbol{\phi_{cl}} \\ \boldsymbol{\phi_{dl}} \\ \boldsymbol{\phi_{ml}}
\end{bmatrix}
=
\begin{bmatrix}
\mathbf{b_c}_s \\ \mathbf{b_d}_s \\ \mathbf{b_m}_s \\ \mathbf{b}^{\phi}_{\mathbf{c}\,l} \\ \mathbf{b}^{\phi}_{\mathbf{d}\,l} \\ \mathbf{b}^{\phi}_{\mathbf{m}\,l}
\end{bmatrix} \tag{6.46}$$

where

$$\mathbf{b}_{\mathbf{c}\,s} = \mathbf{e}_{\mathbf{c}\,s} - \sum_{u=1}^{H_T} \left(\mathbf{L}_{\mathbf{cc}\,u} \mathbf{j}_{\mathbf{c}\,s-u} + \mathbf{L}_{\mathbf{cd}\,u} \mathbf{j}_{\mathbf{d}\,s-u} + \mathbf{K}_{\mathbf{cm}\,u} \mathbf{j}_{\mathbf{m}\,s-u} \right) - \frac{1}{2} \tilde{\mathbf{G}}^{a}_{\Omega_c} \boldsymbol{\phi}_{\boldsymbol{c}\,l-1}, \tag{6.47}$$

$$\mathbf{b}_{\mathbf{d}\,s} = \mathbf{e}_{\mathbf{d}\,s} - \sum_{u=1}^{H_T} \left(\mathbf{L}_{\mathbf{dd}\,u} \mathbf{j}_{\mathbf{d}\,s-u} + \mathbf{L}_{\mathbf{dc}\,u} \mathbf{j}_{\mathbf{c}\,s-u} + \mathbf{K}_{\mathbf{dm}\,u} \mathbf{j}_{\mathbf{m}\,s-u} \right) - \frac{1}{2} \tilde{\mathbf{G}}^{a}_{\Omega_d} \boldsymbol{\phi}_{\boldsymbol{d}\,l-1} - \Delta_T \mathbf{R}_{\mathbf{d}} \sum_{u=1}^{N_T} \mathbf{j}_{\mathbf{d}\,s-u}, \tag{6.48}$$

$$\mathbf{b}_{\mathbf{m}\,s} = \mathbf{h}_{\mathbf{m}\,s} - \sum_{u=1}^{H_T} \left(\mathbf{L}_{\mathbf{mm}\,u} \mathbf{j}_{\mathbf{m}\,s-u} + \mathbf{K}_{\mathbf{mc}\,u} \mathbf{j}_{\mathbf{c}\,s-u} + \mathbf{K}_{\mathbf{dm}\,u} \mathbf{j}_{\mathbf{d}\,s-u} \right) - \frac{1}{2} \tilde{\mathbf{G}}^{a}_{\Omega_m} \boldsymbol{\phi}_{\boldsymbol{m}\,l-1} - \Delta_T \mathbf{R}_{\mathbf{m}} \sum_{u=1}^{N_T} \mathbf{j}_{\mathbf{m}\,s-u}, \tag{6.49}$$

$$\mathbf{b}^{\phi}_{\mathbf{c}\,l} = \Delta_T \Big[\frac{1}{\varepsilon_0} \sum_{u=1}^{H_T} \left(\mathbf{P}_{\mathbf{cc}\,u} \tilde{\mathbf{G}}^{aT}_{\Omega_c} \mathbf{j}_{\mathbf{c}\,s-u} + \mathbf{P}_{\mathbf{cd}\,u} \tilde{\mathbf{G}}^{aT}_{\Omega_d} \mathbf{j}_{\mathbf{d}\,s-u} \right) - \frac{1}{\Delta_T} \boldsymbol{\phi}_{\boldsymbol{c}\,l-1} \Big], \tag{6.50}$$

$$\mathbf{b}^{\phi}_{\mathbf{d}\,l} = \Delta_T \Big[\frac{1}{\varepsilon_0} \sum_{u=1}^{H_T} \left(\mathbf{P}_{\mathbf{dd}\,u} \tilde{\mathbf{G}}^{aT}_{\Omega_d} \mathbf{j}_{\mathbf{d}\,s-u} + \mathbf{P}_{\mathbf{dc}\,u} \tilde{\mathbf{G}}^{aT}_{\Omega_c} \mathbf{j}_{\mathbf{c}\,s-u} \right) - \frac{1}{\Delta_T} \boldsymbol{\phi}_{\boldsymbol{d}\,l-1} \Big], \tag{6.51}$$

$$\mathbf{b}^{\phi}_{\mathbf{m}\,l} = \Delta_T \Big[\frac{1}{\mu_0} \sum_{u=1}^{H_T} \left(\mathbf{P}_{\mathbf{mm}\,u} \mathbf{G}^{aT}_{\Omega_m} \mathbf{j}_{\mathbf{m}\,s-u} \right) - \frac{1}{\Delta_T} \boldsymbol{\phi}_{\boldsymbol{m}\,l-1} \Big]. \tag{6.52}$$

System (6.46) is made by resistance, incidence, and *instantaneous* matrices only (i.e. ones with $u = 0$) and is the same for each time step. The right–hand side is instead updated at each time step by multiplying the *marching* matrices (i.e. ones with $u = 1, \cdots, H_T$) with the previous H_T solutions, as shown in (6.47)–(6.52). It is worth noting that *instantaneous* and *marching* matrices are in general sparse with a sparsity ratio which depends on the choice of Δ_T (i.e. the smaller Δ_T, the lower the sparsity ratio, the greater H_T). As distinctive feature of PEEC, connections with lumped circuit elements are easily considered by adding the circuit currents and node potentials of the lumped components to the unknowns and solving Kirchhoff's Voltage and Currents Laws together with (6.46).

Finally, it is worth noting that the proposed approach has been developed without considering moving domains. Even if the extension of the proposed method to moving domains is theoretically possible, the computational cost for considering such a case would probably significantly increase since the mutual coefficients which model the electromagnetic couplings between the moving parts must be re–evaluated at each time step.

6.2.3 On the choice of the unknowns and temporal shape function

With the aim of increasing the stability and the accuracy of the MOT scheme applied to integral equation methods, several authors in the literature propose different temporal shape functions (e.g. higher order with a more extended [149] and/or not–causal support [147]) and different choices of the unknowns (e.g. electric and magnetic polarizations **P** and **M** or densities field **D** and **B**). Indeed, these different choices (which also allow reducing the number of unknowns by neglecting the scalar potentials from the independent unknowns [147]) seem to generally improve the accuracy and the stability of the MOT method. Indeed, the use of a smoothly varying temporal shape function alleviates the instability issues caused by the numerical integration of integral matrix coefficients subject to the encroachment of the propagating electromagnetic wave [150], [151], [150] (see Fig. 6.3).

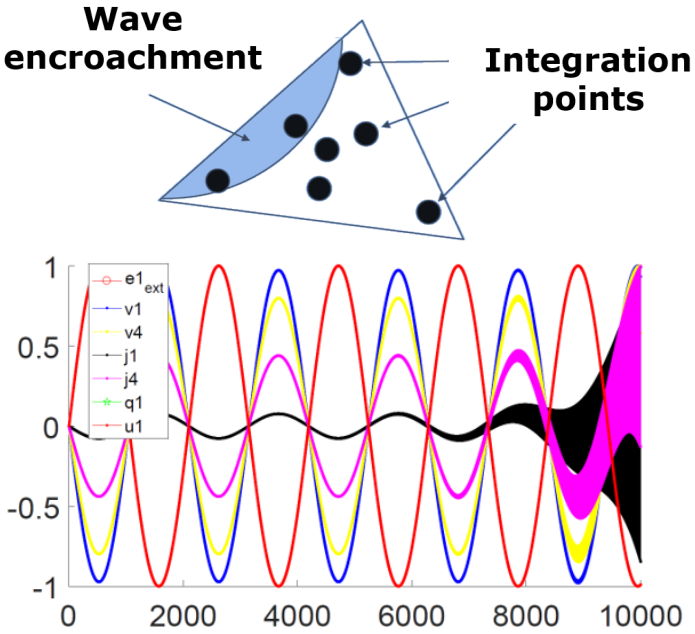

Figure 6.3: Integration inaccuracy leads to oscillating instabilities, graphic representation.

However, the use of temporal shape functions with a large support deteriorates the sparsity ratio of the matrices and, when temporal shape functions with non causal support are chosen, the need to predict several future solutions [152]. In the context of the proposed MOT–PEEC method, in accordance with the analysis presented in [145], hat shape functions have been chosen since they provide a good trade–off between stability, accuracy, and numerical performances. However, the discretization process here proposed can be easily modified by considering different temporal shape functions and/or predictor–corrector schemes [152]. Indeed, the here proposed MOT–PEEC method (which is intended as a basic and general formulation) is however suitable for the application of more sophisticated approaches [153, 154, 155, 156] and parallelization techniques, as proposed in [148].

Lastly, the choice of considering the scalar potential as independent unknowns make it possible to separate the inductive ($\mathbf{L}_{\boldsymbol{\alpha\beta}_u}$) and capacitive ($\mathbf{G}^{a}_{\Omega_\alpha}\mathbf{P}_{\boldsymbol{\alpha\beta}_u}\mathbf{G}^{aT}_{\Omega_\beta}$) effects, avoiding instabilities attributable to *round–off* errors (breakdown in frequency).

6.2.4 Numerical results

In this section, some case study simulated by the proposed MOT–PEEC method is presented. The MOT–PEEC code has been developed with MATLAB® and parallel MEX–FORTRAN functions based on OpenMP libraries. Thin wire, triangular, and hexahedral mesh elements can be considered by the implemented code. Integral matrix coefficients are evaluated numerically with a double Gauss–Legendre quadrature rule with an higher rule for the instantaneous coefficients. The simulations were run on a Linux machine equipped with a dual-Xeon E5-2643 v4 processor (6 core, 12 thread, @3:40 GHz) and 512 GB RAM.

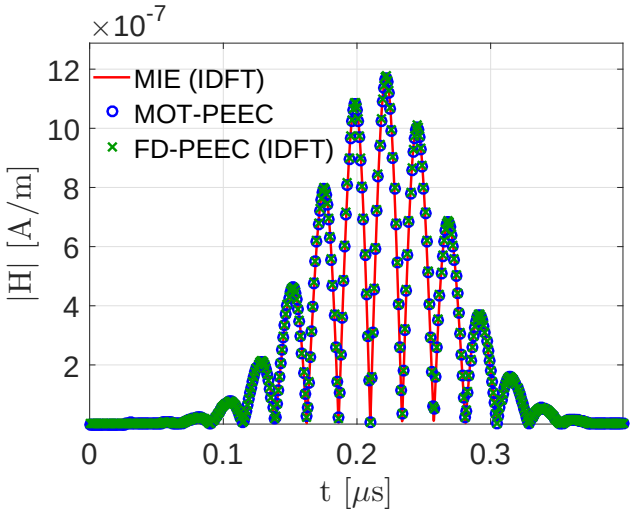

Figure 6.4: Scattered magnetic field norm for case 1).

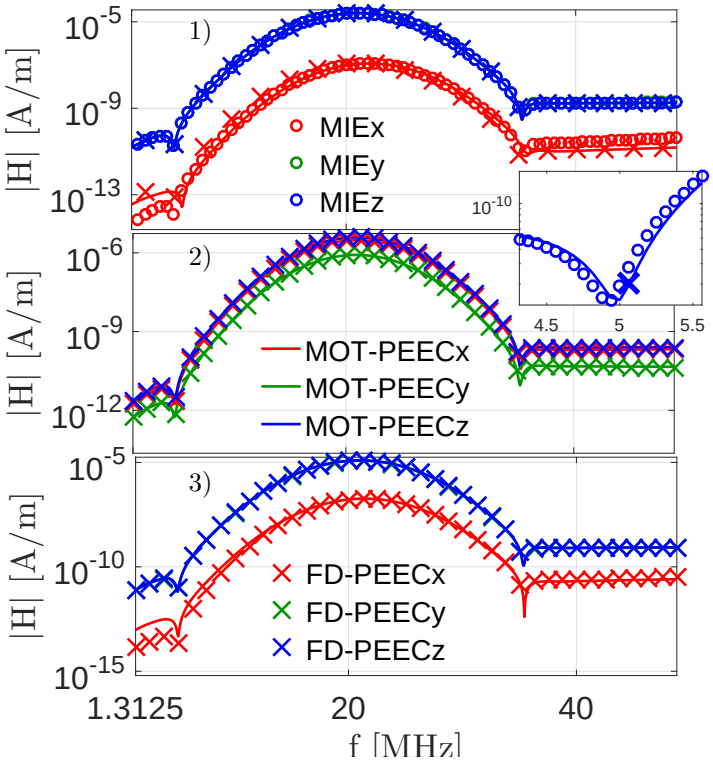

Figure 6.5: Frequency spectra of **H**. Cases 1), 2), and 3).

Dielectric shell

The first test case consists of a dielectric shell (0.5 m outer radius, 0.48 m inner radius) excited by the Gaussian Modulated Pulse (GMP) in [148]:

$$\mathbf{E}_0(x,y,z,t) = \exp\left[-\left(\frac{t-t_0-z/c_0}{\sqrt{2}\varsigma}\right)^2\right]\cos(2\pi f_0(t-t_0-z/c_0))\mathbf{u}_x, \tag{6.53}$$

with $f_0 = 20$ MHz, $f_{bw} = 20$ MHz, $\varsigma = \frac{6}{2\pi f_{bw}}$, and $t_0 = 4\varsigma$. Three cases are here considered:

1. homogeneous medium with $\varepsilon_r = 10$,

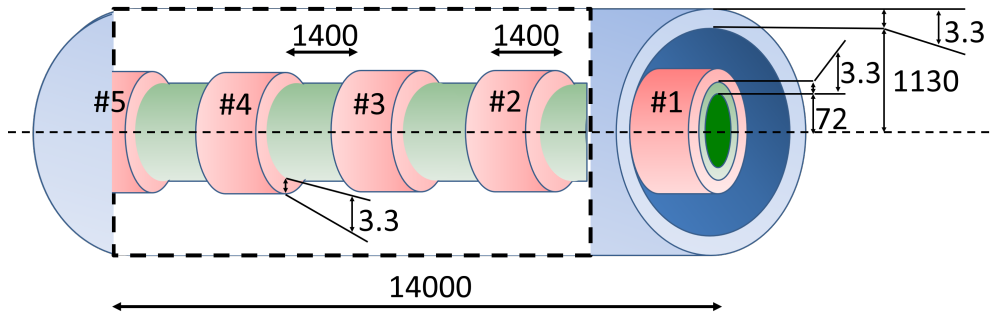

Figure 6.6: NBI PEEC model (not in scale). Blue: external conductive shell; green: internal conductive shell; red: magnetic core snubbers. Values in mm.

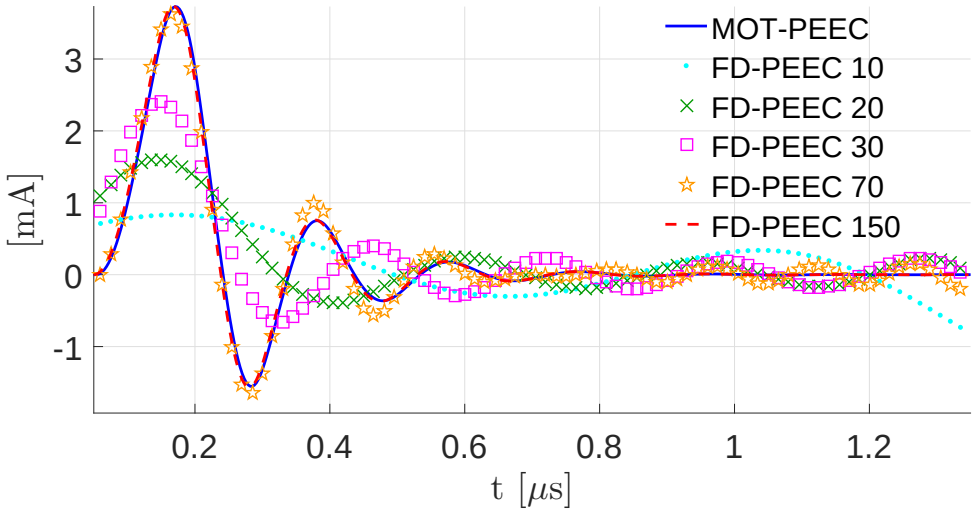

Figure 6.7: Current flowing in the voltage source connected to the NBI.

2. anisotropic medium with $\varepsilon_r = \begin{bmatrix} 3 & 2 & 3 \\ 2 & 8 & 7 \\ 3 & 7 & 9 \end{bmatrix}$,
3. non–homogeneous medium with $\varepsilon_r = 5 + 7z$.

The results obtained from the MOT–PEEC code are compared with the ones obtained from the frequency domain PEEC (FD–PEEC) code [27]. For case 1) only, the results are also compared with the MIE solution. Discrete Fourier Transform (DFT) and Inverse Discrete Fourier Transform (IDFT) are adopted to extract frequency domain results from time simulations and vice-versa.

For case 1), the scattered magnetic field norm (in time domain) evaluated in $[5\text{ m}, 5\text{ m}, 5\text{ m}]$ is shown in Fig. 6.4. For cases 1), 2), and 3), the frequency spectra of the three components of the scattered magnetic field are shown in Fig. 6.5. The same hexahedral mesh with 3,072 elements has been adopted for MOT–PEEC and FD–PEEC.

Results show good agreement and some small discrepancy can be observed only for the smallest components of $\mathbf{H}$.

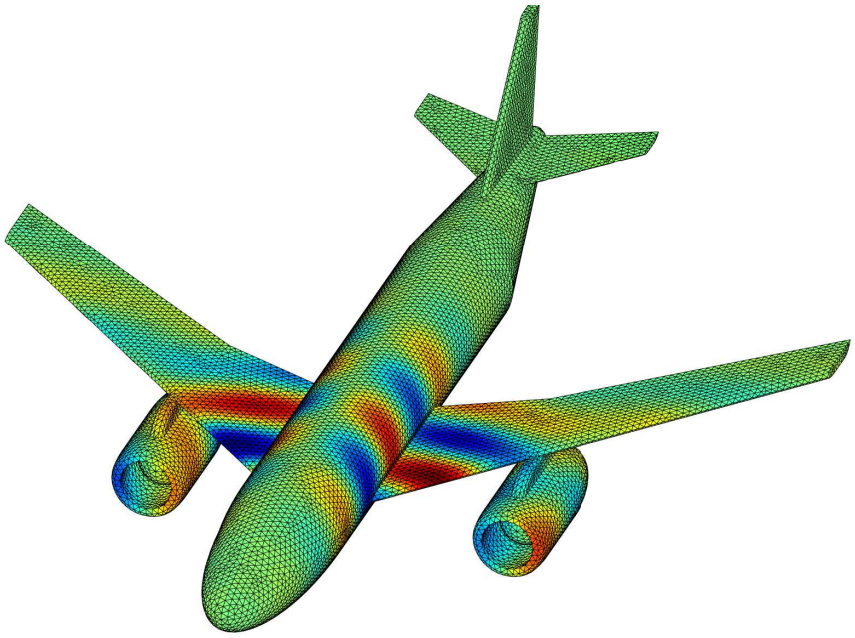

Figure 6.8: Snapshot of the electric potential wave propagating on an equivalent surface model of an Airplane.

Neutral Beam Injector

In the context of Neutral Beam Injector (NBI) for Thermonuclear Fusion applications, the protection against the grid breakdown and other possible failures is a very sensitive issue [157]. NBI are generally complex devices fed by long transmission lines (e.g. $\sim$ 70 m for ITER) which, with a good simplification, can be modeled as coaxial cables operating in electrostatic condition during normal functioning. With the aim of protecting the NBI against possible breakdowns (i.e. damping dangerous voltage oscillations), magnetic core snubbers (combined also with other technologies) are usually adopted.

Here, the simplified case of a NBI is considered. The NBI model (discretized by hexahedral elements) consists of two 14 m long concentric cylindrical shells and it is exemplified in Fig. 6.6. The inner and the outer shells have inner radii of 72 mm and 1.13 m, respectively. Both the shells have a thickness of 3.3 mm and a conductivity of 100 kS/m. The device is fed by a real lumped voltage source (R=50 Ω, L=5 nH) by means of short circuits which connect the end points of the voltage source with all the boundary faces discretizing the initial cross sections of the NBI model. Five equally spaced cylindrical magnetic shells ($\mu_r = 200$, 1.4 m long, thickness $3,3$ mm, inner radius 75.3 mm) are placed around the internal conductive shell of the NBI (magnetic core snubbers). The voltage source generates a unit step voltage (rising time 150 ns). The simulations were run using $\Delta_T = 3$ ns, $N_T = 450$, 6,840 conducting and 1,140 magnetic mesh elements.

The time evolution of the current flowing though the voltage source is shown in Fig. 6.7. The results are compared with those obtained from IDFT FD–PEEC code with a frequency sweep of 150 equally spaced values in the range from 0 Hz to 20 MHz. The results obtained by truncating the sweep after 10, 20, 30, 70, and 150 frequency simulations are shown in Fig. 6.7. Since retardation effects must be considered, the dense integral matrices of FD–PEEC must be updated at each frequency simulation. Thus, to avoid prohibitive computation time, the exponential term of the (harmonic) dynamic Green's function is considered to be constant within every single cell

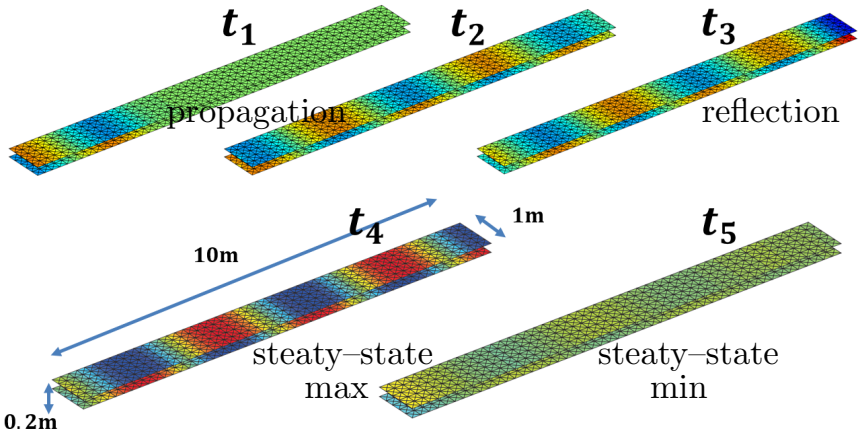

Figure 6.9: EM wave propagation in a Transmission line.

(with a good approximation) and the inductance and potential PEEC matrices are updated at each frequency value by multiplying each matrix entry with the related retardation coefficient.

The Peak Memory Usage (PMU) reached by the MOT–PEEC method is 9.7 GB, the time for the generation of the matrices is $T_g = 324$ s, and the time for a single time solution is $T_s = 1.4$ s. For the sake of comparison, the computational details of the IDFT FD–PEEC are 15 GB of PMU (due to the need of storing the *non–retarded* matrices, the retardation coefficients, and the system to be solved), $T_g = 254$ s, and $T_s = 49$ s (i.e. time for the updating of the matrices and the assembling and solution of the system). Thus, the total simulation time of MOT–PEEC is $T_t = 954$ s while the one of FD–PEEC is $T_t = 7{,}604$ s.

Equivalent surface models: airplane, transmission line, and conducting plate

Following the discussion of section 3.4 concerning the discretization process for equivalent 2–D PEEC models, the MOT–PEEC formulation can be easily modified for the study of equivalent surface models. In Fig. 6.8 a snapshot of the electric potential wave propagating on an airplane excited by a GMP ($f_0 = f_{bw} = 100$ MHz, $\varsigma = \frac{6}{2\pi f_{bw}}$, $t_0 = 4\varsigma$) is shown. The model consists of 83,240 triangular elements, $\rho_c = 7$ mΩ/m, a thickness of 1 mm, $\Delta_T = 0.5$ ns, and $N_T = 800$. Computation time are $T_g = 927$ s, and $T_s = 6.7$ s with PMU of 78 GB.

Fig. 6.9 instead shows the transient evolution of an electromagnetic wave in a transmission line fed by a sinusoidal lumped voltage source ($f = 70$ MHz, $\Delta_T = 0.4$ ns).

Finally, the MOT–PEEC formulation for the case of equivalent surface conductive models is validated on the case of a 1×1 m^2 square plate with normal $[-0.34\mathbf{u}_x, 0.81\mathbf{u}_y, 0.34\mathbf{u}_z]$ excited by the GMP (6.53) with $f_0 = 10^8$ Hz, $\varsigma = \frac{6}{2\pi f_{bw}}$, $t_0 = 4\varsigma$, and $f_{bw} = 10^8$ Hz. The thickness (δ) of the plate is 1 mm and the resistivity is $\rho = 4 \cdot 10^{-5}$ Ω/m. The chosen time step is $\Delta_T = 10^{-9}$ s. Fig. 6.10 shows the temporal evolution of the current density (x–component) in one of the triangular mesh element obtained from the implemented MOT–PEEC code. The result is compared with the ones obtained from the Inverse Discrete Fourier Transform (IDFT) applied to a frequency domain PEEC code and the well–known commercial software FEKO® based on Integral Equation methods.

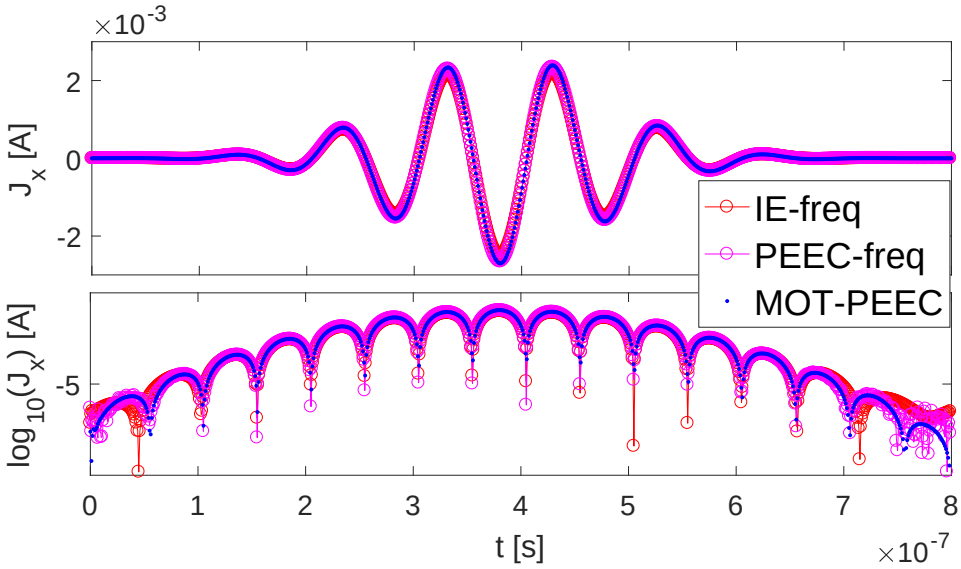

Figure 6.10: Current evolution on the square plate excited by a GMP.

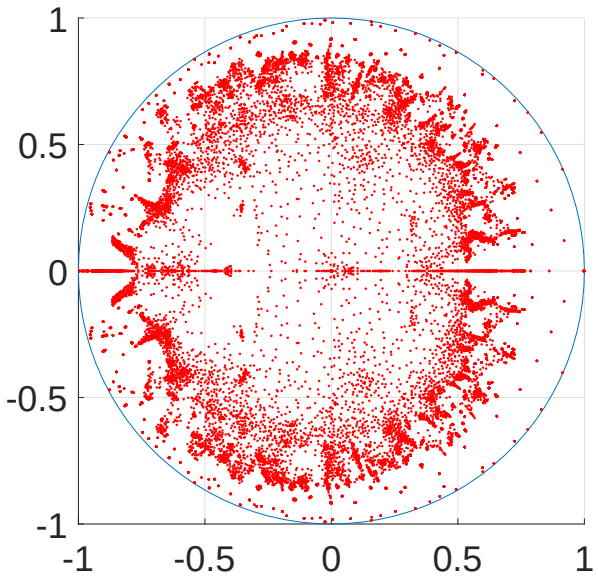

Figure 6.11: Eigenvalues distribution of the transmission MOT matrix in the complex plane for the case of a conducting sphere shell.

Stability analysis: eigenvalues distribution

When the dimension of the problem is relatively small, the stability analysis proposed in [158] and based on the eigenvalues distribution of the MOT transmission matrix can be applied.

Thus, following [158], MOT–PEEC scheme provides an unconditionally stable time–domain method if the magnitude of each eigenvalue of the MOT transmission matrix (constructed following [158]) is lower than 1. Fig. 6.11 shows the eigenvalue distribution of the MOT–PEEC transmission matrix for a 1 m conducting sphere shell with conductivity 10 kS/m and thickness 1 mm (all the eigenvalues have magnitude lower than 1).

Chapter 7

Stochastic–PEEC method

In many electromagnetic applications the values of the material parameters are affected by unavoidable uncertainties. Moreover, conductivity, permittivity, and permeability of media are often strongly influenced by technological uncertainties and external uncontrolled phenomena, such as temperature, pressure, humidity, and other environmental quantities.

Whenever the interest is the extraction of stochastic information of the quantity of interest coming from the aleatory uncertainty in the input material parameters, the traditional Monte Carlo (MC) method can be adopted. However, even considering its generality, the computational effort required by MC is often prohibitive, since several deterministic problems (usually no less than 10,000) must be solved.

To avoid this problem, many different techniques have been proposed in the literature [159]. Most of them are based on the polynomial chaos expansion (PCE) [159], which unfortunately does not allow for easily considering correlated random variables. PCE technique has already been successfully applied to the Finite Integration Technique (FIT) method for magnetostatic [160], eddy–current [161], and electrokinetics [162] problems.

Moreover, the author in [163] successfully applied the PCE technique to an Integral Equation approach based on the PEEC method. However, when the intrusive PCE technique of [163] is applied to IE methods, the computational cost and the memory requirement for the storage of dense matrices rapidly grow with the number of aleatory parameters.

An interesting and efficient alternative which allows for considering both uncorrelated and correlated material parameters has been recently proposed in [164] for electrokinetic problems based on FIT method.

In this chapter, the stochastic PEEC method presented in [163] and based on PCE technique is discussed in Section 7.1. Then, in Section 7.2, an approach equivalent to the one of [164] which combines the well known advantages of Parametric Model Order Reduction (PMOR) with the efficiency of spectral approximation technique is applied PEEC (and more in general to Volume Integral Equation methods). In the here considered formulation, all the effects of the full Maxwell equations are taken into account and conductive, dielectric, and magnetic media can be involved in the simulations.

In this work, only the uncertainty on the material parameters has been considered. Instead, the uncertainty on (general) geometrical parameters and shape of the devices has not been taken into account. Indeed, such case leads to some numerical complications since the dense mutual matrices (which depends on the shape of the devices) are affected by the uncertainties. For this reason, in the context of Integral Equation methods, such case has been poorly considered in the literature [165] and it is still an open matter.

This chapter is the result of an ongoing collaboration with Professors Lorenzo Codecasa and Luca Di Rienzo from Dipartimento di Elettronica, Informazione e Bioingegneria, Politecnico di Milano, Milan, Italy.

7.1 Polynomial Chaos Expansion

In the proposed stochastic PEEC method the advantages of the integral equations method are combined with those of Polynomial Chaos Expansion technique [159]. The described approach allows for quantifying the uncertainty of the output quantities of interest coming from the aleatory uncertainty in the input material parameters, with a potentially less time-consuming process compared to the traditional Monte Carlo (MC) method. Differently from the MC method, which requires to solve several deterministic problems, with the stochastic PEEC based on PCE only one (computationally larger) problem must be solved and only conductive, dielectric ($\varepsilon_r \neq 1$), and magnetic ($\mu_r \neq 1$) media must be discretized, considering one or more material parameters as random variables.

In this section, the Unstructured–PEEC method is adopted but an equivalent formulation can be also derived basing on the Standard–PEEC approach without any additional effort. In the numerical results, the formulation is validated against the MC method considering the cases of a double spherical conductive shield and a double spherical magnetic shield. With the aim of maintaining a feasible simulation time, the MC method is applied to axisymmetric Finite Element Method simulations and to the analytical expression of the shielding factor for the case of the double spherical magnetic shield.

7.1.1 Deterministic PEEC formulation

The proposed stochastic PEEC formulation starts from the deterministic PEEC method. In the following, for the sake of clarity, only homogeneous and piecewise–homogeneous conductive media are considered, while the cases of surface conductive, dielectric, and magnetic media are discussed in section 7.1.3.

With the aim of providing a stand alone presentation and limiting the amount of cross–references with other parts of the thesis, the PEEC formulation is shortly derived.

The Electric Field Integral Equation introduced in Chapter 2 is here reported:

$$\mathbf{E}(\mathbf{r}) = \mathbf{E}_{ext}(\mathbf{r}) + i\omega\mu_0 \int_{\Omega_c} \mathbf{J}_c(\mathbf{r}')g(\mathbf{r},\mathbf{r}')d\Omega' + \nabla\Big[\int_{\Omega_c} \varepsilon_0^{-1}\varrho(\mathbf{r}')g(\mathbf{r},\mathbf{r}')d\Omega' + \int_{\Gamma_c} \varepsilon_0^{-1}\sigma(\mathbf{r}')g(\mathbf{r},\mathbf{r}')d\Gamma'\Big], \tag{7.1}$$

where $\mathbf{E}$ is the (total) electric field, $\mathbf{E}_{ext}$ is the external electric field, and $\mathbf{J}_c$ is the conduction current density vector. ϱ_c and ς_c are the free volume and surface charge densities, respectively, ω is the angular frequency, μ_0 and ε_0 are the permeability and permittivity of the vacuum, respectively. $\mathbf{r}$ is the field point, $\mathbf{r}'$ is the integration point, $g(\mathbf{r},\mathbf{r}')$ is the Green's function, and Ω_c is the conductive domain (computational region) with boundary $\Gamma_c = \partial\Omega_c$. Moreover, the following continuity relations which link $\mathbf{J}_c$ to ϱ_c and ς_c are defined:

$$\nabla \cdot \mathbf{J}_c(\mathbf{r}) = -i\omega\varrho_c(\mathbf{r}), \quad (\mathbf{J}_c^+(\mathbf{r}) - \mathbf{J}_c^-(\mathbf{r})) \cdot \mathbf{n} = i\omega\varsigma_c(\mathbf{r}), \tag{7.2}$$

where the subscripts $+$ and $-$ indicate the two sides of the surface where the conduction current density is discontinuous and $\mathbf{n}$ is the unit normal vector of that surface.

When conductive media are considered, Ohm's law, that locally links $\mathbf{E}$ to $\mathbf{J}_c$, can be applied:

$$\mathbf{E}(\mathbf{r}) = \rho_c(\mathbf{r})\mathbf{J}_c(\mathbf{r}),\ in\ \Omega, \tag{7.3}$$

where $\rho_c = 1/\sigma_c$ is the electric resistivity and σ_c is the electric conductivity. The computational domain Ω_c is then discretized into a tetrahedral or hexahedral mesh consisting on v_c volumes, f_c faces (of which f_c^b boundary faces), e_c edges, and n_c nodes. $\mathbf{J}_c$ is now expanded as:

$$\mathbf{J}_c(\mathbf{r}) = \sum\nolimits_k^{f_c} \mathbf{w}_k(\mathbf{r}) j_{ck}, \tag{7.4}$$

where $\mathbf{w}_k(\mathbf{r})$ is the Whitney face shape function and j_{ck} is the flux of $\mathbf{J}_c$ through the kth face of the mesh.

Combining (7.1) with (7.2), an integral equation where $\mathbf{E}$ only depends on $\mathbf{J}$ (and the external electric field $\mathbf{E}_{ext}$) can be obtained. Thus, combining (7.1) with (7.2) and (7.4), and applying a Galerkin projection to the resulting equation, the following matrix equation is obtained:

$$\tilde{\mathbf{e}} = -\big[i\omega\mathbf{L}_c^c + \frac{1}{i\omega}\mathbf{D}_{\Omega_c}^{aT}\mathbf{P}_c^c\mathbf{D}_{\Omega_c}^a\big]\mathbf{j}_c + \tilde{\mathbf{e}}_0, \tag{7.5}$$

where $\mathbf{j}_c = (j_{ck})$ is the array of degrees of freedom (DoFs) storing j_{ck}. $\tilde{\mathbf{e}}$ and $\tilde{\mathbf{e}}_0$ are the arrays of DoFs related to $\mathbf{E}$ and $\mathbf{E}_{ext}$.

$\mathbf{D}_{\Omega_c}^a$ is the volume–face augmented divergence defined in Chapter 3. $\mathbf{L}_c^c$ and $\mathbf{P}_c^c$ are the (dense) inductance and potential matrices having dimensions $f_c \times f_c$ and $(v_c + f_c^b) \times (v_c + f_c^b)$, respectively. The expression of a generic khth entry of $\mathbf{L}_c^c$ and $\mathbf{P}_c^c$ are given in (3.34) and (3.37), respectively.

The same Galerkin projection can now be applied to equation (7.3), combined with the expansion (7.4). This results in

$$\tilde{\mathbf{e}} = \mathbf{R}_c\mathbf{j}, \tag{7.6}$$

where $\mathbf{R}_c$ is the (sparse) $f_c \times f_c$ resistance matrix. The expression of the matrix entries of $\mathbf{R}_c$ are

$$R_{ckh} = \int_\Omega \rho_c(\mathbf{r})\mathbf{w}_k(\mathbf{r}) \cdot \mathbf{w}_h(\mathbf{r})dr. \tag{7.7}$$

Finally, combining the matrix equations (7.5) and (7.6), the following deterministic algebraic system of equation is obtained:

$$\big[\mathbf{R}_c + i\omega\mathbf{L}_c^c + \frac{1}{i\omega}\mathbf{D}_{\Omega_c}^{aT}\mathbf{P}_c^c\mathbf{D}_{\Omega_c}^a\big]\mathbf{j}_c = \tilde{\mathbf{e}}_0. \tag{7.8}$$

This system requires the storage of f_c^2 complex entries, unless compression techniques are adopted. Equation (7.8) can be solved as is or, eventually, it can be projected into a reduced set of unknowns as proposed in Section 4.2.4. Moreover, the mesh of Ω_c can be interpreted as an electric circuit where the faces represent the circuit branches and the volumes and the boundary faces represent the circuit nodes. Thus, (7.8) can be interpreted as the Kirchhoff's voltage law written for each circuit branch and the electromagnetic problem can be easily coupled with external circuit elements.

Table 7.1: Multi–index with $q = 3$ and $n = 2$

$\|\boldsymbol{\alpha}\|$	multi–index $\boldsymbol{\alpha}$	global–index $\mathbf{k}$
0	$(0,0,0)$	1
1	$(1,0,0)$	2
	$(0,1,0)$	3
	$(0,0,1)$	4
2	$(2,0,0)$	5
	$(1,1,0)$	6
	$(1,0,1)$	7
	$(0,2,0)$	8
	$(0,1,1)$	9
	$(0,0,2)$	10

7.1.2 Stochastic PEEC formulation

In the same fashion and notation of [161], the electric resistivity ρ_c is now assumed to depend on a small number q of random variables $\xi_1, \ldots, \xi_q$, which can be assumed to be statistically independent. In the case of statistical correlation the approach proposed in the Section 7.2 can be adopted. Vector $\boldsymbol{\xi} = [\xi_1, \ldots, \xi_q]$ can be defined so that $\rho_c = \rho_c(\mathbf{r}, \boldsymbol{\xi})$. PCEs can now be introduced for all the electromagnetic fields, e.g.

$$\mathbf{J}_c(\mathbf{r}, \boldsymbol{\xi}) = \sum_{|\boldsymbol{\alpha}| \leq p} \mathbf{J}_{c\boldsymbol{\alpha}}(\mathbf{r}) \boldsymbol{\psi}_{\boldsymbol{\alpha}}(\boldsymbol{\xi}), \tag{7.9}$$

where p is the order chosen for the PCE, $\boldsymbol{\alpha} = (\alpha_1, \ldots, \alpha_q)$ is a multi–index of q elements (see Table 7.1)[159], $|\boldsymbol{\alpha}| = \alpha_1 + \alpha_2 + \ldots + \alpha_q$, and

$$\boldsymbol{\psi}_{\boldsymbol{\alpha}}(\boldsymbol{\xi}) = \psi^1_{\alpha_1}(\xi_1) \psi^2_{\alpha_1}(\xi_2) \ldots \psi^q_{\alpha_q}(\xi_q), \tag{7.10}$$

in which $\psi^k_j(\xi_k)$ with $j = 0, 1, \ldots$ are polynomials of degree not greater than p forming an orthonormal basis in the probability space of random variable ξ_k, for $k = 1, \ldots, q$ [159]. $\mathbf{J}_{c\boldsymbol{\alpha}}(\mathbf{r})$ is the projection of $\mathbf{J}(\mathbf{r}, \boldsymbol{\xi})_c$ onto $\boldsymbol{\psi}_{\boldsymbol{\alpha}}(\boldsymbol{\xi})$; the same expansion is adopted for $\mathbf{E}$ and $\mathbf{E}_{ext}$.

The functions $\boldsymbol{\psi}_{\boldsymbol{\alpha}}(\boldsymbol{\xi})$ form a basis of dimension $n = \binom{p+q}{p}$ and satisfy the nonorthogonality property:

$$\mathbb{E}[\boldsymbol{\psi}_{\boldsymbol{\alpha}}(\boldsymbol{\xi}) \boldsymbol{\psi}_{\boldsymbol{\beta}}(\boldsymbol{\xi})] = \int_{\mathbf{I}} \boldsymbol{\psi}_{\boldsymbol{\alpha}}(\boldsymbol{\xi}) \boldsymbol{\psi}_{\boldsymbol{\beta}}(\boldsymbol{\xi}) f(\boldsymbol{\xi}) d\boldsymbol{\xi} = \boldsymbol{\delta}_{\boldsymbol{\alpha}\boldsymbol{\beta}}, \tag{7.11}$$

where $\mathbb{E}[\cdot]$ indicates the statistical mean value, $\mathbf{I}$ is the support of the polynomials, $\boldsymbol{\delta}_{\boldsymbol{\alpha}\boldsymbol{\beta}}$ is the q–variate Kronecker delta function, and $f(\boldsymbol{\xi})$ is the Probability Density function (PDF).

From (7.9), analogous PCEs are obtained for the arrays of DOFs $\mathbf{j}_c$, $\tilde{\mathbf{e}}$, and $\tilde{\mathbf{e}}_0$, e.g.:

$$\mathbf{j}_c(\boldsymbol{\xi}) = \sum_{|\boldsymbol{\alpha}| \leq p} \mathbf{j}_{c\boldsymbol{\alpha}} \boldsymbol{\psi}_{\boldsymbol{\alpha}}(\boldsymbol{\xi}), \tag{7.12}$$

where $\mathbf{j}_{c\boldsymbol{\alpha}}$ is the projection of $\mathbf{j}(\boldsymbol{\xi})_c$ onto $\boldsymbol{\psi}_{\boldsymbol{\alpha}}(\boldsymbol{\xi})$:

$$\mathbf{j}_{c\boldsymbol{\alpha}} = \mathbb{E}[\mathbf{j}(\boldsymbol{\xi})_c \boldsymbol{\psi}_{\boldsymbol{\alpha}}(\boldsymbol{\xi})]. \tag{7.13}$$

The same procedure can be repeated for $\tilde{\mathbf{e}}$ and $\tilde{\mathbf{e}}_0$, leading to the projections $\tilde{\mathbf{e}}_{\boldsymbol{\alpha}}$ and $\tilde{\mathbf{e}}_{0\boldsymbol{\alpha}}$. These projections can be stored in the global vector arrays

$$\boldsymbol{J}_c = [\mathbf{j}_{c\boldsymbol{\alpha}}], \quad \tilde{\boldsymbol{E}}_0 = [\tilde{\mathbf{e}}_{0\boldsymbol{\alpha}}], \quad \tilde{\boldsymbol{E}} = [\tilde{\mathbf{e}}_{\boldsymbol{\alpha}}], \tag{7.14}$$

where sub–vectors of multi–indices $\boldsymbol{\alpha}$ are stored in lexicographical order as shown in [159].

The vector arrays $\mathbf{j}$, $\tilde{\mathbf{e}}$, and $\tilde{\mathbf{e}}_0$ in (7.5) are now substituted with their PCEs. Then, a Galerkin approach is applied by projecting the resulting matrix equation onto each polynomial $\boldsymbol{\psi}_{\boldsymbol{\alpha}}(\boldsymbol{\xi})$. As result, the following matrix equation is obtained for each polynomial $\boldsymbol{\psi}_{\boldsymbol{\alpha}}(\boldsymbol{\xi})$:

$$\tilde{\mathbf{e}}_{\boldsymbol{\alpha}} = -\big[i\omega\mathbf{L}_c^c + \frac{1}{i\omega}\mathbf{D}_{\Omega_c}^{aT}\mathbf{P}_c^c\mathbf{D}_{\Omega_c}^{a}\big]\mathbf{j}_{c\boldsymbol{\alpha}} + \tilde{\mathbf{e}}_{0\boldsymbol{\alpha}}. \tag{7.15}$$

This equation written for all the multi–indices $\boldsymbol{\alpha}$ (with $|\boldsymbol{\alpha}| \leq p$) results in the following matrix equation

$$\tilde{\boldsymbol{E}} = -\big(\mathbf{1}_n \otimes \big[i\omega\mathbf{L}_c^c + \frac{1}{i\omega}\mathbf{D}_{\Omega_c}^{aT}\mathbf{P}_c^c\mathbf{D}_{\Omega_c}^{a}\big]\big)\boldsymbol{J}_c + \tilde{\boldsymbol{E}}_0, \tag{7.16}$$

where $\otimes$ is the Kronecker product and $\mathbf{1}_n$ is the identity matrix of dimension $n \times n$.

The same procedure can now be applied to the discrete form of the Ohm's law in (7.6). Thus, by projecting (7.6) onto each polynomial $\boldsymbol{\psi}_{\boldsymbol{\beta}}(\boldsymbol{\xi})$ and substituting $\tilde{\mathbf{e}}$ and $\mathbf{j}_c$ with their PCEs, the following equation is obtained:

$$\tilde{\boldsymbol{E}} = \mathcal{R}_c\boldsymbol{J}_c, \tag{7.17}$$

where $\mathcal{R}_c$ can be written in block form

$$\mathcal{R}_c = [\mathbf{R}_{c\boldsymbol{\alpha}\boldsymbol{\beta}}] = \begin{bmatrix} \mathbf{R}_{c\mathbf{1},\mathbf{1}} & \mathbf{R}_{c\mathbf{1},\mathbf{2}} & \cdots \\ \vdots & \ddots & \\ \mathbf{R}_{c\mathbf{n},\mathbf{1}} & & \mathbf{R}_{c\mathbf{n},\mathbf{n}} \end{bmatrix}. \tag{7.18}$$

The $khth$ coefficient of the $n_f \times n_f$ matrix $\mathbf{R}_{c\boldsymbol{\alpha}\boldsymbol{\beta}}$ is given by

$$R_{c\boldsymbol{\alpha}\boldsymbol{\beta},kh} = \int_\Omega \mathbb{E}[\rho_c(\mathbf{r},\boldsymbol{\xi})\boldsymbol{\psi}_{\boldsymbol{\alpha}}(\boldsymbol{\xi})\boldsymbol{\psi}_{\boldsymbol{\beta}}(\boldsymbol{\xi})]\mathbf{w}_k(\mathbf{r})\cdot\mathbf{w}_h(\mathbf{r})dr. \tag{7.19}$$

For homogeneous or piecewise–homogeneous conductive media the resistivity can be considered uniform inside each mesh element, $\rho_c(\mathbf{r},\boldsymbol{\xi}) = \rho_c(\boldsymbol{\xi})$. Thus, the statistical mean in (7.19) can be moved outside the spatial integral. Assuming that ρ_c is uniform and equal to ρ_c^u in each subregion $\Omega_{c,u}$, with $u = 1, \cdots, r$ ($\Omega_c = \Omega_{c,1} \cup \cdots \cup \Omega_{c,r}$), $\mathcal{R}_c$ can be evaluated as

$$\mathcal{R}_c = \sum_{u=1}^{r} \boldsymbol{\Psi}_u \otimes \mathbf{R}_{c,u}, \tag{7.20}$$

where the coefficients of the $n \times n$ matrix $\boldsymbol{\Psi}_u$ are

$$\Psi_{u,\boldsymbol{\alpha}\boldsymbol{\beta}} = \mathbb{E}[\rho_c^u(\boldsymbol{\xi})\boldsymbol{\psi}_{\boldsymbol{\alpha}}(\boldsymbol{\xi})\boldsymbol{\psi}_{\boldsymbol{\beta}}(\boldsymbol{\xi})], \tag{7.21}$$

whereas the entries of the $n_f \times n_f$ matrix $\mathbf{R}_u$ are given by

$$R_{u,kh} = \int_{\Omega_u} \mathbf{w}_k(\mathbf{r})\cdot\mathbf{w}_h(\mathbf{r})dr. \tag{7.22}$$

Finally, combining (7.16) and (7.17), the following stochastic matrix equation is obtained

$$\Big[\sum_{u=1}^{r} \mathbf{\Psi}_u \otimes \mathbf{R}_u + \mathbf{1}_n \otimes (i\omega \mathbf{L}_c^c + \frac{1}{i\omega} \mathbf{D}_{\Omega_c}^{aT} \mathbf{P}_c^c \mathbf{D}_{\Omega_c}^a)\Big] \boldsymbol{J}_c = \tilde{\boldsymbol{E}}_0. \tag{7.23}$$

The $nn_f \times nn_f$ matrix system in (7.23) is characterized by dense diagonal blocks and sparse off–diagonal blocks and it requires the storage of $\sim nn_f^2$ matrix entries. Alternatively, for the particular case of $r = 1$, equation (7.23) can be solved as proposed in [166]. Thus, the inversion of two $n_f \times n_f$ dense matrices and the storage of $\sim 3n_f^2$ complex matrix entries is required but the whole stochastic system is not explicitly assembled. Furthermore, for $r > 1$, compression techniques can be applied to the dense diagonal blocks of (7.23) that can be described with the same low–rank approximation of the dense matrix $i\omega \mathbf{L}_c^c + \frac{1}{i\omega} \mathbf{D}_{\Omega_c}^{aT} \mathbf{P}_c^c \mathbf{D}_{\Omega_c}^a$.

7.1.3 Extension of the formulation

In the previous sections the deterministic and the stochastic PEEC formulations for the case of piecewise–homogeneous volume conductive media have been presented. In the following, the case of equivalent 2–D PEEC models and the cases of dielectric and magnetic media are discussed.

Equivalent 2–D PEEC models

When very thin conductive devices are considered or when the skin effect is dominant, an equivalent 2–D model can be adopted (see section 3.4). When an equivalent 2–D model is adopted, the current density is considered with a known distribution along the thickness. Thus, when the distribution of $\mathbf{J}_c$ is imposed, the coefficient of the resistance matrix depends on $\rho_c^* = \rho_c/\delta$, where δ is the thickness of the equivalent 2–D model. Therefore, ρ_c and δ can be considered also as random variables.

A similar consideration holds for the case of 1–D equivalent models.

Dielectric and magnetic media

The formulation presented here can be easily extended to the case of dielectric media simply by replacing $\mathbf{J}_c$ with the electric current density $\mathbf{J}_e = \mathbf{J}_c + i\omega\mathbf{P}$, where $\mathbf{P}$ is the polarization vector. Moreover, the constitutive equation (7.3) is substituted with

$$\mathbf{E}(\mathbf{r}) = \rho_e(\mathbf{r}) \mathbf{J}_e(\mathbf{r}), \tag{7.24}$$

where ρ_e is the equivalent electric resistivity:

$$\rho_{eq}(\mathbf{r}) = \frac{1}{\sigma_c + i\omega\varepsilon_0(\varepsilon_r(\mathbf{r}) - 1)}, \text{ in } \Omega_e, \tag{7.25}$$

in which Ω_e is the electric domain $\Omega_e = \Omega_c \cup \Omega_d$. Thus, ρ_e can now be assumed as a stochastic quantity.

When magnetic media are considered, an equivalent procedure can be applied staring from the Amperian or Coulombian PEEC discretization proposed in Chapter 3. Thus, all the material parameters of electric and magnetic domains can be considered as random variables. Moreover,

when only magnetic media are considered it is sufficient to perform the following substitutions:

$$\begin{gathered}\mathbf{E} \Rightarrow \mathbf{H}, \quad \mathbf{E}_0 \Rightarrow \mathbf{H}_0, \quad \mathbf{J}_c \Rightarrow \mathbf{J}_m, \quad \varrho \Rightarrow \varrho_m, \quad \varsigma \Rightarrow \varsigma_m, \\ \mu_0 \Rightarrow \varepsilon_0, \quad \varepsilon_0 \Rightarrow \mu_0, \quad \rho \Rightarrow \rho_m,\end{gathered} \tag{7.26}$$

in which $\mathbf{H}$ is the magnetic field, $\mathbf{H}_0$ is the external magnetic field, $\mathbf{J}_m = i\omega\mu_0\mathbf{M}$ is the magnetization current vector (where $\mathbf{M}$ is the magnetization), ϱ_m and ς_m are the volume and surface magnetic bound charge density, respectively, and $\rho_m = (i\omega\mu_0(\mu_r - 1))^{-1}$ is the magnetic resistivity (where μ_r is the relative permeability). Then, applying (7.26), the stochastic PEEC method for magnetic media can be developed following the procedure given in the previous section (Section 7.1.2).

Lumped circuit elements

In the PEEC method, the mesh of the active domain can be interpreted as an electric circuit where the faces represent the circuit branches and the volumes and the boundary faces represent the circuit nodes. Thus, the final PEEC system of equations can be interpreted as the Kirchhoff's voltage law written for each circuit branch. Thanks to this circuit interpretation, the electromagnetic problem can be easily coupled with external circuit elements. Furthermore, the electric parameter (resistance, inductance, or capacitance) of these lumped circuit elements can be considered as stochastic quantities.

7.1.4 Numerical results

The case of a double conductive spherical shield in a uniform time–harmonic magnetic field is now considered. The inner and outer radii of the internal shield are 0.91 m and 0.93 m, respectively, whereas the inner and outer radii of the external shield are 0.98 m and 1.00 m, respectively. The conductivity of the two shells are modeled by two statistically independent conductivities σ_c^{in} and σ_c^{ext}, with uniform probability density functions (PDF) in the range of $30-80$ kS/m for σ_c^{in} and $50-90$ kS/m for σ_c^{ext}. The frequency of the problem is $f = 100$ Hz. In order to impose $\mathbf{H}_{ext} = [0, 0, \mu_0^{-1}]$, the formulation requires to impose $\mathbf{E}_{ext} = [i\omega y/2, -i\omega x/2, 0]$. The PDF of the shielding factor $\mathcal{S} = \mathbf{H}/\mathbf{H}_{ext}$ (evaluated in the center of the spherical shells) is computed with the Stochastic PEEC method. In Fig. 7.1, the results obtained with $p = 4$ are compared with the ones obtained from the MC method (10^4 runs) applied to the simulations of a well–known commercial FEM software. An axisymmetric model of the device is adopted for the FEM simulations. Fig. 7.2 shows the relative errors ϵ_r of the first two moments of $\mathcal{S}$ versus p and with respect to the solution obtained choosing a PCE order equal to 9. The model adopted for the Stochastic PEEC method ($p = 4$) uses 28,200 unknowns and the simulation requires 482 s with a ~ 2.7 GB peak memory usage (PMU). The MC–FEM simulation requires 6,576 s and a ~ 2 GB PMU.

The second test case consists of a double magnetic spherical shield in a uniform magnetostatic field. The "dual" magnetic form of the Stochastic PEEC method has been adopted (i.e. substitutions (7.26) are applied) in its magnetostatic form by simply scaling the final matrix equations by $i\omega$. The results in terms of $\mathcal{S}$ are compared with the ones obtained with MC method ($25 \cdot 10^6$ runs) using the analytical expression of $\mathcal{S}$ [167]. The inner and outer radii of the internal shield are 0.89 m and 0.90 m, respectively, whereas the inner and outer radii of the external shield are 0.99 m and 1.00 m, respectively. The relative permeability of the two shells

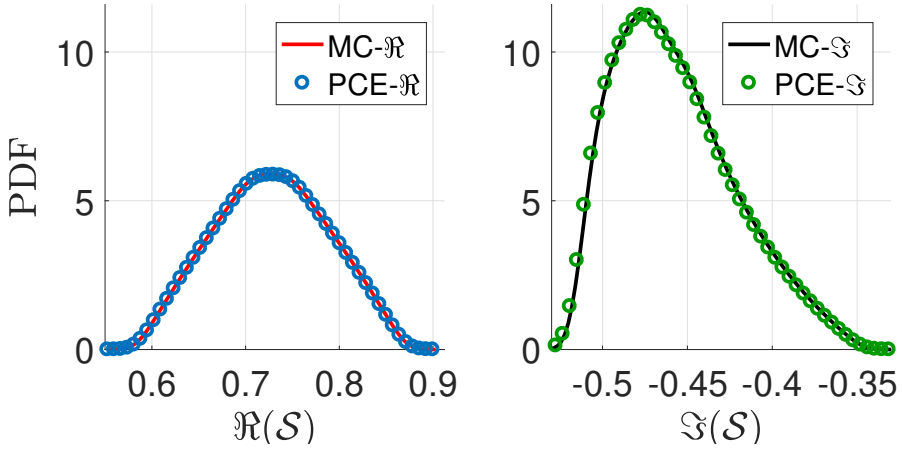

Figure 7.1: PDF of $\mathcal{S}$, stochastic PEEC ($p = 4$) vs MC–FEM

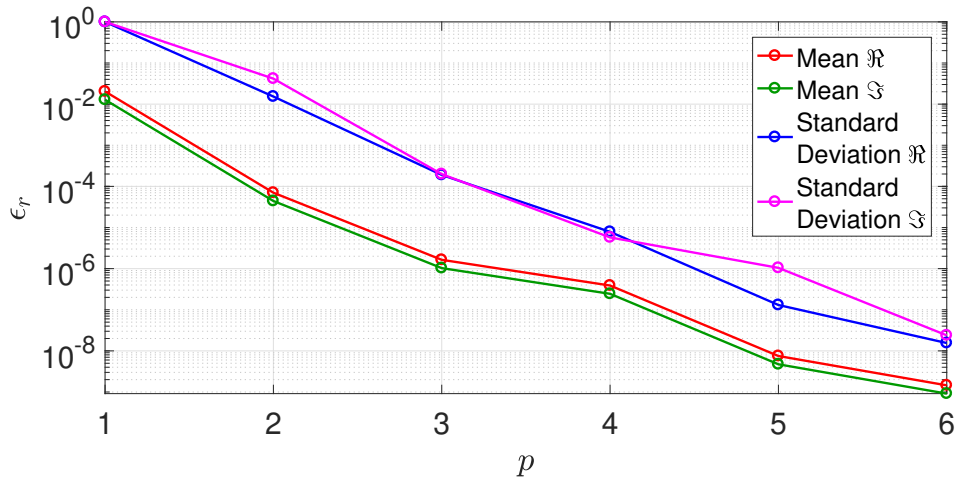

Figure 7.2: Relative error of the first two moments of $\mathcal{S}$ versus p.

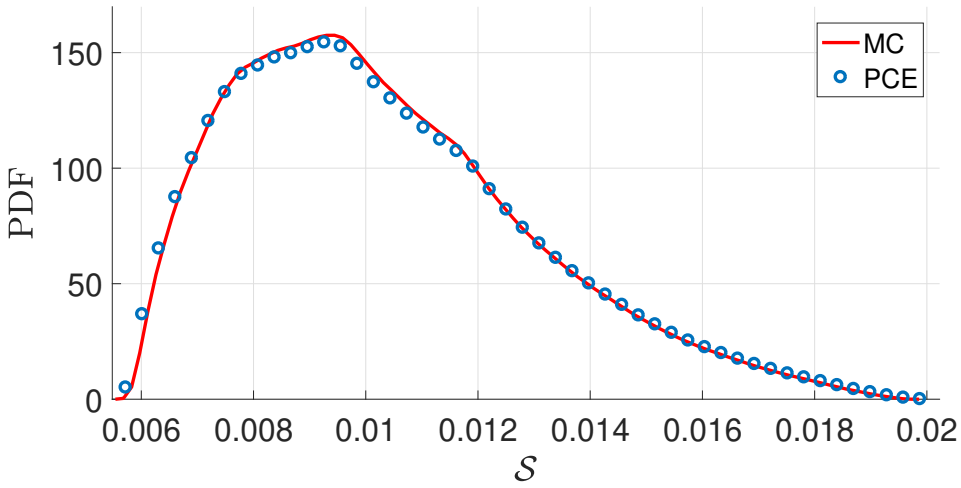

Figure 7.3: PDF of $\mathcal{S}$, stochastic PEEC ($p = 4$) vs MC–Analytic.

are modeled by two statistically independent relative permeabilities μ_r^{in} and μ_r^{ext}, with uniform PDF in the range of $1{,}600 - 3{,}000$ for μ_r^{in} and $1{,}500 - 3{,}500$ for μ_r^{ext}. The comparison between the Stochastic PEEC and the MC method are compared in Fig. 7.3. The model adopted for the

Stochastic PEEC method ($p = 4$) consists of 29,380 unknowns and the simulation requires 1,303 s with a $\sim$ 1.5 GB PMU.

The results in Fig. 7.1, Fig. 7.2, and Fig. 7.3 show the good accuracy and convergence (respect the value of p) of the proposed Stochastic PEEC method. Small disagreements in Fig. 7.3 are due to the mesh discretization of the spherical shells and not to the stochastic method. The simulations were run on a Windows machine equipped with a dual–6-core/12-thread processors (Intel E5645 @2.40GHz) and 104 GB of RAM.

7.2 Parametric Model Order Reduction and spectral approximation

In this chapter, the well known advantages of Parametric Model Order Reduction (PMOR) with the efficiency of spectral approximation technique is applied to Volume Integral Equation (VIE) methods such as PEEC with the aim of overcoming the shortcomings of the Stochastic–PEEC method presented in the previous section ans based on PCE. The discussions of this chapter have been submitted to Journal of Computational Physics and are now under peer–revision.

It is worth noting that, although the PEEC formulation is here considered, the same stochastic approach here proposed can be applied to different VIE formulations.

The following section is organized as follows. In section 7.2.1, the structure of the deterministic parametric problem is first described. Then, in section 7.2.2, the stochastic method is presented and subdivided in three parts. First, a PMOR algorithm which drastically reduces the dimension of the parametric problem is presented and widely discussed. Thank to the choice of the adopted VIE method, at each iteration of the PMOR algorithm only the sparse *material* matrices must be updated, while the dense *integral* ones remain constant. This leads to a very fast and efficient method where the computational cost is headed by the solution of only *few* deterministic VIE (i.e. PEEC) problems. In the second part of the code, a spectral approximation is applied to describe the relationships between the (aleatory) material parameters and the quantities of interest derived from the unknowns of the parametric VIE problem. Then, in the last part of the code, a MC simulations is finally applied to the spectral approximation with a negligible computational cost.

In section 7.2.3, the *analytical* case of a multi–shell dielectric sphere and the *industrial* case of the induction heating pot presented in [135] are considered. The obtained results demonstrate the efficiency and accuracy of the implemented method, which is able to consider both 3–D and axisymmetric electromagnetic problems with a (relatively) high number of random material parameters. The electromagnetic media exhibit complex material quantities, where the real and the imaginary parts are considered as two potentially independent aleatory variables. The considered numerical cases show that a very small dimension of the reduced order model is sufficient to reach very high accuracy. Moreover, the exponential convergence of the spectral approximation is observed in the numerical studies [159].

In the presented numerical test cases, the values of the chosen frequencies allow for neglecting the time delay effects on the propagation of the electromagnetic fields. Indeed, this choice allow for focusing the main attention on the *stochastic part* of the problem, without falling back into the well–known numerical issues of VIE methods (see section 4.2.3, [128]). However, the proposed method can be potentially extended to the case of high frequency problems.

The final results of the implemented code consist of: 1) a reduced order model of the parametric problem and, 2) a further spectral expansion of any quantity derived from the unknowns of the electromagnetic problem. Then, stochastic analysis can be carried out by assuming different probability distributions and correlation between the material parameters, without the need of re–running the code. With respect to [164], sparse grids have been successfully adopted to mitigate the well–known problem of the *curse of dimensionality* and accelerate the code [159]. Moreover, since the construction of the reduced order model relies on the solution of few deterministic problems, *low–rank* approximation techniques could be adopted to further reduce the overall computational effort, as shown in Chapter 5 [19, 77].

7.2.1 Deterministic parametric problem

The starting point of the discussion is the (reduced) system of equation obtained from the C–PEEC. For the sake of clarity the system, which has been first introduced in (4.16), is here reported

$$\begin{bmatrix} \mathbf{R}_e + i\omega\mathbf{L}_e^e + \frac{1}{i\omega}\tilde{\mathbf{G}}^a_{\Omega_e}\mathbf{P}_e\mathbf{D}^a_{\Omega_e} & \mathbf{M}_{1/\varepsilon_0}\mathbf{C}_{\Omega_e}\tilde{\mathbf{N}}^e_m \\ -\tilde{\mathbf{M}}_{1/\mu_0}\tilde{\mathbf{C}}_{\Omega_m}\mathbf{N}^m_e & \tilde{\mathbf{R}}_m + i\omega\tilde{\mathbf{L}}^m_m + \frac{1}{i\omega}\mathbf{G}^a_{\Omega_m}\tilde{\mathbf{P}}_m\tilde{\mathbf{D}}^a_{\Omega_m} \end{bmatrix} \begin{bmatrix} \mathbf{j}_e \\ \tilde{\mathbf{j}}_m \end{bmatrix} = \begin{bmatrix} \tilde{\mathbf{e}}_0 \\ \mathbf{h}_0 \end{bmatrix}. \tag{7.27}$$

Let us now assume that the active domain $\Omega_a = \Omega_e \cup \Omega_m$ consists of K sub–regions where the electric and magnetic resistivities are uniform functions equal to $\bar{\rho}_{e_k}$ and $\bar{\rho}_{m_k}$ in each sub–region Ω_k, with $k = 1, \cdots, K$, i.e.: $\rho_e(\mathbf{r}) = \sum_{k=1}^K \rho_{e_k}(\mathbf{r})$ and $\rho_m(\mathbf{r}) = \sum_{k=1}^K \rho_{m_k}(\mathbf{r})$, where

Thus, (7.27) can be now written as

$$[\mathbf{R} + \mathbf{U}]\mathbf{x} = \mathbf{b}, \tag{7.28}$$

where $\mathbf{U}$, $\mathbf{x}$, and $\mathbf{b}$ are defined independently of the subdivision of Ω_a:

$$\mathbf{x} = \begin{bmatrix} \mathbf{j}_e \\ \tilde{\mathbf{j}}_m \end{bmatrix}, \qquad \mathbf{b} = \begin{bmatrix} \tilde{\mathbf{e}}_0 \\ \mathbf{h}_0 \end{bmatrix}, \qquad \mathbf{U} = \begin{bmatrix} i\omega\mathbf{L}_e^e + \frac{1}{i\omega}\tilde{\mathbf{G}}^a_{\Omega_e}\mathbf{P}_e\mathbf{D}^a_{\Omega_e} & \mathbf{M}_{1/\varepsilon_0}\mathbf{C}_{\Omega_e}\tilde{\mathbf{N}}^e_m \\ -\tilde{\mathbf{M}}_{1/\mu_0}\tilde{\mathbf{C}}_{\Omega_m}\mathbf{N}^m_e & i\omega\tilde{\mathbf{L}}^m_m + \frac{1}{i\omega}\mathbf{G}^a_{\Omega_m}\tilde{\mathbf{P}}_m\tilde{\mathbf{D}}^a_{\Omega_m} \end{bmatrix}. \tag{7.29}$$

Matrix $\mathbf{R}$ instead is given by

$$\mathbf{R} = \sum_{k=1}^K \bar{\rho}_k \mathbf{R}_k, \qquad \text{with} \quad \bar{\rho}_k\mathbf{R}_k = \begin{bmatrix} \bar{\rho}_{e_k}\mathbf{R}_{e_k} & \mathbf{0} \\ \mathbf{0} & \bar{\rho}_{m_k}\tilde{\mathbf{R}}_{m_k} \end{bmatrix}, \tag{7.30}$$

in which $\mathbf{R}_{e_k}$ and $\tilde{\mathbf{R}}_{m_k}$ are defined as in (3.33) and (3.55) setting a unitary value of the electric and magnetic resistivities in the kth sub–region and 0 elsewhere. For the sake of simplicity and with a slight abuse of notation, the *general* resistivity $\bar{\rho}_k = (\bar{\rho}_e, \bar{\rho}_m)$ has been introduced in (7.30).

Equation (7.28) can now be transformed into a *parametric* problem. Indeed, each resistivity value $\bar{\rho}_{e_k}$ and $\bar{\rho}_{m_k}$ (with $k = 1, \cdots, K$) can be considered as a function of a small number Q of parameters $\xi_1, \cdots, \xi_Q$ stored in the vector array $\boldsymbol{\xi}$, i.e. $\bar{\rho}_k = \bar{\rho}_k(\boldsymbol{\xi})$. Each parameter ξ_h, with $k = 1, \cdots, Q$, varies in the set $[-1, 1]$. Thus $\boldsymbol{\xi}$ varies in the set $\boldsymbol{\Xi} = [-1, 1]^Q$, i.e. the Q–dimensional master hypercube. Therefore, the parametric electromagnetic problem is ruled

by

$$\Big[\sum_{k=1}^{K}\bar{\rho}_k(\boldsymbol{\xi})\mathbf{R}_k+\mathbf{U}\Big]\mathbf{x}(\boldsymbol{\xi})=\mathbf{b}. \tag{7.31}$$

When the resistivities $\bar{\rho}_k$, with $k=1,\cdots,K$, are modeled with a given Probability Density Function, a Monte Carlo method can be applied to extract the stochastic informations of some quantity of interest. However, problem (7.31) must be solved for each MC sample. Thus, due to the slow convergence of the MC approach, this method would result in a prohibitive computation time. Moreover, if the assumption on the PDF of the resistivities changes, the MC simulation must be performed again. In the following, an alternative method which drastically reduces the computational time required by the stochastic analysis is proposed.

7.2.2 Stochastic VIE method

The main idea is not to completely avoid the use of MC, which, beyond its slow convergence, is a general and robust method. Instead, the goal is to drastically reduce the computational effort of the problem and finally apply MC to a simple equation. At this purpose, a parametric model order reduction is first applied to (7.31) and then a spectral expansion is applied to the reduced order model. Finally, MC is applied to the spectral expansion with a negligible computational effort. In the following, these three steps are described.

Parametric Model Order reduction

The *reduced parametric model* of (7.31) is constructed by using an iterative approach based on the Parametric Model–Order Reduction algorithm [168] described in Algorithm 2 and previously proposed in [164] for an electrokinetic problem discretized by the Finite Integration Technique (FIT).

According to the PMOR Algorithm 2, at step 0, a Q–dimensional grid defined as $\boldsymbol{\chi}$ is constructed. This grid is here assumed to be the cartesian product of Q sets of P Gaussian points of Legendre polynomials resulting in $N_{\boldsymbol{\chi}}=P^Q$ grid points, but other choices of $\boldsymbol{\chi}$ are possible. The points of the grid are indicated as $\boldsymbol{\zeta}_h$, with $h=1,\cdots,N_{\boldsymbol{\chi}}$. Moreover, the projection matrix $\mathbf{V}_0$ is initialized as the empty set and the index c counting the number of iterations of the algorithm is initialized to 1.

Then, at step 1, the parametric problem ruled by (7.31) is solved for a given choice of $\boldsymbol{\xi}$, which is initialized to $\boldsymbol{\xi}=\mathbf{0}$ at the beginning of the algorithm.

At step 2, the projection matrix $\mathbf{V}_c$ is evaluated by applying a Gram-Schmidt orthogonalization (GSO) to the matrix which stores $\mathbf{V}_{c-1}$ and $\mathbf{x}(\boldsymbol{\xi})$ (i.e. the solution of the parametric problem obtained at step 1):

$$\mathbf{V}_c=\mathrm{GSO}([\mathbf{V}_{c-1},\mathbf{x}(\boldsymbol{\xi})]). \tag{7.32}$$

Columns of $\mathbf{V}_c$ are orthonormal basis vectors of the space spanned by all the solutions obtained at step 1. Thus, $\mathbf{V}_c$ is a $N_x\times c$ orthonormal matrix, where N_x is the dimension of the parametric problem (i.e. the dimension of $\mathbf{x}(\boldsymbol{\xi})$).

At step 3, the parametric reduced model $\mathcal{M}_c$ is finally constructed by projecting (7.31) onto the space spanned by the columns of $\mathbf{V}_c$, i.e.

$$\Big[\sum_{k=1}^{K}\bar{\rho}_k(\boldsymbol{\xi})\hat{\mathbf{R}}_{c_k}+\hat{\mathbf{U}}_c\Big]\hat{\mathbf{x}}(\boldsymbol{\xi})=\hat{\mathbf{b}}_c, \tag{7.33}$$

Algorithm 2 PMOR Algorithm

Input: Matrices $\mathbf{U}$ and $\mathbf{R}_k$ and the functions $\bar{\rho}_k(\boldsymbol{\xi})$, (with $k = 1, \cdots, K$)
Construct $\boldsymbol{\chi}$ // 0
Set $\boldsymbol{\xi} = \mathbf{0}$
Set $r = +\infty$
Set $\mathbf{V}_0 = \emptyset$
Set $c = 1$
Set a desired value of η (e.g. $\eta = 10^{-3}$)
while $r > \eta$ **do**
  Find the solution $\mathbf{x}(\boldsymbol{\xi})$ of (7.31): $\mathbf{x}(\boldsymbol{\xi}) = \left[\sum_{k=1}^{K} \bar{\rho}_k(\boldsymbol{\xi})\mathbf{R}_k + \mathbf{U}\right] \setminus \mathbf{b}$. // 1
  Update the orthonormal basis of dimension c: $\mathbf{V}_c$ =GSO($[\mathbf{V}_{c-1}, \mathbf{x}(\boldsymbol{\xi})]$) // 2
  Generate the reduced order model c: $\hat{\mathbf{U}}_c = \mathbf{V}_c^T\mathbf{U}\mathbf{V}_c$, and $\hat{\mathbf{R}}_{c_k} = \mathbf{V}_c^T\mathbf{R}_k\mathbf{V}_c$, with $k = 1, \cdots, K$ // 3
  for $h = 1, \cdots, N_{\boldsymbol{\chi}}$ (*parallel*) **do**
    Extract the hth grid point $\boldsymbol{\zeta}_h$ of $\boldsymbol{\chi}$
    Find the solution $\hat{\mathbf{x}}(\boldsymbol{\zeta}_h)$ of the reduced order problem (7.33) and then evaluate $\tilde{\mathbf{x}}(\boldsymbol{\zeta}_h) = \mathbf{V}_c\hat{\mathbf{x}}(\boldsymbol{\zeta}_h)$ // 4
    Evaluate the residual: $r'_h = \|\left[\sum_{k=1}^{K} \bar{\rho}_k(\boldsymbol{\zeta}_h)\mathbf{R}_k + \mathbf{U}\right]\tilde{\mathbf{x}}(\boldsymbol{\zeta}_h) - \mathbf{b}\|/\|\mathbf{b}\|$ // 5
  end for
  Find $M \in [1, \cdots, N_{\boldsymbol{\chi}}]$ such that $r'_M = \max(r'_h, \text{with } h = 1, \cdots, N_{\boldsymbol{\chi}})$
  Set $r = r'_M$
  Set $\boldsymbol{\xi} = \boldsymbol{\zeta}_M$ // 6
  if $r > \eta$ **then**
    Set $c = c + 1$
  end if
end while
Output: Reduced order model $\mathcal{M}_c$ consisting of $\hat{\mathbf{U}}_c$ and $\hat{\mathbf{R}}_{k_c}$, with $k = 1, \cdots, K$, and the projection matrix $\mathbf{V}_c$

where

$$\hat{\mathbf{b}}_c = \mathbf{V}_c^T\mathbf{b}, \qquad \hat{\mathbf{U}}_c = \mathbf{V}_c^T\mathbf{U}\mathbf{V}_c, \qquad \hat{\mathbf{R}}_{c_k} = \mathbf{V}_c^T\mathbf{R}_k\mathbf{V}_c, \quad \text{with} \quad k = 1, \cdots, K. \tag{7.34}$$

$\hat{\mathbf{U}}_c$ and $\hat{\mathbf{R}}_{c_k}$ (with $k = 1, \cdots, K$) are square matrices of dimension $c \times c$, $\hat{\mathbf{b}}$ is a vector array of dimension c, and $\hat{\mathbf{x}}(\boldsymbol{\xi})$ is the solution of $\mathcal{M}_c$ for a given choice of $\boldsymbol{\xi}$.

A parametric reduced order model $\mathcal{M}_c$ of dimension c is now constructed. This model of reduced dimension allows obtaining an approximate solution of the original parametric problem (7.31). Indeed, when $\hat{\mathbf{x}}(\boldsymbol{\xi})$ is obtained by solving (7.33), an approximate solution of (7.31) is given by

$$\tilde{\mathbf{x}}(\boldsymbol{\xi}) = \mathbf{V}_c\hat{\mathbf{x}}(\boldsymbol{\xi}), \tag{7.35}$$

where, if $\mathcal{M}_c$ provides an accurate approximation of (7.31), $\mathbf{x}(\boldsymbol{\xi}) \simeq \tilde{\mathbf{x}}(\boldsymbol{\xi})$. In the following steps of the algorithm, $\mathcal{M}_c$ is tested against all the grid points to check if the reduced model actually provides an accurate approximation.

Thus, at step 4, (7.33) is solved for each value of $\boldsymbol{\zeta}_h \in \boldsymbol{\chi}$, with $h = 1, \cdots, N_{\boldsymbol{\chi}}$, and the approximate solutions $\tilde{\mathbf{x}}(\boldsymbol{\zeta}_h)$ are evaluated according to (7.35).

Then, at step 5, the accuracy of each approximate solution $\tilde{\mathbf{x}}(\boldsymbol{\zeta}_h)$, with $h = 1, \cdots, N_{\boldsymbol{\chi}}$, is tested by evaluating the related hth residual as

$$r'_h = \frac{\|\left[\sum_{k=1}^{K} \bar{\rho}_k(\boldsymbol{\zeta}_h)\mathbf{R}_k + \mathbf{U}\right]\tilde{\mathbf{x}}(\boldsymbol{\zeta}_h) - \mathbf{b}\|}{\|\mathbf{b}\|}. \tag{7.36}$$

If for each point $\boldsymbol{\zeta}_h$ belonging to the grid $\boldsymbol{\chi}$, the residual r'_h is smaller than the required tolerance η, then the algorithm stops and the reduced order model $\mathcal{M}_c$ of dimension c is obtained. Instead, if r'_h is greater than η for some points of $\boldsymbol{\zeta}_k \in \boldsymbol{\chi}$, the one which maximizes the value of the residual is chosen as the next candidate of a further iteration of the algorithm.

Thus, at step 6, $\boldsymbol{\xi}$ is set equal to the grid point $\boldsymbol{\zeta}_M$ which maximizes the residual r. Then, if $r > \eta$, the value of the counter c is updated (i.e. $c = c+1$) and the algorithm restarts from step 1. At each iteration of algorithm 2, the reduced order model is not re–constructed from scratch. Instead, only the *new information* obtained from the solution of (7.31) for a new selected grid point is added to $\mathcal{M}_{c-1}$, resulting into $\mathcal{M}_c$. It is worth noting that, due to the adoption of the Gram-Schmidt orthogonalization, it is important to avoid that the algorithm choses an already selected grid point.

The *for–loop* in Algorithm 2 can be executed in parallel by the workers of multi–core computers or clusters. However, due to the well–known problem of the *curse of dimensionality* [159], the number of points of $\boldsymbol{\chi}$ (i.e. $N_{\boldsymbol{\chi}} = P^Q$) exponentially increases with the dimension Q. Therefore, the computation time required by the *for–loop* in Algorithm 2 significantly increases with Q, even with parallelized *for–loop*.

A solution to this problem consists on replacing the Gaussian grid $\boldsymbol{\chi}$ with a sparse grid $\boldsymbol{\chi}^*$ [159]. Sparse grids have been introduced as a computationally more efficient method of integrating multidimensional functions [169]. Indeed, while the Gaussian grid $\boldsymbol{\chi}$ is obtained as a (complete) tensor product of Q sets of Gaussian points, the sparse grid $\boldsymbol{\chi}^*$ is obtained as a much smaller subset of the tensor product. The sparse grid MATLAB® toolbox in [170] based on the Clenshaw-Curtis rule is used in the implementation. The number of points of the sparse grid for this rule is

$$N_{\boldsymbol{\chi}^*} \approx \frac{2^L Q^L}{L!}, \quad \text{with } Q >> 1, \tag{7.37}$$

where L denotes the *level* of the sparse grid [159]. Moreover, contrary to the Gauss–Legendre points, the Clenshaw-Curtis points are mostly located on the boundary of the grid. This allows the PMOR Algorithm to explore the border of $\boldsymbol{\Xi}$ and select the extrema points of $\boldsymbol{\chi}^*$ which usually hold *useful information* of the parametric problem.

The dimension c of the reduced order model $\mathcal{M}_c$ is generally much smaller than N_x (i.e. the dimension of the original parametric problem). Thus, in the context of stochastic analysis, a MC approach can now be adopted by solving the reduced order model $\mathcal{M}_c$ for each sample $\boldsymbol{\xi}_h$, with $h = 1, \cdots, N_{MC}$ and N_{MC} is the number of MC samples. However, since the MC method exhibits a $\mathcal{O}(1/\sqrt{N_{MC}})$ convergence rate, when the stochastic analysis requires an high accuracy, the value of N_{MC} grows significantly, and therefore also the computation time, using the parametric reduced-order model.

In the next section, with the aim of further reducing the computational cost required by the stochastic analysis, a spectral approximation is applied to the reduced order model $\mathcal{M}_c$.

Algorithm 3 Spectral Approximation Algorithm

Input: Reduced order model $\mathcal{M}_c$ consisting of $\hat{\mathbf{U}}_c$ and $\hat{\mathbf{R}}_{k_c}$, with $k = 1, \cdots, K$, and the projection matrix $\mathbf{V}$
for $h = 1, \cdots, N_{\boldsymbol{\chi}}$ (*parallel*) **do**
  Extract the hth grid point $\hat{\mathbf{x}}(\boldsymbol{\zeta}_h)$ of $\boldsymbol{\chi}$
  Find the solution $\hat{\mathbf{x}}(\boldsymbol{\zeta}_h)$ of the reduced order problem (7.33) and then evaluate $\tilde{\mathbf{x}}(\boldsymbol{\zeta}_h) = \mathbf{V}\hat{\mathbf{x}}(\boldsymbol{\zeta}_h)$ // 7
  Evaluate the approximated quantity $w_h(\boldsymbol{\zeta}_h) \simeq \mathcal{F}(\hat{\mathbf{x}}(\boldsymbol{\zeta}_h))$ // 8
  Store w_h in the vector array $\mathbf{w} = (w_h)$
end for
for $|\boldsymbol{\alpha}| \leq P$ (*parallel*) **do**
  Set $w_{\boldsymbol{\alpha}} = 0$
  for $h = 1, \cdots, N_{\boldsymbol{\chi}}$ **do**
    $w_{\boldsymbol{\alpha}} = w_{\boldsymbol{\alpha}} + w_h W_h \boldsymbol{\psi}_{\boldsymbol{\alpha}}(\boldsymbol{\zeta}_h)$ // 9
  end for
end for
Output: Spectral approximation of $w(\boldsymbol{\xi})$

Spectral Approximation

Let us now assume that a given quantity of interest, $w(\boldsymbol{\xi})$, is obtained as a function of $\mathbf{x}(\boldsymbol{\xi})$ (i.e. the solution of the parametric problem (7.31)), i.e.

$$w(\boldsymbol{\xi}) = \mathcal{F}(\mathbf{x}(\boldsymbol{\xi})). \tag{7.38}$$

which can be for instance the value of the electric and magnetic current for a given set of faces of the mesh, the electric and magnetic field components in a given set of target points, the joule losses, etc. All these quantities can be directly obtained from $\mathbf{x}(\boldsymbol{\xi})$ by applying a proper operator here defined as the continuous function $\mathcal{F}(\cdot)$ [159].

A spectral approximation can be then applied to

$$w(\boldsymbol{\xi}) = \sum_{|\boldsymbol{\alpha}| \leq P} w_{\boldsymbol{\alpha}} \boldsymbol{\psi}_{\boldsymbol{\alpha}}(\boldsymbol{\xi}), \tag{7.39}$$

where $w_{\boldsymbol{\alpha}}$ is the projection of $w(\boldsymbol{\xi})$ onto $\boldsymbol{\psi}_{\boldsymbol{\alpha}}(\boldsymbol{\xi})$, i.e.

$$w_{\boldsymbol{\alpha}} = \int_{\boldsymbol{\Xi}} w(\boldsymbol{\xi}) \boldsymbol{\psi}_{\boldsymbol{\alpha}}(\boldsymbol{\xi}) d\boldsymbol{\xi}. \tag{7.40}$$

In (7.40), $\boldsymbol{\alpha} = (\alpha_1, \cdots, \alpha_Q)$ is a multi–index of Q elements with $|\boldsymbol{\alpha}| = \alpha_1 + \cdots + \alpha_Q$, and

$$\boldsymbol{\psi}_{\boldsymbol{\alpha}}(\boldsymbol{\xi}) = \psi_{\alpha_1}(\xi_1)\psi_{\alpha_1}(\xi_2) \cdots \psi_{\alpha_Q}(\xi_{Q-1})\psi_{\alpha_Q}(\xi_Q), \tag{7.41}$$

in which ψ_p, with $p = 0, \cdots, P$, are the first $P + 1$ Legendre polynomials defined in $[-1, 1]$. Functions $\boldsymbol{\psi}_{\boldsymbol{\alpha}}$, with $|\boldsymbol{\alpha}| \leq P$, form a basis of all polynomials in Q variables and of degree smaller or equal to P, with dimension

$$N_{pol} = \binom{P+Q}{P}. \tag{7.42}$$

Starting from the reduced order model $\mathcal{M}_c$ (i.e. the output of Algorithm 2), the spectral approximation of $w(\boldsymbol{\xi})$ shown in (7.39) can be obtained with the non–intrusive method described in Algorithm 3.

According to Algorithm 3, at step 7, the reduced order model is solved for all the points of $\boldsymbol{\chi}$. Thus, for each solution $\hat{\mathbf{x}}(\boldsymbol{\zeta}_h)$, with $h = 1, \cdots, N_{\boldsymbol{\chi}}$, the approximate solution $\tilde{\mathbf{x}}(\boldsymbol{\zeta}_h)$ is obtained from (7.35). At step 8, according to (7.38), an approximation of $w_h(\boldsymbol{\zeta}_h)$ is obtained and then

stored in the array $\mathbf{w} = (w_h)$, with $h = 1, \cdots, N_{\boldsymbol{\chi}}$.

Finally, at step 9, the $\boldsymbol{\alpha}$th spectral projection of $w(\boldsymbol{\xi})$ is approximated by numerically integrating (7.40) with a Gaussian quadrature rule in the grid points of $\boldsymbol{\chi}$:

$$w_{\boldsymbol{\alpha}} = \sum_{h=1}^{N_{\boldsymbol{\chi}}} w_h W_h \psi_{\boldsymbol{\alpha}}(\boldsymbol{\zeta}_h), \tag{7.43}$$

where W_h is the weight related to the hth Gauss point, with $h = 1, \cdots, N_{\boldsymbol{\chi}}$.

As in Algorithm 2, the two *for–loops* of Algorithm 3 can be executed in parallel and they are also affected by the problem of the *curse of dimensionality*. However, as discussed in Section 7.2.2, sparse grids can be adopted again to alleviate this problem. Thus, the Gaussian grid $\boldsymbol{\chi}$ can be replaced with a sparse grid $\boldsymbol{\chi}^*$ [159], which can be also different from that adopted in Algorithm 2.

Monte Carlo Analysis

The above described procedure is completely *deterministic*. Let us now assume that the interest is to quantify the uncertainty of w deriving from the uncertainty of the material parameters (i.e. $\bar{\rho}_k$, with $k = 1, \cdots, Q$). MC analysis can be efficiently carried out by using the spectral approximation of w.

N_{MC} Monte Carlo samples $\boldsymbol{\xi}_h$ are generated according to the Probability Density Function (PDF) of each Q parameter. Then, $w(\boldsymbol{\xi}_h)$ is efficiently evaluated by using (7.39). Thus, even when N_{MC} is very large (e.g. $N_{MC} > 10^6$), the whole computational effort can be reasonably addressed. In this manner unprecedented levels of accuracy in the stochastic analysis when random variables are correlated can be achieved. Moreover, as discussed in [164], a further advantage of the proposed method is the completely independence on the PDF of the material quantities. Furthermore, the case of correlation between the material parameters can be considered as well.

Finally, a significant advantage of the proposed approach is that the spectral approximation of w can be adopted assuming different PDFs of the Q parameters without re–running Algorithm 2 and 3.

7.2.3 Numerical results

A Stochastic–PMOR–VIE code derived from the C–PEEC code has been developed in MATLAB® and parallel MEX–FORTRAN functions based on OpenMP libraries. In this section, an *analytical* case and an *industrial* case are considered. All the simulations have been run on a Linux machine equipped with 6-core/24-thread processors (Intel E5-2643 v4 @3:40GHz) and 516 GB of RAM.

Multi–shell sphere

The case of a dielectric multi–shell sphere consisting of 5 concentric shells is considered (Fig. 7.4). The external radius of the shields are 1 m, 0.8 m, 0.6 m, 0.4 m, and 0.2 m, respectively. The thickness of each layer is 0.1 m. The sphere is excited by an external plane wave $\mathbf{E}_{ext}(\mathbf{r}) = e^{-ik_0 z}\mathbf{u}_x$, where $k_0 = 2\pi f\sqrt{\frac{\varepsilon_0}{\mu_0}}$ and $f = 5 \cdot 10^6$ Hz frequency.

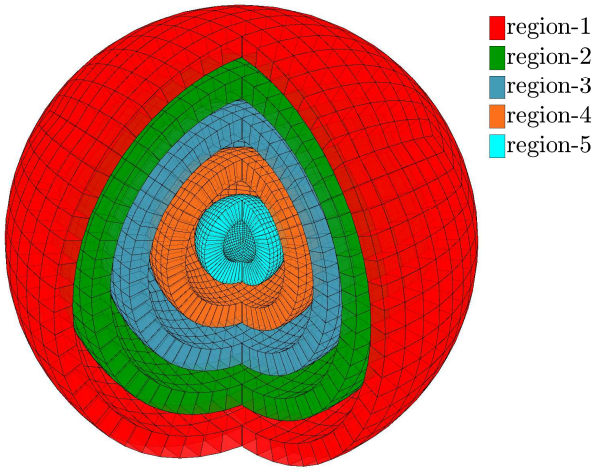

Figure 7.4: Slice view (3/4 of multi–shell sphere model).

Table 7.2: Permittivity values for any shell.

Region	$\Re(\varepsilon_{r_m})$	$\Im(\varepsilon_{r_m})$	$\Re(\Delta\varepsilon_r)$	$\Im(\Delta\varepsilon_r)$
1	25	-25	22	-22
2	15	-15	10	-10
3	20	-15	15	-14
4	17	-15	13	-13
5	20	-18	18	-16

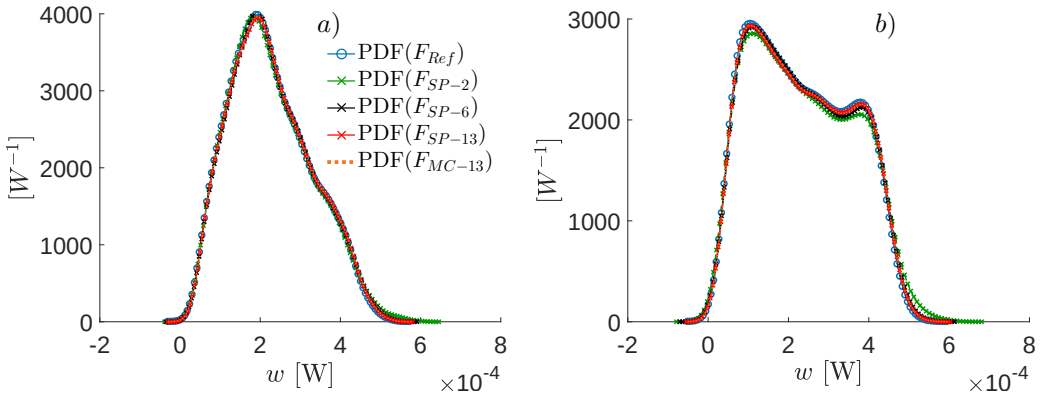

Figure 7.5: PDF of w for the uncorrelated (a) and correlated (b) cases.

The real and the imaginary part of the electric permittivity of each layer is considered as an aleatory variable. Thus, the electric permittivity of the kth layer, with $k = 1, \cdots, 5$, is given by

$$\varepsilon_{r_k} = \Re(\varepsilon_{r_{m,k}}) + \xi_{2k-1}\Re(\Delta\varepsilon_{r_k}) + i\Big(\Im(\varepsilon_{r_{m,k}}) + \xi_{2k}\Im(\Delta\varepsilon_{r_k})\Big),$$

where the mean values and the variation ranges of the real and imaginary parts are the ones given in Table 7.2. Thus, for this analytical case, the number of parameters is $Q = 10$ (i.e. the size of $\boldsymbol{\xi}$). Two different cases are considered: 1) the real and the imaginary parts of

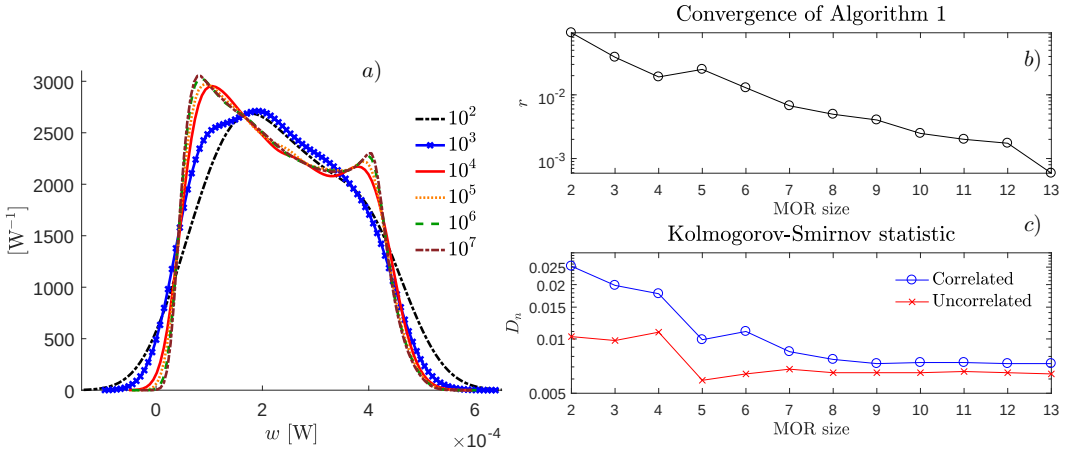

Figure 7.6: (*a*) PDF of w for the correlated case obtained from the spectral approximation for different sets of random samples with $N_{MC} = 10^2, 10^3, \cdots, 10^7$. (*b*) Residual r of Algorithm 2 for iterations $c = 2, \cdots, 13$. (*c*) Kolmogorov–Smirnov statistic (distance) between the set F_{MC_c}, with $c = 2, \cdots, 13$, and the reference set F_{Ref} for the uncorrelated and correlated cases.

the permittivities are considered as 10 statistically independent aleatory variables with uniform PDFs in the ranges defined by Table 7.2 (*uncorrelated* case), 2) the same uniform marginal PDFs are assumed for the 10 aleatory variables and a Gaussian copula with correlation matrix $\mathcal{C}$ with non–zero entries

$$\begin{aligned} \mathcal{C}(k,k) &= 1, \quad \text{with } k = 1, \cdots, 10, \\ \mathcal{C}(1,6) = \mathcal{C}(6,1) &= -0.7250, \qquad \mathcal{C}(9,10) = \mathcal{C}(10,9) = -0.8023, \end{aligned} \tag{7.44}$$

is introduced (*correlated* case) [171].

The spectral approximation procedure described in Section 7.2.2 is applied to the active power losses generated in the dielectric shells. Thus, in this analytical case, the quantity of interest introduced in (7.38) is evaluated as

$$w(\boldsymbol{\xi}) = \mathcal{F}(\mathbf{x}(\boldsymbol{\xi})) = \frac{1}{2}\Re\Big(\mathbf{x}(\boldsymbol{\xi})^T \mathbf{R}\mathbf{x}(\boldsymbol{\xi})\Big).$$

Different (approximated) sets of random samples of w consisting of $N_{MC} = 10{,}000$ values are extracted from the Stochastic–PMOR–VIE algorithm: sets F_{MC-c}, with $c = 2, \cdots, 13$, are obtained by directly applying the MC method on the reduced order model $\mathcal{M}_c$ (as described at the end of section 7.2.2); sets F_{SP-c} are obtained by running a MC method on the spectral approximation (7.39) of order $P = 5$ starting from the reduced order model $\mathcal{M}_c$ with $c = 2, \cdots, 13$. Moreover, the *Reference* set F_{Ref} is obtained by running a MC method on the *Mie solution* of the problem implemented in the free MATLAB® tool available in [132].

Fig. 7.5 shows the PDFs of w for both the *uncorrelated* and *correlated* cases. Such PDFs are extracted from the sets of random samples described above. With the aim of allowing a fair comparison, the same set of N_{MC} samples is adopted for all the MC simulations (i.e. one set for the uncorrelated case, and another set based on the correlation matrix $\mathcal{C}$ for the correlated case). Fig. 7.5 shows a very good agreement between the PDFs for both the correlated and uncorrelated case. Moreover, even if only two correlation coefficients have been introduced between the parameters, a significant difference between the uncorrelated and correlated cases can be noted.

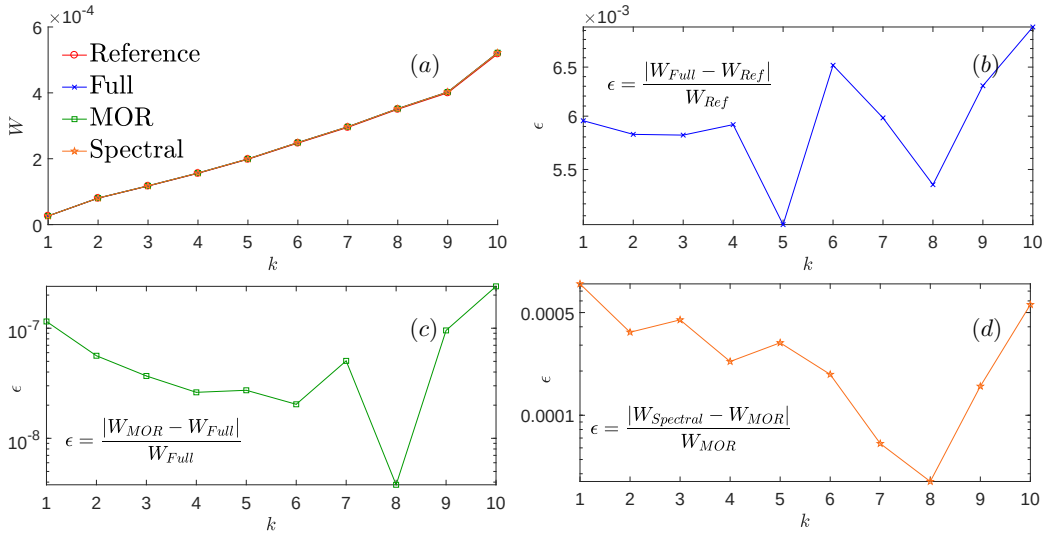

Figure 7.7: Values of w obtained from the MIE, Full–VIE, PMOR, and spectral approximation for 10 selected $\boldsymbol{\xi}$ samples (a). Errors introduced by Full–VIE (b), PMOR (c), and spectral approximation (d).

Fig. 7.6 (a) shows the PDFs of w for the correlated case obtained from the spectral approximation applied to $\mathcal{M}_{13}$ for different sets of random samples with $N_{MC} = 10^2, 10^3, \cdots, 10^7$. It can been seen that when high accuracy is required a large number of random samples N_{MC} is needed, which can be handled by the proposed procedure differently from other literature approaches.

Fig. 7.6 (b) shows the convergence of Algorithm 2, and Fig. 7.6 (c) shows the value of the Kolmogorov–Smirnov statistic D_n [172], which is a measure of the *distance* between the two empirical distribution functions obtained using the analytical solution and the PMOR method. The null hypothesis that the corresponding random samples come from different distributions is always rejected (at 5% significance level), except for $c = 2$.

With the aim of investigating the size of the error introduced by the steps of the algorithm, 10 samples $\boldsymbol{\xi}_k$, with $k = 1, \cdots, 10$, for which the value of w goes from the minimum to the maximum (with respect to F_{Ref}) are selected. The value of w_k (where $k = 1, \cdots, 10$, denotes the extracted sample $\boldsymbol{\xi}_k$) obtained from F_{Ref} (Reference), F_{MC-13} (MOR), and F_{SP-13} (Spectral) are shown in Fig. 7.7 (a) together with the values obtained from the direct solution of (7.31) (Full–VIE). In the other plots of Fig. 7.7, the errors introduced by the VIE discretization, PMOR, and the spectral approximations are shown. It can be observed that the largest error is introduced by the VIE discretization. Instead, the PMOR and the spectral approximation generate errors of orders of magnitude smaller than the Full–VIE one.

In this case study, due to the large number of random variables, the use of a sparse grid $\boldsymbol{\chi}^*$ is mandatory. Indeed, because of the *curse of dimensionality*, the use of a dense Gaussian grid $\boldsymbol{\chi}$ with $P = 5$ gauss points would lead to $N_{\boldsymbol{\chi}} = P^Q = 5^{10} = 9{,}765{,}625$ grid points, resulting in a prohibitive computational time. Instead, a sparse grid $\boldsymbol{\chi}^*$ with *only* $N_{\boldsymbol{\chi}^*} = 8{,}761$ grid points was used.

In Table 7.3, the computation time required by the different steps of the method are reported for the case $c = 13$ and $N_{MC} = 10^6$.

The VIE model of the multi–shell sphere consists of 12,960 DoFs. Thus, the storage of the (full) parametric VIE system requires ~ 2.7 GB, which is also the Peak Memory Usage (PMU)

Table 7.3: Computational time for the case of the multi–shell sphere.

	Algorithm 2	Algorithm 3	MC–Spectral, $N_{MC} = 10^6$	Total time
Time [s]	$\sim 14 \cdot 13 + 62 = 244$	$\sim 23 + 35 = 58$	~ 28	~ 330

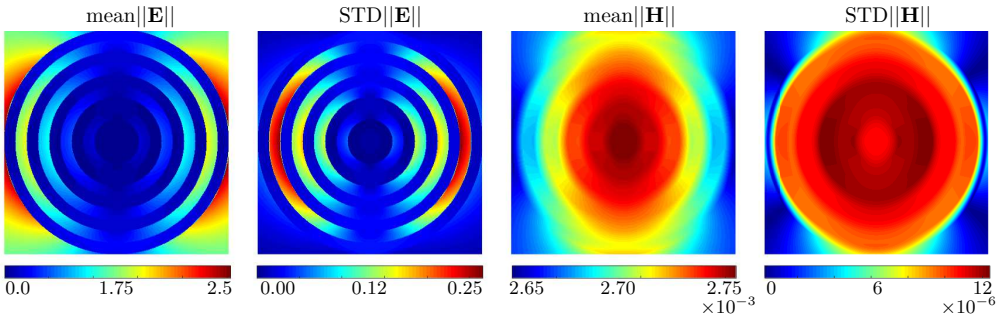

Figure 7.8: Mean and standard deviation of the electric and magnetic field magnitude in [V/m] and [A/m], respectively.

reached during the whole simulation.

Table 7.3 shows that the major computational effort is due to the solution of (7.31), which is solved for 13 selected choices of $\boldsymbol{\xi}$ during Algorithm 2 by means of a LU decomposition which requires $\sim$ 14 s. The remaining part of the computation time is mostly due to the (relatively) high dimensionality of the problem, which requires a (relatively) large amount of grid points. The time required to generate F_{MC-13} and F_{SP-13} (consisting of $N_{MC} = 10{,}000$ samples) are instead $\sim$ 19 s and $\sim$ 0.27 s, respectively. It is noticeable that the spectral approximation drastically reduces the time required by the stochastic analysis with respect to the direct application of MC to $\mathcal{M}_{13}$. Moreover, this gain further increases when N_{MC} grows (i.e. when an higher accuracy is required), and the same spectral approximation can be used with different choices of the PDF and correlation of the parameters. For the sake of comparison, the time required by the direct application of a (non–parallelized) MC method on (7.31) would require $\sim 14 \cdot 10{,}000$=140,000 s, and the time required for the generation of F_{Ref} (MC with 10,000 on the Mie solution) is $\sim$ 272 s.

Finally, the proposed algorithm can be adopted also for the evaluation of stochastic information related to the electromagnetic fields in the whole 3–D space. For instance, Fig. 7.8 shows the mean and the standard deviation of the electric and magnetic field magnitude in the $z = 0$ plane obtained as post–processing from the Stochastic–PMOR–VIE algorithm.

Induction heating pot

The case of the induction cookware presented in [135] is considered. This case has already been considered in Section 5.4 in the context of low–rank approximation. In this kind of application the power electronic supply consists of ac/dc rectifier, a bus filter, and a resonant inverter. In resonant inverters zero–voltage or zero–current switching are attained when the R–L–C circuit, representing the induction system and the matching capacitance, is resonating. In this condition power switching losses are minimized enabling high frequency operations, with limited size and cost of the device. In this framework, the analysis of the equivalent impedance of the coupled inductor-vessel system becomes mandatory in order to obtain an optimal design of its supply system as discussed in [135]. Therefore, the proposed Stochastic–PMOR–VIE method can been

Table 7.4: Material parameters of the induction heating pot.

	σ_c [MS/m]	μ_r
l_1	1.04 ± 0.33	1
l_2	29.1 ± 9.36	1
l_3	0	$400 \pm 100 - i(175 \pm 43.75)$
l_4	1.04 ± 0.33	1
l_5	0	1
l_6	0	2300 ± 575
l_7	29.1 ± 9.36	1

adopted to investigate the effects of the uncertainties of the material parameters on the value of the equivalent impedance.

In order to exploit the axial–symmetry of the electromagnetic problem, the Coloumbian formulation presented in Appendix B is here used.

The geometry of the problem is completely described by Fig. 5.8 where layers l_1, l_2, l_3, and l_4 constitute the bottom part of the pot, layer l_5 is the external current–driven coil (the problem excitation), l_6 is the magnetic flux concentrator, and l_7 is the shield. In Table 7.4, the material parameters of the various parts of the device are given with their uncertainties. The maximum values of the conductivities are that ones given in [135], whereas the minimum values are chosen assuming that the temperature (which can reach different values in the various parts of the device) attains the maximum value of 230°C. The average value of the permeabilities is again the ones given in [135] and an uncertainty of 25% is assumed (consistent with most of the data sheets provided by ferromagnetic producers).

Thus, for this case, the number of parameters is $Q = 7$ and the uncertain material quantities of Table 7.4 are considered as 7 aleatory variables. The same uniform marginal PDFs are assumed for any aleatory variable and a Gaussian copula with correlation matrix $\mathcal{C}$ is introduced [171]. $\mathcal{C}$ has non–zero off–diagonal entries equal to 0.5 for all the parameters which model the materials l_1, l_2, l_3, and l_4 indicated in Fig. 5.8.

The frequency of the problem is set to $f = 20$ kHz and the extracted quantity of interest is the equivalent impedance $w(\boldsymbol{\xi}) = Z_{eq}(\boldsymbol{\xi})$ of the device, with respect a uniform (external) current flowing in the external coil. Different sets of random samples of $w(\boldsymbol{\xi})$ are extracted from the Stochastic–PMOR–VIE algorithm. Contrary to the case of the sphere, for this case the dimension of the reduced order model obtained from Algorithm 2 is kept constant and equal to $c = 7$ with a final residual of $r = 1.82 \cdot 10^{-4}$. Then, F_{MC} is obtained by directly applying the MC method on the reduced order model $\mathcal{M}_7$. Instead, sets F_{SP-s} are obtained by running a MC method on the spectral approximation (7.39) of order $s = 2, \cdots, 6$. Moreover, with the aim of comparing the results obtained from the Stochastic–PMOR–VIE algorithm with a different method, the set of random samples F_{com} is obtained by applying MC on an axisymmetric FEM simulation performed with the commercial software COMSOL®. All the sets described above have been generated from the same set of $N_{MC} = 10{,}000$ samples $\boldsymbol{\xi}$.

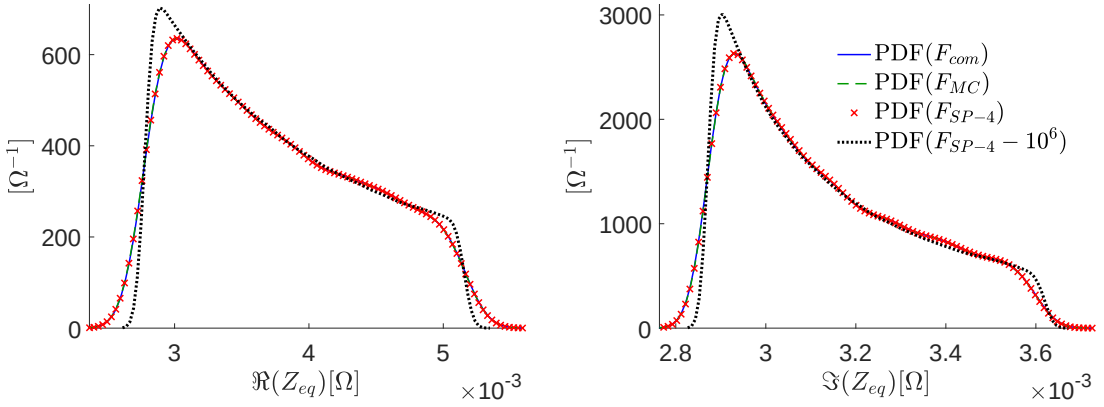

Figure 7.9: Real and imaginary parts of the PDF of $w = Z_{eq}$ obtained from F_{com}, F_{MC}, F_{SP-4}, and $F_{SP-4} - 10^6$.

Table 7.5: Computational time for the case of the induction cookware.

	Algorithm 2	Algorithm 3	MC–Spectral, $N_M C = 10^6$	Total time
Time [s]	$\sim 7 \cdot 8.6 + 12.7 = 72.9$	$\sim 88.4 + 2.2 = 90.6$	~ 18	~ 180

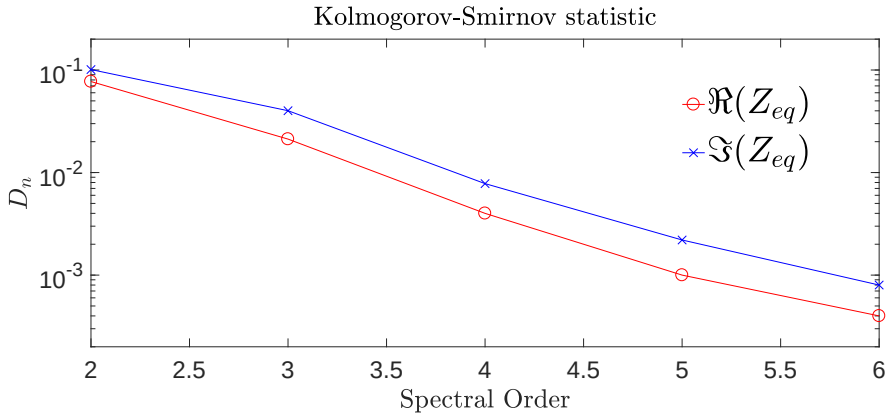

Figure 7.10: Kolmogorov–Smirnov statistic between F_{SP-s}, with $s = 2, \cdots, 6$, and F_{com}.

Fig. 7.9 shows the PDFs of the real and imaginary parts of $w = Z_{eq}$ obtained from F_{MC}, F_{SP-4}, and F_{com}. Moreover, the PDFs obtained by running MC on the spectral approximation of order 4 with a different set of (correlated) random samples consisting of $N_{MC} = 10^6$ is also shown and indicated as $F_{SP-4} - 10^6$. As can been seen, the three PDFs obtained from F_{MC}, F_{SP-4}, and F_{com} show excellent agreements. Instead, the more accurate PDFs obtained from $F_{SP-4} - 10^6$ is quite detached from the others. This shows that when high accuracy is required the MC analysis should be performed with a large amount of samples. As a further remark, this level of accuracy (i.e. large amount of MC samples) is actually achievable with the proposed algorithm, whereas the application of other traditional approaches would easily result in a prohibitive computation time.

Fig. 7.10 instead shows the Kolmogorov–Smirnov statistic, D_n, between the sets F_{SP-s}, with $s = 2, \cdots, 6$, and F_{com}. Numerical results show an exponential convergence of the adopted spectral approximation.

In Table 7.5 the computation time required by the different steps of the algorithm is reported for the case $s = 5$. For the sake of comparison, the time required for the generation of F_{com} and F_{MC} (consisting of 10,000 samples) are $\sim$ 32,160 s and $\sim$ 359.0 s, respectively. Instead, the time required for the generation of F_{SP-4} ($N_{MC} = 10{,}000$) is only $\sim$ 0.17 s. As for the case of the multi–shell sphere, to alleviate the problem of the curse of dimensionality a sparse grid of $N_{\boldsymbol{\chi}^*} = 2{,}437$ points was adopted.

The axisymmetric VIE model of the induction cookware consists of 10,328 DoFs. Thus, the storage of the full parametric VIE system requires $\sim$ 1.7 GB, which is also the PMU attained during the whole simulation.

Chapter 8

Conclusions and outlooks

The goal of the PhD research has been to extend and improve the applicability and the accuracy of the Unstructured PEEC method. The interest on this topic was spurred by the increasing need of fast and efficient numerical methods which may help engineers during the design and other steps of the production of new generation electric components.

This PhD work can be seen as the continuation of the PhD thesis of J. Siau [6], a former PhD student of G2ELab. The work of J. Siau was in turn the continuation of the PhD works of two former PhD students of G2ELab, i.e. the thesis of V. Ardon [173] and the thesis of T.-T. Nguyen [174].

Main outcomes of this PhD are summarized as follows:

- *Extension of PEEC to magnetic media.* The PEEC method, in its unstructured form, has been extended to magnetic media. Two formulations have been developed. The first, based on the Amperian interpretation of the magnetization phenomena, has been derived from the already existing literature concerning the standard (structured) version of PEEC [25, 33]. The result of such work has been presented by the author in [26], where the Cell Method approach has been adopted for the discretization. Then, with the aim of overcoming the shortcomings of the Amperian PEEC method, a new formulation based on the Coulombian interpretation of the magnetic phenomena has been adopted and presented by the author in [40, 20]. In [27], a PEEC formulation based on the total divergence free currents has been presented.

- *PEEC and Volume Integral Method.* With the aim of developing a rigorous and sound formalization of PEEC, a lot of effort has been spent to collocate PEEC in the context of VIE. Some considerations concerning such topic are given in [20]. Indeed, the interpretation of PEEC as a particular form of VIE has made it possible to use the well–established numerical techniques developed in literature (e.g. loop–star basis function) for improving the accuracy of Integral Equation methods. Moreover, the inclusion of PEEC in VIE by means of the Coulombian interpretation has allowed maintaining a strong circuit interpretation also when magnetic media are involved.

- *Low–rank approximation.* Investigations concerning the coupling of PEEC with two different low–rank approximation techniques (one based on $\mathcal{H}/\mathcal{H}^2$ matrices and the other based on HSS–matrices) have been carried out. These studies have allowed for understanding and identifying the main issues which arise when low–rank techniques are applied to PEEC. In this regard, some solutions have been proposed and applied for the study of problems of industrial interest. Some of these results are reported in [19, 77].

- *Time domain PEEC.* The Marching On–in–Time scheme has been successfully applied to the PEEC method for the study of fast transient phenomena. The results of this work have been submitted to IEEE Transaction on Magnetics, Compumag, 2019, and are now under peer–revision.

- *Uncertainty quantification.* In the context of a collaboration with Politecnico di Milano, the PEEC method has been combined with Polynomial Chaos expansion (PCE) for uncertainty quantification analysis. Results have been presented in [163]. Then, with the aim of overcoming the shortcomings of the PCE–PEEC method, a novel approach based on Parametric Model Order Reduction and spectral expansion has been developed. The results of this work have been submitted and are now under peer–revision.

- *Industrial problems.* With the aim of testing the applicability and the performances of PEEC when applied to challenging problems, industrial cases have been considered in several cases reported in this thesis and in some published and submitted papers. In this regard, the results of the collaboration with the Politecnico di Torino, concerning the application of PEEC for the study of a Wireless Power Transfer device are reported in [136] and others are under peer–revision.

- *Reference for future investigation.* Finally, this work also attempts to be an exhaustive reference for future researches and investigations.

From a research perspective, future investigations will concern the coupling of PEEC and compression techniques. Indeed, although some results and solutions concerning this topic have been obtained during this thesis, the issue is still very problem dependent and the best low–rank compression technique to be coupled with PEEC has not yet been identified.

Moreover, since very thin conductive and magnetic objects are often adopted in the new electric components, the development of advanced and accurate Surface Impedance Boundary Conditions would be very useful and would allow strongly reducing the number of unknowns when quantities such as Joule losses must be evaluated. The coupling of PEEC with other numerical techniques for the study of specific problems could be the matter of future research and investigations.

Another interesting subject for future researches would be the study of non–linear materials. In this thesis this kind of media has not been considered. However, the study of inhomogeneous media is essential for the extension of the PEEC method to the case of non linear materials and this is the reason which has motivated the research in this subject.

Finally, during this thesis the topic of *preconditioning* techniques has been differently considered with respect to the PhD thesis of J. Siau [6] where the performances of different preconditioners have been compared. Indeed, in this thesis, such topic has been entirely considered under the context of compression techniques, which are almost always mandatory for the study of industrial problems. The main focus here has been on how to make the PEEC system suitable for low–rank compression techniques. Then, highly optimized and efficient low–rank compression libraries have been adopted for the solution, i.e. HLIBPro [115] and STRUMPACK libraries [116]. The first, which relies on $\mathcal{H}^2$ matrices uses an incomplete $\mathcal{H}$–LU preconditioner, which showed to be efficient for very different problems. The second, instead, relies on HSS–matrices and the solution of the system of equations is finally obtained by a direct solution of the HSS–matrix, which is efficiently obtained by means of a fast Cholesky or ULV decomposition in HSS–algebra.

For these reasons, the *preconditioning* topic has not been central in the research. Thus, if different compression techniques are adopted (or they are not used at all), the issue concerning the choice of the best preconditioning technique is still an open matter which requires future researches. As a very last consideration, recently, in the electromagnetic community framework, the Quantized Tensor Train (QTT) [175] method has been proposed for the solution of Boundary Element Method problems [176]. Such a method is very attractive since it allows for reducing the computational complexity to $\mathcal{O}(log(N))$ only. Thus, the application of QTT to VIE equation methods, such as PEEC, could be the subject of future researches.

Appendix A

Charge inside conductive, dielectric, and magnetic media

In this appendix, some physical considerations concerning the presence of volume charge density inside dielectric, magnetic, and conductive media are given.

The presence or absence of volume charges inside media is directly related to the divergence of the current density vectors. Thus, it is important to know in which case the volume charge density must be zero and when it is not.

A.1 Dielectric media

Lossless dielectric media are considered here. With the term *lossless* we mean non–conductive media: no conduction current density is present, i.e. no free charge is present. This assumption leads to $\nabla \cdot \mathbf{D} = 0$, since $\varrho_c = 0$ and $\varsigma_c = 0$.

Combining the two constitutive equations:

$$\mathbf{D} = \varepsilon_0 \mathbf{E} + \mathbf{P}, \qquad \mathbf{D} = \varepsilon_0 \varepsilon_r \mathbf{E},$$

$\mathbf{D}$ can be written as

$$\mathbf{D} = \frac{\varepsilon_r}{\varepsilon_r - 1} \mathbf{P}. \tag{A.1}$$

Thus, applying the divergence operator to the both sides of the equations we get

$$\nabla \cdot \left(\frac{\varepsilon_r}{\varepsilon_r - 1} \mathbf{P} \right) = 0, \tag{A.2}$$

which, applying the Green's identity, becomes

$$\frac{\varepsilon_r}{\varepsilon_r - 1} \nabla \cdot \mathbf{P} + \mathbf{P} \cdot \nabla \frac{\varepsilon_r}{\varepsilon_r - 1} = 0. \tag{A.3}$$

Thus, since $\nabla \cdot \mathbf{P} = \varrho_d$, one can notice that the presence of the bound volume electric charge density inside dielectric media depends on the material properties of the media: i.e. $\varrho_d = 0$ in homogeneous media and $\varrho_d \neq 0$ in inhomogeneous media.

A.2 Magnetic media

A.2.1 Coulombian interpretation

When the Coulombian interpretation is adopted the magnetization phenomena are modeled by means of magnetic charges and currents which depends on the magnetization vector $\mathbf{M}$. When this interpretation is chosen, magnetic and dielectric media are treated in a completely equivalent way.

Thus, since $\nabla \cdot \mathbf{B} = 0$ (until now magnetic monopoles have not been found in nature which means that not *free* magnetic charge is present), the discussion above concerning dielectric media can be repeated for the magnetic media by simply substituting the electric quantities with the corresponding magnetic ones.

Thus, combining the two constitutive equations:

$$\mathbf{B} = \mu_0 \mathbf{H} + \mu_0 \mathbf{M}, \qquad \mathbf{B} = \mu_0 \mu_r \mathbf{H},$$

$\mathbf{B}$ can be written as

$$\mathbf{B} = \frac{\mu_r}{\mu_r - 1} \mu_0 \mathbf{M}. \tag{A.4}$$

Thus, applying the divergence operator to the the both sides of the equations we get

$$\nabla \cdot \left(\frac{\mu_r}{\mu_r - 1} \mu_0 \mathbf{M} \right) = 0, \tag{A.5}$$

which, applying the Green's identity, becomes

$$\frac{\mu_r}{\mu_r - 1} \nabla \cdot (\mu_0 \mathbf{M}) + \mu_0 \mathbf{M} \cdot \nabla \frac{\mu_r}{\mu_r - 1} = 0. \tag{A.6}$$

Thus, since $\nabla \cdot (\mu_0 \mathbf{M}) = \varrho_m$, one can notice that the presence of the *bound* volume magnetic charge density inside magnetic media depends on the material properties of the media: i.e. $\varrho_m = 0$ in homogeneous media and $\varrho_m \neq 0$ in inhomogeneous media.

A.2.2 Amperian interpretation

When the amperian interpretation of the magnetization phenomena is embraced, magnetic currents and charges are not defined. Instead, volume and surface amperian currents are introduced as the curl of the magnetization, i.e. $\mathbf{J}_a = \nabla \times \mathbf{M}$ and $\mathbf{K}_a = \left(\mathbf{M}^- - \mathbf{M}^+ \right) \times \mathbf{n}$.

This equivalent *electric* currents are, by definition, divergence free, thus no electric charge density is present inside non–conductive magnetic media.

Consideration concerning on the distribution of $\mathbf{J}_a$ and $\mathbf{K}_a$ in homogeneous and inhomogeneous media are given in Section 3.3.

A.3 Conductive media

In conductive media *free* electric charges are present. However, in most of the engineering problems the presence of free volume charge density, ϱ_c, inside conductive media is not considered and only free surface charge density, ς_c is considered.

From the physical point of view, this matter is a sensitive issue known as the *Decay Paradox in Metals* [71].

By combining Maxwell's equations with the Ohm's law, the following well–known time domain equation is obtained

$$\varrho_c(\mathbf{r}, t) = \varrho_c(\mathbf{r}, 0) e^{-\frac{1}{\tau_e} t}. \tag{A.7}$$

where $\tau_e = \frac{\varepsilon_0}{\sigma_c}$ is the electric *relaxation time constant*. For good conductors τ_e is very short, which means that the charge density rapidly decays in conductive media and it is forced to move on the surface of the media. Which is also the reason why in engineering problems involving conductive media the volume electric charges are not considered.

However, as deeply discussed in [71], equation (A.7) leads to a paradox which presupposes that the free electric charges can move faster than the speed of light. Without going deeper in these considerations, such paradox is due to the use of a too simplistic Ohm's law (2.30) that does not properly model the behaviour of real conductive media. Indeed, whenever free electric charges actually move in a conductive media the traditional Ohm's law (which assumes an homogeneous material property) is not valid anymore and a more sophisticated law which includes diffusion and other effects should be instead [71].

Having said that, for engineering purposes, when good conductive media are considered (e.g. copper) the presence of volume free electric charges can be actually neglected. Indeed, decay phenomena and inductive effects (skin effect and proximity effect) lead the electric currents to be mostly concentrated in a thin layer on the border of the conductive domain. Thus, although from the physical point of view volume electric charges are not actually zero (mostly for very high frequency problems), they can be forced to be zero and only the effects of surface charges can be considered.

However, it is worth noting that when conductive media with long τ_e are considered a more sophisticated Ohm's law should be considered instead.

Appendix B

Integral formulation for axisymmetric problems

Axisymmetric problems involving conductive media have been extensively studied in the past [177]. However, the more general case involving conductive and magnetic media does not appear to have been studied in the literature. In this appendix, as done for the PEEC method, two different Integral axisymmetric methods involving conductive and magnetic media are presented: one based on the Amperian PEEC formulation presented in Section 2.2 and the other based on the Coulombian PEEC formulation presented in Section 2.3. As for the PEEC method, The Amperian and the Coulombian methods only differs on the handling of magnetic media.

The case of dielectric media is not considered. Indeed, when the axisymmetric condition holds (the one adopted here), the polarization currents are forced to be divergence free. Thus, the main effect of the dielectric media (i.e. the enhancement of capacitive effects due to the bound electric charges), is not present in the electromagnetic axisymmetric problems. Therefore, the interest in the inclusion of dielectric media fails for problem of practical interest. However, both the methods presented here can be easily extended to the case of dielectric media by simply substituting the conduction current with the electric current (conduction and polarization current). However, only the (weak) inductive effects produced by the polarization currents would be considered while the capacitive effects are not present.

B.1 Amperian axisymmetric method

The 3–D conductive and magnetic domains are defined as Ω_c and Ω_m, respectively. These domains can intersect and their union is defined as the active domain $\Omega_a = \Omega_c \cup \Omega_m$. These domains are obtained from the axial revolution of 2–D domains $\hat{\Omega}_c$, $\hat{\Omega}_m$, and $\hat{\Omega}_a$, i.e. $\Omega_c = \hat{\Omega}_c \times [0, 2\pi]$, $\Omega_m = \hat{\Omega}_m \times [0, 2\pi]$, and $\Omega_a = \hat{\Omega}_a \times [0, 2\pi]$. The boundaries of Ω_c and Ω_m are defined as $\Gamma_c = \partial\Omega_c$ and $\Gamma_m = \partial\Omega_m$, respectively, and analogously $\Gamma_c = \hat{\Gamma}_c \times [0, 2\pi]$, $\Gamma_m = \hat{\Gamma}_m \times [0, 2\pi]$, where $\hat{\Gamma}_c = \partial\hat{\Omega}_c$ and $\hat{\Gamma}_m = \partial\hat{\Omega}_m$.

B.1.1 Formulation

When the *amperian* interpretation of the magnetization phenomena is adopted [39], the integral form of the electromagnetic problem reduces to the solution of the following

$$\mathbf{E}(\mathbf{r}) = -i\omega\mathbf{A}(\mathbf{r}) - \nabla\varphi_e(\mathbf{r}) + \mathbf{E}_{ext}(\mathbf{r}), \tag{B.1}$$

$$\mathbf{B}(\mathbf{r}) = \nabla \times \mathbf{A}(\mathbf{r}) + \mathbf{B}_{ext}(\mathbf{r}), \tag{B.2}$$

where $\mathbf{E}$ and $\mathbf{B}$ are the electric and the magnetic flux density fields, respectively. $\mathbf{A}$ is the vector potential and φ_e is the scalar potential. $\mathbf{E}_{ext}$ and $\mathbf{B}_{ext}$ are the external fields (i.e. the excitation of the electromagnetic problem).

The integral form of $\mathbf{A}$, already given in (2.51), is

$$\mathbf{A}(\mathbf{r}) = \mu_0 \left[\int_{\Omega_c} \mathbf{J}_c(\mathbf{r}')g(\mathbf{r},\mathbf{r}')d\mathbf{r}' + \int_{\Omega_m} \mathbf{J}_a(\mathbf{r}')g(\mathbf{r},\mathbf{r}')d\mathbf{r}' + \int_{\Gamma_m} \mathbf{K}_a(\mathbf{r}')g(\mathbf{r},\mathbf{r}')d\mathbf{r}' \right], \tag{B.3}$$

in which $\mathbf{J}_c$ is the conduction current density, while $\mathbf{J}_a = \nabla \times \mathbf{M}$ and $\mathbf{K}_a = \mathbf{M} \times \mathbf{n}$ are the volume and surface *amperian* currents.

When the axisymmetric condition holds, the electromagnetic quantities can be written in cylindrical coordinates $(\vec{r}, \vec{\phi}, \vec{z})$ and the vector quantities only exhibit some (cylindrical) component:

$$\begin{gathered} \mathbf{J}_c = J_{c_\phi}\vec{\phi}, \quad \mathbf{J}_a = J_{a_\phi}\vec{\phi}, \quad \mathbf{K}_a = K_{a_\phi}\vec{\phi}, \quad \mathbf{E} = E_\phi\vec{\phi}, \quad \mathbf{A} = A_\phi\vec{\phi}, \\ \mathbf{B} = B_r\vec{r} + B_z\vec{z}, \qquad \mathbf{M} = M_r\vec{r} + M_z\vec{z}. \end{gathered} \tag{B.4}$$

When the Lorenz gauge condition is imposed, the scalar electric potential φ_e is related to the volume and surface electric charge densities (ϱ_e and ς_e) by means of the well known:

$$\varphi_e(\mathbf{r}) = \varepsilon_0^{-1} \left[\int_{\Gamma_e} \varsigma_e(\mathbf{r}')g(\mathbf{r},\mathbf{r}')d\mathbf{r}' + \int_{\Omega_e} \varrho_e(\mathbf{r}')g(\mathbf{r},\mathbf{r}')d\mathbf{r}' \right]. \tag{B.5}$$

Moreover, ϱ_e and ς_e are related to $\mathbf{J}_c$ by means of the continuity relations

$$\nabla' \cdot \mathbf{J}_c(\mathbf{r}') = -i\omega\varrho_e(\mathbf{r}'), \qquad \mathbf{J}_c(\mathbf{r}') \cdot \mathbf{n} = -i\omega\varsigma_e(\mathbf{r}'). \tag{B.6}$$

However, when the axisymmetric condition holds, $\mathbf{J}_c$ is divergence free. Thus, no moving electric charge is present and therefore $\varphi_e(\mathbf{r}) = 0$.

The integral expression of $\mathbf{A}$ can be formulated in cylindrical coordinates as shown in [178]:

$$A_\phi(\mathbf{r}) = \mu_0 \left[\int_{\hat{\Omega}_a} \hat{g}(\mathbf{r},\mathbf{r}')(J_{c_\phi}(\mathbf{r}') + J_{a_\phi}(\mathbf{r}'))d\hat{\Omega} + \int_{\hat{\Gamma}_m} \hat{g}(\mathbf{r},\mathbf{r}')K_{a_\phi}(\mathbf{r}')d\hat{\Gamma} \right], \tag{B.7}$$

where $\hat{g}$ is the axisymmetric Green's function [179], $\mathbf{r} = (r, z, \phi)$ is the filed point, and $\mathbf{r}' = (r', \phi', z')$ is the source point. The axisymmetric Green's function (which is the axisymmetric solution of the Poisson equation for a ring carrying a uniform current [180]) is defined as

$$\hat{g}(\mathbf{r},\mathbf{r}') = \frac{4r'}{K} \frac{(2-k^2)\mathcal{K}(k^2) - 2\mathcal{E}(k^2)}{4\pi k^2}, \tag{B.8}$$

where

$$\begin{aligned} K &= \sqrt{(r'+r)^2 + (z'-z)^2}, \\ k^2 &= \frac{4r'r}{K^2}, \end{aligned} \tag{B.9}$$

and $\mathcal{K}$ and $\mathcal{E}$ are the *elliptic integrals* of the first and second kind, respectively (defined with the same convention of [178]).

Equations (B.1) and (B.2) are complemented by the following constitutive equations:

$$\mathbf{E}(\mathbf{r}) = \rho_c(\mathbf{r})\mathbf{J}_c(\mathbf{r}), \ \ \mathbf{r} \in \Omega_c, \tag{B.10}$$

$$\mathbf{B}(\mathbf{r}) = \alpha_m(\mathbf{r})\mathbf{M}(\mathbf{r}), \ \ \mathbf{r} \in \Omega_m. \tag{B.11}$$

where ρ_c is the electric resistivity and $\alpha_m = \frac{\mu_0 \mu_r}{\mu_r - 1}$.

Finally, combining (B.1) with (B.10), and (B.2) with (B.11), the following final continuum equations for an electromagnetic axisymmetric problem are obtained

$$\rho_c(\mathbf{r})\mathbf{J}_c(\mathbf{r}) = -i\omega\mathbf{A}(\mathbf{r}) + \mathbf{E}_{ext}(\mathbf{r}), \ \mathbf{r} \in \Omega_c, \tag{B.12}$$

$$\alpha_m(\mathbf{r})\mathbf{M}(\mathbf{r}) = \nabla \times \mathbf{A}(\mathbf{r}) + \mathbf{B}_{ext}(\mathbf{r}), \ \mathbf{r} \in \Omega_m. \tag{B.13}$$

B.1.2 Cell method discretization

The 2–D domains $\hat{\Omega}_c$ and $\hat{\Omega}_m$ are discretized into two quadrilateral grids: $\mathcal{G}_{\hat{\Omega}_c}$ for $\hat{\Omega}_c$ and $\mathcal{G}_{\hat{\Omega}_m}$ for $\hat{\Omega}_m$. As for the A–PEEC discretization, these two grids consist of (primal) geometric entities: $\hat{\Omega}_c$ consists of f_c faces, e_c edges, and n_c nodes, while $\hat{\Omega}_m$ consists of f_m faces, e_m edges, and n_m nodes. Then, dual grids $\tilde{\mathcal{G}}_{\hat{\Omega}_c}$ and $\tilde{\mathcal{G}}_{\hat{\Omega}_m}$ are obtained by taking the barycentric subdivision of $\mathcal{G}_{\hat{\Omega}_c}$ and $\mathcal{G}_{\hat{\Omega}_m}$, respectively. Moreover, dual geometric entities are defined for the two dual grids: $\tilde{f}_c$, $\tilde{e}_c$, and $\tilde{n}_c$ for $\tilde{\mathcal{G}}_{\hat{\Omega}_c}$, and $\tilde{f}_m$, $\tilde{e}_m$, and $\tilde{n}_m$ for $\tilde{\mathcal{G}}_{\hat{\Omega}_m}$. A one–to–one relation between the entities of the primal and dual grids exists: $f_c \leftrightarrow \tilde{n}_c$, $e_c \leftrightarrow \tilde{e}_c$, $n_c \leftrightarrow \tilde{f}_c$; and the same for the geometric magnetic entities. The primal and dual conductive geometric entities are represented in Fig. B.1.*a*) in a *rectified* axial geometry.

The following incidence matrices can be now defined for the primal grid $\mathcal{G}_{\hat{\Omega}_c}$: $\mathbf{G}_{\hat{\Omega}_c}$ (*primal* edges–*primal* nodes) and $\mathbf{C}_{\hat{\Omega}_c}$ (*primal* faces–*primal* edges). The same can be done for the dual grid $\tilde{\mathcal{G}}_{\hat{\Omega}_c}$: $\tilde{\mathbf{G}}_{\hat{\Omega}_c}$ (*dual* edges–*dual* nodes) and $\tilde{\mathbf{C}}_{\hat{\Omega}_c}$ (*dual* faces–*dual* edges). These primal and dual incidence matrices satisfy the following properties: $\mathbf{C}_{\hat{\Omega}_c}\mathbf{G}_{\hat{\Omega}_c} = \mathbf{0}$, $\tilde{\mathbf{C}}_{\hat{\Omega}_c}\tilde{\mathbf{G}}_{\hat{\Omega}_c} = \mathbf{0}$, $\mathbf{C}_{\hat{\Omega}_c} = -\tilde{\mathbf{G}}^T_{\hat{\Omega}_c}$, and $\mathbf{G}_{\hat{\Omega}_c} = \tilde{\mathbf{C}}^T_{\hat{\Omega}_c}$.

Completely equivalent considerations can be done for the primal and dual magnetic grids; thus, the magnetic incidence matrices are also defined: $\mathbf{C}_{\hat{\Omega}_m}$, $\mathbf{G}_{\hat{\Omega}_m}$, $\tilde{\mathbf{C}}_{\hat{\Omega}_m}$, and $\tilde{\mathbf{G}}_{\hat{\Omega}_m}$.

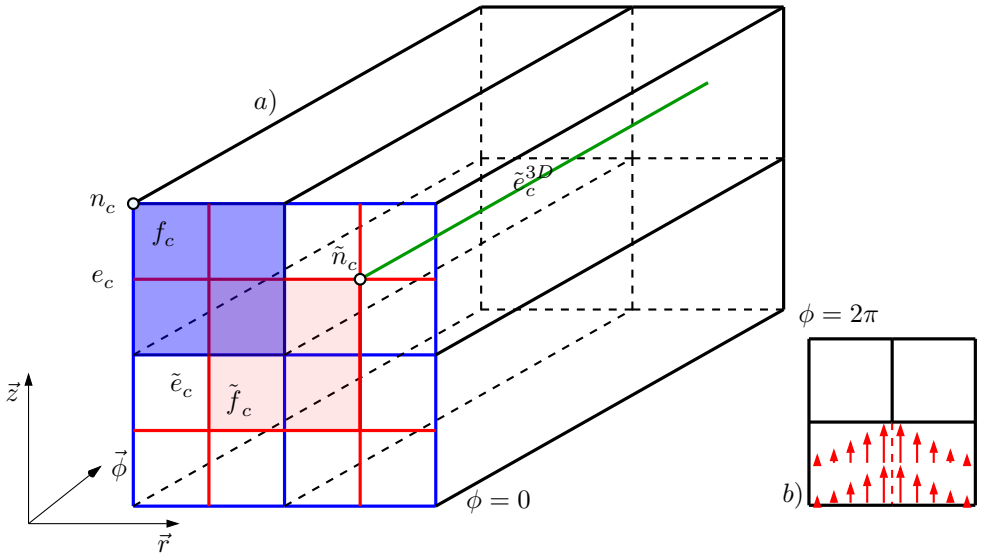

Figure B.1: *a*) Primal and dual geometric entities for the conductive grid; rectified axisymmetric geometry. *b*) Axisymmetric $\mathbf{w}^e$ edge shape function.

The conduction current is then expanded as:

$$\mathbf{J}_c(\mathbf{r}) = \sum_{k=1}^{f_c} \mathbf{w}_k^{\phi}(\mathbf{r}) j_{c_k}, \tag{B.14}$$

where j_{c_k} is the flux related to the kth face of the mesh f_{c_k}. Then, the array of DoFs $\mathbf{j}_c$ which stores j_{c_k}, for $k = 1, \cdots, f_c$ is introduced. $\mathbf{w}_k^{\phi}$ is the vector shape function related to f_{c_k} and defined as

$$\mathbf{w}_k^{\phi}(\mathbf{r}) = \frac{1}{A_k}\vec{\phi}, \ \mathbf{r} \in f_k, \tag{B.15}$$

where A_k is the area of f_{c_k}.

The magnetization instead is discretized as

$$\mathbf{M}(\mathbf{r}) = \sum_{k=1}^{e_m} \mathbf{w}_k^{e}(\mathbf{r}) m_k, \tag{B.16}$$

where $m_k = \int_{e_m} \mathbf{M} \cdot d\mathbf{l}$, is the line integral of $\mathbf{M}$ along e_{m_k}. Thus, the array of DoFs $\mathbf{m}$ which stores m_k, for $k = 1, \cdots, e_m$ is introduced. $\mathbf{w}_k^{e}$ is the (traditional) edge vector shape function related to e_{c_k} and exemplified in Fig. B.1.*b*.

It is useful to introduce also the expansions of $\mathbf{J}_a$ and $\mathbf{K}_a$. The volume amperian currents $\mathbf{J}_a$ are expanded likewise (B.14), i.e.:

$$\mathbf{J}_a(\mathbf{r}) = \sum_{k=1}^{f_m} \mathbf{w}_k^{\phi}(\mathbf{r}) j_{a_k}, \tag{B.17}$$

thus, the array of DoFs $\mathbf{j}_a$ is defined likewise $\mathbf{j}_c$. Analogously, the surface amperian currents $\mathbf{K}_a$ are expanded as

$$\mathbf{K}_a(\mathbf{r}) = \sum_{k=1}^{e_m^b} \mathbf{w}_k^{\phi s}(\mathbf{r}) k_{a_k}, \tag{B.18}$$

where k_{a_k} is the flux of $\mathbf{K}_a$ through the kth *boundary* edge of the mesh $e_{m_k}^b$. Then, the array of DoFs $\mathbf{k}_a$ which stores k_{a_k}, for $k = 1, \cdots, e_m^b$ is introduced. $\mathbf{w}_k^{\phi s}$ is the vector shape function related to $e_{m_k}^b$ and defined as

$$\mathbf{w}_k^{\phi s}(\mathbf{r}) = \frac{1}{L_k}\vec{\phi}, \ \mathbf{r} \in e_k^b, \tag{B.19}$$

where L_k is the length of $e_{m_k}^b$.

As in the A–PEEC method, additional arrays of DoFs can be introduced for $\mathbf{E}$ and $\mathbf{A}$ living on the entities of $\tilde{\mathcal{G}}_{\hat{\Omega}_c}$:

- $\tilde{\mathbf{e}} = (\tilde{e}_k)$ on dual nodes $\tilde{n}_c$, where

$$\tilde{e}_k = 2\pi r_{\tilde{n}_c} E_{\phi}(\mathbf{r}_{\tilde{n}_c}), \tag{B.20}$$

- $\tilde{\mathbf{a}}^c = (\tilde{a}_k^c)$ on dual nodes $\tilde{n}_c$, where

$$\tilde{a}_k^c = 2\pi r_{\tilde{n}_c} A_{\phi}(\mathbf{r}_{\tilde{n}_c}), \tag{B.21}$$

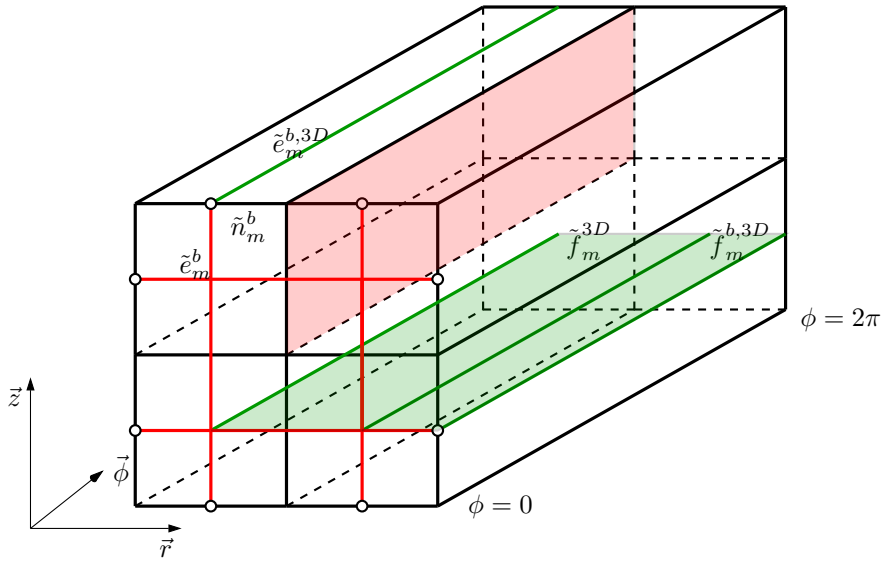

Figure B.2: Augmented axisymmetric magnetic grid $\mathcal{G}^a_{\hat{\Omega}_m}$ for the Amperian formulation.

where $\mathbf{r}_{\tilde{n}_c} = (r_{\tilde{n}_c}, \phi_{\tilde{n}_c}, z_{\tilde{n}_c})$ is the position of the kth dual node $\tilde{n}_c$. The array of DoFs $\tilde{\mathbf{e}}_0$ related to $\mathbf{E}_{ext}$ is defined likewise $\tilde{\mathbf{e}}$.

It is worth noting that, due to the axisymmetric assumption, the dual nodes $\tilde{n}_c$ are in a one–to–one relationship with the 3–D (dual) edges $\tilde{e}_c^{3D}$ obtained the by axial revolution of $\tilde{n}_c$, as represented in Fig. B.1.*a*. Indeed, (B.20) and (B.21) are the line integrals of $\mathbf{E}$ and $\mathbf{A}$ along the kth 3–D edge $\tilde{e}_{ck}^{3D}$.

Other arrays of DoFs related to $\mathbf{B}$ and $\mathbf{A}$ can also be introduced for the magnetic grid $\mathcal{G}_{\hat{\Omega}_m}$. However, before to do that, we need to augment the dual grid $\mathcal{G}_{\hat{\Omega}_m}$. Thus, the *boundary* dual nodes $\tilde{n}_m^b$ (in a one–to–one relation with the set of the boundary edges e_m) are added to the dual magnetic grid. Then, the augmented dual magnetic grid is defined as $\mathcal{G}^a_{\hat{\Omega}_m}$ and it is represented in Fig. B.2. Moreover, the selection matrix $\mathbf{C}_{\hat{\Gamma}_m}$ which extracts the boundary edges e_m^b of $\mathcal{G}_{\hat{\Omega}_m}$ is introduced. The (dual) gradient selection matrix $\tilde{\mathbf{G}}_{\hat{\Gamma}_m} = -\mathbf{C}^T_{\hat{\Gamma}_m}$ and the *augmented* matrices $\mathbf{C}^a_{\hat{\Omega}_m} = [\mathbf{C}_{\hat{\Omega}_m}; \mathbf{C}_{\hat{\Gamma}_m}]$ and $\tilde{\mathbf{G}}^a_{\hat{\Omega}_m} = -\mathbf{C}^{aT}_{\hat{\Gamma}_m} = [\tilde{\mathbf{G}}_{\hat{\Omega}_m}, \tilde{\mathbf{G}}_{\hat{\Gamma}_m}]$ are also introduced. Now, the following arrays of DoFs living on the dual geometric entities of $\tilde{\mathcal{G}}^a_{\hat{\Omega}_m}$ can be defined:

- $\tilde{\mathbf{a}}^m = (\tilde{a}_k^m)$ on dual nodes $\tilde{n}_m$, where

$$\tilde{a}_k^m = 2\pi r_{\tilde{n}_m} A_\phi(\mathbf{r}_{\tilde{n}_m}), \tag{B.22}$$

  where $\mathbf{r}_{\tilde{n}_m} = (r_{\tilde{n}_m}, \phi_{\tilde{n}_m}, z_{\tilde{n}_m})$ is the position of the kth dual node $\tilde{n}_m$;

- $\tilde{\mathbf{a}}^{mb} = (\tilde{a}_k^{mb})$ on *boundary* dual nodes $\tilde{n}_m^b$, where

$$\tilde{a}_k^{mb} = 2\pi r_{\tilde{n}_m^b} A_\phi(\mathbf{r}_{\tilde{n}_m^b}), \tag{B.23}$$

  where $\mathbf{r}_{\tilde{n}_m^b} = (r_{\tilde{n}_m^b}, \phi_{\tilde{n}_m^b}, z_{\tilde{n}_m^b})$ is the position of the kth *boundary* dual node $\tilde{n}_m^b$;

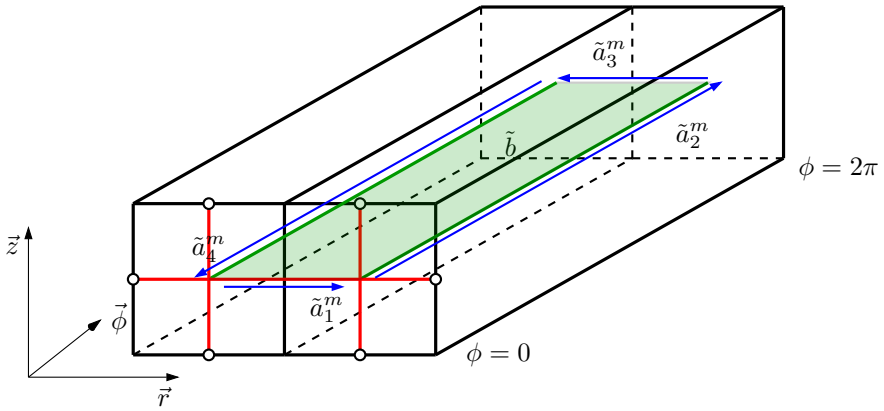

Figure B.3: Algebraic relations between $\tilde{\mathbf{b}}$ and $\tilde{\mathbf{a}}^m$ for the Cell Method approach.

- $\tilde{\mathbf{b}} = (\tilde{b}_k)$ on dual edges $\tilde{e}_m$, where

$$\tilde{b}_k = \int_{\tilde{e}_{m_k}} 2\pi r(\vec{\phi} \times \mathbf{B}) \cdot d\mathbf{l}, \tag{B.24}$$

  i.e. $\tilde{b}_k$ is the flux of $\mathbf{B}$ trough the 3–D (dual) face $\tilde{f}^{3D}_{m_k}$ obtained as the axial revolution of $\tilde{e}_{m_k}$ (see Fig. B.2);

- $\tilde{\mathbf{b}}^b = (\tilde{b}^b_k)$ on dual *boundary* edges $\tilde{e}^b_m$, where

$$\tilde{b}^b_k = \int_{\tilde{e}^b_{m_k}} 2\pi r(\vec{\phi} \times \mathbf{B}) \cdot d\mathbf{l}, \tag{B.25}$$

  i.e. $\tilde{b}^b_k$ is the flux of $\mathbf{B}$ trough the 3–D (dual) *boundary* face $\tilde{f}^{b,3D}_{m_k}$ obtained as the axial revolution of $\tilde{e}^b_{m_k}$ (see Fig. B.2).

The array of DoFs $\tilde{\mathbf{b}}_0$ related to $\mathbf{B}_{ext}$ is defined likewise $\tilde{\mathbf{b}}$.

In the Cell Method approach, the continuum differential relationships between the electromagnetic quantities can be translated into algebraic relations between the arrays of DoFs. For instance, referring to Fig. (B.3), the differential equation $\mathbf{B} = \nabla \times \mathbf{A}$ is translated in

$$\tilde{b} = \tilde{a}_1^m + \tilde{a}_2^m + \tilde{a}_3^m + \tilde{a}_4^m, \tag{B.26}$$

where $\tilde{b}$ is the flux of $\mathbf{B}$ through the green (3–D) face related to a kth dual edge $\tilde{e}_m$ and $\tilde{a}_h^m$ is the line integrals of $\mathbf{A}$ along the edges of the green face of Fig. (B.3) with $h = 1, \cdots, 4$. However, due to the axisymmetric condition and since $\mathbf{A} = A_\phi \vec{\phi} + 0\vec{r} + 0\vec{z}$, we have that $\tilde{a}_1^m = -\tilde{a}_3^m = 0$. Thus, (B.26) becomes

$$\tilde{b} = \tilde{a}_2^m + \tilde{a}_4^m. \tag{B.27}$$

The relation (B.27) written for all the DoFs results in

$$\tilde{\mathbf{b}} = \tilde{\mathbf{G}}^a_{\hat{\Omega}_m}[\tilde{\mathbf{a}}^m, \tilde{\mathbf{a}}^{mb}]. \tag{B.28}$$

Analogously, the continuum relations $\mathbf{J}_a = \nabla \times \mathbf{M}$ and $\mathbf{K}_a = \mathbf{M} \times \mathbf{n}$ are translated in

$$\mathbf{j}_a = \mathbf{C}_{\hat{\Omega}_m} \mathbf{m}, \qquad \mathbf{k}_a = \mathbf{C}_{\hat{\Gamma}_m} \mathbf{m}, \qquad \begin{bmatrix} \mathbf{j}_a \\ \mathbf{k}_a \end{bmatrix} = \mathbf{C}^a_{\hat{\Omega}_m} \mathbf{m}, \tag{B.29}$$

while the algebraic forms of (B.1) and (B.2) are

$$\tilde{\mathbf{e}} = -i\omega \tilde{\mathbf{a}}^{\mathbf{c}} + \tilde{\mathbf{e}}_0, \tag{B.30}$$

$$\tilde{\mathbf{b}} = \tilde{\mathbf{G}}^a_{\hat{\Omega}_m} [\tilde{\mathbf{a}}^m, \tilde{\mathbf{a}}^{mb}] + \tilde{\mathbf{b}}_0. \tag{B.31}$$

Finally, the expansions (B.14) and (B.16) are inserted in (B.12) and (B.13), and the resulting equations are tested following a Galerkin approach. Thus, the following discrete equations which represent the discrete form of (B.12) and (B.13) are obtained:

$$\mathbf{R}_c \mathbf{j}_c + i\omega \tilde{\mathbf{a}}^c = \tilde{\mathbf{e}}_0, \tag{B.32}$$

$$\mathbf{F}\mathbf{m} - \tilde{\mathbf{G}}^a_{\hat{\Omega}_m} [\tilde{\mathbf{a}}^m, \tilde{\mathbf{a}}^{mb}] = \mathbf{b}_0, \tag{B.33}$$

where

$$\tilde{\mathbf{a}}^c = \mathbf{L}^c_c \mathbf{j}_c + [\mathbf{L}^c_m, \mathbf{L}^c_{ms}] \mathbf{C}^a_{\hat{\Omega}_m} \mathbf{m}, \tag{B.34}$$

$$[\tilde{\mathbf{a}}^m, \tilde{\mathbf{a}}^{ms}] = \begin{bmatrix} \mathbf{L}^m_c \\ \mathbf{L}^{ms}_c \end{bmatrix} \mathbf{j}_c + \begin{bmatrix} \mathbf{L}^m_m & \mathbf{L}^m_{ms} \\ \mathbf{L}^{ms}_m & \mathbf{L}^{ms}_{ms} \end{bmatrix} \mathbf{C}^a_{\hat{\Omega}_m} \mathbf{m}. \tag{B.35}$$

The resistance matrix $\mathbf{R}_c$ is defined as:

$$R_{c,kh} = \int_{\hat{\Omega}_c} 2\pi r \mathbf{w}^\phi_k(\mathbf{r}) \cdot \mathbf{w}^\phi_h(\mathbf{r}) \rho_c(\mathbf{r}) d\Gamma, \tag{B.36}$$

while the constitutive matrix $\mathbf{F}$ is

$$F_{kh} = \int_{\hat{\Omega}_m} 2\pi r \mathbf{w}^e_k(\mathbf{r}) \cdot \mathbf{w}^e_h(\mathbf{r}) \alpha_m(\mathbf{r}) d\Gamma. \tag{B.37}$$

The *volume*, *surface*, and *volume–surface* axisymmetric inductance matrices are instead defined as

$$L^\alpha_{\beta_{ku}} = L^\beta_{\alpha_{uk}} = \mu_0 \int_{\hat{\Omega}_\beta} 2\pi r \mathbf{w}^\phi_u(\mathbf{r}) \cdot \int_{\hat{\Omega}_\alpha} \mathbf{w}^\phi_k(\mathbf{r}') \hat{g}(\mathbf{r}, \mathbf{r}') d\hat{\Omega}' d\hat{\Omega}, \tag{B.38}$$

$$L^{ms}_{\alpha_{ku}} = L^\alpha_{ms} = \mu_0 \int_{\hat{\Omega}_\alpha} 2\pi r \mathbf{w}^\phi_u(\mathbf{r}) \cdot \int_{\hat{\Gamma}_m} \mathbf{w}^{\phi s}_k(\mathbf{r}') \hat{g}(\mathbf{r}, \mathbf{r}') d\hat{\Gamma}' d\hat{\Omega}, \tag{B.39}$$

$$L^{ms}_{ms_{uk}} = \mu_0 \int_{\hat{\Gamma}_m} 2\pi r \mathbf{w}^{\phi s}_u(\mathbf{r}) \cdot \int_{\hat{\Gamma}_m} \mathbf{w}^{\phi s}_k(\mathbf{r}') \hat{g}(\mathbf{r}, \mathbf{r}') d\hat{\Gamma}' d\hat{\Gamma}, \tag{B.40}$$

where $\alpha = c, m$ and $\beta = c, m$.

Therefore, the discrete electromagnetic problem can be represented as the following algebraic system of equations

$$\begin{bmatrix} \mathbf{R}_c + i\omega \mathbf{L}^c_c & i\omega [\mathbf{L}^c_m, \mathbf{L}^c_{ms}] \mathbf{C}^a_{\hat{\Omega}_m} \\ -\begin{bmatrix} \mathbf{L}^m_c \\ \mathbf{L}^{ms}_c \end{bmatrix} & \mathbf{F} - \tilde{\mathbf{G}}^a_{\hat{\Omega}_m} \begin{bmatrix} \mathbf{L}^m_m & \mathbf{L}^m_{ms} \\ \mathbf{L}^{ms}_m & \mathbf{L}^{ms}_{ms} \end{bmatrix} \mathbf{C}^a_{\hat{\Omega}_m} \end{bmatrix} \begin{bmatrix} \mathbf{j}_c \\ \mathbf{m} \end{bmatrix} = \begin{bmatrix} \tilde{\mathbf{e}}_0 \\ \tilde{\mathbf{b}}_0 \end{bmatrix}, \tag{B.41}$$

which can be made symmetric by multiplying the second row for $-i\omega$.

Once obtained the solution of (B.41), the unknown distributions of $\mathbf{J}_c$, $\mathbf{J}_a$, $\mathbf{K}_a$ and $\mathbf{M}$ can be re–constructed by using the expansions (B.14), (B.16), (B.17), and (B.18). Then, the solutions in terms of the electromagnetic fields can be evaluated in the whole 3–D space by post processing using (B.2), (B.1), and (B.7).

As discussed more in detail in section 4.2.4, system (B.41) naturally enforce the electromagnetic properties of the magnetization, but not in a numerically strong sense. For instance, in steady state condition and for homogeneous non–conductive magnetic media, only the surface amperian currents exist while the volume amperian currents are zero ($\nabla \times \mathbf{M} = \mathbf{J}_a \approx 0$). This condition is not strongly enforced by (B.41) and a distribution of $\mathbf{J}_a$ close to the boundary is obtained also when a zero frequency problem is solved. Anyhow, this usually does not particularly affect the global quality of the solution but it could be an issue when high accuracy is required or when an accurate knowledge of magnetization distribution is important. However, this condition can be enforced by imposing

$$\mathbf{m} = \mathbf{G}_{\hat{\Omega}_m} \boldsymbol{\phi}_m, \tag{B.42}$$

where $\boldsymbol{\phi}_m$ is the array of DoFs related to a *discrete scalar magnetic potential* associated to the primal nodes n_m (except one considered as reference) of $\mathcal{G}_{\hat{\Omega}_m}$. Thus, (B.42) can be applied to (B.41) and the second row of (B.41) can be projected into a new set of equation by using $\mathbf{G}^T_{\hat{\Omega}_m}$ (without one column for each magnetic sub–domain). The resulting system has a reduced dimension and, since $\mathbf{j}_a = 0$, the evaluation of $\mathbf{L}^m_c$, $\mathbf{L}^c_m$, and $\mathbf{L}^m_m$ is not needed anymore.

This method is based on the amperian interpretation of the electromagnetic phenomena as done for the A–PEEC method. Unfortunately, as the A–PEEC method, this method suffers from a numerical issue when magnetic media with high permeability are actually involved. Indeed, the constitutive relation (B.11) depends on α_m. With the increasing of the relative permeability the coefficient α_m tends to the value μ_0 (i.e. $\alpha_m \to \mu_0$ with the increasing of μ_r). For instance, numerically speaking, the difference between $\mu_r = 100$ and $\mu_r = 1000$ is left to the last significant digits of α_m and this *numerical information* can be completely lost when floating-point arithmetic is used.

This numerical issue is discussed more in detail in section 4.2.3 in *Material coefficients of A–PEEC and C–PEEC methods.*

B.2 Coulombian axisymmetric method

In the following an alternative method for the study of axisymmetric electromagnetic problems is proposed. In the previous section, the magnetization phenomena have been considered following the amperian interpretation. Here, instead, the *magnetic currents and charges* are introduced and different electric and magnetic potentials are adopted.

B.2.1 Formulation

In this section, an integral axisymmetric method based on the C–PEEC formulation is derived. When the magnetization phenomena are interpreted introducing the *magnetic currents and*

charges, the integral form of the electromagnetic problem reduces to

$$\mathbf{E}(\mathbf{r}) = -i\omega\mathbf{A}_e(\mathbf{r}) - \nabla\varphi_e(\mathbf{r}) - \frac{1}{\varepsilon_0}\nabla\times\mathbf{A}_m(\mathbf{r}) + \mathbf{E}_{ext}(\mathbf{r}), \tag{B.43}$$

$$\mathbf{H}(\mathbf{r}) = -i\omega\mathbf{A}_m(\mathbf{r}) - \nabla\varphi_m(\mathbf{r}) + \frac{1}{\mu_0}\nabla\times\mathbf{A}_e(\mathbf{r}) + \mathbf{H}_{ext}(\mathbf{r}), \tag{B.44}$$

where $\mathbf{A}_e$ and $\mathbf{A}_m$ are the electric and magnetic vector potentials [43], φ_m is the scalar magnetic potential, $\mathbf{H}(\mathbf{r})$ is the magnetic field, and $\mathbf{H}_{ext}(\mathbf{r})$ is the external magnetic field.

The integral form of $\mathbf{A}_e$ and $\mathbf{A}_m$ is given by

$$\mathbf{A}_e(\mathbf{r}) = \mu_0\int_{\Omega_c}\mathbf{J}_c(\mathbf{r}')g(\mathbf{r},\mathbf{r}')d\mathbf{r}', \tag{B.45}$$

$$\mathbf{A}_m(\mathbf{r}) = \varepsilon_0\int_{\Omega_m}\mathbf{J}_m(\mathbf{r}')g(\mathbf{r},\mathbf{r}')d\mathbf{r}', \tag{B.46}$$

in which $\mathbf{J}_m = i\omega\mu_0\mathbf{M}$ is the magnetic current density.

Equations (B.4) are still valid and they are complemented with

$$\mathbf{A}_e = A_{e_\phi}\vec{\phi}, \qquad \mathbf{H} = H_r\vec{r} + H_z\vec{z}, \qquad \mathbf{J}_m = J_{m_r}\vec{r} + J_{m_r}\vec{z}, \qquad \mathbf{A}_m = A_{m_r}\vec{r} + A_{m_r}\vec{z}. \tag{B.47}$$

When the Lorenz gauge condition is imposed for $\mathbf{A}_e$ and $\mathbf{A}_m$, the scalar electric potential φ_e is related to ϱ_e and ς_e by means of (B.5) while φ_m is related to the volume and surface magnetic charges (ϱ_m and ς_m) by:

$$\varphi_m(\mathbf{r}) = \mu_0^{-1}\left[\int_{\bar{\Gamma}_m}\varsigma_m(\mathbf{r}')g(\mathbf{r},\mathbf{r}')d\mathbf{r}' + \int_{\Omega_m}\varrho_m(\mathbf{r}')g(\mathbf{r},\mathbf{r}')d\mathbf{r}'\right], \tag{B.48}$$

where, ϱ_m and ς_m are related to $\mathbf{J}_m$ by means of the continuity relations

$$\nabla'\cdot\mathbf{J}_m(\mathbf{r}') = -i\omega\varrho_m(\mathbf{r}'), \qquad \mathbf{J}_m(\mathbf{r}')\cdot\mathbf{n} = -i\omega\varsigma_m(\mathbf{r}'). \tag{B.49}$$

As in section B.1.1, when the axisymmetric condition holds, $\mathbf{J}_c$ is divergence free. Thus, no moving electric charge is present and therefore $\varphi_e(\mathbf{r}) = 0$.

The integral expression of $\mathbf{A}_e$ can be formulated in cylindrical coordinates as shown in [178]:

$$A_{e_\phi}(\mathbf{r}) = \mu_0\int_{\hat{\Omega}_c}\hat{g}(\mathbf{r},\mathbf{r}')J_{c_\phi}(\mathbf{r}')d\hat{\Omega}, \tag{B.50}$$

with the same definition given for (B.7).

The definition of φ_m can be also derived from [178]:

$$\varphi_m(\mathbf{r}) = \frac{1}{\mu_0}\left[\int_{\hat{\Omega}_c}\bar{g}(\mathbf{r},\mathbf{r}')\varrho_m(\mathbf{r}')d\hat{\Omega} + \int_{\hat{\Gamma}_c}\bar{g}(\mathbf{r},\mathbf{r}')\varsigma_m(\mathbf{r}')d\hat{\Gamma}\right], \tag{B.51}$$

where $\bar{g}$ is the axisymmetric Green's function of the scalar potential and the other quantities keep the same definitions given for (B.50). The axisymmetric Green's function $\bar{g}$ (which is the axisymmetric solution of the Poisson equation for a uniformed charged ring [181, 182]) is defined as

$$\bar{g}(\mathbf{r},\mathbf{r}') = \frac{4r'}{4\pi K}\mathcal{K}(k^2), \tag{B.52}$$

where the quantities are defined as in (B.8).

The author fails on finding a proper reference for the expression of $\mathbf{A}_m$ in cylindrical coordinates. However, this integral expression can be extrapolated from the one of the scalar magnetic potential, i.e.

$$A_{m_\alpha}(\mathbf{r}) = \varepsilon_0 \int_{\hat{\Omega}_m} \bar{g}(\mathbf{r}, \mathbf{r}') J_{m_\alpha}(\mathbf{r}') d\hat{\Omega}, \tag{B.53}$$

where $\alpha = r, z$.

Equations (B.43) and (B.44) are complemented by (B.10) and the following constitutive equation:

$$\mathbf{H}(\mathbf{r}) = \rho_m(\mathbf{r}) \mathbf{J}_m(\mathbf{r}), \ \mathbf{r} \in \Omega_m. \tag{B.54}$$

where $\rho_m = (i\omega\mu_0(\mu_r - 1))^{-1}$ is the magnetic resistivity.

Finally, combining (B.43) with (B.10), and (B.44) with (B.54), the following final continuum equations for an electromagnetic axisymmetric problem are obtained

$$\rho_c(\mathbf{r}) \mathbf{J}_c(\mathbf{r}) = -i\omega \mathbf{A}_e(\mathbf{r}) - \nabla\varphi_e(\mathbf{r}) - \frac{1}{\varepsilon_0} \nabla \times \mathbf{A}_m(\mathbf{r}) + \mathbf{E}_{ext}(\mathbf{r}), \ \mathbf{r} \in \Omega_c, \tag{B.55}$$

$$\rho_m(\mathbf{r}) \mathbf{J}_m(\mathbf{r}) = -i\omega \mathbf{A}_m(\mathbf{r}) - \nabla\varphi_m(\mathbf{r}) + \frac{1}{\mu_0} \nabla \times \mathbf{A}_e(\mathbf{r}) + \mathbf{H}_{ext}(\mathbf{r}), \ \mathbf{r} \in \Omega_m, \tag{B.56}$$

where, however, $\nabla\varphi_e(\mathbf{r}) = 0$ since $\varphi_e(\mathbf{r}) = 0$.

B.2.2 Cell Method discretization

As in the A–formulation of section B.1.2, conductive and magnetic domains are now represented by means of $\hat{\Omega}_c$ and $\hat{\Omega}_m$, respectively. These 2–D domains are discretized into two quadrilateral grids: $\mathcal{G}_{\hat{\Omega}_c}$ for the conductive domain $\hat{\Omega}_c$, and $\mathcal{G}_{\hat{\Omega}_m}$ for the magnetic domain $\hat{\Omega}_m$.

All the geometric entities previously defined in B.1.2 (A–formulation) for the conductive grid $\mathcal{G}_{\hat{\Omega}_c}$ are introduced also for the C–formulation. Moreover, the dual conductive grid $\tilde{\mathcal{G}}_{\hat{\Omega}_c}$ is defined likewise B.1.2, as well all the conductive primal and dual incidence matrices. The conduction current density $\mathbf{J}_c$ is also expanded as in (B.14). The only difference concerning the conductive media between the Amperian and Coulombian formulations is on the definition of the arrays of DoFs related to the vector potentials. Indeed, while in the Amperian formulation $\mathbf{a}^c$ is defined for $\mathbf{A}$, in the Coulombian formulation $\mathbf{A}$ is substituted with $\mathbf{A}_e$ and $\mathbf{A}_m$ (i.e. $\mathbf{A} = \mathbf{A}_e + \frac{1}{i\omega\varepsilon_0} \nabla \times \mathbf{A}_m$). Thus $\mathbf{a}^c$ is not defined for the Coulombian formulation and the following arrays of DoFs related to $\mathbf{A}_e$ and $\mathbf{A}_m$ are instead introduced:

- $\tilde{\mathbf{a}}_e^c = (\tilde{a}_{e,k}^c)$ on dual nodes $\tilde{n}_c$, where

$$\tilde{a}_{e,k}^c = 2\pi r_{\tilde{n}_c} A_{e_\phi}(\mathbf{r}_{\tilde{n}_c}), \tag{B.57}$$

  where $\mathbf{r}_{\tilde{n}_c} = (r_{\tilde{n}_c}, \phi_{\tilde{n}_c}, z_{\tilde{n}_c})$ is the position of the kth dual node $\tilde{n}_c$,

- $\mathbf{a}_m^c = (a_{m,k}^c)$ on primal edges e_c, where

$$a_{m,k}^c = \int_{e_{m,k}} \mathbf{A}_m(\mathbf{r}) \cdot d\mathbf{l}. \tag{B.58}$$

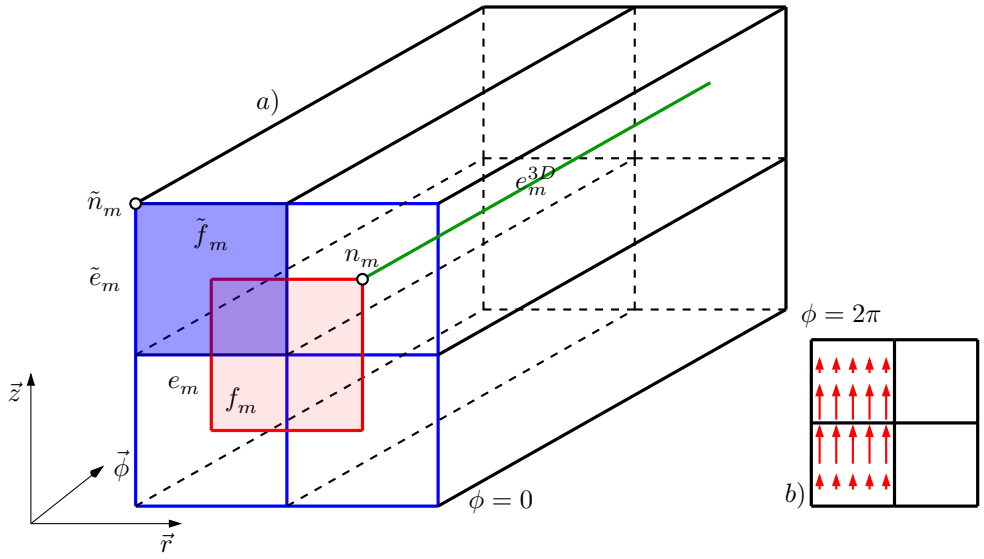

Figure B.4: *a*. Primal and dual geometric entities for the magnetic grid of the Coulombian axisymmetric formulation. *b*. Axial symmetric $\mathbf{w}^{rz}$ edge shape function.

Magnetic media instead are differently considered by the A– and C– formulations. Thus, in the following, the discretization will only consider the magnetic domains.

As for the C–PEEC discretization, following the Tonti scheme of Fig. 3.10, the role of the primal and dual grid for the magnetic domains is now exchanged with respect of the A–formulation. Thus, the *dual* magnetic grid $\tilde{\mathcal{G}}_{\hat{\Omega}_m}$ now consists of quadrilateral elements while the *primal* magnetic grid $\mathcal{G}_{\hat{\Omega}_m}$ is taken as the barycentric subdivision of $\tilde{\mathcal{G}}_{\hat{\Omega}_m}$. The two grids consist of dual and primal geometric entities that are in a one–to–one relationships: $f_m \leftrightarrow \tilde{n}_m$, $e_m \leftrightarrow \tilde{e}_m$, $n_m \leftrightarrow \tilde{f}_m$. The magnetic geometric entities are represented in Fig. B.4 in a *rectified* axial geometry.

Magnetic incidence matrices can now be introduced for the dual and primal magnetic grids: $\tilde{\mathbf{G}}_{\hat{\Omega}_m}$ (*dual* edges–*dual* nodes), $\tilde{\mathbf{C}}_{\Gamma_m}$ (*dual* faces–*dual* edges), $\mathbf{G}_{\hat{\Omega}_m}$ (*primal* edges–*primal* nodes), and $\mathbf{C}_{\hat{\Omega}_m}$ (*primal* faces–*primal* edges). These primal and dual incidence matrices satisfy the following properties: $\tilde{\mathbf{C}}_{\hat{\Omega}_m}\tilde{\mathbf{G}}_{\hat{\Omega}_m} = \mathbf{0}$, $\mathbf{C}_{\hat{\Omega}_m}\mathbf{G}_{\hat{\Omega}_m} = \mathbf{0}$.

The magnetic current density $\mathbf{J}_m$, which is one of the unknown of the integral electromagnetic problem, is now expanded as

$$\mathbf{J}_m(\mathbf{r}) = \sum_{k=1}^{\tilde{e}_m} \mathbf{w}_k^f(\mathbf{r})\tilde{j}_{m,k}, \tag{B.59}$$

where

$$\tilde{j}_{m,k} = \int_{\tilde{e}_m} 2\pi r(\vec{\phi} \times \mathbf{J}_m(\mathbf{r})) \cdot d\mathbf{l},$$

is the flux of $\mathbf{J}_m$ through the 3–D (dual) face $\tilde{f}_{m_k}^{3D}$ represented in Fig. B.5.*a* and related to the kth dual edge $\tilde{e}_{m_k}$ (i.e. $\tilde{f}_{m_k}^{3D}$ is the axial–revolution of $\tilde{e}_{m_k}$ as shown in Fig. B.5.*a*). Thus, the array of DoFs $\tilde{\mathbf{j}}_m$ which stores $\tilde{j}_{m,k}$, for $k = 1, \cdots, \tilde{e}_m$ is introduced. $\mathbf{w}_k^f$ is the (scaled) face vector shape function related to $\tilde{e}_{m_k}$ and exemplified in Fig. B.4.*b*. The face shape functions $\mathbf{w}_k^f$ satisfies

$$\mathbf{w}_k^f \cdot (\vec{\phi} \times \vec{e}) = \frac{1}{A_k},$$

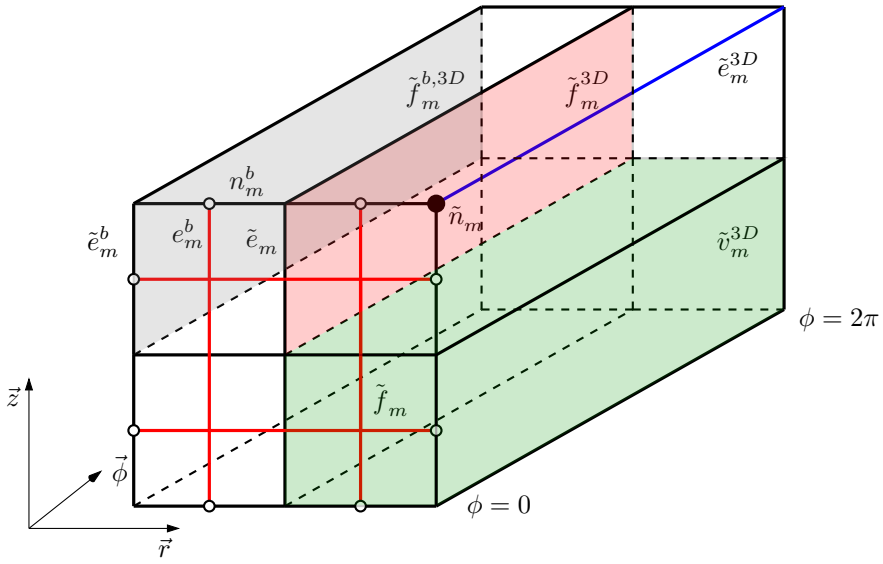

Figure B.5: Augmented axisymmetric magnetic grid $\mathcal{G}^a_{\tilde{\Omega}_m}$ for the EB formulation.

where $\vec{e}$ is the unit vector in the direction of $\tilde{e}_{m_k}$ and A_k is the area of $\tilde{f}^{3D}_{m_k}$.

The expansion (B.59) introduced for $\mathbf{J}_m$ also induces an expansion for ϱ_m and ς_m when combined with (B.49). Thus, the following expansions can be introduced for the volume magnetic charge density

$$\varrho_m(\mathbf{r}) = \sum_k^{\tilde{f}_m} \frac{1}{V_k} \tilde{q}^v_{m,k}, \tag{B.60}$$

where

$$\tilde{q}^v_{m,k} = \int_{\tilde{f}_{m_k}} 2\pi r \varrho_m(\mathbf{r}) d\Gamma = \int_{\tilde{v}^{3D}_{m_k}} \varrho_m(\mathbf{r}) d\Omega$$

is the (net) magnetic charge inside the kth 3–D (dual) volume $\tilde{v}^{3D}_{m_k}$ obtained from the axial revolution of $\tilde{f}_{m_k}$ (see Fig. B.5) and V_k is the volume of $\tilde{v}^{3D}_{m_k}$. Thus, the array of DoFs $\tilde{\mathbf{q}}^v_m$ which stores $\tilde{q}^v_{m,k}$, for $k = 1, \cdots, \tilde{f}_m$, is introduced.

Analogously, the surface magnetic charge density is expanded as

$$\varsigma_m(\mathbf{r}) = \sum_k^{\tilde{e}^b_m} \frac{1}{A_k} \tilde{q}^s_{m,k}, \tag{B.61}$$

where

$$\tilde{q}^s_{m,k} = \int_{\tilde{e}_{m_k}} 2\pi r \varsigma_m(\mathbf{r}) d\Lambda = \int_{\tilde{f}^{b,3D}_{m_k}} \varsigma_m(\mathbf{r}) d\Gamma$$

is the (net) magnetic charge laying on the kth 3–D (dual) boundary face $\tilde{f}^{b,3D}_{m_k}$ obtained from the axial revolution of the boundary edge $\tilde{e}^b_{m_k}$ (see Fig. B.5) and A_k is the area of $\tilde{f}^{b,3D}_{m_k}$. Thus, the array of DoFs $\tilde{\mathbf{q}}^s_m$ which stores $\tilde{q}^s_{m,k}$, for $k = 1, \cdots, \tilde{e}^b_m$, is introduced.

Additional arrays of DoFs can be now introduced for $\mathbf{H}$, $\mathbf{A}_e$, $\mathbf{A}_m$, and φ_m. Before to do that, the primal grid $\mathcal{G}_{\hat{\Omega}_m}$ must be augmented. Thus, the *boundary* nodes n^b_m (in a one–to–one relation with the set of dual boundary edges $\tilde{e}^b_m$) are added to the primal magnetic grid $\mathcal{G}_{\hat{\Omega}_m}$. Then, the *augmented* primal grid is defined as $\mathcal{G}^a_{\hat{\Omega}_m}$. Moreover, the selection matrix $\tilde{\mathbf{C}}_{\hat{\Gamma}_m}$ which extracts

the set of dual boundary edges $\tilde{e}^b_m$ is introduced. The (primal) gradient selection matrix $\mathbf{G}_{\hat{\Gamma}_m} = -\tilde{\mathbf{C}}^T_{\hat{\Gamma}_m}$ and the *augmented* matrices $\tilde{\mathbf{C}}^a_{\hat{\Omega}_m} = [\tilde{\mathbf{C}}_{\hat{\Omega}_m}; \tilde{\mathbf{C}}_{\hat{\Gamma}_m}]$ and $\mathbf{G}^a_{\hat{\Omega}_m} = \tilde{\mathbf{C}}^{aT}_{\hat{\Omega}_m} = [\mathbf{G}_{\hat{\Omega}_m}, \mathbf{G}_{\hat{\Gamma}_m}]$ are also introduced.

Now, the following arrays of DoFs living on the primal geometric entities of $\mathcal{G}^a_{\hat{\Omega}_m}$ can be defined:

- $\mathbf{h} = (h_k)$ on primal edges e_m, where

$$h_k = \int_{e_{m,k}} \mathbf{H}(\mathbf{r}) \cdot d\mathbf{l}, \tag{B.62}$$

- $\mathbf{a}^m_m = (a^m_{m,k})$ on primal edges e_m, where

$$a^m_{m,k} = \int_{e_{m,k}} \mathbf{A}_m(\mathbf{r}) \cdot d\mathbf{l}, \tag{B.63}$$

- $\boldsymbol{\phi}^v_m = (\phi^v_{m,k})$ on primal nodes n_m, where

$$\phi^v_{m,k} = \frac{\varphi_m(\mathbf{r})}{V_k}, \tag{B.64}$$

  and V_k is the volume of $v^{3D}_{m_k}$,

- $\boldsymbol{\phi}^s_m = (\phi^s_{m,k})$ on primal boundary nodes n^b_m, where

$$\phi^s_{m,k} = \frac{\varphi_m(\mathbf{r})}{A_k}, \tag{B.65}$$

  and A_k is the area of $f^{b,3D}_{m_k}$,

- $\tilde{\mathbf{a}}^m_e = (\tilde{a}^m_{e,k})$ on dual nodes $\tilde{n}_m$, where

$$\tilde{a}^m_{e,k} = 2\pi r_{\tilde{n}_m} A_{e_\phi}(\mathbf{r}_{\tilde{n}_m}), \tag{B.66}$$

  where $\mathbf{r}_{\tilde{n}_m} = (r_{\tilde{n}_m}, \phi_{\tilde{n}_m}, z_{\tilde{n}_m})$ is the position of the kth dual node $\tilde{n}_m$. $\tilde{a}^m_{e,k}$ is the line integral of $\mathbf{A}_e$ along the 3–D (dual) edge $\tilde{e}^{3D}_k$ obtained from the axial revolution of $\tilde{n}_m$ shown in Fig. B.5.

The array of DoFs $\mathbf{h}_0$ related to $\mathbf{H}_{ext}$ is defined likewise $\mathbf{h}$.

In the Cell Method approach, as for the Amperian formulation, the arrays of DoFs satisfy algebraic relations equivalent to the continuum differential equations. For instance, the continuity equation (B.49) in discrete form becomes

$$\tilde{\mathbf{C}}_{\hat{\Omega}_m}\tilde{\mathbf{j}}_m = -i\omega\tilde{\mathbf{q}}^v_m, \qquad \tilde{\mathbf{C}}_{\hat{\Gamma}_m}\tilde{\mathbf{j}}_m = -i\omega\tilde{\mathbf{q}}^s_m, \qquad \tilde{\mathbf{C}}^a_{\hat{\Omega}_m}\tilde{\mathbf{j}}_m = -i\omega \begin{bmatrix} \tilde{\mathbf{q}}^v_m \\ \tilde{\mathbf{q}}^s_m \end{bmatrix}. \tag{B.67}$$

Finally, the expansions (B.55) and (B.56) are inserted in (B.43) and (B.44), and the resulting equations are tested following a Galerkin approach. Thus, the following discrete equations which

represent the discrete form of (B.55) and (B.56) are obtained

$$\mathbf{R}_c\mathbf{j}_c + i\omega\tilde{\mathbf{a}}_e^c + \mathbf{M}_{1/\varepsilon_0}\mathbf{C}_{\hat{\Omega}_c}\mathbf{a}_m^c = \tilde{\mathbf{e}}_0, \tag{B.68}$$

$$\tilde{\mathbf{R}}_m\tilde{\mathbf{j}}_m + i\omega\mathbf{a}_m^m + \mathbf{G}^a_{\hat{\Omega}_m}[\boldsymbol{\phi}_m^v, \boldsymbol{\phi}_m^s] - \tilde{\mathbf{M}}_{1/\mu_0}\tilde{\mathbf{G}}_{\hat{\Omega}_m}\tilde{\mathbf{a}}_e^m = \mathbf{h}_0, \tag{B.69}$$

where

$$\begin{gathered}\tilde{\mathbf{a}}_e^c = \mathbf{L}_c^c\mathbf{j}_c, \qquad \mathbf{a}_m^c = \tilde{\mathbf{N}}_m^c\tilde{\mathbf{j}}_m, \qquad \mathbf{a}_m^m = \tilde{\mathbf{L}}_m^m\tilde{\mathbf{j}}_m, \\ [\boldsymbol{\phi}_m^v, \boldsymbol{\phi}_m^s] = \tilde{\mathbf{P}}_m\begin{bmatrix}\tilde{\mathbf{q}}_m^v \\ \tilde{\mathbf{q}}_m^s\end{bmatrix}, \qquad \tilde{\mathbf{a}}_e^m = \mathbf{N}_c^m\mathbf{j}_c.\end{gathered} \tag{B.70}$$

The axisymmetric resistance $\mathbf{R}_c$ and inductance $\mathbf{L}_c^c$ matrices are already defined in (B.36) and (B.38), respectively. The magnetic axisymmetric inductance matrix $\tilde{\mathbf{L}}_m^m$ is instead given by

$$\tilde{L}_{m_{ku}}^m = \varepsilon_0\int_{\hat{\Omega}_m} 2\pi r\mathbf{w}_u^f(\mathbf{r})\cdot\int_{\hat{\Omega}_m}\mathbf{w}_k^f(\mathbf{r}')\hat{g}(\mathbf{r},\mathbf{r}')d\hat{\Omega}'d\hat{\Omega}, \tag{B.71}$$

and the magnetic axisymmetric resistance matrix $\tilde{\mathbf{R}}_m$ is defined as

$$\tilde{R}_{ma_{ku}} = \int_{\hat{\Omega}_m} 2\pi r\mathbf{w}_u^f(\mathbf{r})\cdot\mathbf{w}_k^f(\mathbf{r})\rho_m(\mathbf{r})d\hat{\Omega}. \tag{B.72}$$

The magnetic axisymmetric potential matrix, $\tilde{\mathbf{P}}_m$, is subdivided into

$$\tilde{\mathbf{P}}_m = \begin{bmatrix}\tilde{\mathbf{P}}_m^{vv} & \tilde{\mathbf{P}}_m^{vs} \\ \tilde{\mathbf{P}}_m^{sv} & \tilde{\mathbf{P}}_m^{ss}\end{bmatrix} \tag{B.73}$$

in which

$$\tilde{P}_{m_{ku}}^{vv} = \frac{1}{A_kV_u^{3D}\mu_0}\int_{\tilde{f}_{m,k}}\int_{\tilde{f}_{m,u}}\bar{g}(\mathbf{r},\mathbf{r}')d\hat{\Omega}'d\hat{\Omega}, \tag{B.74}$$

where V_u^{3D} is the volume of the uth 3–D volume $\tilde{v}_{m_u}^{3D}$ (i.e. the axial revolution of $\tilde{f}_{m,u}$) and A_k is the area of $\tilde{f}_{m,k}$;

$$\tilde{P}_{m_{ku}}^{sv} = \frac{1}{L_kV_u^{3D}\mu_0}\int_{\tilde{e}_{m,k}^b}\int_{\tilde{f}_{m,u}}\bar{g}(\mathbf{r},\mathbf{r}')d\hat{\Omega}'d\hat{\Gamma}, \tag{B.75}$$

where L_k is the length of the dual boundary edge $\tilde{e}_{m,k}^b$;

$$\tilde{P}_{m_{ku}}^{vs} = \frac{1}{A_kA_u^{3D}\mu_0}\int_{\tilde{f}_{m,k}}\int_{\tilde{e}_{m,u}^b}\bar{g}(\mathbf{r},\mathbf{r}')d\hat{\Gamma}'d\hat{\Omega}, \tag{B.76}$$

where A_u^{3D} is the area of the uth 3–D face $\tilde{f}_{m_u}^{b,3D}$ (i.e. the axial revolution of $\tilde{e}_{m,u}^b$);

$$\tilde{P}_{m_{ku}}^{ss} = \frac{1}{L_kA_u^{3D}\mu_0}\int_{\tilde{e}_{m,k}^b}\int_{\tilde{e}_{m,u}^b}\bar{g}(\mathbf{r},\mathbf{r}')d\hat{\Gamma}'d\hat{\Gamma}. \tag{B.77}$$

It is worth noting that $\bar{g}(\mathbf{r},\mathbf{r}')$ is a non–symmetric function (i.e. $\bar{g}(\mathbf{r},\mathbf{r}') \neq \bar{g}(\mathbf{r}',\mathbf{r})$) while $\tilde{\mathbf{P}}_m$ is a symmetric matrix.

$\mathbf{M}_{1/\varepsilon_0}$ and $\tilde{\mathbf{M}}_{1/\mu_0}$ are projection matrices defined as

$$M_{1/\varepsilon_0,kh} = \int_{\hat{\Omega}_c} 2\pi r \mathbf{w}_k^{\phi}(\mathbf{r}) \cdot \mathbf{w}_h^{\phi}(\mathbf{r}) \frac{1}{\varepsilon_0} d\hat{\Omega}, \tag{B.78}$$

$$\tilde{M}_{1/\mu_0,ku} = \int_{\hat{\Omega}_m} 2\pi r \mathbf{w}_u^{f}(\mathbf{r}) \cdot \mathbf{w}_k^{f}(\mathbf{r}) \frac{1}{\mu_0} d\hat{\Omega}. \tag{B.79}$$

Matrices $\tilde{\mathbf{N}}_c^m$ and $\tilde{\mathbf{N}}_m^c$ (which represent the coupling between the electric and magnetic domains) are defined with a Discrete Hodge, i.e.

$$N_{c_{ku}}^m = \mu_0 2\pi r_{\tilde{n}_{m,k}} \vec{\phi} \cdot \int_{\hat{\Omega}_c} \mathbf{w}_u^{\phi}(\mathbf{r}') \hat{g}(\mathbf{r}, \mathbf{r}') d\hat{\Omega}', \tag{B.80}$$

where $r_{\tilde{n}_m}$ is the coordinate along $\vec{r}$ of $\tilde{n}_{m,k}$;

$$\tilde{N}_{m_{ku}}^c = \varepsilon_0 \int_{e_c} \vec{e} \cdot \int_{\hat{\Omega}_m} \mathbf{w}_k^{f}(\mathbf{r}') \bar{g}(\mathbf{r}, \mathbf{r}') d\hat{\Omega}' d\hat{\Gamma}, \tag{B.81}$$

where $\vec{e}$ is the unit vector in the direction of e_c.

Finally, the discrete electromagnetic problem derived from the C–formulation can be represented as the following algebraic system of equation

$$\begin{bmatrix} \mathbf{R}_c + i\omega \mathbf{L}_c^c & \mathbf{M}_{1/\varepsilon_0} \mathbf{C}_{\hat{\Omega}_c} \tilde{\mathbf{N}}_m^c \\ -\tilde{\mathbf{M}}_{1/\mu_0} \tilde{\mathbf{G}}_{\hat{\Omega}_m} \mathbf{N}_c^m & \tilde{\mathbf{R}}_m + i\omega \tilde{\mathbf{L}}_m^m + \frac{1}{i\omega} \mathbf{G}_{\hat{\Omega}_m}^a \tilde{\mathbf{P}}_m \tilde{\mathbf{C}}_{\hat{\Omega}_m} \end{bmatrix} \begin{bmatrix} \mathbf{j}_c \\ \tilde{\mathbf{j}}_m \end{bmatrix} = \begin{bmatrix} \tilde{\mathbf{e}}_0 \\ \mathbf{h}_0 \end{bmatrix}. \tag{B.82}$$

From the physical point of view, the matrix blocks $(1,2)$ and $(2,1)$ should satisfy

$$\mathbf{M}_{1/\varepsilon_0} \mathbf{C}_{\hat{\Omega}_c} \tilde{\mathbf{N}}_m^c = -(-\tilde{\mathbf{M}}_{1/\mu_0} \tilde{\mathbf{G}}_{\hat{\Omega}_m} \mathbf{N}_c^m)^T. \tag{B.83}$$

However, since $\tilde{\mathbf{N}}_m^c$ and $\mathbf{N}_c^m$ are only *numerical approximations* of integral discrete operators, this property is numerically lost. However, property (B.83) can be enforced resulting in a more accurate method which strongly satisfies the physical properties of the electromagnetic fields. Moreover, by substituting the matrix block $(1,2)$ with $-(2,1)^T$, matrices $\tilde{\mathbf{M}}_{1/\mu_0}$ and $\mathbf{N}_c^m$ are not needed anymore (or vice–versa). Thus, multiplying the second row of (B.82) by -1, the system can be made symmetric.

Finally, as more deeply discussed in Section 3.3.1, when homogeneous magnetic media are considered $\nabla \cdot \mathbf{J}_m = 0$ (thus $\varrho_m = 0$). This property is enforced by (B.82) but not in a numerically strong sense. However, the vanishing of the volume magnetic charges can be strongly enforced by imposing

$$\tilde{\mathbf{j}}_m = \tilde{\mathbf{G}}_{\hat{\Omega}_m} \tilde{\mathbf{x}}_m, \tag{B.84}$$

where $\tilde{\mathbf{x}}_m$ is the array of DoFs related to a discrete vector potential associated to the dual nodes $\tilde{n}_m$ (3–D edges $\tilde{n}_m^{3D}$) of $\tilde{\mathcal{G}}_{\hat{\Omega}_m}$, (except one considered as reference). Then, (B.84) is applied to (B.82) and $\tilde{\mathbf{G}}_{\hat{\Omega}_m}$ (without one column for each magnetic sub–domain) is used to project the second matrix row of (B.82) into a new set of equations. The resulting system has a reduced dimension and it strongly enforces $\tilde{\mathbf{C}}_{\hat{\Omega}_m} \tilde{\mathbf{j}}_m = 0$ (i.e. $\tilde{\mathbf{q}}_m^v = \mathbf{0}$ and $\nabla \cdot \mathbf{J}_m = 0$). Moreover, matrices $\tilde{\mathbf{P}}_m^{vv}$, $\tilde{\mathbf{P}}_m^{vs}$, and $\tilde{\mathbf{P}}_m^{sv}$ are not needed anymore.

The system (B.82) derived from the C–formulation does not suffer from the numerical issue

discussed for system (B.41) derived from the A–formulation. Moreover, when the frequency is not very high, the effects related to matrix $\tilde{\mathbf{L}}_m^m$ are negligible. Thus, system (B.82) can be further simplified by neglecting the presence of the term $i\omega\tilde{\mathbf{L}}_m^m$ in the matrix block $(2,2)$.

B.3 Comparison between A– and C– formulations

The method proposed in section B.1 is based on the amperian interpretation of the magnetization phenomena. When this approach is adopted, the inductance matrices are the only full *integral matrices* to be evaluated, resulting in a relatively easy implementation. Moreover, several analytical expressions for the self and mutual inductances of loops with rectangular cross section exist [177, 183]. Thus, all the inductance matrices can be efficiently evaluated using analytical formulas.

As already stated, the main drawback of this method consists in a poor numerical performance when magnetic media with relative high permeability are involved. Especially when they have a non–zero conductivity or when they are very close to conductive media. This problem is alleviated when (B.42) is enforced. However this is only possible when non–conductive magnetic media are considered.

The effort required by the implementation of the *Coulombian* method described in section B.2 is slightly more expensive since different integral matrices must be evaluated and matrix $\mathbf{L}_m^m$ does not allow for an easy analytical evaluation. Moreover, when properties (B.42) and (B.84) are enforced, the amperian approach leads to a magnetic matrix equation with a lower sparsity ratio ($\sim n_m^b/n_m$) while the magnetic equation of (B.82) remains full. However, system (B.82) does not suffer from the numerical issue described above for conductive magnetic media with high permeability. Moreover, when the frequency is sufficiently low, $\mathbf{L}_m^m \approx 0$. Thus, system (B.82) can be further simplified by neglecting the presence of the term $i\omega\mathbf{L}_m^m$ in the matrix block $(2,2)$, which leads to a relatively sparse magnetic equation when property (B.84) is enforced (sparsity ratio $\sim n_m^b/n_m$).

B.4 Low–rank compression techniques

Both systems (B.41) and (B.82) are suitable for the application of low–rank approximation techniques, allowing a drastic reduction of the storage and the computational cost arising from the handling of full matrices. In the numerical studies presented in Section 5.4, the low–rank approximation techniques implemented in HLIBPro library have been applied to both the proposed methods.

HLIBPro relies on the hierarchical ($\mathcal{H}$)-matrix representation coupled with adaptive cross approximation. Such library also provides a partitioning algorithm, based on geometric bisection, which splits the DoFs into disjoint clusters and builds a binary tree which terminates as soon as a prescribed condition is reached. However, in order to obtain matrix blocks which are actually low–rank (see Section 5.3 for a more detailed discussion), it is important to force the first clustering partition of the unknowns. Thus, when (B.41) (or (B.82)) is solved, $\mathbf{j}_c$ and $\mathbf{m}$ (or $\mathbf{j}_c$ and $\mathbf{j}_m$) must be subdivided into two different clusters, and $\mathbf{m}$ (or $\mathbf{j}_m$) should be further subdivided into *boundary* and *internal* unknowns. Then, as described in Section 5.2.1, the partitioning algorithm proceeds with the construction of the cluster tree starting from these three master cluster nodes. A completely equivalent discussion holds for $\boldsymbol{\psi}_m$ (or $\mathbf{t}_m$) when

(B.42) (or (B.84)) is enforced. When these measures are embraced, thanks to the smoothness of the Green's kernel, very low compression ratios can be reached (e.g. less than 3%, as shown in the numerical studies).

Finally, it is worth noting that both (B.41) and (B.82) can be adopted for the solution of steady state problems: (B.41) can be directly solved when $\omega = 0$ while (B.82) only requires a scaling of the unknowns $\mathbf{j}_m$ by $i\omega$.

Appendix C

Publications

C.1 Published and/or presented

- V. Cirimele, R. Torchio, A. Virgillito, F. Freschi, P. Alotto,

  "Challenges in the Electromagnetic Modeling of Road Embedded Wireless Power Transfer,"

  in **Energies**, vol. 14, no. 12, July 2019.

  doi: 10.3390/en12142677

  URL: https://www.mdpi.com/1996-1073/12/14/2677

- R. Torchio,

  "A Volume PEEC Formulation Based on the Cell Method for Electromagnetic Problems from Low to High Frequency,"

  in **IEEE Transactions on Antennas and Propagation**, July 2019, (In initial production stage with IEEE Publishing Operations).

  doi: 10.1109/TAP.2019.2927789

  URL: -

- S. R. Moreno, C. E. Klein, V. C. Mariani, L. dos S. Coelho, P. Alotto, R. Torchio, T. Bauernfeind, P. Baumgartner,

  "Non-uniformly spaced linear antenna array design by means of PEEC approach applying Cheetah optimization algorithm,"

  in **International Journal of Applied Electromagnetics and Mechanics**, vol. 60, no. S1, pp. S15-S24, 2019

  doi: 10.3233/JAE-191102

  URL: https://content.iospress.com/articles/international-journal-of-applied-electromagnetics-and-mechanics/jae191102

- R. Torchio, L. Di Rienzo, L. Codecasa,

  "Stochastic PEEC Method Based on Polynomial Chaos Expansion,"

  in **IEEE Transactions on Magnetics**, vol. 55, no. 6, pp. 1-4, June 2019.

  doi: 10.1109/TMAG.2019.2908588

  URL: http://ieeexplore.ieee.org/stamp/stamp.jsp?tp=&arnumber=8699116&isnumber=8716604

- D. Voltolina, P. Bettini, P. Alotto, F. Moro, R. Torchio,

  "High-Performance PEEC Analysis of Electromagnetic Scatterers,"

  in **IEEE Transactions on Magnetics**, vol. 53, no. 6, pp. 1-4, June 2019.

  doi: 10.1109/TMAG.2019.2894618

  URL: http://ieeexplore.ieee.org/stamp/stamp.jsp?tp=&arnumber=8638854&isnumber=8716604

- R. Torchio, F. Moro, G. Meunier, J.-M. Guichon, O. Chadebec,

  "An Extension of Unstructured-PEEC Method to Magnetic Media,"

  in **IEEE Transactions on Magnetics**, vol. 53, no. 6, pp. 1-4, June 2019.

  doi: 10.1109/TMAG.2018.2889435

  URL: https://ieeexplore.ieee.org/document/8613806/authors#authors

- R. Torchio, P. Alotto, P. Bettini, D. Voltolina, F. Moro,

  "A 3-D PEEC Formulation Based on the Cell Method for Full-Wave Analyses With Conductive, Dielectric, and Magnetic Media,"

  in **IEEE Transactions on Magnetics**, vol. 54, no. 3, pp. 1-4, 2018.

  doi: 10.1109/TMAG.2017.2750319

  URL: http://ieeexplore.ieee.org/stamp/stamp.jsp?tp=&arnumber=8168416&isnumber=4479871

- R. Torchio, P. Bettini, P. Alotto,

  "PEEC-Based Analysis of Complex Fusion Magnets During Fast Voltage Transients With H-Matrix Compression,"

  in **IEEE Transactions on Magnetics**, vol. 53, no. 6, pp. 1-4, June 2017.

  doi: 10.1109/TMAG.2017.2651638

  URL: http://ieeexplore.ieee.org/stamp/stamp.jsp?tp=&arnumber=7814211&isnumber=7934107

- P. Baumgartner, T. Bauernfeind, O. Bíró, A. Hackl, C. Magele, W. Renhart, R. Torchio,

  "Multi-Objective Optimization of Yagi-Uda Antenna Applying Enhanced Firefly Algorithm With Adaptive Cost Function,"

  in **IEEE Transactions on Magnetics**, vol. 54, no. 3, pp. 1-4, 2018.

  doi: 10.1109/TMAG.2017.2764319

  URL: http://ieeexplore.ieee.org/stamp/stamp.jsp?tp=&arnumber=8168407&isnumber=4479871

- T. Bauernfeind, P. Baumgartner, O. Bíró, A. Hackl, C. Magele, W. Renhart, R. Torchio,

  "Multi-Objective Synthesis of NFC-Transponder Systems Based on PEEC Method,"

  in **IEEE Transactions on Magnetics**, vol. 54, no. 3, pp. 1-4, 2018.

  doi: 10.1109/TMAG.2017.2771366

  URL: http://ieeexplore.ieee.org/stamp/stamp.jsp?tp=&arnumber=8125565&isnumber=4479871

- T. Bauernfeind, P. Baumgartner, O. Bíró, C. A. Magele, K. Preis, R. Torchio,

  "PEEC-Based Multi-Objective Synthesis of Non-Uniformly Spaced Linear Antenna Arrays,"

  in **IEEE Transactions on Magnetics**, vol. 53, no. 6, pp. 1-4, June 2017.

  doi: 10.1109/TMAG.2017.2670679

  URL: http://ieeexplore.ieee.org/stamp/stamp.jsp?tp=&arnumber=7858629&isnumber=7934107

- P. Baumgartner, T. Bauernfeind, W. Renhart, O. Bíró, R. Torchio,

  "Limitations of the pattern multiplication technique for uniformly spaced linear antenna arrays,"

  2016 International Conference on Broadband Communications for Next Generation Networks and Multimedia Applications (CoBCom), Graz, 2016, pp. 1-7.

  doi: 10.1109/COBCOM.2016.7593492

  URL: http://ieeexplore.ieee.org/stamp/stamp.jsp?tp=&arnumber=7593492&isnumber=7593486

- R. Torchio, P. Alotto, P. Bettini, D. Voltolina, F. Moro,

  "A DC to HF volume PEEC formulation based on hertz potentials and the cell method,"

  2018 International Applied Computational Electromagnetics Society Symposium (ACES), Denver, CO, 2018, pp. 1-2.

  doi: 10.23919/ROPACES.2018.8364123

  URL: http://ieeexplore.ieee.org/stamp/stamp.jsp?tp=&arnumber=8364123&isnumber=8364084

- P. Baumgartner, T. Bauernfeind, O. Biro, C. Magele, W. Renhart, R. Torchio,

  "Synthesis of NFC antenna structure under multi-card condition,"

  2018 International Applied Computational Electromagnetics Society Symposium (ACES), Denver, CO, 2018, pp. 1-2.

  doi: 10.23919/ROPACES.2018.8364095

  URL: http://ieeexplore.ieee.org/stamp/stamp.jsp?tp=&arnumber=8364095&isnumber=8364084

- T. Bauernfeind, P. Baumgartner, O. Biro, C. Magele, W. Renhart, R. Torchio,

  "PEEC-based multi-objective synthesis of NFC antennas in the presence of conductive structures,"

  2018 International Applied Computational Electromagnetics Society Symposium (ACES), Denver, CO, 2018, pp. 1-2.

  doi: 10.23919/ROPACES.2018.8364094

  URL: http://ieeexplore.ieee.org/stamp/stamp.jsp?tp=&arnumber=8364094&isnumber=8364084

- R. Torchio, L. Codecasa, L. Di Rienzo, F Moro,

  "Fast stochastic volume integral equation method for uncertainty quantification in electromagnetic problems,"

  in **IEEE Access**, in publishing.

  doi: 10.1109/ACCESS.2019.2952723

  URL: -

- R. Torchio, D. Voltolina, F. Moro, P. Alotto, P. Bettini, G. Meunier, J.-M. Guichon, O. Chadebec

  "Volume Integral Equation Methods for Axisymmetric Problems with Conductive and Magnetic Media,"

  in **IEEE Transactions on Magnetics**, in publishing

  doi: 10.1109/TMAG.2019.2947394

  URL: -

- V. Voltolina, R. Torchio, P. Bettini, P. Alotto, R. Cavazzana, M. Moresco

  "PEEC modeling of planar spiral resonators,"

  in **IEEE Transactions on Magnetics**, in publishing

  doi: 10.1109/TMAG.2019.2949481

  URL: -

C.2 Submitted

- R. Torchio, D. Voltolina, P. Alotto, P. Bettini, F. Moro,

  "Marching On–In–Time Unstructured–PEEC for Conductive, Dielectric, and Magnetic Media,"

  in IEEE Transactions on Magnetics,

- R. Torchio, V. Cirimele, P. Alotto, F. Freschi,

  "Modelling of Road–Embedded Transmitting Coils for Wireless Power Transfer,"

  in IEEE Transactions on Magnetics,

Appendix D

Riassunto

L'obiettivo principale di questa tesi è di estendere e migliorare l'applicabilità e l'accuratezza del metodo Partial Element Equivalent Circuit (PEEC) non strutturato (Unstructured PEEC). L'interesse riguardo tale argomento è stimolato dalla crescente necessità di metodi numerici rapidi ed efficienti, che possono aiutare gli ingegneri durante la progettazione e altre fasi della produzione di componenti elettrici ed elettronici di nuova generazione. Durante la prima fase della tesi, il metodo PEEC (nella sua forma non strutturata) è esteso ai mezzi magnetici. A questo proposito, vengono sviluppate e confrontate due formulazioni: la prima, basata sull'interpretazione amperiana dei fenomeni di magnetizzazione, deriva dalla letteratura esistente relativa alla versione standard (strutturata) del metodo PEEC; il secondo, basato sull'interpretazione coulombiana dei fenomeni di magnetizzazione, è proposto dall'autore con l'obiettivo di collocare il metodo PEEC nel contesto dei metodi di integrali di volume (Volume Integral Equation). Successivamente, la ricerca si focalizza sull'utilizzo di tecniche di compressione a basso rango al fine di risolvere problemi PEEC in maniera computazionalmente efficiente, salvaguardando tempo e memoria di calcolo. A tal proposito, vengono applicati due metodi diversi: il primo si basa su matrici gerarchiche (matrici $\mathcal{H}$ e $\mathcal{H}^2$) mentre il secondo si basa su matrici gerarchiche-semi-separabili (HSS). I due metodi vengono confrontati e vengono analizzati i principali problemi numerici che emergono applicando tali tecniche di compressione a basso rango al metodo PEEC. In seguito, il metodo PEEC non strutturato viene combinato con l'approccio Marching On-In Time (MOT) per lo studio di fenomeni transitori rapidi con un ricco contenuto armonico. Infine, sono stati sviluppati due diversi metodi PEEC stocastici per la quantificazione dell'incertezza. Il primo si basa sull'espansione Polynomial Chaos, mentre il secondo si basa sulla tecnica di riduzione d'ordine parametrica (Parametric Model Order Reduction) unita all'espansione spettrale.

Appendix E

Résumé

L'objectif principal de cette thèse est d'étendre et d'améliorer la précision de la méthode des circuits équivalents à éléments partiels non structurés (Unstructured PEEC). L'intérêt pour ce sujet est stimulé par le besoin croissant de méthodes numériques rapides et efficaces, qui peuvent aider les ingénieurs pendant la conception et les autres phases de la production de composants électriques et électroniques de nouvelle génération. Dans un premier temps, la méthode PEEC sous sa forme non structurée est étendue aux supports magnétiques. Deux formulations sont développées et comparées: la première, basée sur l'interprétation ampérienne des phénomènes d'aimantation, provient de la littérature relative à la version standard (structurée) de la méthode PEEC. La seconde, basée sur l'interprétation Coulombienne des phénomènes d'aimantation, est proposée par l'auteur dans le but de recentrer la méthode PEEC dans le contexte des méthodes d'intégrale de volume (Volume Integral Equation). Dans un deuxième temps, les travaux portent sur l'utilisation de techniques de compression de bas rang afin de résoudre efficacement les problèmes de PEEC et de préserver le temps et la mémoire de calcul. Deux méthodes différentes sont appliquées: la première est basée sur des matrices hiérarchiques (matrices $\mathcal{H}$ et $\mathcal{H}^2$), tandis que la seconde repose sur des matrices hiérarchiques semi-séparables (HSS). Les deux méthodes sont comparées et les principaux problèmes numériques qui se posent en appliquant ces techniques de compression de bas rang à la méthode PEEC sont analysés. La méthode PEEC non structurée est ensuite combinée à l'approche Marching On-In Time (MOT) pour l'étude des phénomènes transitoires rapides avec un contenu harmonique riche. Enfin, deux méthodes PEEC stochastiques différentes ont été développées pour la quantification des incertitudes. La première est basée sur l'expansion Polynomial Chaos, tandis que la seconde repose sur la technique de réduction de l'ordre du modèle paramétrique (Parametric Model Order Reduction) combinée à une expansion spectrale.

Bibliography

[1] I. A. Shah and H. Yoo. "Assessing Human Exposure With Medical Implants to Electromagnetic Fields From a Wireless Power Transmission System in an Electric Vehicle". In: *IEEE Transactions on Electromagnetic Compatibility* (2019), pp. 1–8. DOI: 10.1109/TEMC.2019.2903844.

[2] Y. Lembeye, P. Goubier, and J.-P. Ferrieux. "Integrated planar L-C-T component: Design,Characterization and Experimental Efficiency analysis". In: *IEEE Transactions on Power Electronics* 20.3 (2005), pp. 593–599. DOI: 10.1109/TPEL.2005.846558.

[3] G. Meunier. *The Finite Element Method for Electromagnetic Modeling*. ISBN: 9781848210301. DOI: 10.1002/9780470611173.

[4] P. Yla-Oijala et al. "Surface and Volume Integral Equation Methods for Time-Harmonic Solutions of Maxwell's Equations". In: *Progress In Electromagnetics Research* 149 (2014), pp. 15–44. DOI: 10.2528/PIER14070105.

[5] P. K. Banerjee and R. Butterfield. *Boundary element methods in engineering science*. McGraw-Hill Book Co. (UK), 1981. ISBN: 9780070841208. DOI: 10.1002/nag.1610070213.

[6] J. Siau. "Unstructured PEEC formulations considering resistive, inductive and capacitive effects for power electronics". Theses. Université Grenoble Alpes, Dec. 2016.

[7] M. Bebendorf. *Hierarchical Matrices: A Means to Efficiently Solve Elliptic Boundary Value Problems*. Springer, 2008. ISBN: 9783540771470. DOI: 10.1007/978-3-540-77147-0.

[8] W. C. Chew. *Fast and efficient algorithms in computational electromagnetics*. Boston: Artech House, 2001. Print, 2001.

[9] G. Antonini. "Fast multipole method for time domain PEEC analysis". In: *IEEE Transactions on Mobile Computing* 2.4 (2003), pp. 275–287. DOI: 10.1109/TMC.2003.1255643.

[10] Z. Kezhong, M. N. Vouvakis, and L. Jin-Fa. "The adaptive cross approximation algorithm for accelerated method of moments computations of EMC problems". In: *IEEE Transactions on Electromagnetic Compatibility* 47.4 (2005), pp. 763–773. DOI: 10.1109/TEMC.2005.857898.

[11] D. Cai et al. "SMASH: Structured matrix approximation by separation and hierarchy". In: *Numerical Lin. Alg. with Applic.* 25 (2018). DOI: 10.1002/nla.2204.

[12] A. E. Ruehli. "Equivalent Circuit Models for Three-Dimensional Multiconductor Systems". In: *IEEE Transactions on Microwave Theory and Techniques* 22.3 (1974), pp. 216–221. DOI: 10.1109/TMTT.1974.1128204.

[13] A. E. Ruehli, G. Antonini, and L. Jiang. *Circuit Oriented Electromagnetic Modeling Using the Peec Techniques*. John Wiley & Sons, Inc., 2017. DOI: 10.1002/9781119078388.

[14] A. E. Ruehli and H. Heeb. "Circuit models for three-dimensional geometries including dielectrics". In: *IEEE Transactions on Microwave Theory and Techniques* 40.7 (1992), pp. 1507–1516. DOI: 10.1109/22.146332.

[15] H. Heeb, S. Ponnapalli, and A. E. Ruehli. "Frequency Domain Microwave Modeling Using Retarded Partial Element Equivalent Circuits". In: *30th ACM/IEEE Design Automation Conference* (1993), pp. 702–706. DOI: 10.1145/157485.165097.

[16] A. Ruehli, J. Garrett, and C. Paul. "Circuit models for 3D structures with incident fields". In: *1993 International Symposium on Electromagnetic Compatibility* (1993), pp. 28–32. DOI: 10.1109/ISEMC.1993.473786.

[17] D. Romano and G. Antonini. "Augmented Quasi-Static Partial Element Equivalent Circuit Models for Transient Analysis of Lossy and Dispersive Magnetic Materials". In: *IEEE Transactions on Magnetics* 52.5 (2016), pp. 1–11. DOI: 10.1109/TMAG.2015.2507998.

[18] S. Safavi and J. Ekman. "Feasibility analysis of specialized PEEC solvers in comparison to SPICE-like solvers". In: *Journal of Computational Electronics* 11.4 (2012), pp. 440–452. DOI: 10.1007/s10825-012-0425-8.

[19] R. Torchio, P. Bettini, and P. Alotto. "PEEC-Based Analysis of Complex Fusion Magnets During Fast Voltage Transients With H-Matrix Compression". In: *IEEE Transactions on Magnetics* 53.6 (2017), pp. 1–4. DOI: 10.1109/TMAG.2017.2651638.

[20] R. Torchio. "A Volume PEEC Formulation Based on the Cell Method for Electromagnetic Problems from Low to High Frequency". In: *IEEE Transactions on Antennas and Propagation* 67 (2019), pp. 703–723. DOI: 10.1109/TAP.2019.2927789.

[21] F. Freschi and M. Repetto. "A general framework for mixed structured/unstructured PEEC modelling". In: *Applied Computational Electromagnetics Society Journal* 23.3 (2008), pp. 200–206.

[22] P. Alotto et al. *The Cell Method for Electrical Engineering and Multiphysics Problems: An Introduction*. Springer Berlin Heidelberg, 2013. ISBN: 9783642361012.

[23] J. Siau et al. "Volume Integral Formulation Using Face Elements for Electromagnetic Problem Considering Conductors and Dielectrics". In: *IEEE Transactions on Electromagnetic Compatibility* 58.5 (2016), pp. 1587–1594. DOI: 10.1109/temc.2016.2559801.

[24] P. Alotto et al. "Dual-PEEC Modeling of a Two-Port TEM Cell for VHF Applications". In: *IEEE Transactions on Magnetics* 47.5 (2011), pp. 1486–1489. DOI: 10.1109/tmag.2010.2088381.

[25] G. Antonini, M. Sabatini, and G. Miscione. "PEEC". In: *2006 IEEE International Symposium on Electromagnetic Compatibility, 2006. EMC 2006.* ().

[26] R. Torchio et al. "A 3-D PEEC Formulation Based on the Cell Method for Full-Wave Analyses With Conductive, Dielectric, and Magnetic Media". In: *IEEE Transactions on Magnetics* PP.99 (2017), pp. 1–4. DOI: 10.1109/TMAG.2017.2750319.

[27] R. Torchio et al. "An Extension of Unstructured-PEEC Method to Magnetic Media". In: *IEEE Transactions on Magnetics* 55.6 (2019), pp. 1–4. DOI: 10.1109/TMAG.2018.2889435.

[28] S. A. Schelkunoff. *Electromagnetic Fields*. Blaisdell Publishing Company, 1963.

[29] Y. Xiaoyan et al. "A New Efie Method Based on Coulomb Gauge for the Low-frequency Electromagnetic Analysis". In: (2013). DOI: 10.2528/PIER13040303.

[30] J. A. Stratton. *Electromagnetic Theory*. John Wiley & Sons, Inc., 2015. DOI: 10.1002/9781119134640.

[31] J. G. Van Bladel. *Electromagnetic Fields*. John Wiley & Sons, 2007. ISBN: 9780471263883.

[32] A. Hartman et al. "A descriptor form implementation of PEEC models incorporating dispersive and lossy dielectrics". In: *2016 IEEE International Symposium on Electromagnetic Compatibility (EMC)* (2016), pp. 206–211. DOI: 10.1109/ISEMC.2016.7571645.

[33] D. Romano and G. Antonini. "Quasi-Static Partial Element Equivalent Circuit Models of Linear Magnetic Materials". In: *IEEE Transactions on Magnetics* 51.7 (2015), pp. 1–15. DOI: 10.1109/TMAG.2014.2385662.

[34] G. Antonini, M. Sabatini, and G. Miscione. "PEEC modeling of linear magnetic materials". In: *2006 IEEE International Symposium on Electromagnetic Compatibility, 2006. EMC 2006.* 1 (2006), pp. 93–98. DOI: 10.1109/ISEMC.2006.1706270.

[35] H. Long et al. "A novel accurate PEEC-based 3D modeling technique for RF devices of arbitrary conductor-magnet structure". In: *Microw. Opt. Technol* (). DOI: 0.1002/mop.11025.

[36] T. Le-Duc et al. "Coupling between PEEC and magnetic moment method". In: *COMPEL - The international journal for computation and mathematics in electrical and electronic engineering* 32.1 (2012), pp. 383–395. DOI: https://doi.org/10.1108/03321641311293948.

[37] R. F. Harrington. *Field Computation by Moment Methods*. Wiley-IEEE Press, 1993. ISBN: 0780310144.

[38] I. F. Kovačević et al. "Full PEEC Modeling of EMI Filter Inductors in the Frequency Domain". In: *IEEE Transactions on Magnetics* 49.10 (2013), pp. 5248–5256. DOI: 10.1109/TMAG.2013.2260344.

[39] R. M. Fano, L. J. Chu, and R. B. Adler. *Electromagnetic fields, energy, and forces*. Wiley, 1960. ISBN: 0262561700.

[40] R. Torchio et al. "A DC to HF Volume PEEC Formulation Based on Hertz Potentials and the Cell Method". In: *ACES Conference* (2018). DOI: 10.23919/ROPACES.

[41] G. Meunier, O. Chadebec, and J. M. Guichon. "A Magnetic-Electric Current Volume Integral Formulation Based on Facet Elements for Solving Electromagnetic Problems". In: *IEEE Transactions on Magnetics* 51.3 (2015), pp. 1–4. DOI: 10.1109/TMAG.2014.2365500.

[42] A. G. Polimeridis et al. "On the Computation of Power in Volume Integral Equation Formulations". In: *IEEE Transactions on Antennas and Propagation* 63.2 (2015), pp. 611–620. DOI: 10.1109/TAP.2014.2382636.

[43] A. Nisbet. "Hertzian electromagnetic potentials and associated gauge transformations". In: *Proceedings of the Royal Society of London A: Mathematical, Physical and Engineering Sciences* 231.1185 (1955), pp. 250–263. DOI: 10.1098/rspa.1955.0170.

[44] R. P. Feynman, R. B. Leighton, and M. L. Sands. *The Feynman Lectures on Physics*. v. 2. Pearson/Addison-Wesley, 1963. ISBN: 9780805390476.

[45] G. Antonini, A. E. Ruehli, and J. Esch. "Nonorthogonal PEEC formulation for time and frequency domain modeling". In: *2002 IEEE International Symposium on Electromagnetic Compatibility* 1 (2002), 452–456 vol.1. DOI: 10.1109/ISEMC.2002.1032521.

[46] J. Ekman. "Electromagnetic Modeling Using the Partial Element Equivalent Circuit Method". PhD thesis. 2003.

[47] A. E. Ruehli. "Inductance Calculations in a Complex Integrated Circuit Environment". In: *IBM Journal of Research and Development* 16.5 (1972), pp. 470–481. DOI: 10.1147/rd.165.0470.

[48] D. Romano and G. Antonini. "Quasi-static partial element equivalent circuit models of magneto-dielectric materials". In: *IET Microwaves, Antennas Propagation* 11.6 (2017), pp. 915–922. DOI: 10.1049/iet-map.2016.0534.

[49] D. Romano, G. Antonini, and A. E. Ruehli. "Time-domain partial element equivalent circuit solver including non-linear magnetic materials". In: *2015 IEEE MTT-S International Conference on Numerical Electromagnetic and Multiphysics Modeling and Optimization (NEMO)* (2015), pp. 1–3. DOI: 10.1109/NEMO.2015.7415058.

[50] C. J. Carpenter. "Finite-element network models and their application to eddy-current problems". In: *Proceedings of the Institution of Electrical Engineers* 122.4 (1975), pp. 455–462. DOI: 10.1049/piee.1975.0125.

[51] L. Codecasa. "Refoundation of the Cell Method Using Augmented Dual Grids". In: *IEEE Transactions on Magnetics* 50.2 (2014), pp. 497–500. DOI: 10.1109/TMAG.2013.2280504.

[52] P. Dular, R. Specogna, and F. Trevisan. "Constitutive matrices using hexahedra in a discrete approach for eddy currents". In: *2006 12th Biennial IEEE Conference on Electromagnetic Field Computation* (2006), pp. 185–185. DOI: 10.1109/CEFC-06.2006.1632977.

[53] A. Bossavit. *Computational Electromagnetisms*. BAcademic Press, 1998.

[54] G. Meunier, O. Chadebec, and J. Guichon. "A Magnetic Flux–Electric Current Volume Integral Formulation Based on Facet Elements for Solving Electromagnetic Problems". In: *IEEE Transactions on Magnetics* 51.3 (2015), pp. 1–4. DOI: 10.1109/TMAG.2014.2365500.

[55] L. Codecasa, R. Specogna, and F. Trevisan. "Geometrically defined basis functions for polyhedral elements with applications to computational electromagnetics". In: *ESAIM: M2AN* 50.3 (2016), pp. 677–69. DOI: 10.1051/m2an/2015077.

[56] "A new set of basis functions for the discrete geometric approach". In: *Journal of Computational Physics* 229.19 (2010), pp. 7401 –7410. DOI: https://doi.org/10.1016/j.jcp.2010.06.023.

[57] L. Codecasa, R. Specogna, and F. Trevisan. "Base functions and discrete constitutive relations for staggered polyhedral grids". In: *Computer Methods in Applied Mechanics and Engineering* 198.9 (2009), pp. 1117 –1123. DOI: https://doi.org/10.1016/j.cma.2008.11.021.

[58] E. Tonti. *The Mathematical Structure of Classical and Relativistic Physics*. Birkhäuser, 2013. DOI: 978-1-4614-7422-7.

[59] A. Bossavit. "Generalized Finite Differences' in Computational Electromagnetics". In: *Progress In Electromagnetics Research* 32 (2001), pp. 45–64. DOI: 10.2528/PIER00080102.

[60] S. Järbenpää, M. Taskinen, and P. Ylä-Oijala. "Singularity extraction technique for integral equation methods with larger order basis functions on plane triangles and tetrahedra". In: *International Journal for Numerical Methods in Engineering* 58 (2003), pp. 1149–1165. DOI: 10.1002/nme.810.

[61] M. Fabbri. "Magnetic Flux Density and Vector Potential of Uniform Polyhedral Sources". In: *IEEE Transactions on Magnetics* 44.1 (2008), pp. 32–36. DOI: 10.1109/tmag.2007.2088381.

[62] P. Arcioni, M. Bressan, and L. Perregrini. "On the evaluation of the double surface integrals arising in the application of the boundary integral method to 3-D problems". In: *IEEE Transactions on Microwave Theory and Techniques* 45.3 (1997), pp. 436–439. DOI: 10.1109/22.563344.

[63] D. Sievers, T. F. Eibert, and V. Hansen. "Correction to "On the Calculation of Potential Integrals for Linear Source Distributions on Triangular Domains"". In: *IEEE Transactions on Antennas and Propagation* 53.9 (2005), pp. 3113–3113. DOI: 10.1109/TAP.2005.854549.

[64] R. D. Graglia. "On the numerical integration of the linear shape functions times the 3-D Green's function or its gradient on a plane triangle". In: *IEEE Transactions on Antennas and Propagation* 41.10 (1993), pp. 1448–1455. DOI: 10.1109/8.247786.

[65] M. S. Tong and W. C. Chew. "A Novel Approach for Evaluating Hypersingular and Strongly Singular Surface Integrals in Electromagnetics". In: *IEEE Transactions on Antennas and Propagation* 58.11 (2010), pp. 3593–3601. DOI: 10.1109/TAP.2010.2071370.

[66] R. Hospital-Bravo, J. Sarrate, and P. Díez. "A semi-analytical scheme for highly oscillatory integrals over tetrahedra". In: *International Journal for Numerical Methods in Engineering* 111 (2017), pp. 703–723. DOI: 10.1002/nme.5474.

[67] M. Taskinen. "On the fully analytical integration of singular double integrals arising from the integral equation methods". In: *Computational Electromagnetics International Workshop (CEM), 2011* (2011), pp. 13–18. DOI: 10.1109/CEM.2011.6047319.

[68] L. Blattner Martinho et al. "Generalized PEEC Analysis of Inductive Coupling Phenomena in a Transmission Line Right-of-Way". In: *IEEE Transactions on Magnetics* 52.3 (2016), pp. 1–4. DOI: 10.1109/TMAG.2015.2470249.

[69] S. Omar and D. Jiao. "A New Volume Integral Formulation for Broadband 3-D Circuit Extraction in Inhomogeneous Materials With and Without External Electromagnetic Fields". In: *IEEE Transactions on Microwave Theory and Techniques* 61.12 (2013), pp. 4302–4312. DOI: 10.1109/TMTT.2013.2285355.

[70] M. E. Verbeek. "Partial element equivalent circuit(PEEC) models for on-chip passives and interconnects". In: *International Journal of Numerical Modelling: Electronic Networks, Devices and Fields* 17.1 (2004), pp. 61–84. DOI: 10.1002/jnm.524.

[71] A. E. Seaver. "Some Comments on the Charge Decay Paradox in Metals," in: *Proc. ESA Annual Meeting on Electrostatics* Paper D4 (2008).

[72] W. C. Chew. *Waves and Fields in Inhomogenous Media*. Wiley-IEEE Press, 1995.

[73] D. Schaubert, D. Wilton, and A. Glisson. "A tetrahedral modeling method for electromagnetic scattering by arbitrarily shaped inhomogeneous dielectric bodies". In: *IEEE Transactions on Antennas and Propagation* 32.1 (1984), pp. 77–85. DOI: 10.1109/TAP.1984.1143193.

[74] M. Bandinelli et al. "A Surface PEEC Formulation for High-Fidelity Analysis of the Current Return Networks in Composite Aircrafts". In: *IEEE Transactions on Electromagnetic Compatibility* 57.5 (2015), pp. 1027–1036. DOI: 10.1109/TEMC.2015.2422672.

[75] D. Romano and G. Antonini. "Partial Element Equivalent Circuit-Based Transient Analysis of Graphene-Based Interconnects". In: *IEEE Transactions on Electromagnetic Compatibility* 58.3 (2016), pp. 801–810. DOI: 10.1109/TEMC.2016.2533918.

[76] Z. De Grève et al. "A Mixed Surface Volume Integral Formulation for the Modeling of High-Frequency Coreless Inductors". In: *IEEE Transactions on Magnetics* 52.3 (2016), pp. 1–4. DOI: 10.1109/TMAG.2015.2497004.

[77] D. Voltolina et al. "High-Performance PEEC Analysis of Electromagnetic Scatterers". In: *IEEE Transactions on Magnetics* 55.6 (2019), pp. 1–4. DOI: 10.1109/TMAG.2019.2894618.

[78] S. Barmada et al. "The Use Of Surface Impedance Boundary Conditions In Time Domain Problems: Numerical And Experimental Validation". In: *ACES Journal* (2004).

[79] S. Yuferev and L. Di Rienzo. "Surface Impedance Boundary Conditions in Terms of Various Formalisms". In: *IEEE Transactions on Magnetics* 46.9 (2010), pp. 3617–3628. DOI: 10.1109/TMAG.2010.2049363.

[80] I. O. Sukharevsky and A. Altintas. "Validation of Higher-Order Approximations and Boundary Conditions for Lossy Conducting Bodies". In: *IEEE Transactions on Antennas and Propagation* 62.9 (2014), pp. 4656–4663. DOI: 10.1109/TAP.2014.2331991.

[81] L. Giussani et al. "An Integral Formulation for an Array of Wires in a 3-D Magneto-Quasi-Static Field". In: *IEEE Transactions on Magnetics* 54.7 (2018), pp. 1–8. DOI: 10.1109/TMAG.2018.2834883.

[82] T. Bauernfeind et al. "PEEC-Based Multi-Objective Synthesis of Non-Uniformly Spaced Linear Antenna Arrays". In: *IEEE Transactions on Magnetics* 53.6 (2017), pp. 1–4. DOI: 10.1109/TMAG.2017.2670679.

[83] P. Baumgartner et al. "Limitations of the pattern multiplication technique for uniformly spaced linear antenna arrays". In: *2016 International Conference on Broadband Communications for Next Generation Networks and Multimedia Applications (CoBCom)*. 2016, pp. 1–7. DOI: 10.1109/COBCOM.2016.7593492.

[84] P. Baumgartner et al. "Multi-Objective Optimization of Yagi-Uda Antenna Applying Enhanced Firefly Algorithm With Adaptive Cost Function". In: *IEEE Transactions on Magnetics* 54.99 (2017), pp. 1–4. DOI: 10.1109/TMAG.2017.2764319.

[85] T. Bauernfeind et al. "Multi-Objective Synthesis of NFC-Transponder Systems Based on PEEC Method". In: *IEEE Transactions on Magnetics* PP.99 (2017), pp. 1–4. DOI: 10.1109/TMAG.2017.2771366.

[86] D. Romano et al. "Rigorous DC Solution of Partial Element Equivalent Circuit Models". In: *IEEE Transactions on Circuits and Systems I: Regular Papers* 63.9 (2016), pp. 1499–1510. DOI: 10.1109/TCSI.2016.2578286.

[87] L. Lombardi, D. Romano, and G. Antonini. "Accurate and Efficient Low-Frequency Solution of Partial Element Equivalent Circuit Models". In: *IEEE Transactions on Electromagnetic Compatibility* 59.5 (2017), pp. 1514–1522. DOI: 10.1109/TEMC.2017.2651022.

[88] T. Davis. *Direct Methods for Sparse Linear Systems*. Society for Industrial and Applied Mathematics, 2006. DOI: 10.1137/1.9780898718881.

[89] F. Freschi. "Fast Block-Solution of PEEC Equations". In: *IEEE Transactions on Magnetics* 49.5 (2013), pp. 1753–1756. DOI: 10.1109/TMAG.2013.2238225.

[90] J. Markkanen, P. Yla-Oijala, and S. Jarvenpaa. "On the spectrum and preconditioning of electromagnetic volume integral equations". In: *2016 URSI International Symposium on Electromagnetic Theory (EMTS)* (2016), pp. 834–837. DOI: 10.1109/URSI-EMTS.2016.7571533.

[91] R. Misawa, N. Nishimura, and M. S. Tong. "Preconditioning of Periodic Fast Multipole Method for Solving Volume Integral Equations". In: *IEEE Transactions on Antennas and Propagation* 62.9 (2014), pp. 4799–4804. DOI: 10.1109/TAP.2014.2327652.

[92] T. Xia et al. "An Enhanced Augmented Electric-Field Integral Equation Formulation for Dielectric Objects". In: *IEEE Transactions on Antennas and Propagation* 64.6 (2016), pp. 2339–2347. DOI: 10.1109/TAP.2016.2537389.

[93] L. Jeonghwa, Z. Jun, and L. Cai-Cheng. "Incomplete LU preconditioning for large scale dense complex linear systems from electromagnetic wave scattering problems". In: *Journal of Computational Physics* 185.1 (2003), pp. 158 –175. DOI: https://doi.org/10.1016/S0021-9991(02)00052-9.

[94] P. Yla-Oijala and M. Taskinen. "Well-conditioned Muller formulation for electromagnetic scattering by dielectric objects". In: *IEEE Transactions on Antennas and Propagation* 53.10 (2005), pp. 3316–3323. DOI: 10.1109/TAP.2005.856313.

[95] K. F. Warnick. *Numerical analysis for electromagnetic integral equations*. Artech House, 2008.

[96] W. Chew, M. Tong, and B. Hu. *Integral Equation Methods for Electromagnetic and Elastic Waves*. Morgan and Claypool, 2008. ISBN: 9781598291490.

[97] F. P. Andriulli. "Loop-Star and Loop-Tree Decompositions: Analysis and Efficient Algorithms". In: *IEEE Transactions on Antennas and Propagation* 60.5 (2012), pp. 2347–2356. DOI: 10.1109/TAP.2012.2189723.

[98] A. M. Turing. "Rounding–Off Errors In Matrix Process". In: *The Quarterly Journal of Mechanics and Applied Mathematics* 1.1 (1948), pp. 287–308. DOI: 10.1093/qjmam/1.1.287.

[99] N. Higham. *Accuracy and Stability of Numerical Algorithms*. Society for Industrial and Applied Mathematics, 2002. DOI: 10.1137/1.9780898718027.

[100] J. Markkanen et al. "Analysis of Volume Integral Equation Formulations for Scattering by High-Contrast Penetrable Objects". In: *IEEE Transactions on Antennas and Propagation* 60.5 (2012), pp. 2367–2374. DOI: 10.1109/TAP.2012.2189704.

[101] I. Munteanu. "Tree-Cotree Condensation Properties". In: *International COMPUMAG Society Newsletter* (2002), pp. 10–14.

[102] R. Albanese and G. Rubinacci. *Finite Element Methods for the Solution of 3D Eddy Current Problems*. Ed. by P. W. Hawkes. Vol. 102. Elsevier, 1997, pp. 1 –86. DOI: https://doi.org/10.1016/S1076-5670(08)70121-6.

[103] P. Dłotko and R. Specogna. "Physics inspired algorithms for (co)homology computations of three-dimensional combinatorial manifolds with boundary". In: *Computer Physics Communications* 184.10 (2013), pp. 2257 –2266. DOI: https://doi.org/10.1016/j.cpc.2013.05.006.

[104] M. K. Li and W. C. Chew. "Applying divergence-free condition in solving the volume integral equation". In: *Progress in Electromagnetics Research* 57 (2006), pp. 311–333. DOI: 10.2528/PIER05061303.

[105] L. O. Chua and P. Y. Lin. *Computer-Aided Analysis of Electronic Circuits: Algorithms and Computational Techniques*. Prentice Hall Professional Technical Reference, 1975. ISBN: 0131654152.

[106] A. Ataei. *Fast Reduced Row Echelon Form MATLAB® library*. 2016. URL: https://www.mathworks.com/matlabcentral/fileexchange/21583-fast-reduced-row-echelon-form.

[107] T. T. Nguyen et al. "An Integral Formulation for the Computation of 3-D Eddy Current Using Facet Elements". In: *IEEE Transactions on Magnetics* 50.2 (2014), pp. 549–552. DOI: 10.1109/TMAG.2013.2282957.

[108] G. Karypis et al. *METIS - Serial Graph Partitioning and Fill-reducing Matrix Ordering*. 2019. URL: http://glaros.dtc.umn.edu/gkhome/metis/metis/overview.

[109] X. Qi et al. "Discrete Quasi-Helmholtz Decomposition for 3-D High-Contrast Lossy Dielectric Problems". In: *IEEE Antennas and Wireless Propagation Letters* 16 (2017), pp. 1480–1483. DOI: 10.1109/LAWP.2016.2646747.

[110] G. Vecchi. "Loop-star decomposition of basis functions in the discretization of the EFIE". In: *IEEE Transactions on Antennas and Propagation* 47.2 (1999), pp. 339–346. DOI: 10.1109/8.761074.

[111] C. Forestiere et al. "A Frequency Stable Volume Integral Equation Method for Anisotropic Scatterers". In: *IEEE Transactions on Antennas and Propagation* 65.3 (2017), pp. 1224–1235. DOI: 10.1109/TAP.2016.2647585.

[112] J.-F. Lee, R. Lee, and R. J. Burkholder. "Loop star basis functions and a robust preconditioner for EFIE scattering problems". In: *IEEE Transactions on Antennas and Propagation* 51.8 (2003), pp. 1855–1863. DOI: 10.1109/TAP.2003.814736.

[113] T. Bauernfeind et al. "Finite Element Simulation of Impedance Measurement Effects of NFC Antennas". In: *IEEE Transactions on Magnetics* 51.3 (2015), pp. 1–4. DOI: 10.1109/TMAG.2014.2354982.

[114] P. Goubier. "Etude et Conception de composants passifs LCT intégrés". Theses. Université Joseph-Fourier - Grenoble I, 2003.

[115] R. Kriemann. *HLIBPro (v.2.7)*. 2017. URL: http://www.hlibpro.com.

[116] F. H. Rouet et al. *STRUMPACK (v.1.1.1)*. 2018. URL: http://portal.nersc.gov/project/sparse/strumpack/.

[117] S. Massei, D. Palitta, and L. Robol. "Solving Rank-Structured Sylvester and Lyapunov Equations". In: *SIAM Journal on Matrix Analysis and Applications* 39 (2017). DOI: 10.1137/17M1157155.

[118] T.-L. Lee, T.-Y. Li, and Z. Zeng. "A Rank-Revealing Method with Updating, Downdating, and Applications." In: *SIAM J. Matrix Anal. Appl.* 31.2 (May 2009), pp. 503–525. DOI: 10.1137/07068179X.

[119] J. Xia et al. "Fast algorithms for hierarchically semiseparable matrices". In: *Numerical Linear Algebra with Applications* 17.6 (2010), pp. 953–976. DOI: 10.1002/nla.691.

[120] W. Hackbusch and S. Börm. "Data-sparse Approximation by Adaptive H2-Matrices". In: *Computing* 69.1 (2002), pp. 1–35. DOI: 10.1007/s00607-002-1450-4.

[121] S. Börm, L. Grasedyck, and W. Hackbusch. "Introduction to hierarchical matrices with applications". In: *Engineering Analysis with Boundary Elements* 27.5 (2003), pp. 405 – 422. DOI: https://doi.org/10.1016/S0955-7997(02)00152-2.

[122] R. Kriemann and S. Le Borne. "H-FAINV: hierarchically factored approximate inverse preconditioners". In: *Computing and Visualization in Science* 17 (2015). DOI: 10.1007/s00791-015-0254-y.

[123] R. Kriemann. "H-LU factorization on many-core systems". In: *Computing and Visualization in Science* 16.3 (2013), pp. 105–117. DOI: 10.1007/s00791-014-0226-7.

[124] W. Hackbush L. Grasedyck and R. Kriemann. "Performance Of H-Lu Preconditioning For Sparse Matrices". In: *Computational Methods in Applied Mathematics* 8.4 (2008), pp. 336–349. DOI: 10.2478/cmam-2008-0024.

[125] L. Grasedyck, Ronald Kriemann, and Sabine Le Borne. "Parallel black box H-LU preconditioning for elliptic boundary value problems". In: *Computing and Visualization in Science* 11.4 (2008), pp. 273–291. DOI: 10.1007/s00791-008-0098-9.

[126] F.-H. Rouet et al. "A Distributed-Memory Package for Dense Hierarchically Semi-Separable Matrix Computations Using Randomization". In: *ACM Trans. Math. Softw.* 42.4 (2016), 27:1–27:35. DOI: 10.1145/2930660.

[127] P. Martinsson. "A Fast Randomized Algorithm for Computing a Hierarchically Semiseparable Representation of a Matrix". In: *SIAM Journal on Matrix Analysis and Applications* 32.4 (2011), pp. 1251–1274. DOI: 10.1137/100786617.

[128] J. Markkanen and P. Yla-Oijala. "Discretization of Electric Current Volume Integral Equation With Piecewise Linear Basis Functions". In: *IEEE Transactions on Antennas and Propagation* 62 (2014), pp. 4877–4880. DOI: 10.1109/TAP.2014.2334705.

[129] J. Markkanen, P. Yla-Oijala, and A. Sihvola. "Discretization of Volume Integral Equation Formulations for Extremely Anisotropic Materials". In: *IEEE Transactions on Antennas and Propagation* 60.11 (2012), pp. 5195–5202. DOI: 10.1109/TAP.2012.2207675.

[130] D. Voltolina et al. "High-Performance PEEC Analysis of Electromagnetic Scatterers". In: *IEEE Transactions on Magnetics* 55.6 (2019), pp. 1–4. DOI: 10.1109/TMAG.2019.2894618.

[131] G. Mie. "Beiträge zur Optik trüber Medien, speziell kolloidaler Metallösungen". In: *Annalen der Physik* 330.3 (1908), pp. 377–445. DOI: 10.1002/andp.19083300302.

[132] J. Schäfer. *MatScat MATLAB® library*. 2016. URL: https://it.mathworks.com/matlabcentral/fileexchange/36831-matscat.

[133] W. Tierens et al. "3-Dimensional density profiles in edge plasma simulations for ICRF heating". In: *EPJ Web Conf.* 157 (2017), p. 03053. DOI: 10.1051/epjconf/201715703053.

[134] P. Alotto, P. Bettini, and R. Specogna. "Sparsification of BEM Matrices for Large-Scale Eddy Current Problems". In: *IEEE Transactions on Magnetics* 52.3 (2016), pp. 1–4. DOI: 10.1109/TMAG.2015.2488699.

[135] F. Moro et al. "Impedance design of cooking appliances with multilayer induction-efficient cookware". In: *IECON 2013 - 39th Annual Conference of the IEEE Industrial Electronics Society* (2013), pp. 5040–5045. DOI: 10.1109/IECON.2013.6699952.

[136] A. Virgillito F. Freschi P. Alotto V. Cirimele R. Torchio. "Challenges in the Electromagnetic Modeling of Road Embedded Wireless Power Transfer". In: *Energies* 12 (2019), pp. 1–22. DOI: 10.3390/enxx010005.

[137] O. Chadebec G. Meunier T.-S. Nguyen J.-M. Guichon and B. Vincent. "An Independent Loops Search Algorithm for Solving Inductive Peec Large Problems". In: *Progress In Electromagnetics Research* 23 (2012), pp. 53–63. DOI: doi:10.2528/PIERM11111503.

[138] R. Mittra. *Integral equation methods for transient scattering*. Berlin, Heidelberg: Springer Berlin Heidelberg, 1976. ISBN: 978-3-540-38095-5. DOI: 10.1007/3540075534_7.

[139] A. Quarteroni. *Numerical Models for Differential Problems*. Springer, 2014. ISBN: 9788847055216.

[140] G. Manara, A. Monorchio, and R. Reggiannini. "A space-time discretization criterion for a stable time-marching solution of the electric field integral equation". In: *IEEE Transactions on Antennas and Propagation* 45.3 (1997), pp. 527–532. DOI: 10.1109/8.558668.

[141] A. Ruehli. "Partial element equivalent circuit (PEEC) method and its application in the frequency and time domain". In: *Proceedings of Symposium on Electromagnetic Compatibility* (1996), pp. 128–133. DOI: 10.1109/ISEMC.1996.561214.

[142] H. Heeb and A. E. Ruehli. "Three-dimensional interconnect analysis using partial element equivalent circuits". In: *IEEE Transactions on Circuits and Systems I: Fundamental Theory and Applications* 39.11 (1992), pp. 974–982. DOI: 10.1109/81.199878.

[143] H. Heeb and A. Ruehli. "Approximate time-domain models of three-dimensional interconnects". In: *Proceedings., 1990 IEEE International Conference on Computer Design: VLSI in Computers and Processors* (1990), pp. 201–205. DOI: 10.1109/ICCD.1990.130202.

[144] T. Sekine and H. Asai. "Full-wave PEEC time domain solver based on leapfrog scheme". In: *2011 IEEE 20th Conference on Electrical Performance of Electronic Packaging and Systems* (2011), pp. 181–184. DOI: 10.1109/EPEPS.2011.6100221.

[145] G. Antonini C. Gianfagna L. Lombardi. "Marching-on-in-time solution of delayed PEEC models of conductive and dielectric objects". In: *IET Microwaves, Antennas and Propagation* 13.1 (2019), pp. 42–47. DOI: 10.1049/iet-map.2018.5233.

[146] L. Lombardi et al. "Time-Domain Sensitivity Analysis of Delayed Partial Element Equivalent Circuits". In: *IEEE Transactions on Electromagnetic Compatibility* (2018), pp. 1–9. DOI: 10.1109/TEMC.2018.2866378.

[147] S. B. Sayed, H. A. Ulku, and H. Bagci. "A Stable Marching On-In-Time Scheme for Solving the Time-Domain Electric Field Volume Integral Equation on High-Contrast Scatterers". In: *IEEE Transactions on Antennas and Propagation* 63.7 (2015), pp. 3098–3110. DOI: 10.1109/TAP.2015.2429736.

[148] Y. Liu et al. "A Scalable Parallel PWTD-Accelerated SIE Solver for Analyzing Transient Scattering From Electrically Large Objects". In: *IEEE Transactions on Antennas and Propagation* 64.2 (2016), pp. 663–674. DOI: 10.1109/TAP.2015.2508483.

[149] E. van't Wout et al. "Design of Temporal Basis Functions for Time Domain Integral Equation Methods With Predefined Accuracy and Smoothness". In: *IEEE Transactions on Antennas and Propagation* 61.1 (2013), pp. 271–280. DOI: 10.1109/TAP.2012.2220318.

[150] B. Shanker et al. "Time Domain Integral Equation Analysis of Scattering From Composite Bodies via Exact Evaluation of Radiation Fields". In: *IEEE Transactions on Antennas and Propagation* 57.5 (2009), pp. 1506–1520. DOI: 10.1109/TAP.2009.2016700.

[151] Y. Shi et al. "Stable Electric Field TDIE Solvers via Quasi-Exact Evaluation of MOT Matrix Elements". In: *IEEE Transactions on Antennas and Propagation* 59.2 (2011), pp. 574–585. DOI: 10.1109/TAP.2010.2096402.

[152] H. A. Ülkü, H. Bağcı, and E. Michielssen. "Marching On-In-Time Solution of the Time Domain Magnetic Field Integral Equation Using a Predictor-Corrector Scheme". In: *IEEE Transactions on Antennas and Propagation* 61.8 (2013), pp. 4120–4131. DOI: 10.1109/TAP.2013.2262016.

[153] A. Sadigh and E. Arvas. "Treating the instabilities in marching-on-in-time method from a different perspective (electromagnetic scattering)". In: *IEEE Transactions on Antennas and Propagation* 41.12 (1993), pp. 1695–1702. DOI: 10.1109/8.273314.

[154] D. Jiao et al. "A fast higher-order time-domain finite element-boundary integral method for 3-D electromagnetic scattering analysis". In: *IEEE Transactions on Antennas and Propagation* 50.9 (2002), pp. 1192–1202. DOI: 10.1109/TAP.2002.801375.

[155] J. Li and B. Shanker. "Time-Dependent Debye–Mie Series Solutions for Electromagnetic Scattering". In: *IEEE Transactions on Antennas and Propagation* 63.8 (2015), pp. 3644–3653. DOI: 10.1109/TAP.2015.2439294.

[156] D. S. Weile et al. "A novel scheme for the solution of the time-domain integral equations of electromagnetics". In: *IEEE Transactions on Antennas and Propagation* 52.1 (2004), pp. 283–295. DOI: 10.1109/TAP.2003.822450.

[157] A. Pesce, A. De Lorenzi, and L. Grando. "A new approach to passive protection against high energy and high current breakdowns in the ITER NBI accelerator". In: *Fusion Engineering and Design* 84.7 (2009), pp. 1499 –1504. DOI: https://doi.org/10.1016/j.fusengdes.2009.01.019.

[158] S. P. Walker, M. J. Bluck, and I. Chatzis. "The stability of integral equation time-domain scattering computations for three-dimensional scattering; similarities and differences between electrodynamic and elastodynamic computations". In: *International Journal of Numerical Modelling: Electronic Networks, Devices and Fields* 15.5-6 (2002), pp. 459–474. DOI: 10.1002/jnm.473.

[159] D. Xiu. *Numerical Methods for Stochastic Computations: A Spectral Method Approach*. Princeton, NJ, USA: Princeton Univ. Press, 2010.

[160] L. Codecasa and . Di Rienzo. "Stochastic finite integration technique for magnetostatic problems". In: *International Journal of Numerical Modelling: Electronic Networks, Devices and Fields* 30.6 (2017), e2209. DOI: 10.1002/jnm.2209.

[161] L. Codecasa and L. Di Rienzo. "Stochastic Finite Integration Technique for Eddy-Current Problems". In: *IEEE Transactions on Magnetics* 51.3 (2015), pp. 1–4. DOI: 10.1109/TMAG.2014.2356716.

[162] L. Codecasa and L. Di Rienzo. "Stochastic Finite Integration Technique Formulation for Electrokinetics". In: *IEEE Transactions on Magnetics* 50.2 (2014), pp. 573–576. DOI: 10.1109/TMAG.2013.2280522.

[163] R. Torchio, L. Di Rienzo, and L. Codecasa. "Stochastic PEEC Method Based on Polynomial Chaos Expansion". In: *IEEE Transactions on Magnetics* 55.6 (2019), pp. 1–4. DOI: 10.1109/TMAG.2019.2908588.

[164] L. Codecasa and L. Di Rienzo. "MOR-Based Approach to Uncertainty Quantification in Electrokinetics With Correlated Random Material Parameters". In: *IEEE Transactions on Magnetics* 53.6 (2017), pp. 1–4. DOI: 10.1109/TMAG.2017.2666845.

[165] A. Litvinenko et al. "Computation of Electromagnetic Fields Scattered From Objects With Uncertain Shapes Using Multilevel Monte Carlo Method". In: *IEEE Journal on Multiscale and Multiphysics Computational Techniques* 4 (2019), pp. 37–50. DOI: 10.1109/JMMCT.2019.2897490.

[166] K. S. Miller. "On the Inverse of the Sum of Matrices". In: *Mathematics Magazine* 54.2 (1981), pp. 67–72. DOI: 10.2307/2690437.

[167] T. Rikitake. *Magnetic and Electromagnetic Shielding*. Springer Netherlands, 1987. ISBN: 9789027724069.

[168] G. Rozza, D B P Huynh, and A. T Patera. "Reduced Basis Approximation and a Posteriori Error Estimation for Affinely Parametrized Elliptic Coercive Partial Differential Equations". In: *Archives of Computational Methods in Engineering* 15.3 (2008), pp. 229–275. DOI: 10.1007/s11831-008-9019-9.

[169] P. Chen. "Model Order Reduction Techniques for Uncertainty Quantification Problems". PhD thesis. EPFL, 2014. DOI: 10.5075/epfl-thesis-6118.

[170] G. von Winckel. *SPARSE_GRI_HW MATLAB® library*. URL: https://it.mathworks.com/matlabcentral/fileexchange/36831-matscat.

[171] R. B. Nelsen. *An Introduction to Copulas*. Springer, 1999.

[172] F. J. Massey Jr. "The Kolmogorov-Smirnov Test for Goodness of Fit". In: *Journal of the American Statistical Association* 46.253 (1951), pp. 68–78. DOI: 10.1080/01621459.1951.10500769.

[173] V. Ardon. "Méthodes Numériques et outils logiciels pour la prise en compte des effets capacitifs dans la modélisation CEM de dispositifs d'électronique de puissance". Theses. Institut National Polytechnique de Grenoble - INPG, June 2010.

[174] T. T. Nguyen. "Méthode PEEC inductive par élément de facette pour la modélisation des régions conductrices volumiques et minces". Thèse de doctorat dirigée par Meunier, Gérard, Chadebec, Olivier et Guichon, Jean-Michel Génie électrique Grenoble 2014. PhD thesis. 2014.

[175] I. V. Oseledets. "Tensor-Train Decomposition". In: *SIAM Journal on Scientific Computing* 33.5 (2011), pp. 2295–2317. DOI: 10.1137/090752286.

[176] E. Corona, A. Rahimian, and D. Zorin. "A Tensor-Train accelerated solver for integral equations in complex geometries". In: *Journal of Computational Physics* 334 (2017), pp. 145 –169. ISSN: 0021-9991. DOI: https://doi.org/10.1016/j.jcp.2016.12.051.

[177] G. Chitarin, M. Guarnieri, and A. Stella. "An integral formulation for eddy current analyses in axisymmetric configurations". In: *IEEE Transactions on Magnetics* 25.5 (1989), pp. 4330–4342. DOI: 10.1109/20.42600.

[178] S. Datta. "Electric and Magnetic Fields from a Circular Coil Using Elliptic Integrals". In: *Phys. Educ.* (2007).

[179] A. Weinstein. "Generalized axially symmetric potential theory". In: *Bull. Amer. Math. Soc.* 59.1 (1953), pp. 20–38.

[180] J. Simpson et al. "Simple Analytic Expressions for the Magnetic Field of a Circular Current Loop". In: (2003).

[181] O. Ciftja and I. Hysi. "The electrostatic potential of a uniformly charged disk as the source of novel mathematical identities". In: *Applied Mathematics Letters* 24.11 (2011), pp. 1919 –1923. DOI: https://doi.org/10.1016/j.aml.2011.05.019.

[182] J.-M Huré. "Solutions of the axi-symmetric Poisson equation from elliptic integrals". In: *Astronomy and Astrophysics* (2004). DOI: 10.1051/0004-6361:20034194.

[183] R. P. Clayton. *Inductance: Loop and Partial*. John Wiley & Sons, Inc., 2010. DOI: 10.1002/9780470561232.